
Optically and X-ray Selected Galaxy Groups at Intermediate Redshift

Jennifer Lynn Connelly



München 2012

Optically and X-ray Selected Galaxy Groups at Intermediate Redshift

Jennifer Lynn Connelly

Dissertation
an der Physik
der Ludwig–Maximilians–Universität
München

vorgelegt von
Jennifer Lynn Connelly
aus Williamsport, PA, USA

München, den 18. Mai 2012

The universe as we know it is a joint product of the observer
and the observed.

Pierre Teilhard de Chardin

Erstgutachter: Prof. Dr. Roberto Saglia
Zweitgutachter: Prof. Dr. Joseph Mohr
Tag der mündlichen Prüfung: 6. Juli 2012

Contents

Table of Contents	v
List of Figures	ix
List of Tables	xi
Abstract	xiii
Zusammenfassung	xv
1 Introduction	1
1.1 What is a Group?	1
1.2 Group Identification & Previous Surveys	2
1.2.1 Identification Methods Ideal for Clusters	2
1.2.2 Group Identification Methods	4
1.2.3 Existing Group Surveys	6
1.3 Scaling Relations and Masses of Groups	7
1.4 Aims and Outline of the Thesis	11
2 GEEC Project Background	13
2.1 Optically (Spectroscopically) Selected Groups	13
2.2 GEEC Project	14
2.3 Paper I	18
2.3.1 Number Density and Detection of Groups	18
2.3.2 Stacked Weak Lensing Analysis	20
3 X-ray Data, Sample Definition, and Brightness	23
3.1 X-ray Data & Reduction	23
3.1.1 XMM Data Reduction	24
3.1.2 Chandra Data & Reduction	27
3.1.3 Combined X-ray Imaging	28
3.2 X-ray Group Sample Definition & X-ray Brightness	28
3.2.1 Extended Source Detection	28
3.2.2 Significance, Fluxes, and Luminosities	28
3.2.3 Aperture Tests	39
4 Follow-up Spectroscopy and Measured Group Properties	43

4.1	Follow-up Spectroscopy	43
4.1.1	FORS2 Observations	44
4.1.2	IMACS Observations	51
4.1.3	Additional Spectroscopy	55
4.1.4	Object Redshift Catalog	55
4.2	Measuring Group Properties	56
4.2.1	X-ray Selected Group Redshifts	57
4.2.2	Group Membership	62
4.2.3	Group Centers	64
4.2.4	Radial Cuts	64
4.3	Matched X-ray - Optical Systems	69
4.4	Dynamical Complexity	69
4.4.1	Descriptions of Tests	69
4.4.2	Effect of Dynamical Complexity	70
5	L_X-σ Relation	89
5.1	Bayesian Best Fits	89
5.2	L _X - σ Relation Results	92
6	Group Masses	95
6.1	NIR Photometry and Stellar Mass	95
6.1.1	NIR Observations	95
6.1.2	Galaxy Stellar Masses	95
6.2	Group Mass Estimates	96
6.2.1	Group Dynamical Mass	96
6.2.2	Group X-ray Mass	96
6.2.3	Group Stellar Mass	97
6.3	Total Mass Measurements	103
6.4	Mass in Stars	105
6.4.1	M _{stellar} - σ Relation	105
6.4.2	Stellar Versus ‘Total’ Group Mass	107
6.4.3	Stellar Mass Fractions	112
7	Exploring Stellar Mass and X-ray Brightness: Underluminous Groups	115
7.1	X-ray Underluminous Groups	117
7.2	X-ray Overluminous Groups	120
8	Conclusions	121
Appendix: Spectroscopic Redshifts		125
Bibliography		188
Acknowledgements		189

List of Figures

1.1	Optical image of Stephan's Quintet with X-ray image overlaid	2
1.2	Illustration of wavelet decomposition	5
1.3	Zimer et al. (2002) $L_X - \sigma$ relation for X-ray detected groups and clusters	10
2.1	Multiwavelength coverage map of the CNOC2 RA14h field	15
2.2	Multiwavelength coverage map of the CNOC2 RA21h field	16
2.3	Predicted number density as a function of redshift	19
2.4	Probability of group detection as a function of halo mass	20
2.5	Weak lensing: stacked tangential shear profiles	22
3.1	X-ray exposure maps	25
3.2	X-ray signal-to-noise maps	29
3.3	X-ray wavelet maps of the RA14h field	30
3.4	X-ray wavelet maps of the RA21h field	31
3.5	X-ray significance of optically selected systems	32
3.6	X-ray luminosity as a function of redshift	34
3.7	X-ray aperture comparison for matched X-ray - optical systems	40
3.8	X-ray aperture comparison for all X-ray systems	41
4.1	Example FORS2 mask	45
4.2	FORS2 sky subtraction results example	48
4.3	Raw spectra example	49
4.4	Reduced spectra example	49
4.5	ZSPEC redshift evaluation example	50
4.6	Redshift offset and error evaluation	52
4.7	Redshift error evaluation continued	53
4.8	X-ray group redshift evaluation Q=1 group example	59
4.9	X-ray group redshift evaluation Q=1 group example continued	60
4.10	X-ray group redshift evaluation Q=3 group example	61
4.11	X-ray group redshift evaluation Q=3 group example continued	62
4.12	Velocity dispersion as a function of redshift for all X-ray and optical systems	63
4.13	Histogram of offset between X-ray and luminosity-weighted group centers	64
4.14	Results of dynamical complexity tests for group XR14h09	72
4.15	Bubble-plots and velocity distributions for all systems with dynamical complexity	73

4.16 Comparison of velocity dispersions measured within $r_{200,X}$ and calculated as in Eq. 4.4 using $r_{200,X}$	85
4.17 X-ray substructure groups image	87
5.1 Example of evaluation of Kelly Bayesian best fit results	91
5.2 $L_X-\sigma$ relation for X-ray and optically selected systems for all radial cuts	93
6.1 Stellar mass limit as a function of redshift	98
6.2 M_X-M_{dyn} relation for quality 1 & 2 X-ray and optical systems within $r_{200,X}$	104
6.3 $M_{stellar}-\sigma$ relation for X-ray and optically selected systems for all radial cuts	106
6.4 $M_{dyn}-M_{stellar}$ relation for quality 1 & 2 X-ray and optical systems within $r_{200,X}$	108
6.5 $M_X-M_{stellar}$ relation for quality 1 & 2 X-ray systems within $r_{200,X}$	109
6.6 Histograms of the offset of the most massive galaxy from the group center and versus total (X-ray) group mass	111
6.7 Stellar mass fraction versus total mass	113
7.1 $M_{stellar}-L_X$ and $M_{dyn}-L_X$ relations for X-ray and optically selected systems with underluminous optical systems highlighted.	116
7.2 Histograms of $M_{stellar}^{MMG}/M_{stellar}$ for different subsets of groups	118
7.3 Cumulative distribution of matched sample groups having $M_{stellar}^{MMG}/M_{stellar} < 40\%$	119
7.4 Cumulative distribution of matched sample groups having $M_{stellar}^{MMG}/M_{stellar} > 50\%$	119

List of Tables

2.1	Weak Lensing Results	21
3.1	Basic Properties of X-ray Selected Groups	36
3.2	Basic Properties of Optically Selected Groups	38
4.1	Summary of Supplemental Spectroscopy	56
4.2	Measured Properties of X-ray Selected Groups	66
4.3	Measured Properties of Optically Selected Groups	68
4.4	Summary of Dynamical Complexity Test Results	71
5.1	L_X - σ Relation Bayesian Best Fits	90
5.2	L_X - σ Relation Bayesian Best Fits with Groups Subdivided at $N_{mem} = 10$	94
6.1	Masses of X-ray Selected Groups	100
6.2	Masses of Optically Selected Groups	102
6.3	$M_{stellar}$ - σ Relation Bayesian Best Fits	105
6.4	M_{dyn} - $M_{stellar}$ Relation Bayesian Best Fits	110
6.5	M_X - $M_{stellar}$ Relation Bayesian Best Fits	110
7.1	L_X - $M_{stellar}$ Relation Bayesian Best Fits	117
1	Spectroscopic Redshifts	125

Abstract

In this thesis I present the properties of two samples of galaxy groups containing 39 high quality X-ray selected systems and 38 optically (spectroscopically) selected systems in coincident spatial regions at $0.12 < z < 0.79$. Only nine optical systems are associable with X-ray systems. I discuss the confusion inherent in the matching of both galaxies to extended X-ray emission and of X-ray emission to already identified optical systems. Extensive spectroscopy has been obtained and the resultant redshift catalog and group membership are provided here. X-ray, dynamical, and total stellar masses (integrated down to a limit of $10^{10} M_{\odot}$) of the groups are also derived and presented. The total mass range of the combined sample is $\sim 10^{12} - 5 \times 10^{14} M_{\odot}$. I explore the effects of utilizing different centers and applying three different kinds of radial cut to the systems: a constant cut of 1 Mpc and two r_{200} cuts (roughly approximating a virial radius), one based on the velocity dispersion of the system and the other on the X-ray emission. I find that an X-ray based r_{200} tends to result in less scatter in scaling relations and less dynamical complexity of member galaxies as evidenced by results of the Anderson-Darling and Dressler-Shectman tests, indicating that this radius tends to isolate the virialized part of the system. The constant and velocity dispersion based cuts can overestimate membership and can work to inflate velocity dispersion and dynamical and stellar mass. I fit L_X - σ and $M_{stellar}$ - L_X scaling relations for X-ray and optically selected systems and find they are not dissimilar. The mean fraction of mass found in stars for my systems is ~ 0.014 with a logarithmic standard deviation of 0.398 dex. I also define and investigate a sample of groups which are X-ray underluminous given the total group stellar mass. For these systems the fraction of stellar mass contributed by the most massive galaxy is typically lower than that found for the total population of groups. 80% of 15 underluminous groups have less than 40% of their stellar mass in the most massive galaxy which only happens in less than 1% of cases with samples matched in stellar mass, taken from the combined group catalog. These results imply that there may be less Intra-Group Medium contributed from the most massive member in these systems, supporting the model of hierarchical collapse wherein a group begins with a massive galaxy and accretes mass smoothly, resulting in a group with a higher gas fraction and a more massive central galaxy than would result from the merger of roughly equivalent mass ‘subgroups’ (clumps) comprised of similar mass / luminosity galaxies.

Zusammenfassung

In dieser Doktorarbeit stelle ich zwei Samples von Galaxiengruppen vor, mit 39 Röntgenselektierten Systemen hoher Qualität und 38 optisch (spektroskopisch) selektierten Systemen in derselben Himmelsregion und im Rotverschiebungsbereich $0.12 < z < 0.79$. Nur 9 der optisch selektierten Gruppen sind mit Röntgenselektierten Gruppen assoziierbar. Ich diskutiere die Probleme sowohl bei der Zuordnung von Galaxien zu den ausgedehnten Röntgenquellen als auch bei der Zuordnung von Röntgenquellen zu optisch bereits identifizierten Systemen. Umfangreiche Spektroskopie wurde unternommen und die daraus resultierenden Rotverschiebungen und die Gruppenzugehörigkeiten werden hier in Katalogform vorgestellt. Röntgen-, dynamische- und stellare Massed (bis zu einer Grenze von $10^{10} M_{\odot}$ integriert) werden zusätzlich präsentiert. Der Massenbereich des gesamten Samples ist $\sim 10^{12} - 5 \times 10^{14} M_{\odot}$. Ich untersuche die Auswirkungen der Annahme unterschiedlicher Zentren, sowie dreier verschiedener radialer Grenzwerte: einer Konstante von 1 Mpc radius und zweier r_{200} -Grenzwerte (einem Virialradius ähnlich), einer basierend auf der Geschwindigkeitsdispersion des systems und ein zweiter basierend auf der Röntgenleuchtkraft. Ein r_{200} basierend auf der Röntgenleuchtkraft liefert weniger Streuung in Skalierungsrelationen und einer geringeren dynamischen Komplexität von Galaxien wie von den Anderson-Darling and Dressler-Shectman Tests bezeugt wird. Dies ist eine Indikation das dieser Radius den virialisierten Teil des Systems isoliert. Die Grenze basierend auf einem konstanten Radius und die basierend auf der Geschwindigkeitsdispersion überschätzen die Gruppenmitgliedschaft und führen zu überhöhten dynamischen und stellaren Massen. Ich fitte die $L_X-\sigma$ und $M_{stellar}-L_X$ Relationen der optisch- und Röntgenselektierten Systeme und finde, dass sie nicht unähnlich sind. Die mittlere Massenfraktion in Sterne in diesen Systemen ist ~ 0.014 mit einer logarithmischen Standardabweichung von 0.398 dex. Ich untersuche auch ein Sample von Gruppen die leuchtschwach im Röntgenbereich sind verglichen mit ihrer gesamtenstellaren Masse. In diesen Systemem ist der Anteil derstellaren Masse, die von der massivsten Galaxie in der Gruppe beigetragen wird, typischerweise niedriger als in der Gesamtpopulation der Gruppen. 80% von 15 leuchtschwachen Gruppen haben einen Massenbeitrag von weniger als 40% von der massivsten Galaxie. Dies ist nur in 0.89% der Gruppen der Fall, wenn das gesamte Sample betrachtet wird. Diese Ergebnisse bedeuten, dass der Beitrag der massivsten Galaxie zum Intragruppenmedium in solchen Gruppen kleiner ist. Dies stärkt das Modell der hierarchischen Kollaps in dem eine Gruppe mit einer massiven Galaxie beginnt und dann kontinuierlich Masse akkretiert, was zu einer Gruppe mit einem höheren Gasanteil und einer massiveren zentralen Galaxie führt, als der Fall wäre wenn die Gruppe das Ergebniss eines Mergers von Subgruppen von vergleichbarer Masse und vergleichbarer Galaxien (-leuchtkraft) wäre.

Introduction

The majority of galaxies in the Universe, including our own, lie in galaxy groups: concentrations of galaxies embedded in extended dark matter halos (Eke et al., 2004). Over cosmic time, groups grow hierarchically by accreting individual galaxies and smaller groups from their surrounding filamentary structure; thus, they are evolving environments. Even within limited redshift regimes, groups are observed to have diverse properties. Local studies (e.g. Zabludoff & Mulchaey, 2000) reveal that their galaxy populations vary from being dominated by early (as in typical clusters) to late-type (as in the field population) galaxies. They range from ‘poor’ groups containing a relatively small number of galaxies (commonly identified via optical selection methods) to massive systems (commonly identified via X-ray emission and weak lensing). The typical velocity dispersion within galaxy groups is comparable to the internal velocities of the galaxies they contain, making them ideal for galaxy-galaxy mergers and interactions.

Therefore, groups are both important in their own right and as the predominant environment of galaxies.

1.1 What is a Group?

Typically, groups possess dark matter halos with masses of roughly $10^{12.5}$ - 10^{14} M_{\odot} (Huchra & Geller, 1982). The velocity dispersion (σ ; the range of velocities about the mean velocity of the group) is on average of order $\sigma \sim 250$ km s $^{-1}$ but can range from tens to several hundreds, and the extent is typically less than a megaparsec [Mpc]. Groups can be very compact. One such example, and the first of its kind ever discovered, is a group of four galaxies in a visual grouping of galaxies called Stephan’s Quintet (Huchra & Geller, 1982, see Fig. 1.1) called Hickson Compact Group 92. The galaxies in these aptly named ‘compact’ groups are separated on the sky by only a few galactic radii while ‘loose’ groups appear more diffuse. Groups are composed of galaxies which are physically associated – but are not necessarily virialized systems. They are the intermediate link between the isolated field and cluster environments. Groups *may* share cluster properties (e.g. cD-like galaxy at center, X-ray emitting Intra-Group Medium, etc.) but

are less massive, contain fewer galaxies with lower velocity dispersions, and may be in a range of evolutionary states.



Figure 1.1: Optical image of Stephan’s Quintet (including Hickson Compact Group 92) with X-ray image overlaid. The galaxy at bottom right is not part of the group.

Image Credits: X-ray (cyan): NASA/CXC/CfA/E. O’Sullivan

Optical: Canada-France-Hawaii-Telescope/Coelum

1.2 Group Identification & Previous Surveys

1.2.1 Identification Methods Ideal for Clusters

Despite their ubiquity, galaxy groups are not trivial to identify. Large surveys of clusters are more common, as samples of these higher mass systems, which are brighter than groups at all wavelengths, are more easily defined. In the cluster regime, both gravitational lensing (see e.g. Marian & Bernstein, 2006; Miyazaki et al., 2007; Massey et al., 2007 or review by Refregier, 2003) and the Sunyaev-Zel’dovich (SZ) effect (Sunyaev & Zeldovich, 1972 and e.g. LaRoque

et al., 2003) can be used to identify systems up to intermediate redshifts. Additionally, the so-called red sequence method can be used and has been particularly successful at high redshifts. I describe these three techniques briefly here.

- **Gravitational Lensing:**

Strong Lensing – Clusters can act as strong gravitational lenses, bending (lensing) the light of a background source such that multiple images are formed. At present, only a relatively small number of systems have been detected in this way although work to make this method more applicable to large surveys is in progress (e.g. Gladders et al., 2003).

Weak Lensing – Gravitational weak lensing is the *minor* distortion of the shapes and sizes of background sources due to a massive foreground object. At high redshifts, only the most massive clusters can be found via this method since the cross section for gravitational lensing falls relatively rapidly with z . Cluster mass and density profiles on large scales are dominated by dark matter, and weak lensing provides a measure of the shape of the system's gravitational potential at relatively large radii. The method has become very successful in recent years (Dahle, 2007; Hoekstra & Jain, 2008; Sheldon et al., 2009; Okabe et al., 2010). Currently, weak lensing measurements can only reliably detect relatively massive systems ($M \gtrsim 10^{14} M_{\odot}$) individually, though stacking techniques allow for the exploration of multiple systems as an ensemble (Parker et al., 2005). The weak lensing method will also likely produce group samples dominated by constituents which are more concentrated than the typical group population (Broadhurst et al., 2005; Oguri et al., 2009).

- **SZ Effect:**

The Sunyaev-Zeldovich (SZ) effect is the distortion of the cosmic microwave background (CMB) spectrum due to the hot intracluster medium (ICM). Since the SZ signal changes brightness with the mass of the cluster, but does not decrease with redshift, it is a potentially powerful tool for identifying clusters at high z . Unfortunately, this is limited by confusion with resultant errors increasing for lower mass objects. Thus, the signal of SZ may be overwhelmed by the background before reaching the sensitivity needed to detect objects with masses typical of galaxy groups (Holder et al., 2007).

- **Red Sequence Technique:**

The Red Sequence Technique uses the early-type (red) galaxies as markers for cluster detection and utilizes the existence of a population of galaxies which exhibit a tight relationship in color-magnitude space (the so-called red sequence, Gladders & Yee, 2005; see e.g. Koester et al., 2007). The technique has already produced large (10^4) cluster samples. However, because this method requires a significant number of red galaxies and may result in samples biased towards relaxed dynamical states or older formation ages of the group (Smith & Taylor, 2008; Dariush et al., 2010), it is not ideal for identifying typical groups.

1.2.2 Group Identification Methods

For group sample identification, there are currently two primary methods utilized: X-ray emission detection (e.g. Böhringer et al., 2000; Hasinger et al., 2001; Finoguenov et al., 2007; Vikhlinin et al., 2009) and redshift surveys (e.g. Gerke et al., 2005; Miller et al., 2005; Knobel et al., 2009).

- X-ray Emission Detection:

Groups may be found via the X-ray emission of their Intra-Group Medium (IGM). Plasma heated to temperatures $\gtrsim 10^7$ K (equivalent to $\gtrsim 1$ keV) radiates very brightly in the X-ray band due primarily to thermal bremsstrahlung. Clusters glow in X-rays with typical luminosities of $\sim 10^{44}\text{--}10^{45}$ erg s $^{-1}$, while groups are normally in the range of $10^{41}\text{--}10^{43}$ erg s $^{-1}$ and have energies of roughly 0.3–2 keV. X-ray surveys are biased towards selecting groups with rich IGM, and may not be typical of the dominant group population which shapes most galaxies in the Universe.

A now commonly used technique for identifying cluster, and more recently group, emission in X-ray images is wavelet decomposition (e.g. Vikhlinin et al., 1998; Valtchanov et al., 2004; Andreon et al., 2005; Kenter et al., 2005). Wavelet analysis allows for the detection of extended sources in the presence of contaminating point sources. Like traditional Fourier methods, wavelet analysis involves approximation using the superposition of functions. While Fourier basis functions are sines and cosines, wavelet transformation requires more complicated basis functions (wavelets) which are localized in space. The advantage of wavelet analysis is that each component of the data is studied with a resolution matched to its scale. Wavelet decomposition involves first detecting point sources in an image, subtracting these, and then searching for emission from extended sources (Vikhlinin et al., 1998). This is the method which we adopt and it is illustrated in Fig. 1.2.

- Redshift Surveys:

Groups can be found as overdensities in spectroscopic redshift surveys (Eke et al., 2004; Yang et al., 2007) and this is currently a very common method for defining group, and cluster, samples. Spectroscopic redshifts allow for what is essentially a three-dimensional search for overdensities. Although relatively large numbers of spectra are required, the observations can be made from the ground and have thus been easier to obtain than X-ray studies covering similar areas of the sky. Samples selected optically may be dominated by overdensities of galaxies not yet fully virialized.

In the early 1980s, Geller & Huchra (1983) pioneered group-finding in redshift space, developing the friends-of-friends (also known as the percolation) method. In this method, a linking length b is defined which links every galaxy to those neighboring galaxies ('friends') a distance b or less away. The networks of galaxies ('friends of friends') which result from linking together these neighbors are groups or clusters. Geller & Huchra's Center for Astrophysics (CfA) redshift survey of galaxies yielded 176 groups at redshifts $z\sim 0.03$.

1.2.3 Existing Group Surveys

Since $z\sim 1$, the fraction of galaxies in groups has tripled (Knobel et al., 2009). To fully understand groups as the environment in which the majority of galaxies reside and evolve requires both

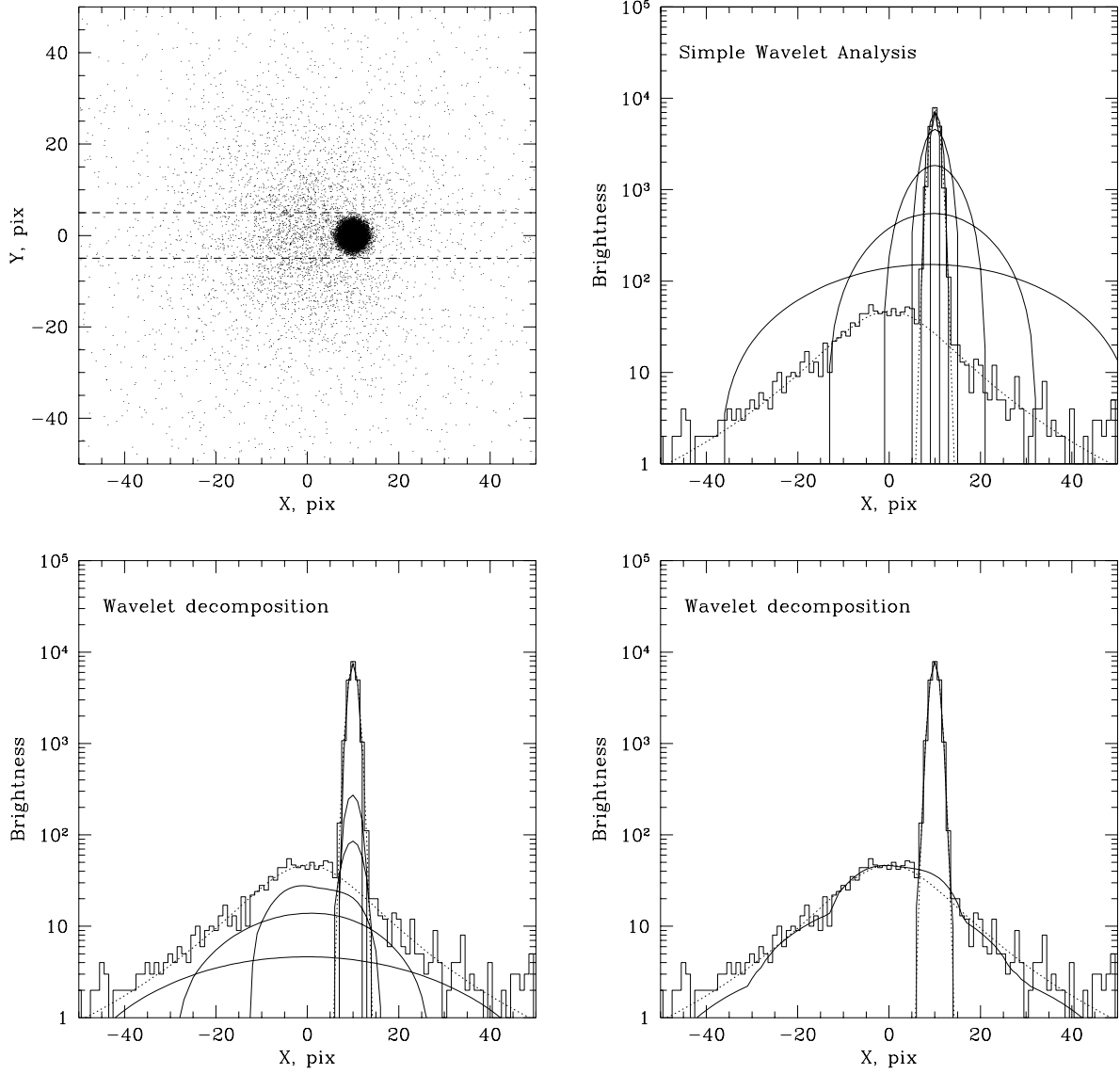


Figure 1.2: Illustration of wavelet decomposition from Vikhlinin et al. (1998). Top Left: Image of cluster with point source superposed. Dashed lines indicate the section in which brightness profiles (next three panels) were extracted. Top Right: Result of simple wavelet convolution of the image with wavelet kernels of scales 1, 2, 4,...,32 pixels. The solid histogram shows the data profile and solid lines show the profiles of convolved images. The convolution is dominated by the point source at all scales with no separate peak corresponding to the cluster. Bottom Left: Vikhlinin wavelet decomposition method where the original image is ‘decomposed’ into components with the characteristic size 1, 2, 4,...,32 pixels. The point source is modeled by the small-scale components, while at large scales the cluster becomes apparent and well separated from the point source. Bottom Right: The sum of the three smallest and three largest scales of the wavelet decomposition. This provides excellent decomposition of the raw image into its original components.

a significant number of groups and significant information on the galaxy group members themselves. Wide-field surveys such as zCOSMOS and DEEP2 have identified many galaxy groups up to redshift ~ 1 and ~ 1.3 respectively (Lilly et al. 2009, Gerke et al. 2007). The large sample sizes assembled from these types of surveys allow for the rigorous determination of global trends in groups. Evolution of low-mass galaxies appears to be accelerated in groups (Iovino et al., 2010) and transformation rates such as those from late to early-type galaxy morphologies and from active to passive star formation activity are more than twice that in the field (Kovač et al., 2010). The build-up of stellar mass on the red sequence since $z \sim 1$ involves L^* galaxies moving to the red sequence preferentially in groups (Cooper et al., 2007). The low sampling rate and bright magnitude limits of these surveys mean, however, that the majority of groups have only a few confirmed members and thus that individual systems can be difficult to examine in detail. A brief outline of some of the most relevant large group samples follows.

- Large Group Samples:

As mentioned above, the first large volume survey of galaxy groups was the CfA redshift survey. Gradually the size and depth of group samples has expanded. Eke et al. (2004) compiled a catalog (2dF Percolation-Inferred Galaxy or 2PIGG) containing more than 3×10^4 groups extending up to redshift $z \sim 0.25$, which also used a friends-of-friends algorithm to define groups from the 2dF Galaxy Redshift Survey (2dFGRS). Another local survey, the Sloan Digital Sky Survey (SDSS), began in 1998 and has now obtained spectra for nearly a million nearby galaxies. Berlind et al. (2006) have used a percolation algorithm to find $\sim 57,000$ groups out to $z \sim 0.1$. Yang et al. have also defined groups in both the 2dFGRS and SDSS, developing a halo-based group finder (Yang et al., 2005) and finding $> 4,800$ and $> 6,800$ groups respectively. In 2001, Carlberg et al. defined a moderate-redshift galaxy sample using a friends-of-friends method to identify ~ 200 galaxy groups in the Canadian Network for Observational Cosmology Field Galaxy Redshift Survey (CNOC2). Two major surveys have allowed for the definition of large group samples at even higher redshift: the DEIMOS/DEEP (or DEEP2) and zCOSMOS surveys. Gerke et al. (2005) identified 899 groups with two or more members in the redshift range $0.7 < z < 1.4$ using the Voronoi-Delaunay method of Marinoni et al. (2002), a more sophisticated group-finding scheme. This method defines groups using local density information derived by computing the three-dimensional Voronoi tessellation and Delaunay mesh of the galaxies in redshift space. The Voronoi tessellation uniquely partitions space around galaxies such that each galaxy is assigned a unique polyhedral volume of space that is closer to itself than to any other galaxy. The Delaunay mesh links each galaxy to the galaxies in immediately adjacent Voronoi cells, forming a network of line segments. Approximately 800 $0.1 < z < 1$ groups have been found in zCOSMOS by Knobel et al. (2009) using both the friends-of-friends and Voronoi-Delaunay methods.

A complementary approach to these large volume surveys involves studying a smaller but well defined and well sampled selection of groups. The Group Environment Evolution Collaboration (GEEC) has taken this approach, defining samples at $z \sim 0.5$ and recently extending studies up to a redshift of 1. Intermediate redshift work has focused on optically selected groups and examined stellar masses, colors, morphologies, and star formation histories in these sys-

tems, comparing them to trends observed in the field (Wilman et al., 2005a,b; Balogh et al., 2007; Wilman et al., 2008; McGee et al., 2008; Wilman et al., 2009; Balogh et al., 2009; McGee et al., 2011; Tyler et al., 2011; Hou et al., 2012; Connelly et al., submitted). Our higher redshift study involves X-ray selected systems and first results show a prominent transient population, migrating from the blue cloud to the red sequence, in these groups (Balogh et al., 2011b). Other noteworthy small group samples are described here.

- Small Group Samples:

Nine X-ray selected groups with $0.2 < z < 0.6$ have been identified by Mulchaey et al. and six of these have had multi-wavelength follow-up (Mulchaey et al., 2006; Jeltema et al., 2006). The sample provided evidence that, despite their high X-ray luminosities, many of the systems were not dynamically evolved, providing further motivation to study groups selected in this way. At intermediate to high redshifts, $0.4 < z < 1$, the ESO Distant Clusters Survey (EDisCS) allowed for the definition of ten groups with $\sigma \sim 150 - 400 \text{ km s}^{-1}$ and eight or more spectroscopically confirmed members, as well as some ‘poor’ groups (3-6 members) (White et al., 2005), primarily using the red sequence technique. The dataset includes VLT deep imaging and spectroscopy, ACS/HST imaging, in addition to X-ray and IR observations. The Group Evolution Multiwavelength Study (GEMS) selected low-redshift groups from the literature which had been identified using optical catalogs and also had deep X-ray observations and further added to this a comparison sample of X-ray selected groups, obtaining a total of 60 systems (Osmond & Ponman, 2004). In addition to the X-ray and optical data, many of these groups also have near-IR and neutral hydrogen imaging.

1.3 Scaling Relations and Masses of Groups

Comparing properties such as derived mass, X-ray luminosity and temperature, velocity dispersion, and richness via scaling relations allows us to explore the integrated properties of groups and clusters and how they relate to one another. In clusters, minimizing the scatter in these relations is a necessity in order to obtain accurate constraints on cosmological parameters. Through large, uniform samples, these relations are now reasonably well constrained and seem to be very tight, even up to relatively high redshifts. Although group samples of similar size and quality are only recently available, group scaling relations exhibit a much greater scatter due to both larger measurement errors and greater intrinsic scatter in group properties (e.g. Osmond & Ponman, 2004; Rykoff et al., 2008b; Giordini et al., 2009; Balogh et al., 2011a). Understanding the scatter in the relations in the group regime is a key part of illuminating the physical processes at play.

- $L_X-\sigma$ Relation:

Since both the X-ray luminosity of a group and the velocity dispersion of the member galaxies provide a measure of the gravitational potential strength, it is logical that these two quantities should correlate. Beginning with the temperature, and deriving several other scaling relations

along the way, I outline the basic theoretical and empirical background of the L_X - σ relation here.

For a group or cluster in virial equilibrium, the thermal energy per gas particle, T , should be proportional to the binding energy:

$$T \propto M/r. \quad (1.1)$$

To use this relation, r must be the radius within which the group or cluster is virialized (r_{virial}) and, for clusters, is defined such that the average mass density within a sphere of this radius is 200 times as high as the critical density ($\rho_{critical}$) of the Universe. This virial mass is defined as

$$M_{virial} = \frac{4\pi}{3} \times 200\rho_{critical} r_{virial}^3. \quad (1.2)$$

Using this definition of the mass and recalling that the temperature is proportional to this mass divided by the radius, the temperature can then be expressed as

$$T \propto \frac{M_{virial}}{r_{virial}} \propto r_{virial}^2 \propto M_{virial}^{2/3}. \quad (1.3)$$

This is the mass-temperature relation. The velocity dispersion, σ_{virial} , can also be related to the virial mass as

$$M_{virial} = \frac{3r_{virial}\sigma_{virial}^2}{G}. \quad (1.4)$$

As T is also proportional to M_{virial}/r_{virial} and to $M_{virial}^{2/3}$, this provides a mass-velocity dispersion relation:

$$M_{virial} \propto \sigma_{virial}^3. \quad (1.5)$$

Theoretically, assuming an isothermal and virialized gas emitting thermal bremsstrahlung, the luminosity of the gas is

$$L_X \propto \rho_{gas}^2 T(r)^{0.5} dV \quad (1.6)$$

where ρ is the gas density, $T(r)$ is the temperature at a given radius, and V is the volume. At the virial radius, this is equivalent to $L_X \propto \rho_{gas}^2 T^{1/2} r_{virial}^3$ and, recalling Eq. 1.3, $L_X \propto \rho_{gas}^2 T^{1/2} M_{virial}$. Estimating the gas density as $\rho_{gas} \sim M_{gas} r_{virial}^{-3} = f_{gas} M_{virial} r_{virial}^{-3}$ with $f_{gas} = M_{gas}/M_{virial}$ indicating the gas fraction with respect to the total cluster mass and recalling $r_{virial} \propto M_{virial}^{2/3}$, then it follows $L_X \propto f_{gas}^2 M_X^{4/3}$. From this we have obtained an approximate X-ray luminosity-mass relation,

$$L_X \propto M_X^{4/3} \quad (1.7)$$

and, again assuming virial equilibrium and recalling Eq. 1.5, L_X should be approximately proportional to σ^4 (Navarro et al., 1995). We have now obtained a theoretical luminosity-velocity dispersion relation,

$$L_X \propto \sigma^4. \quad (1.8)$$

For the cluster regime, the assumptions made to arrive at this relation, mainly that of isothermalization and virialization, are likely to be relatively robust but in the group regime, where systems

could be dynamically young, these may not hold.

Comparing a sample of local groups to the cluster regime, Zimer et al. (2002) found the relation for groups is indeed consistent with those for clusters. Fig. 1.3 shows their data in comparison to other samples. Slopes for the relation derived from ROSAT (short for Röntgensatellit) X-ray studies by Mulchaey & Zabludoff (1998), Ponman et al. (1996) and Helsdon & Ponman (2000b) are $L_X - \sigma^{4.3}$, $\sigma^{4.9}$, and $\sigma^{4.5}$ respectively, in relatively good agreement with the theory. Ponman et al. (1996) and Helsdon & Ponman (2000b) did find however that, for groups with low velocity dispersions, the relation is somewhat flatter. Also using ROSAT data, Mahdavi et al. (1997) derived a significantly flatter slope ($\sigma^{1.56}$) and suggested that for the low velocity dispersion systems the X-ray emission is dominated by hot gas clumped around individual galaxies. Significant intrinsic scatter may exist in $L_X - \sigma$, and other, group scaling relations. As a single value for a slope in the group regime is not established observationally at present, it is possible that significant intrinsic scatter exists in $L_X - \sigma$ (and indeed other) group scaling relations. In their 2000 study of such scaling relations, Helsdon & Ponman used a sample of X-ray selected systems and, contrasting their work with studies finding significantly flatter $L_X - \sigma$ relations slopes, suggested that the distinction between clusters, compact, and loose groups is not as useful as that of X-ray bright and faint systems.

- Group Masses:

Cluster mass estimates are myriad; obtainable from galaxy dynamics, stellar/baryonic content, the properties of the IGM (L_X , T_X , etc.), gravitational lensing, and, most recently, the Sunyaev-Zel'dovich effect. The first three tracers may also be used to measure an individual group's mass. The dynamical mass is based on the velocity dispersion of the system. Summing the stellar masses of member galaxies (and, ideally, the mass contribution of baryons in the intra-group light, but this is very difficult to measure) provides the stellar mass. The X-ray mass may be derived from the properties of the hot gas. Since both the dynamical and X-ray mass trace the group halo mass, they are akin to total mass measurements and theoretically should be very similar. Factors such as the group age, merger history, and inter-group gas heating (and cooling) history can however cause disagreement. Unfortunately, few direct comparisons of these mass measures exist. Girardi et al. (1998) used a sample of 66 clusters from the literature to compare dynamical and X-ray masses (M_{dyn} and M_X respectively), finding relatively good agreement between the two but significant scatter. However, inhomogeneity of the sample prevented exploration of causation. Popesso et al. (2007a) studied the X-ray properties using ROSAT data of 137 Abell clusters, finding that over a third, which they term X-ray-underluminous Abell clusters or AXU clusters, do not follow the $L_X - M_{dyn}$ scaling relation traced by the other clusters.

Since there is substantial evidence that the characteristics of the population of galaxies in a group (e.g. the fraction of passive galaxies) is correlated with both the halo and stellar mass of the group, measurements of both kinds of system mass are essential. Andreon (2010) obtained stellar and dynamical masses for a sample of 52 nearby clusters from SDSS, finding that even at fixed cluster mass there was significant intrinsic spread in stellar mass and that the stellar mass fraction dependence on halo mass has a slope of -0.55 ± 0.08 , with intrinsic scatter 0.15 ± 0.02 dex at

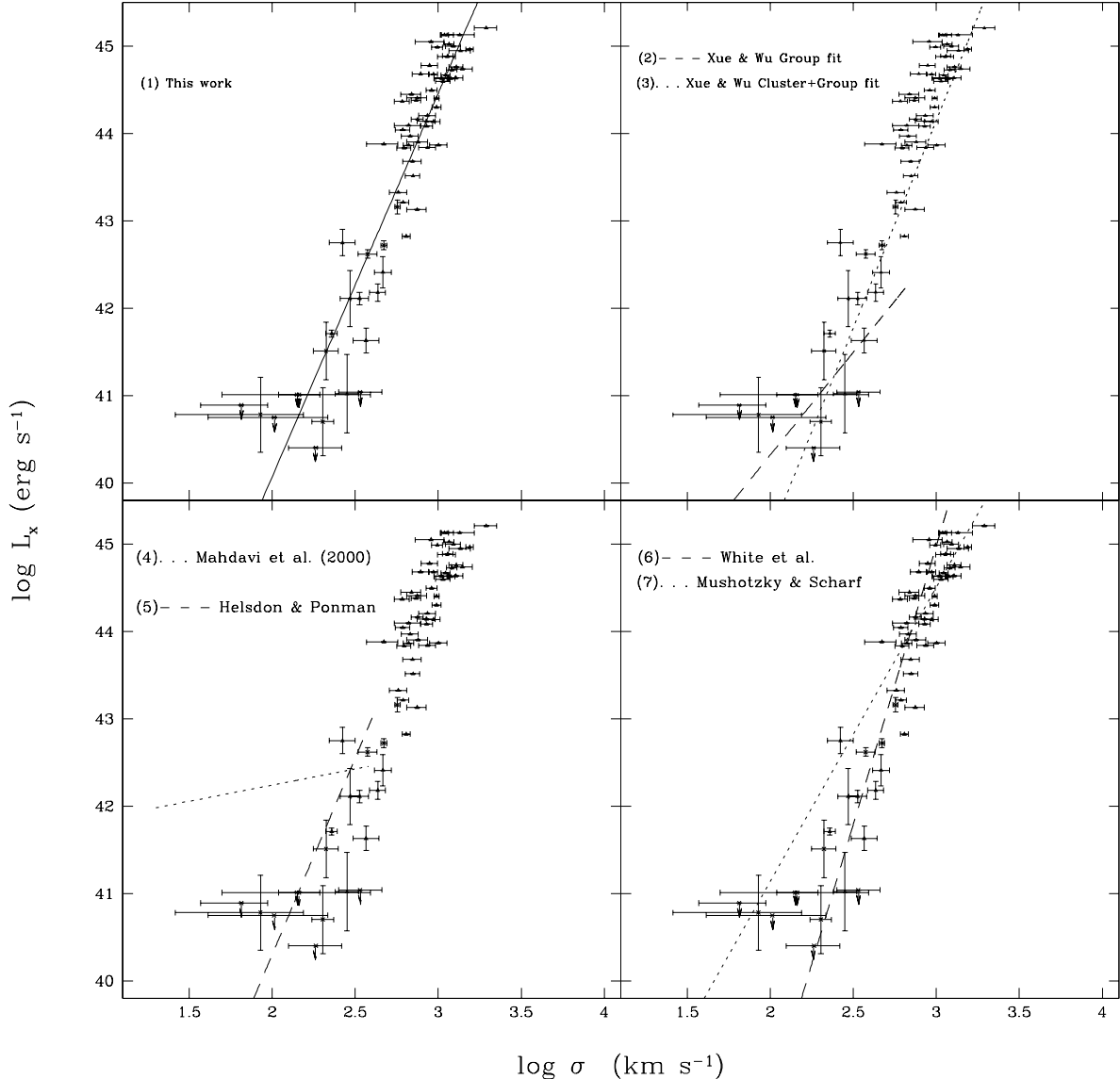


Figure 1.3: Zimer et al. (2002) L_X - σ relation for X-ray detected groups and clusters. The top left panel shows the Zimer et al. data and best fit while the subsequent panels compare this data to the best fit relation for other samples. Groups without an X-ray detection are marked with arrows. Note the differing slopes even within the group regime.

fixed cluster mass. Balogh et al. (2011b) explored the 18 low mass nearby clusters (dynamical mass of $M/M_{\odot} \sim 5 \times 10^{14}$) selected from the 2dfGRS to compare X-ray, stellar, and dynamical masses, finding evidence that several systems are underluminous in X-ray emission. In the group regime, Yang et al. (2009) use a sample from SDSS to find stellar mass-halo mass relation for a relatively large range of halo masses. Giordini et al. (2009) have begun the process of exploring a wide range of masses out to higher redshifts using a $0.1 < z < 1$ sample of groups from the COSMOS survey.

In summary, until recently the sparse sampling of the range in total mass spanned by groups and clusters made studying their overall properties problematic both in terms of the mean and the scatter of the population, and comparisons between samples are often complicated by masses being calculated within very different radii. Current data now allow for the exploration of a wider range of system masses, closer examination of scatter, and exploration of interesting subsamples such as X-ray underluminous systems (e.g. Rykoff et al., 2008a) which may not follow assumed scaling relations.

1.4 Aims and Outline of the Thesis

In order to study groups spanning a significant mass and evolutionary range and to compare the results obtained from two of the most common group identification methods, I define two different samples within the same physical area; one via optical spectroscopy and the other via X-ray emission. Different physical processes are likely to be active in the optical and X-ray regimes and thus a comparison of groups selected via these two disparate methods can illuminate these physical phenomena. In Finoguenov et al., 2009 (hereafter Paper I), we presented the X-ray observations of our fields and preliminary results for our sample of X-ray selected groups. We have since finished an extensive spectroscopic campaign, significantly improving the sampling rate and depth of galaxies in our fields, and I present here my full sample of X-ray and optically selected systems. In addition to X-ray derived luminosities and masses, well constrained membership now allows for the measurement of velocity dispersions and dynamical masses, stellar masses, and for an analysis of dynamical complexity in our groups (see Connelly et al., submitted). In this thesis I present the full catalog of groups and explore these global group properties. Throughout this thesis a cosmology of $H_0 = 75 \text{ km s}^{-1} \text{ Mpc}^{-1}$, $\Omega_M = 0.3$, and $\Omega_{\Lambda} = 0.7$ is assumed unless mentioned otherwise.

In Chapter 2 I discuss the GEEC project, data which existed prior to the inception of this thesis work, origins of the optically selected sample, and analysis conducted with a preliminary optical and X-ray sample. Chapter 3 describes the X-ray measurements of both optical and X-ray selected groups. Chapter 4 details the follow-up spectroscopy of the X-ray selected systems, the group-finder algorithm and radial cuts for all systems, and the global group properties including membership and velocity dispersions along with dynamical complexity results from the Dressler-Shectman (DS) and Anderson-Darling (AD) tests for all systems. The $L_X-\sigma$ relations for my samples are presented in Chapter 5. Chapter 6 explores the X-ray and dynamical estimates of total group mass, and the total mass in stars. The definition of a sample of groups underluminous

in X-rays given their stellar mass is presented and possible formation scenarios discussed in Chapter 7. The most important conclusions for this work are outlined and several lines of further inquiry proposed in Chapter 8.

Chapter 2

GEEC Project Background

2.1 Optically (Spectroscopically) Selected Groups

The optical sample is selected from the Canadian Network for Observational Cosmology Field Galaxy Redshift Survey 2 (CNOC2), a survey consisting of four sky patches, roughly equally spaced in right ascension (RA) at approximate positions of 2h, 9h, 14h, and 21h, with a total area of about 1.5 square degrees (Carlberg et al., 1999). UBVR_CI_C photometry of the patches yielded $\sim 40,000$ galaxies above the survey's $R_C \simeq 23.0$ limit. Follow-up spectroscopy of these fields with the Multi-Object Spectrograph (MOS) on the Canada-France-Hawaii Telescope (CFHT) resulted in redshifts for over 6,000 galaxies with a completeness of 48% down to $R_C = 21.5$ (Yee et al., 2000).

Groups present in the survey were then detected as pure galaxy overdensities in redshift space by Carlberg et al. (2001) using a variant of a simple friends-of-friends (FOF) algorithm (see §1.2) optimized to identify virialized systems with a minimum of three members. The Carlberg algorithm was designed to be analogous to that used by N-body simulations to identify virialized dark matter halos which require the mean interior density to exceed 200 times the critical density (the average density of matter required for the Universe to halt its expansion but only at infinite time). After groups were detected using the FOF algorithm, a group center, line-of-sight velocity dispersion (σ_1), and approximate virial radius ($r_{200} = \sqrt{3}\sigma_1/10H(z)$) were defined and used to add or discard group members, requiring them to be within $3\sigma_1$ and $1.5r_{200}$, in an iterative fashion. In total, over 200 groups ranging in redshift $0.12 < z < 0.55$ were detected. Given the optical wavelength range for CNOC2 spectroscopy, the effective redshift range for the full sample corresponds to the available wavelength range of the Ca II H and K spectral features.

26 of the CNOC2 groups at $0.3 < z < 0.55$ have since been actively targeted with the Low Dispersion Survey Spectrograph (LDSS2) on the Magellan-Baade telescope to improve the spectroscopic completeness and depth of the sample. 392 unique LDSS2 redshifts were obtained in three of the four CNOC2 patches elevating the average completeness at the coordinates of the targeted groups to 74% above a limiting magnitude of $R_C = 22$ (Wilman et al., 2005a). Ten groups (six in the RA14h field and four in the RA21h) were observed with the FOcal Reducer and low dispersion Spectrograph (FORS2) for the Very Large Telescope (VLT) in June and July

of 2005. These data have recently been reduced and yielded 233 previously unknown redshifts and a magnitude limit of $R = 23.2$ (Henderson, 2010). The original CNOC2 optical groups sample was also modified to be more representative of the loose group population, relaxing the trimming radius by increasing the aspect ratio and imposing a more stringent velocity dispersion criterion, requiring group members to be within 2σ of the group.

Additional members of optical groups have been identified through the spectroscopic follow-up campaign of X-ray systems (see §4.1) and membership allocation further tuned to this X-ray group sample (see §4.2.2). Throughout this thesis I consider only those 38 optical groups in the RA14h and RA21h fields within the regions observed by XMM-Newton + Chandra described in the next chapter, ensuring that the most direct comparisons between these differently identified systems are possible. We have also decided *not* to supplement the Carlberg et al. sample of groups with new overdensity-defined groups which would be detectable with the additional post-CNOC2 spectroscopic coverage. We made this decision on the basis that it would make the selection function of those groups much more non-uniform and difficult to understand.

2.2 GEEC Project

Complementary to the existing spectroscopy in the CNOC2 fields, the GEEC has built up a multiwavelength dataset, including Hubble Space Telescope (HST) Advanced Camera for Surveys (ACS), infrared (IR), and ultraviolet (UV) imaging as well as X-ray data (described and utilized in this thesis), in order to study galaxy groups in these fields in detail. Figures 2.1 and 2.2 show the two CNOC2 fields used in this thesis work (the RA14h and RA21h patches) with relevant coverage overlaid. In summary, we have the following data (with variable spatial completeness):

- the original CNOC2 UBVRI photometry and spectroscopy
- high resolution HST-ACS imaging
- deep Magellan-LDSS2, Magellan Inamori Magellan Areal Camera and Spectrograph (IMACS), & VLT-FORS2 spectroscopy
- New Technology Telescope Son of ISAAC (NTT-SOFI; Ks-band), CFHT Wide-field InfraRed Camera (WIRcam), & William Herschel Telescope (WHT) Isaac Newton Group Red Imaging Device (INGRID) near infrared imaging
- mid-infrared imaging from the Spitzer Space Telescope Multiband Imaging Photometer (MIPS) & Infrared Array Camera IRAC
- improved optical imaging with CFHT-MegaCam & CFH12K
- Galaxy Evolution Explorer (GALEX) UV imaging
- X-ray data from both Chandra & X-ray Multi-Mirror Mission (XMM-Newton or XMM)

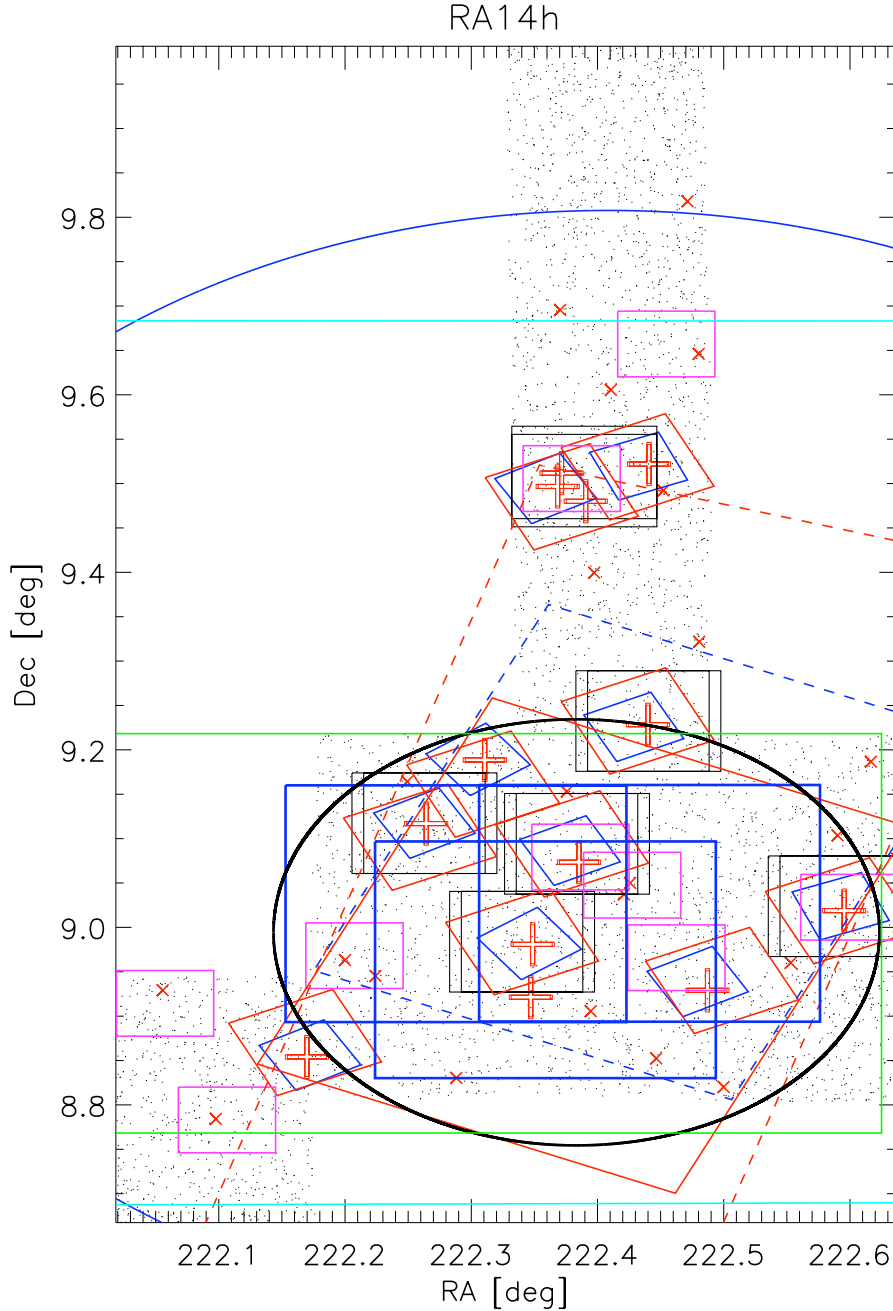


Figure 2.1: Multiwavelength coverage of the CNOC2 RA14h field. Red x's mark Carlberg et al. groups and pluses those groups subsequently targeted with LDSS2. Small blue squares show regions covered by ACS. Black rectangles show previously observed FORS2 spectroscopic regions. Pink and red squares indicate SOFI and INGRID near IR respectively, while large red and blue dashed show archival IRAC and MIPS mid-IR. The green rectangle outlines our deep CFH12K optical imaging and cyan rectangle the MegaCam coverage. The large blue circle shows GALEX UV coverage. Finally, black circles show the XMM and large blue squares the Chandra X-ray coverage areas which are the focus of this thesis.

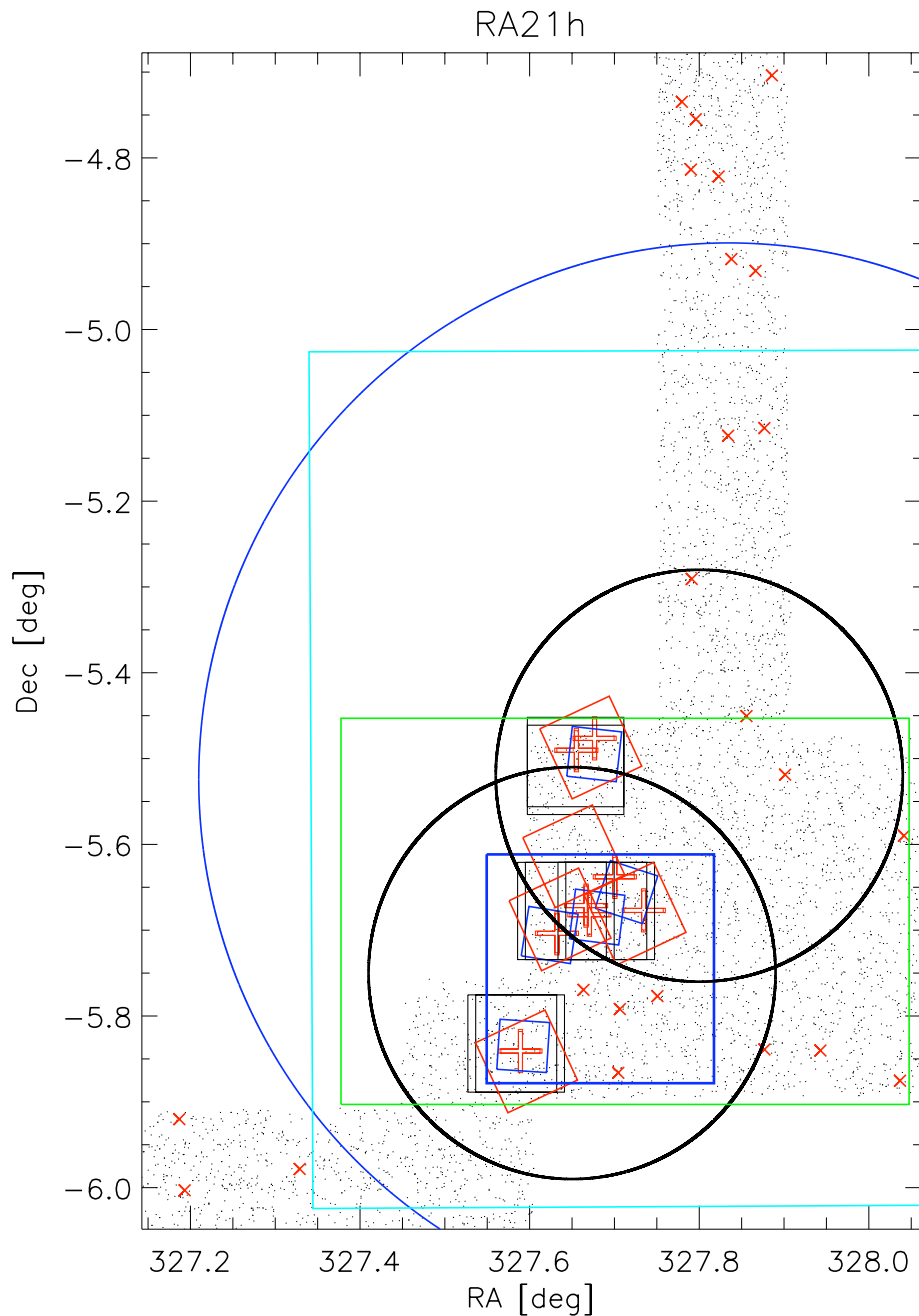


Figure 2.2: Multiwavelength coverage of the CNOC2 RA21h field. Symbols are the same as in Fig. 2.1.

Using this dataset, GEEC optical systems have now been extensively explored. Prior to the start of this thesis, several papers had already been published. Wilman began the in-depth study (and expansion, see §2.1) of the Carlberg et al. groups and found trends in the fraction of passive galaxies consistent with the differences between group and field galaxies seen in the local universe (Wilman et al., 2005a) and evidence that the star formation history in groups is influenced by their environment (Wilman et al., 2005b). The stellar mass of these systems was presented in Balogh et al. (2007) and no significant evidence for environment-driven evolution in group stellar mass from $z \sim 0.4$ to today found.

After the initiation of this thesis work, study of the optically-selected GEEC groups continued. Using an IRAC color to identify passive galaxies in a stellar mass selected sample of the GEEC groups, Wilman et al. (2008) found a deficit in the fraction of infrared-excess galaxies at fixed group stellar mass in groups, relative to the field. Quantitative morphologies of the GEEC systems were compared to those of a low redshift sample of groups (drawn from the Millennium Galaxy Catalogue) with both showing a deficit of disc-dominated galaxies with respect to the field (McGee et al., 2008). Wilman et al. (2009) presented the HST-based visually classified morphologies of group galaxies, finding that groups contain significantly higher fractions of S0 galaxies than the field at fixed luminosity, with a similar fraction to that found in $z \sim 0.4$ clusters, and suggesting that interaction with a bright X-ray emitting IGM is not important for the formation of these objects.

Balogh et al. (2009) detailed the photometric analysis of the GEEC fields, which combined optical CHF12K and Megacam observations with near IR data. The resulting photometric catalogs have been utilized in this thesis work. Galaxy colors and star formation for 98 of the GEEC groups were also presented, confirming the earlier conclusions that star formation is not significantly enhanced in the group environment and that current galaxy formation models overpredict quenching. A study of ten of the GEEC groups extending membership to fainter magnitudes conducted by Henderson (2010) found little evidence for strong evolution of the luminosity function in groups with redshift and a tendency of the faint galaxies in groups to be blue (e.g. a strong trend of decreasing red fraction toward fainter magnitudes). The star formation properties of the GEEC systems were further explored by McGee et al. (2011) and supplemented with those of lower redshift ($z \sim 0.08$) groups from the Sloan Digital Sky Survey (SDSS). Though the fraction of passive galaxies was found to be higher in groups than the field, the star formation properties of star-forming galaxies were similar in both environments. MIPS 24 micron observations were also used to study star formation in the GEEC groups by Tyler et al. (2011) and member galaxies were found to lie between field and cluster galaxies in terms of mass, morphology, and star formation rates. Hou et al. (2009, 2012) characterized dynamical complexity and substructure in the most massive GEEC systems, finding evidence that groups containing significant substructure have global properties and galaxy populations differing from those of groups without detected substructure but no sign of star-formation quenching in galaxies residing in regions of substructure. Currently, the GEEC sample is being extended to higher redshifts and preliminary results, including evidence for a significant population of galaxies with intermediate colors (between blue, star forming spiral galaxies and red, ‘dead’ galaxies which are primarily early types), have been presented in Balogh et al. (2011b).

2.3 Paper I

At the time of the publication of Paper I, led by Dr. Alexis Finoguenov and published in 2009 (Finoguenov et al., 2009), and before the final X-ray observations in the RA21h field were in hand (which made it comparable in depth to the RA14h patch), a preliminary definition and analysis of our systems was undertaken. Specifically, redshifts for those objects in and around X-ray contours were determined in order to define an initial catalog of X-ray groups. Though the vast majority of analysis has been repeated/expanded for this thesis using the complete, finalized groups and membership, some work performed by collaborators has *not* been re-examined in light of the final spectroscopic and X-ray catalogs but are included here for completeness. This includes predictions of the number density of groups, group detection as a function of mass, and a stacked weak lensing study. Note that in addition to the definition of groups and their membership, individual group masses, utilized in §2.3.1, may have since changed with improvements in X-ray data and analysis.

2.3.1 Number Density and Detection of Groups

Fig. 2.3 presents a model of the redshift distribution of X-ray selected systems (solid line), adding the area and sensitivity of the two CNOC2 patches. This assumes a WMAP5 cosmology (Komatsu et al., 2009) and the L_X -M relation from Rykoff et al. (2008b) with evolutionary corrections applied. The short (long) dashed line illustrates the number density of halos of mass $\geq 10^{13} M_\odot$ ($3 \times 10^{13} M_\odot$), and demonstrates the relative contribution of halos above these mass thresholds. The X-ray detection mass threshold (where the solid and dashed lines cross) increases with redshift, from below $10^{13} M_\odot$ at $z \lesssim 0.3$ to above $3 \times 10^{13} M_\odot$ at $z \gtrsim 0.8$. X-ray selection at this depth provides groups at $0 \lesssim z \lesssim 1$, and so although the total number of systems per square degree is high (~ 100), the expected match to optically selected groups within a more limited redshift interval is moderate. Nonetheless, the depth of our observations provides a peak in the redshift distribution at $0.2 \lesssim z \lesssim 0.7$, which is well suited to the CNOC2 redshift range of $0.1 \lesssim z \lesssim 0.55$. The solid gray histogram, illustrating the averaged number density of CNOC2 optically selected groups, contains roughly twice the number of X-ray groups within this redshift range. Thus, a naive estimate of X-ray detected groups would be $\sim 50\%$; however, we note that there is a strong variation in the efficiency of optical group detection in the CNOC2 survey that is not included here. Nonetheless, this effectively demonstrates that our X-ray survey provides a selection of groups down to a canonical mass value of $10^{13} M_\odot$, below which the use of X-ray selection is not yet established.

This contrasts with the situation at higher redshift, for which the number density of X-ray detected groups is expected to drop off as the detection threshold gets pushed to higher and higher mass. This is the case for the DEEP2 optically selected group sample (I) at $0.75 < z < 1.03$ from Gerke et al. (2007, dashed gray histogram), which shows that at exposures similar to our survey the full strength of the X-ray selection of galaxy groups is not yet exploited, while the DEEP2 spectroscopic galaxy group survey would allow a comparison down to the $10^{13} M_\odot$ mass limit. Note that the modeling in Fig. 2.3 makes a simplistic assumption that the spectroscopic survey

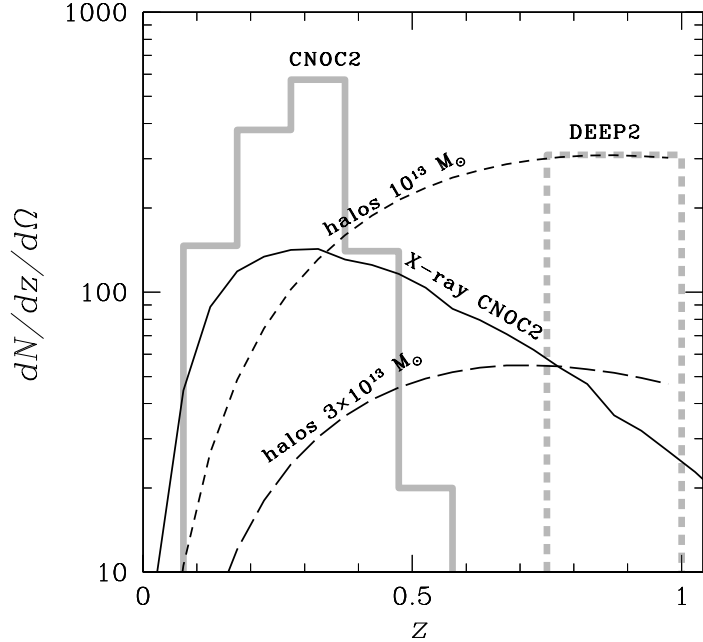


Figure 2.3: Predicted number density as a function of redshift, $dN/dz/d\Omega$ (dN/dz per unit area in deg^2) of galaxy groups. The solid curve shows the prediction for systems found in the X-ray survey. Short (long) dashed line shows the prediction for 10^{13} M_\odot ($3 \times 10^{13} \text{ M}_\odot$) halos in WMAP5 cosmology. Grey histograms show the observed abundance of optically selected groups found in the CNOC2 (solid) and DEEP2 (dashed) surveys.

for galaxy groups is complete, which may introduce further differences between optically and X-ray selected group samples, which we consider next.

Fig. 2.4 illustrates the recovery of groups as a function of halo mass, detected using both X-ray (at RA14h depth) and optical selection methods. The figure is constructed to show the percentage of groups detected as a function of mass, evaluated at a typical CNOC2 redshift $z=0.4$. X-ray groups are modeled as in Fig. 2.3, and scatter in the L_X - M relation is ignored, providing a mass threshold which is a simple function of halo mass: the non-abrupt mass cut-off is merely a result of the variable depth across the RA14h field. Introducing scatter would introduce a higher sensitivity toward low-mass systems, smearing the boundary by an additional 30% in mass (Vikhlinin et al., 2009). The modeling of the group recovery rate in the CNOC2 spectroscopic survey is based on applying the spectroscopic survey characteristics (including mean sampling rate) to the semi-analytic galaxy formation model in the Millennium Simulation (Font et al., 2008), as described by McGee et al. (2008). Optically selected samples will inevitably include a large number of lower mass groups, as the drop in recovery rate is compensated by an increase in number density. The correlation of the richness and X-ray luminosity is accounted in the plot, while we ignored the second-order effects associated with the possible covariance in the deviation from the richness-mass and L_X -mass relations.

It is interesting to examine the expected mass of groups detected only by X-ray or spectroscopic methods, and the intersection between the two samples (indicated by gray lines in Fig. 2.4) to compliment the actual data. In the RA14h field, all three of the confirmed $0.14 \leq z \leq 0.5$ X-ray selected groups are also in the spectroscopically selected sample (which is only sensitive to this limited redshift range). In the shallower RA21h field only three out of the ten $0.14 \leq z \leq 0.5$ significant X-ray groups within the area covered by the CNOC2 survey are in the spectroscopically selected sample. Of the seven undetected groups, five have estimated masses less than $\sim 3 \times 10^{13} \text{ M}_\odot$; from Fig. 2.4 we see that the spectroscopic completeness in this mass range is

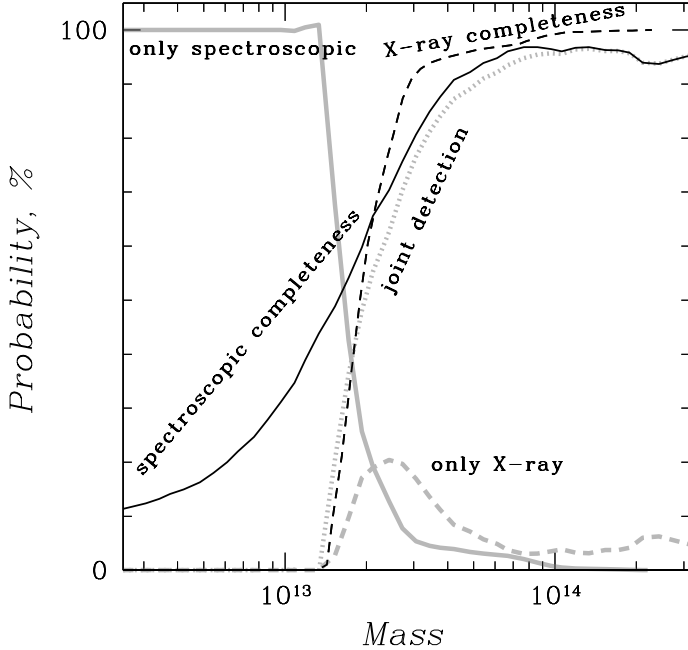


Figure 2.4: Probability of group detection as a function of halo mass at $z \sim 0.4$. Both X-ray selection at the depth of the RA14h field (dashed black curve) and spectroscopic selection in CNOC2 (including the effects of incompleteness, solid black curve) are modeled as described in the text. We ignored a possible covariance between optical richness and X-ray luminosity in predicting the percentage of groups only detected in X-rays (dashed grey line), the percentage of groups only detected optically (solid grey line) and the percentage of groups detected jointly (dotted gray line).

less than $\sim 80\%$, due primarily to the sparse sampling; therefore perfect recovery of such low-mass X-ray groups is not expected. However, two X-ray groups with masses $> 7 \times 10^{13} M_{\odot}$ are absent from the spectroscopic catalog. This may be due to the spatial variation of the spectroscopic completeness, which is not included in the completeness function of Fig. 2.4; we also note that group X21h13 is right near the edge of the CNOC2 coverage. Thus, overall we find 6 out of 13 X-ray detected groups are also identified in an independent spectroscopic survey over the area and redshift range that they can be fairly compared. This is approximately consistent with expectations, given the sparse sampling of that survey. Only one group is a surprising non-detection, given its estimated mass.

2.3.2 Stacked Weak Lensing Analysis

Though study of weak lensing for our individual groups would not be statistically significant, a *stacked* weak lensing analysis of a large sample of CNOC2 spectroscopically selected groups has been carried out based on deep CFHT and KPNO 4 m data by a collaborator, Dr. Laura Parker (Parker et al., 2005). High quality R- and I-band data were used to measure the shapes of faint background galaxies. The analysis for each of the four CNOC2 fields was based on single-band photometry, so the redshifts for the background sources had to be estimated based on the $N(z)$ distribution from the Hubble Deep Field (Fernández-Soto et al., 1999). Without accurate redshifts for the background sources, there could be some contamination in the source catalogs from faint group members. However, we do not find an excess source density around the groups, compared with the field, which suggests that the level of this contamination is small relative to other uncertainties.

In order to compare the weak lensing properties of the optically and X-ray selected groups,

the tangential shear signal was recomputed for optically selected groups within the RA14h and RA21h hour CNOC2 fields, as well as the area within those two fields overlapping with the region observed with XMM. The source catalogs used in this analysis were identical to those used in Parker et al. (2005) and were thoroughly tested for systematics. The stacked weak lensing results are presented in Fig. 2.5a and Tab. 2.1. The tangential shear for a sample of group lenses can be used to calculate the ensemble-averaged velocity dispersion, assuming an isothermal sphere density profile, as follows

$$\gamma_T = \frac{\theta_E}{2\theta} = \frac{2\pi\sigma^2}{c^2\theta} \frac{D_{LS}}{D_S} \quad (2.1)$$

where θ_E is the Einstein radius of the lenses, θ is the angular distance from the group center, D_{LS} is the angular diameter distance between the lenses and sources, and D_S is the angular diameter distance to the sources. The best fitting isothermal sphere yields a velocity dispersion of $228 \pm 137 \text{ km s}^{-1}$ for all optically selected groups in the two patches and $260 \pm 110 \text{ km s}^{-1}$ for those within the region of the survey covered by X-ray data. The sample of all X-ray groups yielded a best fitting isothermal sphere with a velocity dispersion of $247 \pm 138 \text{ km s}^{-1}$. The errors in velocity dispersion were calculated from weighted fits to an isothermal sphere profile, with weights defined by the errors in the shear measurements. The errors in the shear estimates were determined from the uncertainties in the source shape measurements as described in Hoekstra et al. (2000).

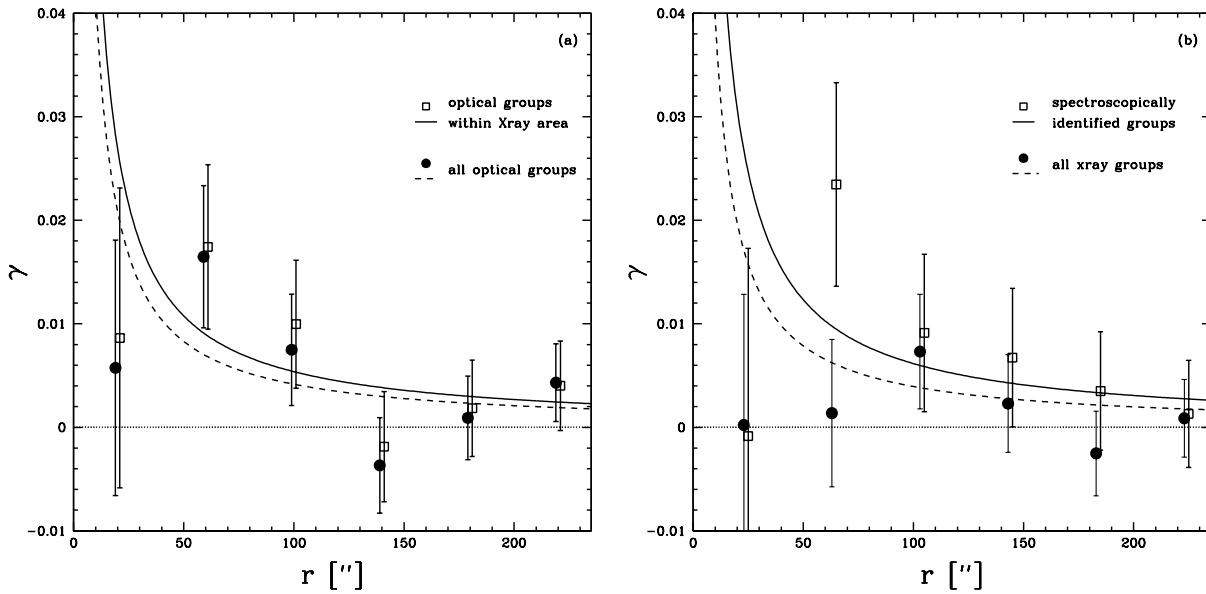


Figure 2.5: a) Stacked tangential shear profile of spectroscopically selected and b) X-ray selected groups. Overplotted lines are the best fits for an isothermal sphere model.

The tangential shear was also computed for two samples of X-ray selected groups: the groups that at the time of publication had confirmed spectroscopic redshifts, and the entire sample of extended X-ray sources. These results are presented in Fig. 2.5b and Tab. 2.1. The X-ray

Table 2.1: Weak lensing results

Sample	N_{groups}	Mean z	Mean shear ($<2'$)	$\sigma \text{ km s}^{-1}$
Spectroscopic groups in 21h & 14h fields	70	0.33	0.077 ± 0.024	228 ± 137
Spectroscopic groups within X-ray survey	35	0.33	0.099 ± 0.028	260 ± 110
Spectroscopic groups with no X-rays	13	0.33	0.100 ± 0.045	101 ± 326
All X-ray detected systems	49	$N(z)$	0.032 ± 0.025	247 ± 138
X-ray groups with redshifts	24	0.41	0.090 ± 0.035	309 ± 106

Note: Spectroscopic groups refer to optically selected systems.

groups with identified spectroscopic redshifts have an ensemble-averaged velocity dispersion of $309 \pm 106 \text{ km s}^{-1}$, consistent with the result for optically selected groups. We also stack all X-ray groups (including those with no confirmed redshift) which requires an assumption of their $N(z)$ which we take from the modeling presented in Fig. 2.3. It is clear from Fig. 2.5 that the isothermal sphere model does not do a particularly good job of recovering the shear profile, and thus the formal measurement of velocity dispersion and its associated error do not provide a full description of the data.

The stacked signal at the position of X-ray extended sources is completely dominated by the RA21h field groups (3σ). There is no clear weak lensing detection in the RA14h field alone ($<1\sigma$). We have also attempted a detection of stacked shear signal from the 13 spectroscopic groups located inside the X-ray survey for which we are confident that there is no X-ray emission. The obtained result is listed in Tab. 2.1. While the isothermal model fit is easily consistent with zero, there is a $\sim 2\sigma$ significant detection of shear within $120''$. This can tentatively be taken as detection of non X-ray bright groups, although we stress the low number statistics and suggest that much better statistics would be required for confident weak lensing detection of mass in groups beyond our X-ray detection limit.

Chapter 3

X-ray Data, Sample Definition, and Brightness

X-ray observations of two of the four CNOC2 fields were obtained and used to identify a comparison sample of X-ray selected galaxy groups. These groups are selected from deep XMM-Newton + Chandra data in the RA14h and RA21h CNOC2 patches using a wavelet algorithm. This chapter describes the X-ray data, its reduction, extended source detection, and X-ray flux/luminosity measurements. Note that Chandra data reduction was performed by a collaborator, Dr. John Mulchaey, while the XMM-Newton data reduction, joint detection, and luminosity calculations were performed by Dr. Alexis Finoguenov.

3.1 X-ray Data & Reduction

For the RA14h patch, the XMM-Newton OBSIDs are 0148520101, 0148520301, and 0149010201, and the Chandra OBSIDs are 5032, 5033, and 5034. XMM-Newton OBSIDs for the RA21h patch are 0404190101, 0404190201, 0603590101, and 060359020, while the Chandra OBSID for this patch is 6791. The total XMM exposure time for the RA21h field was 271.46 ksec and the Chandra exposure time in this field 101.88 ksec. In the RA14h field, a total exposure time of 210.40 ksec with XMM and 89.02 ksec with Chandra were obtained. The total area covered by the X-ray observations was 0.2 and 0.3 square degrees for the RA14h and RA21h fields, respectively. For the RA14h field, all pointings were essentially coincident while in the RA21h field two partially overlapping pointings were chosen. This arrangement can be seen clearly in Figures 3.1 and 3.2.

To increase our sensitivity to low level X-ray emission, we combine our XMM-Newton and Chandra data to produce X-ray mosaics for each patch. Throughout this thesis, I will list effective exposure times in each patch in units of the equivalent Chandra exposure that would be required to reach the observed sensitivity in the 0.5–2 keV band for a 2 keV thermal diffuse emission source at $z=0.2$. In the following section, the careful background and point source removal of data from both instruments and patches necessary for the creation of a joint exposure map are

described. The combined maximum effective exposure times in units of the equivalent Chandra exposure at the center of the field are 691 ksec for the RA21h patch and 469 ksec for the RA14h patch. Fig. 3.1 shows the final exposure maps for both fields with contours indicating effective 100, 200, and 300 ksec equivalent Chandra exposure times.

3.1.1 XMM Data Reduction

The X-ray Multi-Mirror Mission (XMM)-Newton spacecraft was launched in 1999 by the European Space Agency. The observatory consists of three coaligned 7.5 m focal length telescopes each consisting of 58 nested shells. XMM has an angular resolution of $\sim 15''$ (on-axis half energy width) and a large, $\gtrsim 30'$, field of view. It can observe the sky in energies of 0.15–15 keV. Detectors onboard include the European Photon Imaging Camera (EPIC); a set of three X-ray CCD cameras. Two of these cameras are Metal Oxide Semi-conductor CCD arrays (referred to as MOS1 and MOS2 specifically or in general as the MOS cameras) while the third is a pn-junction (pn) CCD camera. The MOS cameras are both installed behind separate X-ray telescopes equipped with the gratings of the Reflection Grating Spectrometers (RGS). The gratings divert roughly half of the telescope's incident flux towards the RGS detectors, with $\sim 44\%$ of the original incoming flux reaching the MOS cameras. The MOS CCDs detect energies of 0.15–12 keV. The third X-ray telescope has an unobstructed beam and the pn camera resides at its focus and detects in an energy range of 0.15–15 keV (XMM-Newton SOC, 2011).

Reduction of XMM-Newton data begins with the standard data processing of the EPIC data with XMMSAS version 6.5 (Watson et al., 2001; Kirsch et al., 2004; Saxton et al., 2005) with the creation of calibrated concatenated event lists. In addition to the standard removal of bad pixels, bad columns, etc., a more conservative removal of time intervals affected by solar flares, following the procedure described in Zhang et al. (2004), is applied. Next, a more sophisticated background removal, which I describe in the next subsection, is applied in order to allow for secure detection of extended, low surface brightness emission.

Background Removal

The X-ray background consists of two parts: a cosmic X-ray background (CXB) and an instrumental background. The instrumental background itself has two components: the first is created by interaction of particles with the detectors and the structure surrounding the detectors and is most important at high energies ($>$ a few keV) and the second is a detector noise component, important at low energies ($<$ 200 eV). The CXB is produced by foreground galactic emission, as well as unresolved X-ray background. We apply a four part ‘quadruple background subtraction’ procedure to remove the background. Details of this method can be found in Finoguenov et al. (2007) and an outline is provided here.

- 1) Photons in the energy band corresponding to the Al $K\alpha$ line for pn and both MOS detectors are removed. This line is part of the X-ray fluorescence produced by the instrumentation.
- 2) The out-of-time events (OOT) for pn detections are subtracted. The OOTE are photons registered during the readout of the CCD.
- 3) & 4) Instrumental and cosmic background are subtracted using two templates (Lumb et al.

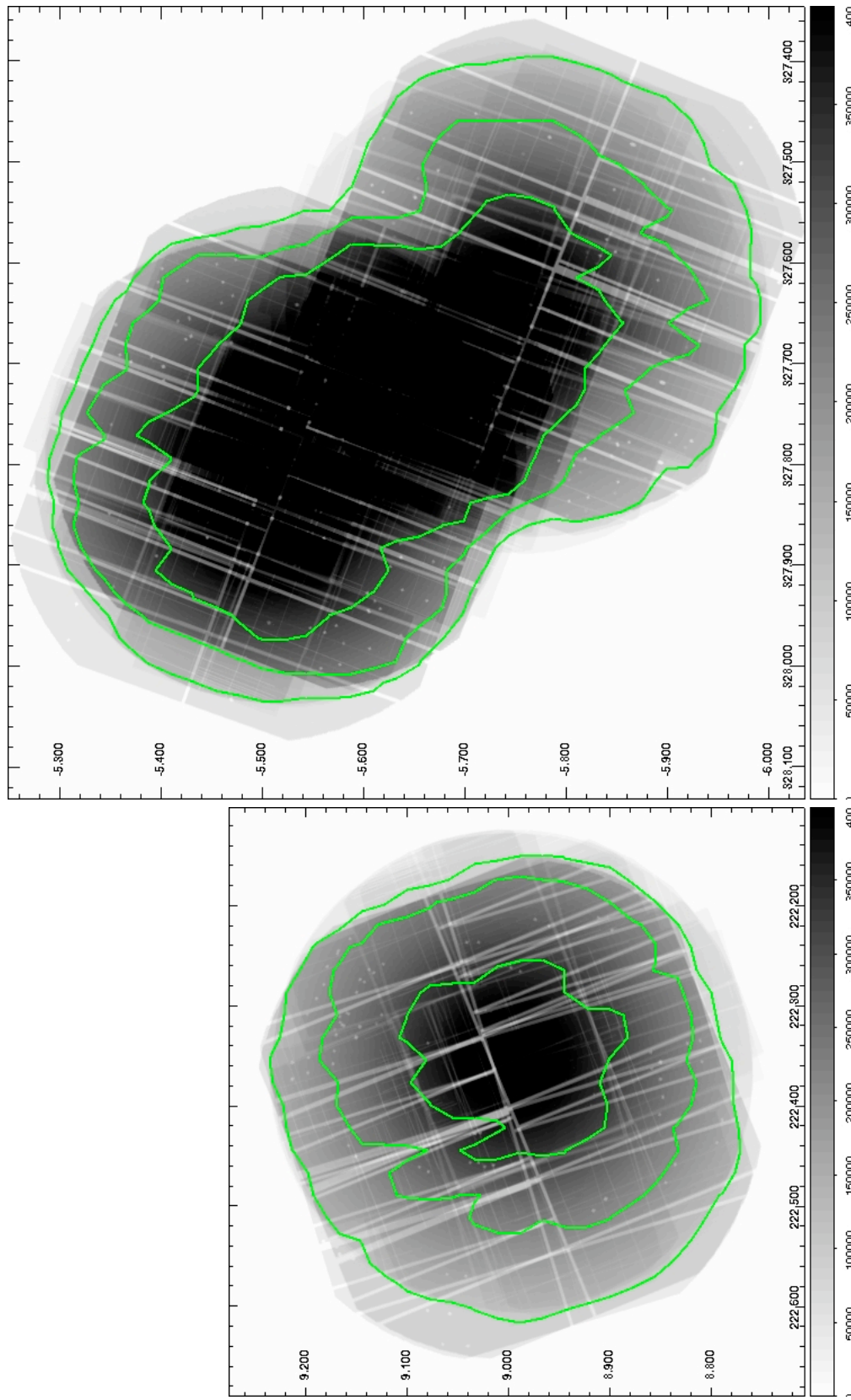


Figure 3.1: Exposure maps of RA14h (left) and RA21h (right) patch of CNOC2. Co-added XMM and Chandra exposures are shown with greyscale corresponding to seconds of exposure in the 0.5–2 keV band for a 2 keV source at $z=0.2$ (see text). The contours (green) indicate the achieved level of effective 100, 200, and 300 ksec equivalent Chandra depth. The total area covered by X-ray observations is 0.2 and 0.3 square degrees for the RA14h and RA21h fields, respectively.

2002, 2003) which are carefully normalized.

Additionally, because one chip in either MOS1 or MOS2 episodically exhibits a distinctly higher background below 1 keV, these ‘hot’ MOS chip data are removed as in Snowden et al. (2008).

Point Source Removal

Adequate point source removal is vital for identifying extended X-ray sources in our data since our exposures are deep and the formal confusion limit for the XMM Point-Spread Function (PSF) precludes using large scales for source detection at exposures exceeding 100 ksec. The XMM PSF has a large width but is cuspy, appearing a bit like the superposition of a simple point source and cluster flux shown in Fig. 1.2. Since the shape of the XMM PSF is not Gaussian, the information on large scales *can* be restored using the detection of point sources on small scales and subsequent modeling and removal of the point source flux. The XMM-Newton PSF can be approximated by a sum of three Gaussians with the most narrow being equivalent to the width of the core of the PSF (5"). This defines the theoretical lower limit on recovering the information content in XMM-Newton images with information at scales larger than this core being retained. Our procedure adopts a symmetric model for the XMM PSF and uses the calibrations of Ghizzardi & Molendi (2002, see also Ferrando et al., 2003).

Flux removal is conducted in three, wavelet-specific, steps in order to achieve a correct flux estimate for each detected point source. The wavelet decomposition is both a spatial and a significance filter, so flux is stored and subtracted from the input image before applying the next spatial scale filtering *only* if its significance is larger than a given threshold (Vikhlinin et al., 1998). As a result, in the wavelet decomposition the flux attributed to each spatial scale varies: as the significance of the source increases, more flux is attributed to smaller scales. A simplified procedure would result in either underestimation of flux pollution from the faint point sources or in the overestimation of the pollution from the strong point sources (typically luminous AGN). To properly subtract the PSF-induced contribution of small-scales to large-scale features, we perform two reconstructions of the small scales, using the detection thresholds of 100, 30, and 4σ . The 4σ image receives the full weight according to PSF models and the other two reconstructions are subtracted from it with proper weights, which are defined by both the XMM PSF on small scales and properties of the wavelet transformation.

On large scales, there are large systematic uncertainties which have now been parameterized by tests on several deep fields (e.g. COSMOS). Luckily the XMM PSF model describing the detections on small scales also predicts the flux on large scales. As discussed in Finoguenov et al. (2007), our selection of spatial scales is done to reduce the variation of this prediction with off-axis angle and greatly simplify the procedure of point source flux removal. Instead of carefully modeling the PSF at each specific position on the chip and off-axis angle, to subtract the expected flux spread from small to large scales we convolve the point source image reconstructed above with Gaussians of width 16, 32, and 64 arcseconds, weighted according to the observed PSF, and finally subtract this from the image together with the wavelet reconstruction on the small scales. Rather than calculating an error for each position, we apply conservative systematic errors across the entire FOV. We add 5% systematic error associated with our model on the 16 and 32 arcsecond scales and 200% systematic error associated with our model on the 64 arcsecond

scale in order to account for deviations between the simplified symmetric PSF model and a two-dimensional PSF characterization. These systematic errors correspond to differences occurring at the edge of the field of view where the shape of the PSF is particularly elongated due to off-axis aberration (Lumb et al., 2003).

3.1.2 Chandra Data & Reduction

Like XMM-Newton, the Chandra X-ray Observatory was launched in 1999. The National Aeronautics and Space Administration's observatory has a $30' \times 30'$ FOV and angular resolution (half energy width) of $0.5''$. Its telescope is comprised of four pairs of mirrors and it carries two X-ray detectors in the focal plane: the Advanced CCD Imaging Spectrometer (ACIS) and the High Resolution Camera (HRC). Both instruments cover a range of 0.1–10 keV and have a spectral (-S) and an imaging (-I) component. Additionally, high resolution spectroscopy is possible with the High Energy Transmission Grating Spectrometer (HETGS) for medium to high (0.4–10 keV) energy and the Low Energy Transmission Grating Spectrometer (LETGS) for low (0.08–2 keV) energy (Chandra Project Science, MSFC, 2011). All Chandra observations were obtained with ACIS-I in VFAINT mode without gratings. In this work we use the available Chandra observations of the CNOC2 fields to further improve the sensitivity toward the detection of extended X-ray emission.

Reduction & Background Removal

Initial Chandra data reduction was performed using the standard reduction procedures of the Chandra Interactive Analysis of Observations (CIAO) package version 3.48¹ with the latest calibration files. In summary, to reprocess the raw data, it is first filtered to reduce particle background, remove cosmic rays and bad pixels, and apply gain and charge transfer inefficiency (CTI) corrections. Background flares are then removed. Finally, the cleaned event files are binned to produce images in the selected energy range.

Point Source Removal

For Chandra, the on-axis scattering of point source flux into $32''$ scales is negligible, while it becomes important at off-axis angles exceeding $3'$. Our simplified point source removal is based on the PSF model which shows that once the scales of $8''$ and $16''$ are polluted, so are the larger scales. Therefore we remove point sources from the Chandra data using the following procedure. Since we use the $32''$ and $64''$ scales to search for extended emission with XMM, we similarly remove the emission on smaller spatial scales from Chandra data (1, 2, 4, 8, and 16 arcseconds). After the removal of point source flux on these small scales, we use the emission detected at scales of $8''$ and $16''$ to predict and subtract the effect of the Chandra PSF on larger scales. Residual variations in the off-axis behavior of the Chandra PSF are treated as systematic errors in our model. We add in quadrature a 20% systematic error associated with this model to the error budget.

¹<http://cxc.harvard.edu/ciao/>

3.1.3 Combined X-ray Imaging

After instrument-specific background and point source removal, the residual XMM and Chandra images were co-added, taking into account the difference in the sensitivity of each instrument to produce a joint exposure map for each patch. Specifically, the Chandra ACIS-I exposure is taken as it is, each XMM EPIC MOS exposure is counted as equal to the Chandra exposure, and the XMM EPIC pn exposure is multiplied by 3.6 times the read-out time correction (0.93-0.98 depending on the read-out mode). The resulting signal-to-noise images are shown in Fig. 3.2.

3.2 X-ray Group Sample Definition & X-ray Brightness

3.2.1 Extended Source Detection

Wavelet reconstructions of the signal-to-noise images for both the final co-added image and the separate XMM and Chandra images were then produced and extended source detection carried out at $32''$ and $64''$ spatial scales. I show wavelet reconstructions for the RA14h and RA21h fields, illustrating the difference between spatial scales, in Figures 3.3 and 3.4 respectively. Our catalog of objects is produced using the Source-Extractor package (SExtractor; Bertin & Arnouts, 1996). The objects are defined as ellipses, with information including the center, FWHM, and position angle recorded in the catalog. The positional uncertainty for the X-ray centers is of order of $10''$ but can reach $30''$ for low significance sources. SExtractor also performs deblending of overlapping extended objects and where necessary/possible, positions and/or redshifts of galaxies within X-ray crowded regions are used to help determine whether emission was likely from distinct sources. The total number of secure detections in the RA14h and RA21h patches is 31 and 33, respectively. An additional five sources with low significance (significance < 2) are detected in each field.

3.2.2 Significance, Fluxes, and Luminosities

In order to measure the X-ray flux (and luminosity) of our systems, an aperture must first be defined in which to extract an initial flux measurement. For X-ray selected systems, this area is defined via the wavelet reconstruction of the X-ray images, to optimize the S/N for the source. The source's flux is measured from the residual image (after the background and point sources have been subtracted off) and so the estimate of flux signal-to-noise ratio is *not* the same as the significance of the source detection (estimated using the wavelet image). All X-ray sources have a wavelet detection $\geq 4\sigma$, corresponding to a certain detection in flux, but in cases where the aperture has been reduced in order to prevent merging of adjacent sources, the final measurement of significance may be much lower. To ensure that only robust X-ray measurements are included, I choose to include X-ray derived properties only for X-ray systems having a significance ≥ 1 in subsequent analysis. Note that negative values of significance reflect that the measured flux is lower than the average background level. Statistical background removal sets the mean of the background to zero, while the statistical spread of actually observed counts results in a distribution around zero.

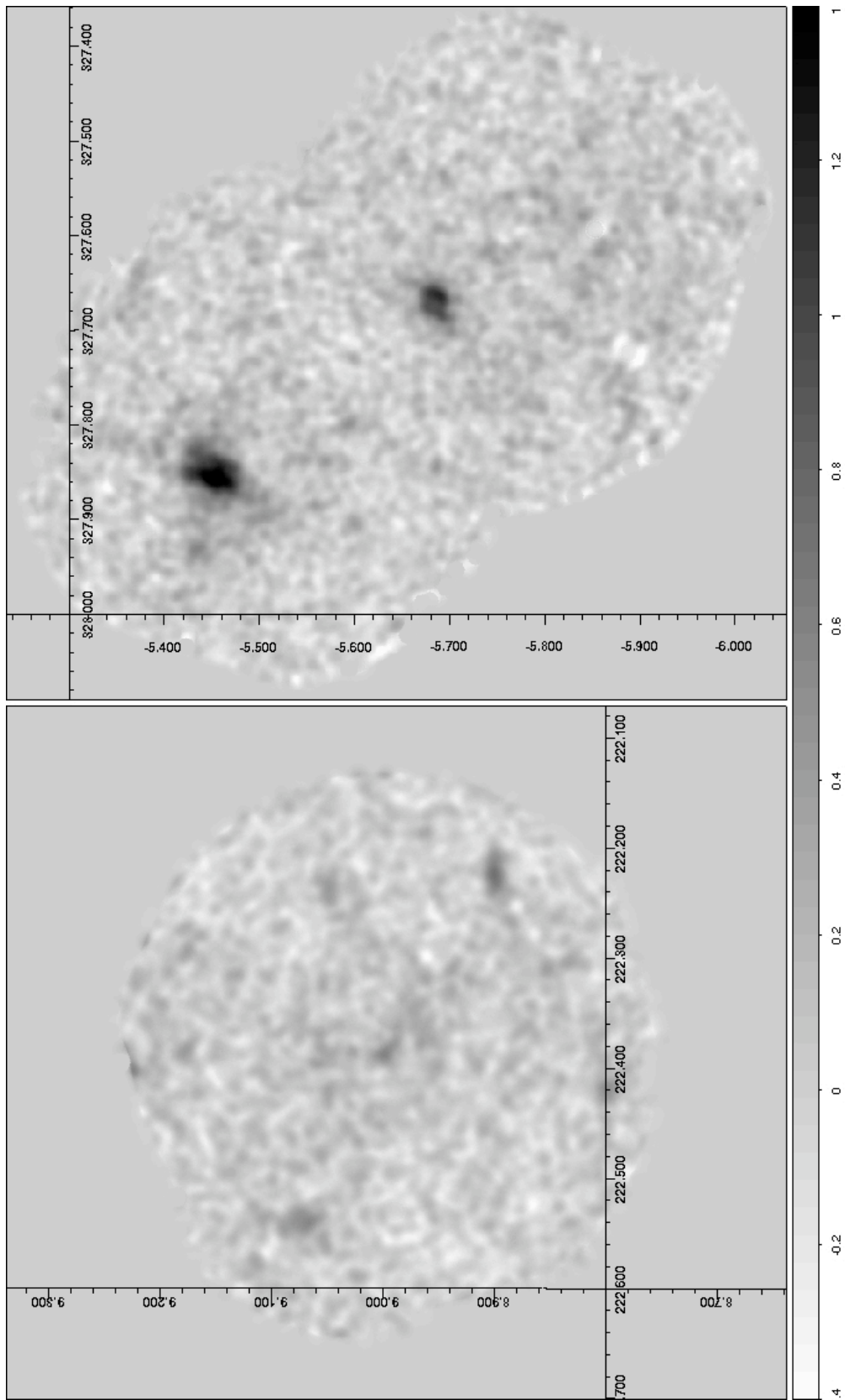


Figure 3.2: Signal-to-noise ratio of the point-source-removed X-ray images in the 0.5–2 keV energy range of the RA14h (left) and the RA21h (right) CNOC2 patches smoothed with a Gaussian of 4 pixels width.

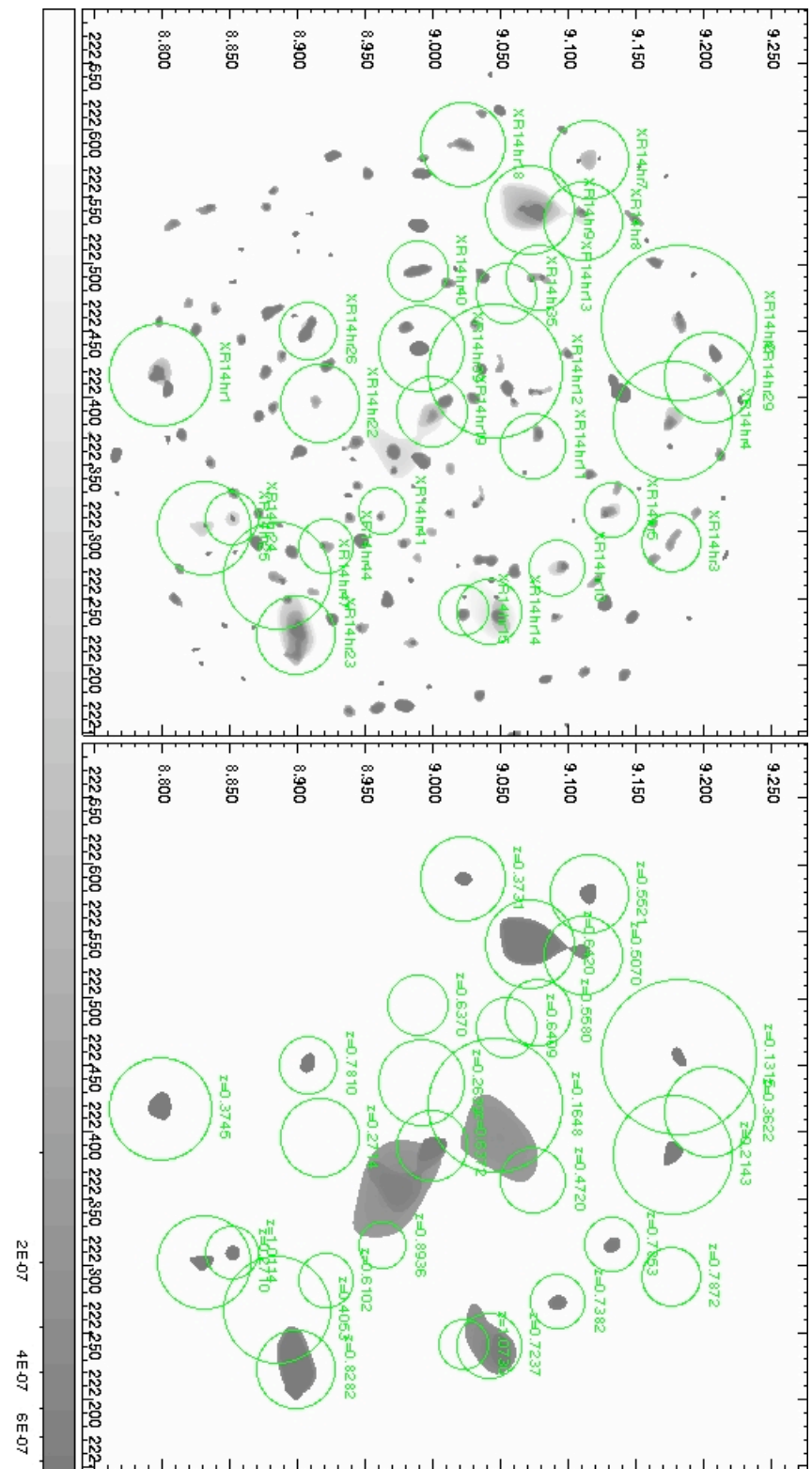


Figure 3.3: Wavelet reconstruction of the point-source-removed X-ray image of the RA14h CNOC2 patch on all spatial scales (left) and scales from $32''$ to $25''$ (right). The units of the image are $\text{ergs s}^{-1} \text{cm}^{-2} \text{arcmin}^{-2}$. Circles indicate the spectroscopically identified X-ray systems with radii of the circles showing the Γ_{200} .

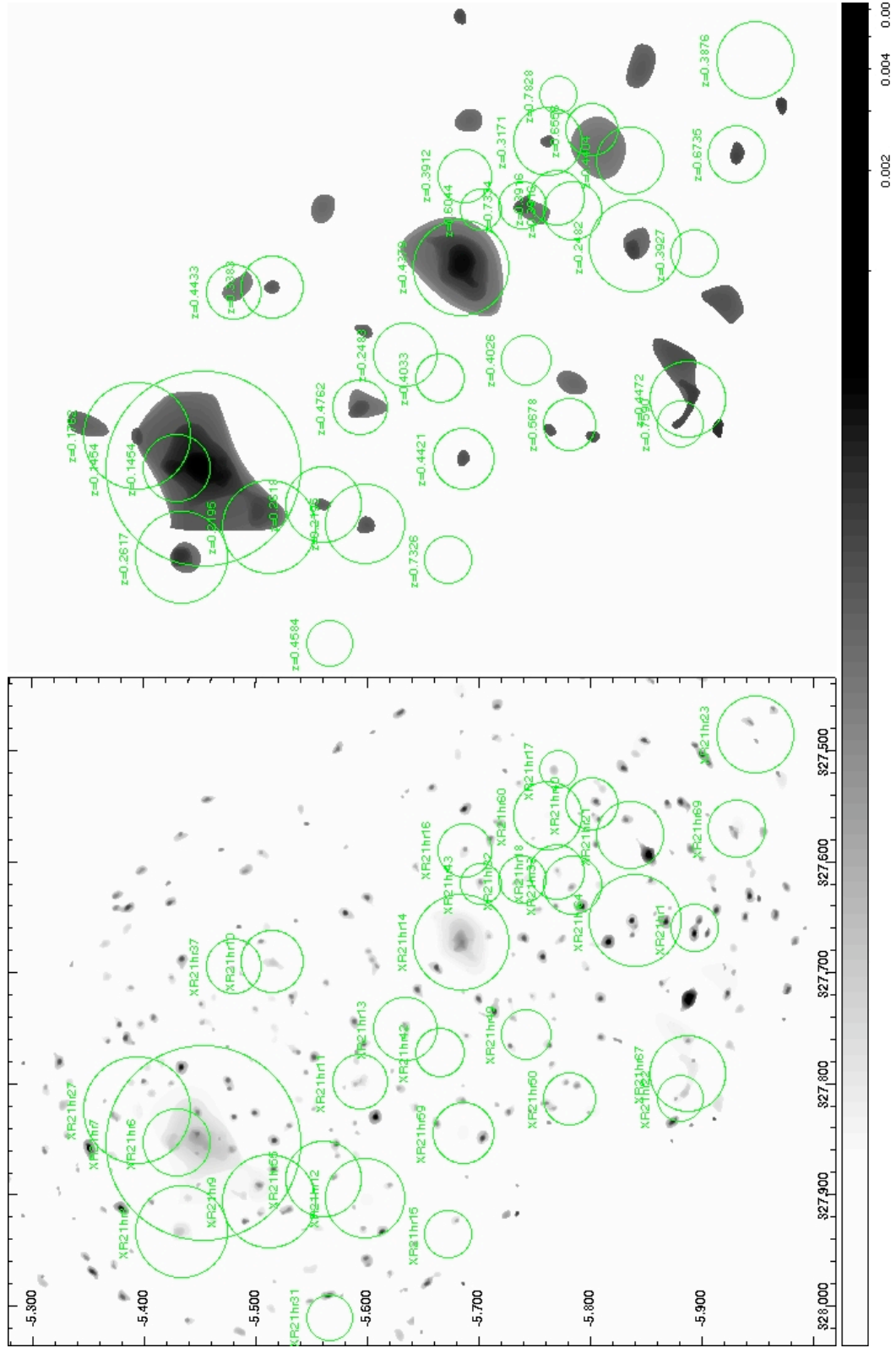


Figure 3.4: Wavelet-reconstruction of the point-source removed X-ray image of the RA21h CNOc2 patch on all spatial scales (left) and scales from $32''$ to $256''$ (right). The units of the image are $\text{ergs s}^{-1} \text{cm}^{-2} \text{arcmin}^{-2}$. Circles indicate the spectroscopically identified X-ray systems with radii of the circle showing r_{200} .

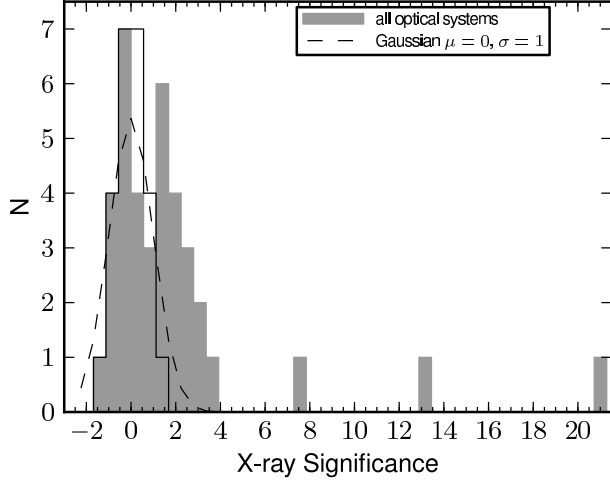


Figure 3.5: X-ray significance of optically selected systems. The black solid line indicates the negative portion of the histogram and its reflection above zero while the black dashed line shows a Gaussian approximation having a mean, μ , of 0 and variance, σ , of 1.

above zero. Comparison of this to the dashed Gaussian approximation line shows that the noise is slightly over-estimated, and thus the significance underestimated. To help ensure the X-ray emission is real, only X-ray derived properties for optical systems having a significance ≥ 2 are included in subsequent analysis.

Once an area is defined, flux measurement for all systems is performed on background and point source subtracted XMM images only. In summary, the total flux for each group in the 0.5–2 keV band is computed as in Eq. 1 of Finoguenov et al. (2007), extrapolating the surface brightness to r_{500} . This is the radius within the average group density is 500 times the critical density at the redshift of the group and is equivalent to $\sim 0.6r_{200}$. The total flux and corresponding $r_{200,x}$ are then derived iteratively from the corrected observed flux using the redshift of the group (see §4.2.1 and 4.2.4) and appropriate scaling relations. These assumed scaling relations for systems of similar mass and redshift have been verified using weak lensing calibrations of X-ray groups in the COSMOS survey (Leauthaud et al., 2010).

In detail, the process of defining the flux (and luminosity) begins by extrapolating the measured flux (F_d) to the flux within r_{500} for each group, assuming the surface brightness profile measured for local groups. The flux within r_{500} is

$$F(< r_{500}) = C_\beta(z, T) F_d \quad (3.1)$$

where F_d is the total counts in the area defined by the detection algorithm and $C_\beta(z, T)$ is a correction iteratively defined using the current estimate of r_{500} , flux, and redshift of the system and assuming a β -model characterization of the emission. The β -model assumes that both the

In order to measure the X-ray flux of our *optically selected* systems, a constant circular aperture is defined, with a radius of $0.5'$, surrounding the R-band luminosity-weighted center of the group members. This aperture is derived from the confusion limit in the X-ray imaging. I discuss the choice of this aperture especially in relation to that used for the X-ray systems in §3.2.3. The distribution of the S/N of the X-ray flux estimate (hereafter X-ray significance) estimated using the residual, background and point-source removed, image of our optical systems can be seen in Fig. 3.5. The histogram is double-peaked, with the first peak resulting from the noise in our flux measurements and the second being the ‘real’ peak of the X-ray significant systems. The noise peak can be approximated by a Gaussian having a mean of 0 and variance of 1 (shown as a dashed line). The solid line indicates the negative portion of the histogram and its reflection

hot gas and the galaxies are in hydrostatic equilibrium and isothermal. In this model, the surface brightness at a given radius ($S(R)$) is:

$$S(R) = S_o(1 + (R/r_{core})^2)^{-3\beta+0.5} \quad (3.2)$$

r_{core} is the core radius of the gas distribution and β is the ratio of the energy per unit mass in galaxies to the energy per unit mass in the hot gas. We parameterize these as follows:

$$\beta = 0.4(kT/1keV)^{1/3} \quad (3.3)$$

and

$$r_{core} = 0.07(kT/1keV)^{0.63}r_{500} \quad (3.4)$$

The rest-frame X-ray luminosity in the 0.1–2.4 keV band can then be calculated iteratively by k-correcting the flux measurement within an estimated $r_{200,x}$. This k-correction, $K(z,T)$, is the ratio of the luminosity integrated in the observed (redshifted) and rest frame 0.1–2.4 keV band and assumes an elemental abundance of 1/3 solar as in Böhringer et al. (2004):

$$L_{0.1-2.4keV} = 4\pi d_L^2 K(z,T) C_\beta(z,T) F_d \quad (3.5)$$

or, equivalently:

$$L_{0.1-2.4keV} = 4\pi d_L^2 K(z,T) F(< r_{500}) \quad (3.6)$$

where d_L is the luminosity distance. The $L_{0.1-2.4keV}$ -T relations of Voit (2005) are used to estimate the temperature T as in Leauthaud et al. (2010):

$$kT/keV = 0.2 + 6 \times 10^{[\log_{10}(L_{0.1-2.4keV} E_z^{-1}) - 44.45]/2.1} \quad (3.7)$$

where

$$E_z^{-1} = [\Omega_M(1+z)^3 + \Omega_M]^{1/2} \quad (3.8)$$

Finally, the total group mass within the estimated r_{200} ($r_{500} \sim 0.6r_{200}$) is calculated following the $z \sim 0.25$ relation from Rykoff et al. (2008b) assuming standard evolution. For X-ray systems, this mass is then used to calculate a new r_{500} and this aperture is then used to recalculate the flux and luminosity and the whole process is repeated until a stable solution is obtained.

The luminosities for our systems as a function of redshift are shown in Fig. 3.6. It is clear from this figure and Fig. 4.12 that, with increasing redshift, the sample is biased towards systems with higher X-ray luminosities and velocity dispersions. For X-ray and optical systems with low X-ray significance, we calculate upper limits for the X-ray flux, radius, luminosity, and mass, and these measures are demarcated by grey points in the appropriate relations. Note that we are unable to *robustly* measure X-ray temperatures for our systems given the depth of our data as secure measurements of temperature require $\gtrsim 10\sigma$ detection on the wavelet image (Mainieri et al., 2007). Sources in our sample that meet this criterion, which is based on the number of bins and counts required to properly characterize the spectrum, are few and will be biased towards high mass, cluster-like systems.

Our X-ray and optically selected group positions, redshifts (see §4.2), and basic X-ray properties are presented in Tables 3.1 and 3.2 respectively. Tab. 3.1 lists the group identification

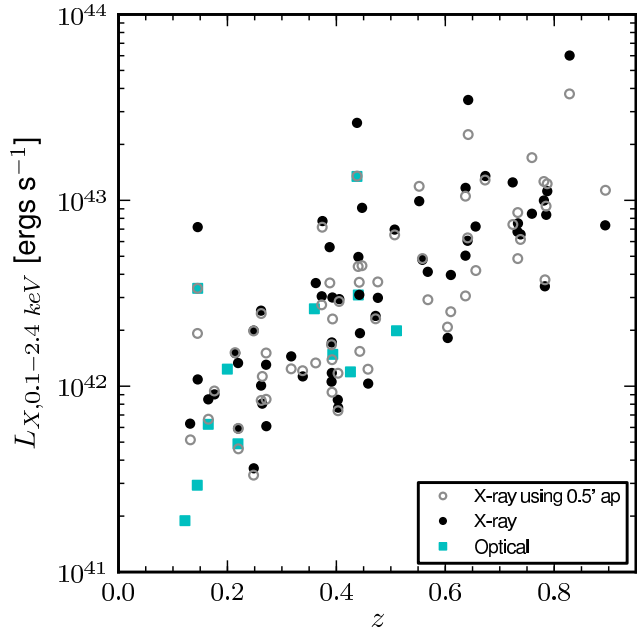


Figure 3.6: X-ray luminosity as a function of redshift for all X-ray (black circles) and optical (cyan squares) systems with X-ray significance ≥ 1 and 2 respectively. Note that 2σ upper limits on X-ray luminosity for optical systems with low significance are not shown here. For X-ray systems, the X-ray luminosity derived using a fixed $0.5'$ aperture is shown in grey open circles.

number for the X-ray system (column 1); IAU name (2); R.A. and Decl. of the center of the extended X-ray emission for Equinox J2000.0 (3 & 4); spectroscopic redshift (5, see §4.2.4); group redshift quality (6); the total flux in the $0.5-2$ keV band (7); and significance of the X-ray flux (8). Tab. 3.2 is similarly structured, classifying the optical systems according to the group number from the optically selected group catalog of Carlberg et al. and with an additional column (column 5) listing the X-ray group ID where there is a confident match.

Table 3.1: Basic Properties of X-ray Selected Groups

XID	IAU name	RA J2000	Dec J2000	z	Q	X-ray Flux 10^{-14} ergs cm $^{-2}$ s $^{-1}$	X-ray Significance
XR14h02	144949+0910.9	222.45584	+9.18167	0.1315	1.0	0.89±0.31	2.84
XR14h09	145009+0904.3	222.54075	+9.07188	0.6420	1.0	1.23±0.12	9.75
XR14h10	144905+0905.5	222.27293	+9.09198	0.7382	1.0	0.13±0.05	2.48
XR21h08	215143−0526.0	327.93324	−5.43371	0.2617	1.0	0.77±0.10	7.74
XR21h10	215045−0530.9	327.68966	−5.51535	0.3383	1.0	0.17±0.05	3.23
XR21h11	215111−0535.6	327.79834	−5.59362	0.4762	1.0	0.20±0.04	4.5
XR21h12	215136−0535.8	327.90274	−5.59811	0.2195	1.0	0.25±0.08	3.2
XR21h14	215041−0541.0	327.67186	−5.68486	0.4379	1.0	2.34±0.08	26.24
XR21h15	215144−0540.3	327.93620	−5.67284	0.7326	1.0	0.14±0.05	2.69
XR21h60	215014−0545.7	327.55853	−5.76198	0.3171	1.0	0.27±0.06	4.14
XR21h64	215036−0550.4	327.65308	−5.84050	0.2482	1.0	0.68±0.13	5.17
XR21h09	215137−0530.7	327.90525	−5.51241	0.2195	1.5	0.61±0.08	7.47
XR14h03	144910+0910.5	222.29202	+9.17579	0.7872	2.0	0.20±0.05	3.53
XR14h08	145007+0906.6	222.53225	+9.11101	0.5070	2.0	0.41±0.09	4.22
XR14h18	145021+0901.3	222.58939	+9.02196	0.3731	2.0	0.39±0.12	3.01
XR14h22	144934+0854.9	222.39582	+8.91603	0.2714	2.0	0.16±0.07	2.14
XR14h25	144912+0849.8	222.30276	+8.83071	0.2710	2.0	0.36±0.10	3.56
XR14h35	144954+0903.2	222.47810	+9.05440	0.6409	2.0	0.18±0.05	3.23
XR14h40	144958+0859.3	222.49465	+8.98870	0.6370	2.0	0.15±0.09	1.66
XR14h44	144909+0855.2	222.28837	+8.92101	0.6102	2.0	0.13±0.05	2.61
XR21h06	215124−0525.7	327.85298	−5.42894	0.1454	2.0	1.26±0.18	6.81
XR21h07	215124−0527.1	327.85378	−5.45297	0.1454	2.0	8.18±0.18	44.98
XR21h13	215100−0538.0	327.75085	−5.63451	0.2483	2.0	0.11±0.07	1.49
XR21h18	215026−0546.2	327.60980	−5.77096	0.3916	2.0	0.12±0.04	2.66
XR21h20	215111−0548.5	327.79831	−5.80904	0.1434	2.0	< 0.42	−0.34
XR21h23	214956−0556.8	327.48498	−5.94810	0.3876	2.0	0.65±0.17	3.85
XR21h31	215202−0533.9	328.01069	−5.56647	0.4584	2.0	0.07±0.06	1.11
XR21h32	215027−0544.3	327.61643	−5.73947	0.7334	2.0	0.16±0.03	4.74
XR21h33	215029−0547.0	327.62119	−5.78424	0.3916	2.0	0.19±0.08	2.18
XR21h37	215046−0528.8	327.69397	−5.48061	0.4433	2.0	0.15±0.04	3.56
XR21h42	215105−0539.9	327.77157	−5.66557	0.4033	2.0	0.07±0.03	1.97
XR21h50	215115−0546.8	327.81375	−5.78166	0.5678	2.0	0.17±0.08	2.19
XR21h55	215132−0533.6	327.88562	−5.56036	0.2618	2.0	0.30±0.06	4.81
XR14h11	144927+0904.4	222.36371	+9.07427	0.4720	2.5	0.16±0.04	3.51
XR14h12	144940+0902.7	222.41983	+9.04645	0.1648	2.5	0.74±0.17	4.22
XR14h19	144933+0859.9	222.38956	+8.99939	0.6372	2.5	0.38±0.05	6.82
XR14h29	144939+0912.2	222.41519	+9.20452	0.3622	2.5	0.49±0.11	4.46
XR14h33	144936+0908.2	222.40358	+9.13817	0.8120	2.5	< 0.35	−0.13
XR21h27	215117−0523.6	327.82295	−5.39383	0.1762	2.5	0.70±0.14	4.99
XR14h01	144940+0847.8	222.41731	+8.79825	0.3745	3.0	0.98±0.13	7.29
XR14h05	144915+0907.9	222.31547	+9.13188	0.7853	3.0	0.15±0.05	2.93

XID	IAU name	RA	Dec	z	Q	X-ray Flux	X-ray Significance
XR14h07	145018+0906.9	222.57809	+9.11531	0.5521	3.0	0.47±0.14	3.35
XR14h13	144957+0904.6	222.48963	+9.07809	0.5580	3.0	0.21±0.07	2.95
XR14h23	144853+0853.9	222.22288	+8.89904	0.8282	3.0	1.19±0.09	12.63
XR14h24	144914+0851.0	222.30994	+8.85140	1.0114	3.0	0.18±0.04	3.95
XR14h26	144948+0854.5	222.45019	+8.90837	0.7810	3.0	0.18±0.09	2.07
XR14h37	145016+0859.5	222.56919	+8.99258	0.5567	3.0	< 0.23	0.34
XR14h38	145007+0859.3	222.52976	+8.99000	0.2968	3.0	< 0.61	-0.02
XR14h39	144944+0859.4	222.43683	+8.99109	0.2639	3.0	0.23±0.21	1.1
XR14h41	144915+0857.7	222.31469	+8.96299	0.8936	3.0	0.08±0.03	2.53
XR14h47	144904+0853.0	222.26735	+8.88464	0.4053	3.0	0.30±0.08	3.48
XR21h16	215021-0541.2	327.58912	-5.68771	0.3912	3.0	0.11±0.05	2.08
XR21h17	215004-0546.3	327.51681	-5.77184	0.7828	3.0	0.05±0.04	1.14
XR21h19	215115-0548.0	327.81629	-5.80110	0.5674	3.0	< 0.12	0.91
XR21h21	215018-0550.1	327.57591	-5.83644	0.4404	3.0	0.42±0.08	5.14
XR21h30	215047-0533.8	327.69873	-5.56387	0.3949	3.0	< 0.07	0.13
XR21h40	215011-0548.0	327.54848	-5.80150	0.6556	3.0	0.21±0.06	3.45
XR21h41	215011-0552.9	327.54919	-5.88323	0.8705	3.0	< 0.15	0.77
XR21h43	215028-0542.1	327.61959	-5.70213	0.6044	3.0	0.05±0.03	1.47
XR21h48	215111-0544.1	327.79699	-5.73500	0.2613	3.0	< 0.16	0.52
XR21h49	215101-0544.5	327.75567	-5.74279	0.4026	3.0	0.08±0.05	1.47
XR21h59	215122-0541.1	327.84397	-5.68637	0.4421	3.0	0.26±0.06	4.29
XR21h69	215016-0555.9	327.56980	-5.93195	0.6735	3.0	0.39±0.08	4.58
XR14h04	144932+0910.6	222.38352	+9.17669	0.2143	3.5	0.72±0.15	4.74
XR14h14	144857+0902.4	222.24015	+9.04137	0.7237	3.5	0.30±0.05	5.21
XR21h22	215115-0552.8	327.81317	-5.88123	0.7590	3.5	0.17±0.09	1.89
XR21h67	215109-0553.2	327.79085	-5.88775	0.4472	3.5	0.74±0.13	5.49

*Column description: group identification number for the X-ray system (column 1); IAU name (2); R.A. and Decl. of the center of the extended X-ray emission for Equinox J2000.0 (3 & 4); spectroscopic redshift, see §4.2.4 (5); group redshift quality (6); the total flux in the 0.5–2 keV band (7); and significance of the X-ray flux (8)

Table 3.2: Basic Properties of Optically Selected Groups

OID	RA J2000	Dec J2000	z	XID	X-ray Flux 10^{-14} ergs cm $^{-2}$ s $^{-1}$	X-ray Significance
OP14h01	222.42588	+9.05001	0.1648	XR14h12	0.53 ± 0.15	3.45
OP14h08	222.24931	+9.16426	0.2287	...	< 0.18	-1.5
OP14h09	222.22414	+8.94529	0.2616	...	< 0.11	1.25
OP14h10	222.38704	+8.89722	0.2709	XR14h22*	< 0.10	-0.53
OP14h11	222.28817	+8.83040	0.2710	XR14h25*	< 0.11	1.39
OP14h15	222.19998	+8.96308	0.3070	...	< 0.13	0.38
OP14h16	222.59024	+9.10364	0.3065	...	< 0.31	0.87
OP14h19	222.55307	+8.96008	0.3251	...	< 0.18	-0.54
OP14h24	222.26426	+9.11689	0.3593	...	< 0.12	0.19
OP14h25	222.43995	+9.22828	0.3619	XR14h29*	< 2.72	-0.13
OP14h27	222.42101	+9.03718	0.3729	...	< 0.19	1.95
OP14h28	222.59535	+9.01885	0.3729	XR14h18*	< 0.14	1.43
OP14h29	222.44650	+8.85237	0.3737	...	< 0.12	-0.58
OP14h30	222.49989	+8.82020	0.3941	...	< 0.13	1.53
OP14h31	222.31070	+9.18861	0.3934	...	0.16 ± 0.07	2.11
OP14h32	222.48710	+8.92912	0.3948	...	< 0.10	-0.84
OP14h34	222.16981	+8.85406	0.4658	...	< 1.89	-0.06
OP14h37	222.38534	+9.07346	0.4717	XR14h11*	< 0.08	-0.12
OP14h36	222.37571	+9.15315	0.4693	...	< 0.11	0.69
OP14h38	222.34864	+8.98095	0.5104	...	0.10 ± 0.04	2.59
OP14h40	222.34715	+8.92136	0.5424	...	< 0.06	-0.54
OP21h101	327.75074	-5.77684	0.1220	...	0.28 ± 0.13	2.15
OP21h102	327.66348	-5.76956	0.1446	...	0.31 ± 0.11	2.78
OP21h104	327.85585	-5.45052	0.1454	XR21h07	3.91 ± 0.18	20.91
OP21h111	327.87688	-5.83900	0.1790	...	< 2.44	-0.75
OP21h113	327.79113	-5.29070	0.1998	...	0.70 ± 0.21	3.34
OP21h117	327.90130	-5.51873	0.2193	XR21h09	0.21 ± 0.06	3.18
OP21h119	327.70455	-5.86617	0.2365	...	< 0.14	1.33
OP21h120	328.04147	-5.58994	0.2414	...	< 0.41	-0.56
OP21h123	327.70645	-5.79192	0.2641	...	< 0.10	0.93
OP21h129	327.73460	-5.67694	0.3171	...	< 0.07	0.27
OP21h132	327.66658	-5.67135	0.3596	...	0.36 ± 0.04	7.61
OP21h133	327.70045	-5.63780	0.3733	...	< 0.06	-0.97
OP21h134	327.63220	-5.70360	0.3918	...	< 0.04	1.34
OP21h137	327.65508	-5.49026	0.4258	...	0.10 ± 0.05	2.04
OP21h138	327.67050	-5.68197	0.4378	XR21h14	1.17 ± 0.08	13.32
OP21h139	327.58913	-5.84084	0.4403	...	0.25 ± 0.11	2.25
OP21h140	327.67658	-5.47646	0.4658	...	< 0.07	0.02

* match to X-ray system but low X-ray significance using the optical center and aperture

† Column description: group identification number for the optical system (column 1); R.A. and Decl. of the center of the extended X-ray emission for Equinox J2000.0 (2 & 3); spectroscopic redshift given an X-ray derived r_{200} radial cut, see §4.2.4 (4); X-ray group ID where there is a confident match (5); the total flux in the 0.5–2 keV band (6); and significance of the X-ray flux (7).

3.2.3 Aperture Tests

To ensure that the assignment of a *constant* aperture centered on the luminosity-weighted group center for optical groups and a *variable* aperture centered on the X-ray emission peak for X-ray systems does not significantly bias our comparison, I first compare the flux measurements for groups which are independently detected both as optical and X-ray systems (see §4.3) in Fig. 3.7. There are only four such, relatively bright, systems having X-ray significance greater than our cut off and which are not located near the X-ray and/or optical survey edges where luminosity-weighted centers can be particularly inaccurate and X-ray apertures incomplete. All four have higher X-ray fluxes for the X-ray selected system than for the optical counterpart. On average, the difference is a factor of two, indicating that our choice of the $0.5'$ fixed aperture may lead to an underestimated flux despite the correction. In all these cases, the X-ray defined aperture is larger (up to a factor of two) than $0.5'$. As the larger aperture is resulting in a larger flux this indicates that our systems likely have a flatter surface brightness profile than the applied assumed relation derived from local groups.

We then test the effect of using a constant aperture for all X-ray selected systems, measuring the flux using the fixed $0.5'$ aperture but centered on the X-ray emission peak and calculating the difference between this measurement and the flux measured using the variable aperture. Both the flux and luminosity measured for X-ray systems with these two different apertures are shown in Fig. 3.8. The average resultant percentage change in the flux measures is less than 4% with measures scattered within a factor of two in both directions. We further find that X-ray flux measures can be greatly affected by the emission of neighboring groups. Since this ‘confusion’ may bias measurement of flux, I flag systems which lie in crowded X-ray regions (see §4.2).

I conclude that for individual X-ray systems, the use of the $0.5'$ aperture may provide results more comparable to the optical systems but that, on average, the use of the X-ray aperture produces measures which are comparable to those resulting from a constant aperture but with higher S/N and less contamination. I thus choose to use this variable aperture for the X-ray systems. Fig. 3.6 shows the X-ray luminosity (see §3.2.2) as a function of redshift for all systems and includes for the X-ray systems luminosities measured with both choices of aperture. The overall relation is very similar regardless of the choice of aperture. For the brightest X-ray systems, the use of the fixed aperture usually results in a noticeably lower L_X . This again indicates the applied local relation has a steeper surface brightness profile than our systems and implies that feedback may be more important in groups at higher redshift. This echoes the conclusion reached using the four matched systems; that smaller X-ray apertures can lead to an under-estimation of flux for bright systems and produce greater uncertainty in X-ray derived properties.

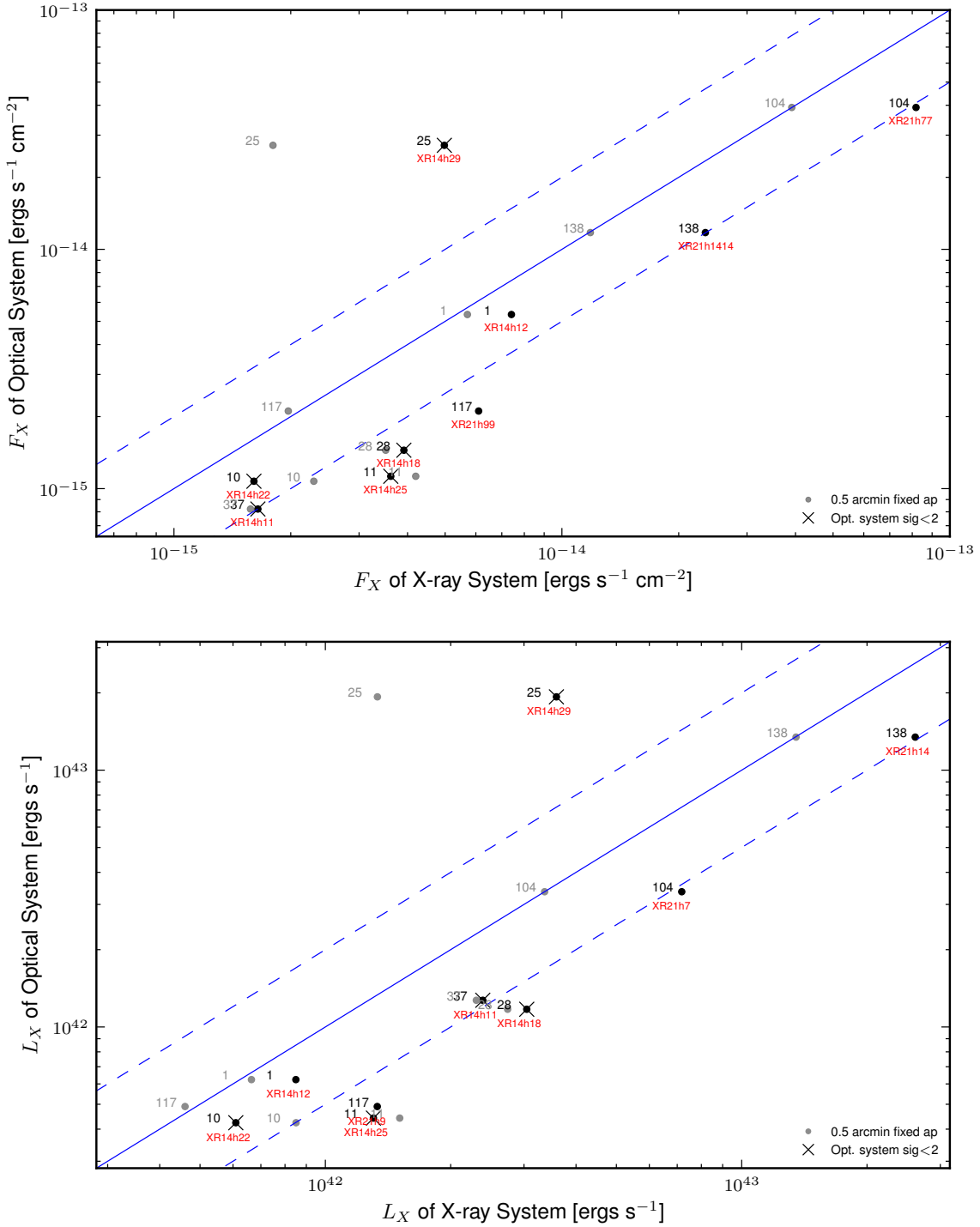


Figure 3.7: X-ray aperture comparison for matched X-ray - optical systems. Flux (top) and luminosity (bottom). Grey points are measurements using the $0.5'$ aperture while black X's indicate optical systems with X-ray significance < 2 . 1:1 relation is marked by solid while 2:1 and 1:2 are shown by dashed blue lines. X-ray group IDs appear in red and the number of the corresponding optical system in black. To aid in matching the fixed and X-ray aperture measurements, the optical ID numbers are repeated above the former in grey.

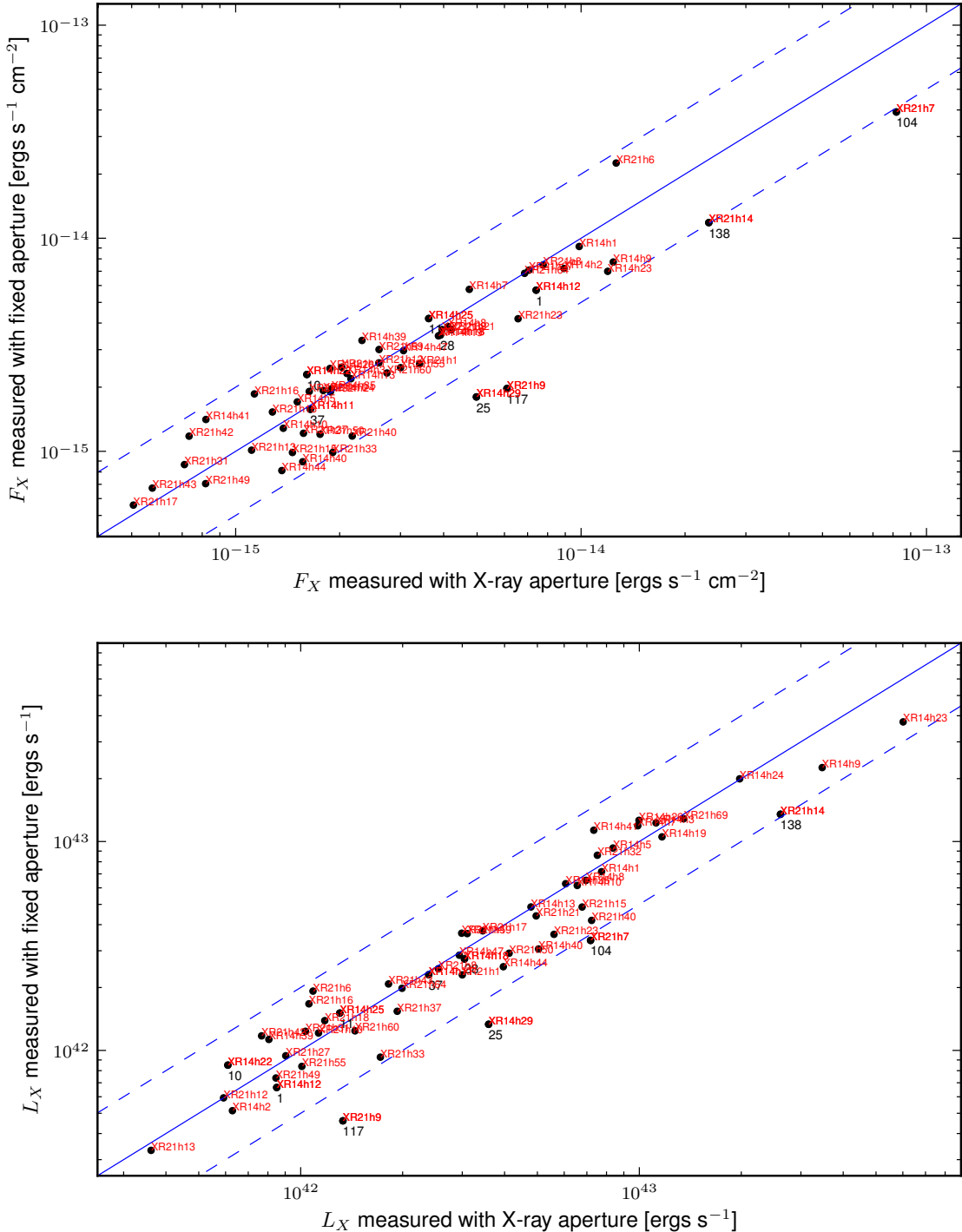


Figure 3.8: X-ray aperture comparison for all X-ray systems. Flux (top) and luminosity (bottom). 1:1 relation is marked by solid while 2:1 and 1:2 are shown by dashed blue lines. X-ray group IDs appear in red and the number of the corresponding optical system in black.

Follow-up Spectroscopy and Measured Group Properties

4.1 Follow-up Spectroscopy

Although spectroscopic completeness is relatively high in areas containing most of our optically selected groups, the extended X-ray sources (the X-ray selected systems) are often located in regions with very few previously determined redshifts. In many cases, a system redshift was impossible to determine from the available spectroscopy. A program of targeted follow-up spectroscopy for the X-ray detected systems was executed primarily using the VLT-FORS2 and Magellan-IMACS spectrographs. Objects brighter than $R \approx 22$ and those close to the center of the X-ray contours were preferentially targeted with both instruments. The magnitude constraint relates to the redshift range of the groups, luminosity range of galaxies, depth of telescopes and available time, target density, depth of photometric catalog, and consistency with the LDSS2 depth for optically selected groups. Objects identified as highly point-like in our photometry, which are likely to be stars, were generally avoided. However, we preferred to risk targeting some stars than to spuriously avoid galaxies. A handful of objects with previously determined redshifts were also re-observed to allow for calibration. Some additional Gemini-GMOS spectroscopy has also been acquired as part of a program to extend this type of group study to higher redshift (Balogh et al., 2011b). A summary of the follow-up spectroscopy can be found in Tab. 4.1 and includes for each instrument the wavelength range and area of the FOV and the total number of masks, spectra, and redshifts for each field. In total, 1,946 previously unknown, secure redshifts have been measured, yielding a full sample of nearly 5,000 redshifts in the RA14h and RA21h CNOC2 fields. I provide a full table of the high quality redshifts used in this analysis in Appendix A. The following section details the observations, data reduction, and redshift determination.

4.1.1 FORS2 Observations

FORS2 is a multi-mode optical instrument with a 6.8' X 6.8' FOV operating in the wavelength range 330-1100 nm, capable of imaging, polarimetry, and long-slit and multi-object spectroscopy. It is mounted on UT1 (Antu), one of the four 8.2 m Unit Telescopes of the Very Large Telescope array at the European Southern Observatory's Paranal Observatory in Chile. In multi-object spectroscopy mode, a mask with up to 470 slits is inserted into the focal plane. Each slit can have different length, width, and even shape, and these are cut into this mask with a dedicated laser cutting machine. Masks are exchangeable, with a maximum of ten mountable inside the instrument simultaneously. In addition to employing active optics, atmospheric dispersion has to be further corrected to use narrow slits. The Atmospheric Dispersion Correctors (ADC) on the FORS instruments allow targets to be observed away from the meridian, correcting distortions due to the variation of air mass which results from changing the altitude angle of the telescope. This provides a distinct advantage over other multi-object spectrographs, such as the VLTs VIable MultiObject Spectrograph (VIMOS).

In order to create a mask, accurate astrometry, which was obtained with pre-imaging, is required and the FORS Instrumental Mask Simulator (*FIMS*) software tool must be used. Masks were placed to cover as many X-ray groups as possible. Due to a lack of accurate pre-existing astrometry, slits were placed carefully by hand, using the pre-imaging obtained several weeks before the observing runs and the available photometric and spectroscopic catalogs. A slit width of 1'' was used for all objects with a dispersion of $1.68 \text{ \AA pixel}^{-1}$. Slit lengths were set to $\geq 5''$ in order to maximize the total number of objects per mask and obtain as many redshifts in the central X-ray source regions as possible while still obtaining a measure of the sky background level. Fig. 4.1 shows an example of a finding chart with a FIMS mask overlaid.

Utilizing GTO time taken from an allocation awarded for building the OmegaCAM instrument for the VLT Survey Telescope, FORS2 observations were conducted over the course of three visitor-mode observing runs in 2007-2008. The GRIS300V grism and GG375 filter were used, resulting in an effective wavelength range of $\approx 430\text{--}700$ nm. The first observing run consisted of 0.6 of a night, on October 5, 2007 (run ID of 080.A-0427(D)), and was conducted by Dr. Laura Parker. A further two half nights, starting March 1, 2008 (080.A-0427(B)) were conducted by myself and Prof. Dr. Roberto Saglia. Finally, run ID 081.A-0103(B) consisted of two half nights starting August 24, 2008 and was conducted by myself and Dr. David Wilman. Observational conditions were overwhelmingly ideal with seeing $\lesssim 1$ arcseconds and negligible moon. On March 2, 2008, observations were delayed due to a mechanical failure involving the tertiary mirror and seeing above average at the beginning of the night (~ 1.25 arcsec). The total integration time per mask ranged from 49 to 77 minutes and was varied in order to maximize the amount of time on each mask, given the specific time and visibility constraints. A total of 21 MXU masks were observed. In addition to the science exposures, bias, flat field, and arc lamp frames were taken to allow for accurate calibration. Bias frames are taken throughout the night to measure the random readout noise from the amplifier and the noise from the camera electronics. Flat fields measure the response of the telescope-camera system to a source of uniform radiation and allow for the removal of multiplicative variations produced by illumination differences (vignetting and dust halos) and pixel-to-pixel sensitivity differences. For VLT observations, flat

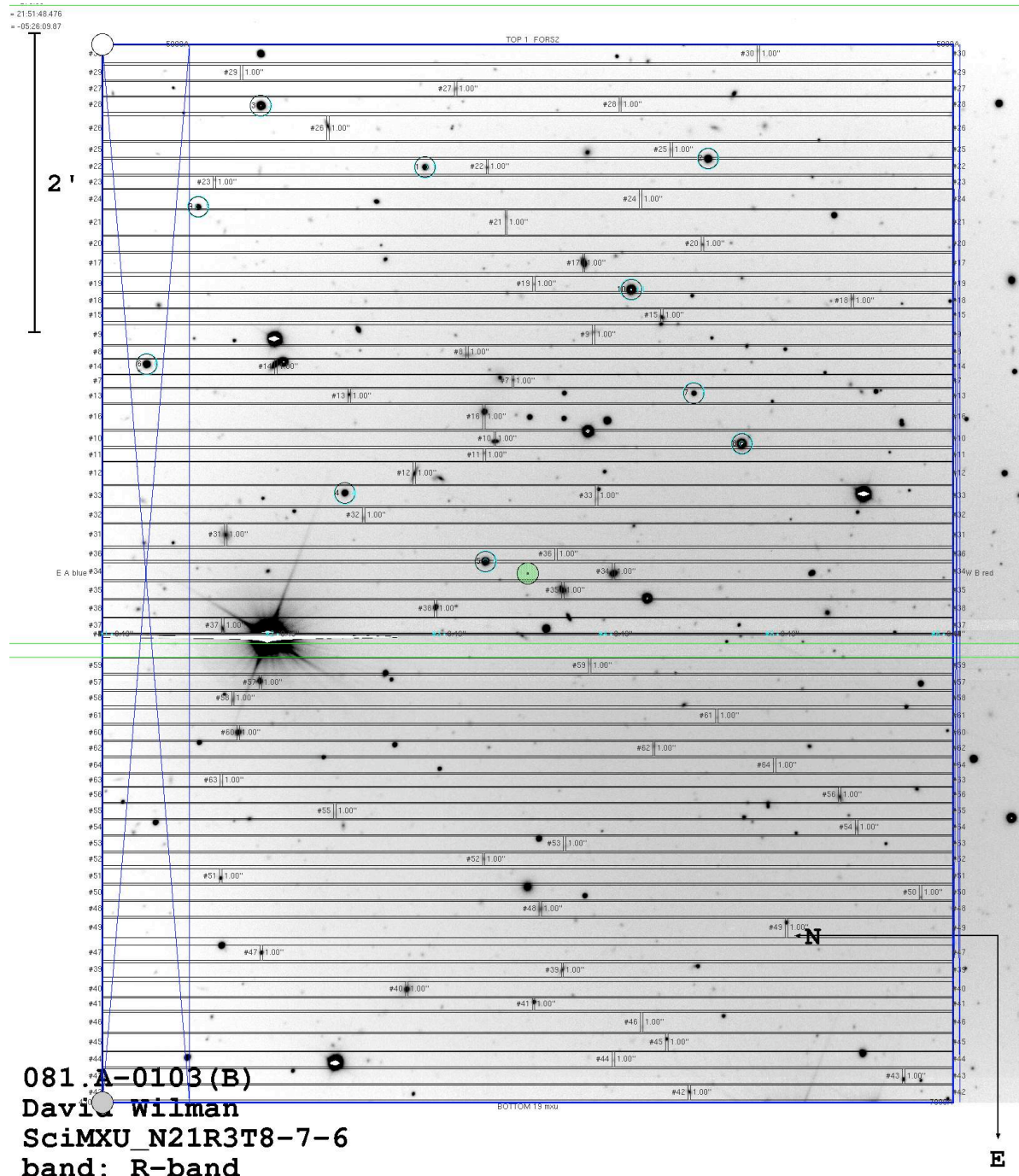


Figure 4.1: Example FORS2 mask. The field pre-imaging is used to design each mask and slits placed by hand using existing photometric and spectroscopic catalogs for target choice.

fields are sky exposures taken of the sky at twilight. Arc lamp frames are wavelength calibration exposures taken during the day with the telescope at zenith. For MXU observations, flat fields and arc lamp frames must be obtained for all masks.

FORS2 Data Reduction

Reduction of the FORS2 data primarily involved a modification of the standard FORS2 pipeline procedure. The pipeline process is divided into two main parts: calibration and science. As no co-adding of exposures can be done using the pipeline, chip images from consecutive exposures were co-added using the Image Reduction and Analysis Facility (IRAF^{*}) *imcombine* tool with cosmic-ray rejection applied before further pipeline reduction steps were applied. The data calibration was then performed with version 4.3.5 of the FORS pipeline, which performs bias correction, flat-fielding, correction for optical distortions, and wavelength calibration (Appenzeller et al., 1998). This process requires bias, lamp, and screen flat images and a master catalog containing reference arc lamp lines and a so-called grism table containing default parameters appropriate for the grism and filter used during the observations. First, a master (median) bias is created and removed from the flat and arc lamp exposures. Then, slits are located and spectral curvature modeled. Master flat fields are then created. Finally, a wavelength calibration map and model of the global optical distortions are produced.

After the initial calibration steps, the ‘science’ reduction, where the data are reduced, wavelength correction applied, sky background subtracted, and individual spectra extracted, was performed. This process required a single science image and the products from the calibration process: master bias, master flat, table of slit locations (object table), and the coefficients for the wavelength solution and spectral curvature corrections. Additionally, a grism table (FORS2_GRS_300V_20_GG375_80.fits) containing the default parameters appropriate for the filter and grism used and a catalog of reference arc lamp lines (FORS2_ACAT_300V_20_GG375_80.fits) were needed. First, the master bias and normalized flat field were removed from the science exposure frame and the images remapped to eliminate optical distortions. The wavelength solution was then aligned to the exposure and checked against skylines for accuracy (typical mean accuracy of ~ 0.15 pix or 0.5 \AA). As accurate line strengths are not needed and our exposures were not significantly separated in time, I did not apply additional alignment.

Though the pipeline performs sky subtraction and detects and extracts individual object spectra, the standard sky subtraction and object detection pipeline procedures are not ideal for our purposes. As our slits are relatively narrow and spaced closely together, the detection of slit positions is often imperfect. I corrected the object table containing the slit and spectra positions for each image in order to recover those slits not identified by the pipeline, modify already identified but poorly defined slits where necessary, and ensure that object spectra positions were accurate. Sky subtraction was done in two ways: first, using a local (on-slit) sky subtraction and then using a ‘global plus median’ method. The latter produces a sky spectrum computed as the median level of all the pixel values of all the CCD spectra in each wavelength bin, renormalized after flat-fielding and the other initial calibration steps. This method is the most robust as our small slit

^{*}IRAF is distributed by the National Optical Astronomy Observatories, which are operated by the Association of Universities for Research in Astronomy, Inc., under cooperative agreement with the National Science Foundation.

size and separation often causes spurious results for local subtraction. However, for large slits containing faint objects, local subtraction is superior and extracted spectra processed in this way are used when measuring redshifts for such objects. A third method, global sky subtraction, was also tested, but frequently resulted in over-subtraction of background. Fig. 4.2 shows an example of 2D spectra with the three different forms of sky subtraction applied. After the careful definition of positions and removal of sky, the spectra are extracted using the default Horne optimal extraction, where each extracted spectrum is an average weighted by the spatial profile (rather than an aperture extraction which simply averages the signal over a few rows), and final 2D and 1D spectra are then ready for redshift measurement. Fig. 4.3 shows a raw science image and Fig. 4.4 shows the same image fully reduced with global+median sky subtraction applied.

FORS2 Redshifts

In order to determine redshifts, I adapted the *ZSPEC* software, originally developed by Renbin Yan and used by the DEEP2 redshift survey (Davis et al., 2003, 2007), for use with our FORS2 MXU data. In *ZSPEC*, an Interactive Data Language (IDL) based tool, spectra are first cross-correlated to eigen-templates (stellar, galaxy, and QSO templates) and the ten best-fitted redshifts and χ^2 are provided. The spectra (both 2D and 1D) and their redshift fits were then visually examined in order to confirm or determine the correct redshift. Usually the first or second best χ^2 fit provided is a good fit. Instances where artifacts from sky line subtraction confuse the fitting, the signal-to-noise of the spectrum is relatively low, only a single emission line is detected, the spectrum is relatively featureless, or a bad pixel column exists, often result in the first or second-ranked fits being incorrect. In these cases, the appropriate solution often appears in a fit with a higher χ^2 . When none of the ten choices was a good match, any spectral features easily identified by eye were used to identify a probable redshift, which could be confirmed by manual cross-correlation. Fig. 4.5 shows an example of the *ZSPEC* redshift evaluation.

Objects without a successful redshift determination were re-evaluated with additional information, such as object magnitude and slit position which can indicate for example that a redshift is unlikely to be obtainable or, in the case of very bright objects a stellar template is preferable, in a final attempt to establish a redshift. However, most objects for which we could not measure redshifts were very faint or – in the case of very bright objects – in an area where sky subtraction was not robust or where extraction was compromised due to slit edge proximity. At this stage, template fits were possible for the majority of FORS2 objects ($\sim 970/1270$). Finally, redshifts were assigned a quality flag to reflect the stellar or galactic nature of the object and the confidence of the redshift measurement. Quality (Q) flags are defined as follows:

- Q=1: minimum of two very clearly identified spectral features (emission and/or absorption)
- Q=2: minimum of two relatively well identified features (emission and/or absorption)
- Q=3: only one strong identifiable feature
- Q=4: no features unequivocally identified but spectra is of good quality and may yield a redshift with significant additional effort in processing
- Q=-1: redshift is not determinable and the data will likely never yield one
- Q=-2: stellar spectrum

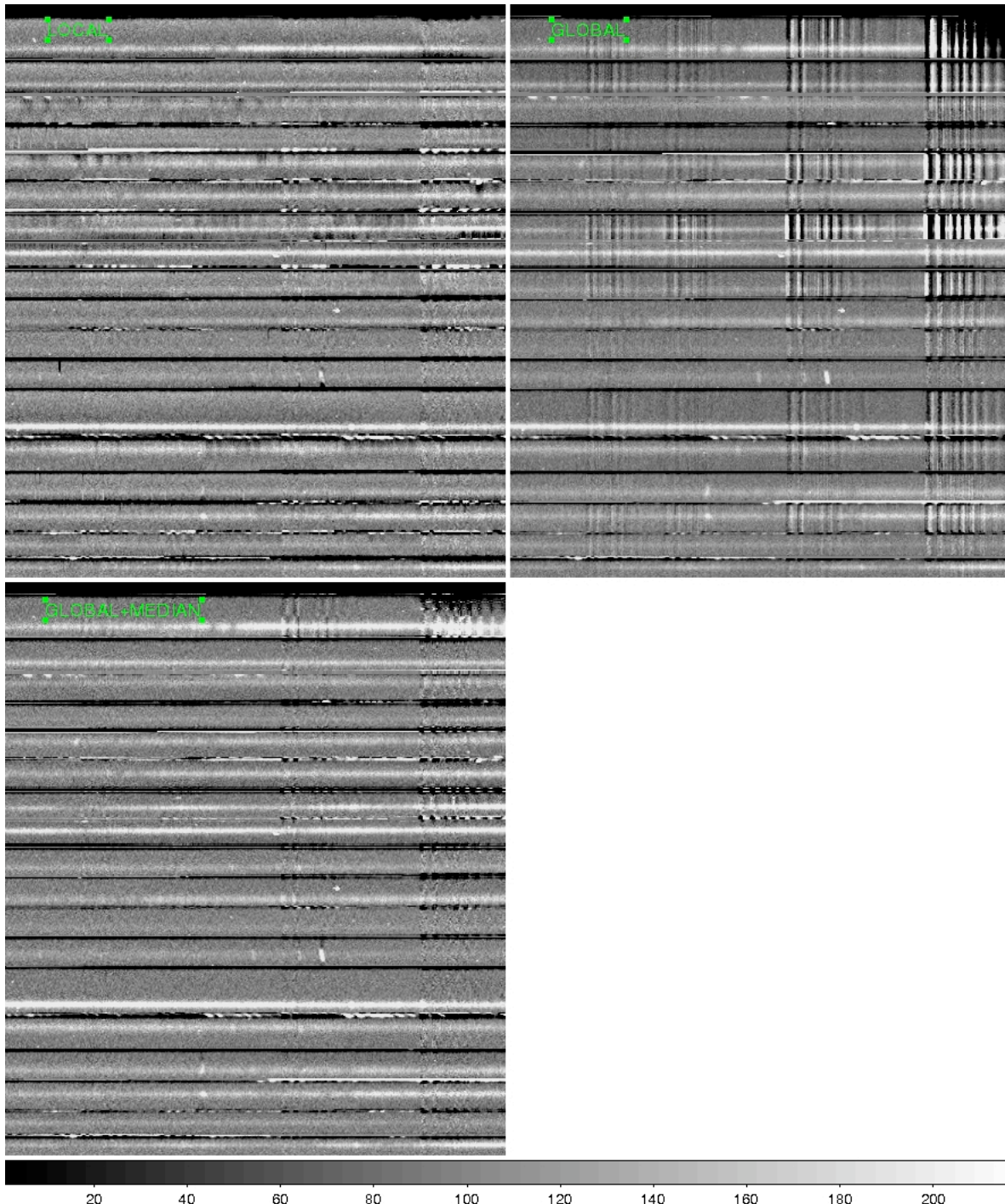


Figure 4.2: FORS2 sky subtraction results example. 2D FORS2 spectra produced using the three different methods of sky subtraction. The global method (upper right corner) is not used in the reduction because of the over-subtraction, most readily seen in the area of sky lines (the vertical columns aligned across the image).

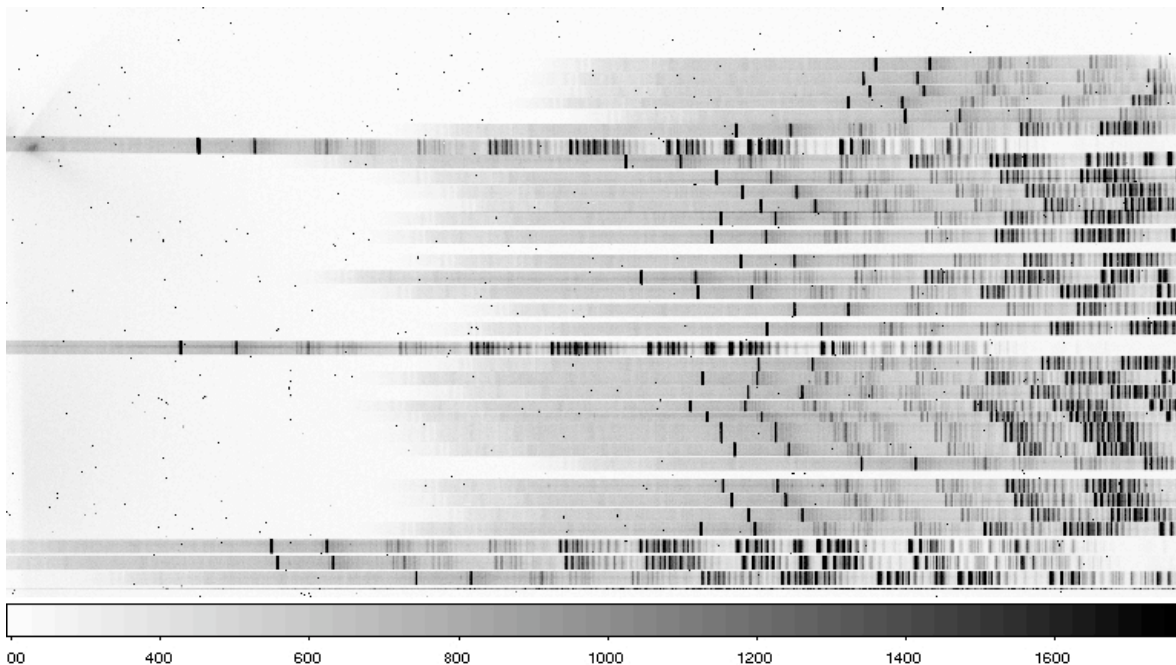


Figure 4.3: Raw spectra example.

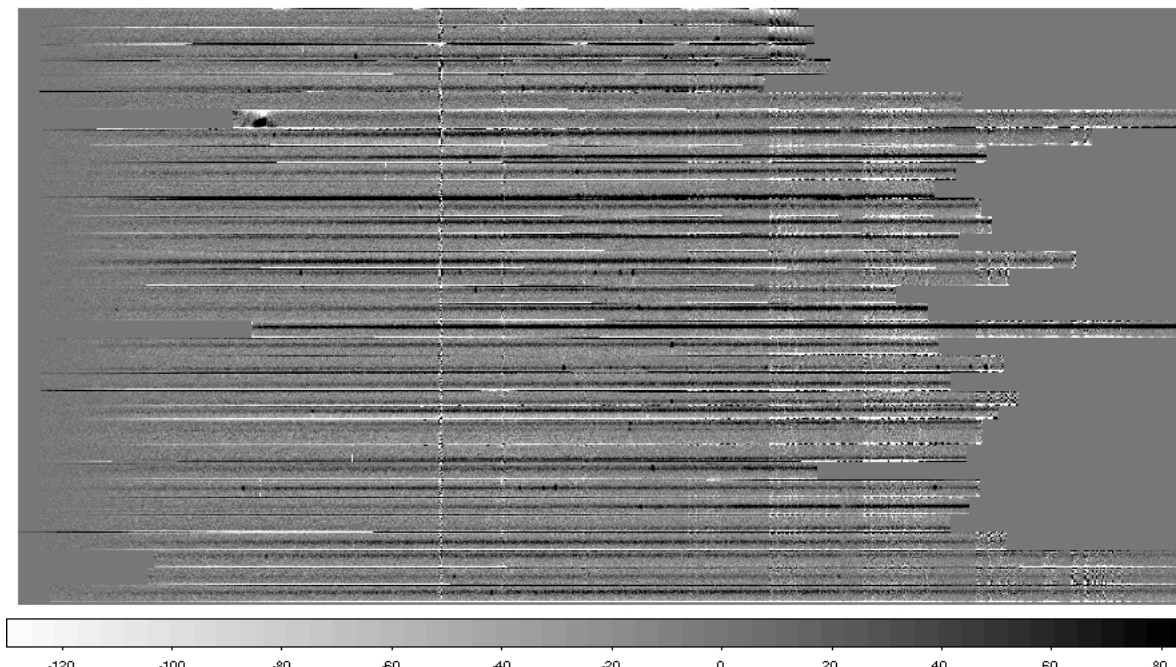


Figure 4.4: Reduced spectra example.

4. Follow-up Spectroscopy and Measured Group Properties

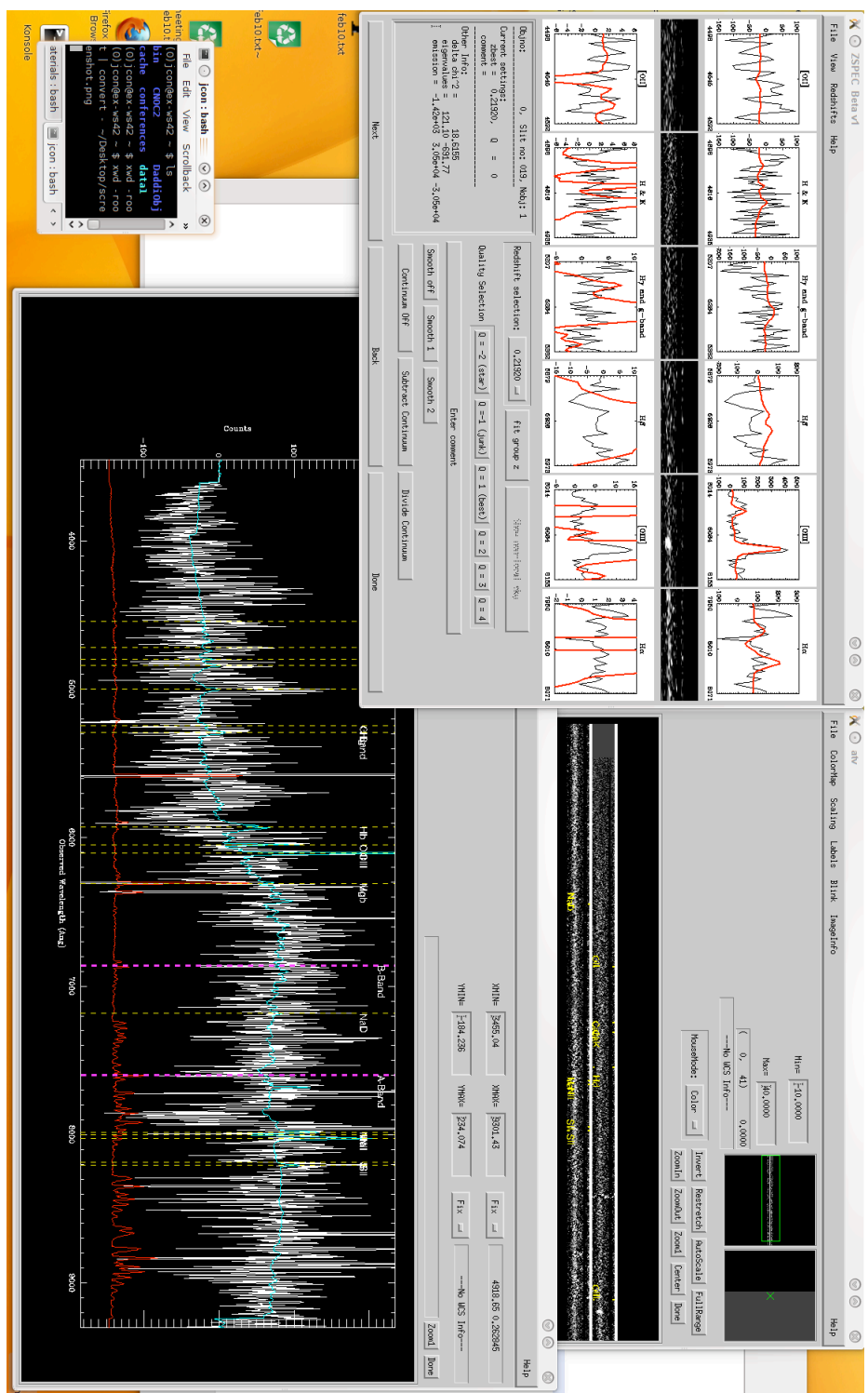


Figure 4.5: *ZSPEC* redshift evaluation example. Top right: A 2D spectrum is displayed (split in two) with emission and absorption line positions for the current redshift solution marked in yellow. Bottom right: The extracted spectrum is plotted (counts versus wavelength). If desired the spectrum can be smoothed, the continuum plotted, and the spectrum divided by the continuum. Yellow dotted lines show line positions for the current redshift solution. Top left: Control panel where redshift solution can be modified and the cross-correlation (red line) fit evaluated at line positions compared to the 1D and 2D spectra. Here the redshift and χ^2 are also listed and notes on the type or quality of the fit can be added.

In this analysis I use only the best quality redshifts ($Q=1$, 2, & -2), excluding objects with ambiguous fits. In total, 780 high quality galaxy redshifts ($\sim 60\%$ of targets) were obtained. Stars make up approximately 7% of the FORS2 spectra. Comparing to CNOC2 and IMACS redshift measurements from duplicate observations, I find a typical error of 100 km s^{-1} for the FORS2 redshifts and, examining the stellar spectra, an offset of 0.0006 (180 km s^{-1}). Fig. 4.6 shows a comparison of FORS2 redshift measurements to those from IMACS and repeat FORS2 observations along with FORS2 stellar redshifts, used to determine offsets, while Fig. 4.7 compares CNOC2 redshifts to those obtained with FORS2 and IMACS for similar objects. Because the FIMS software does not produce accurate target lists, it was necessary to manually identify targets and record their CNOC IDs. Discussion of the matching and final redshift catalog can be found in § 4.1.4.

4.1.2 IMACS Observations

We also obtained spectroscopy for both fields using Magellan-IMACS, an instrument capable of optical imaging and multi-slit, long-slit, or centerfield slit-viewing spectroscopy. The large field of view, wavelength range, and close slit placement capability make the IMACS instrument excellent for observing galaxy groups at intermediate redshift in general and, specifically, its $15'$ FOV is an excellent match to that of XMM and thus to our X-ray selected systems follow-up. IMACS is mounted on the Walter Baade Telescope, one of the two 6.5 m Magellan telescopes on Cerro Manqui at the Las Campanas Observatory in Chile. Six masks are mountable inside the instrument and it is possible to replace these with an additional six during the night. As for FORS2 masks, sub-arcsecond astrometric accuracy is required.

It is possible to design masks with >1000 slits using the *maskgen* software package. This software uses a list of target positions and priorities to maximize the number of slits while avoiding overlap in the spatial or dispersion direction. Priorities can be set to guarantee an object is observed and conflicts can be evaluated iteratively. In addition to targeting galaxies close to X-ray group centers, potential optical group members were also prioritized.

Two multi-object masks of the RA14h field were observed on July 17-18, 2007 by Dr. John Mulchaey. These were taken with a grism of $200 \text{ lines mm}^{-1}$, giving a wavelength range of $\approx 5000 - 9500 \text{ \AA}$ and a dispersion of $2.0 \text{ \AA pixel}^{-1}$. A slit width of $1''$ was used and the exposure time was two hours for both masks. For these observations, the WB4800-7800 filter was used. These observations were made under relatively poor conditions, namely significant moon. This, and the restricted wavelength range produced by the filter applied, lowered the overall redshift determination success rate for these masks. A further three masks in the RA14h field and two in the RA21h field were obtained on May 18-22, 2009 by myself and Dr. Mulchaey, all with similar setup but without this filter. Seeing on this observing run was excellent ($0.5''$) and conditions photometric.

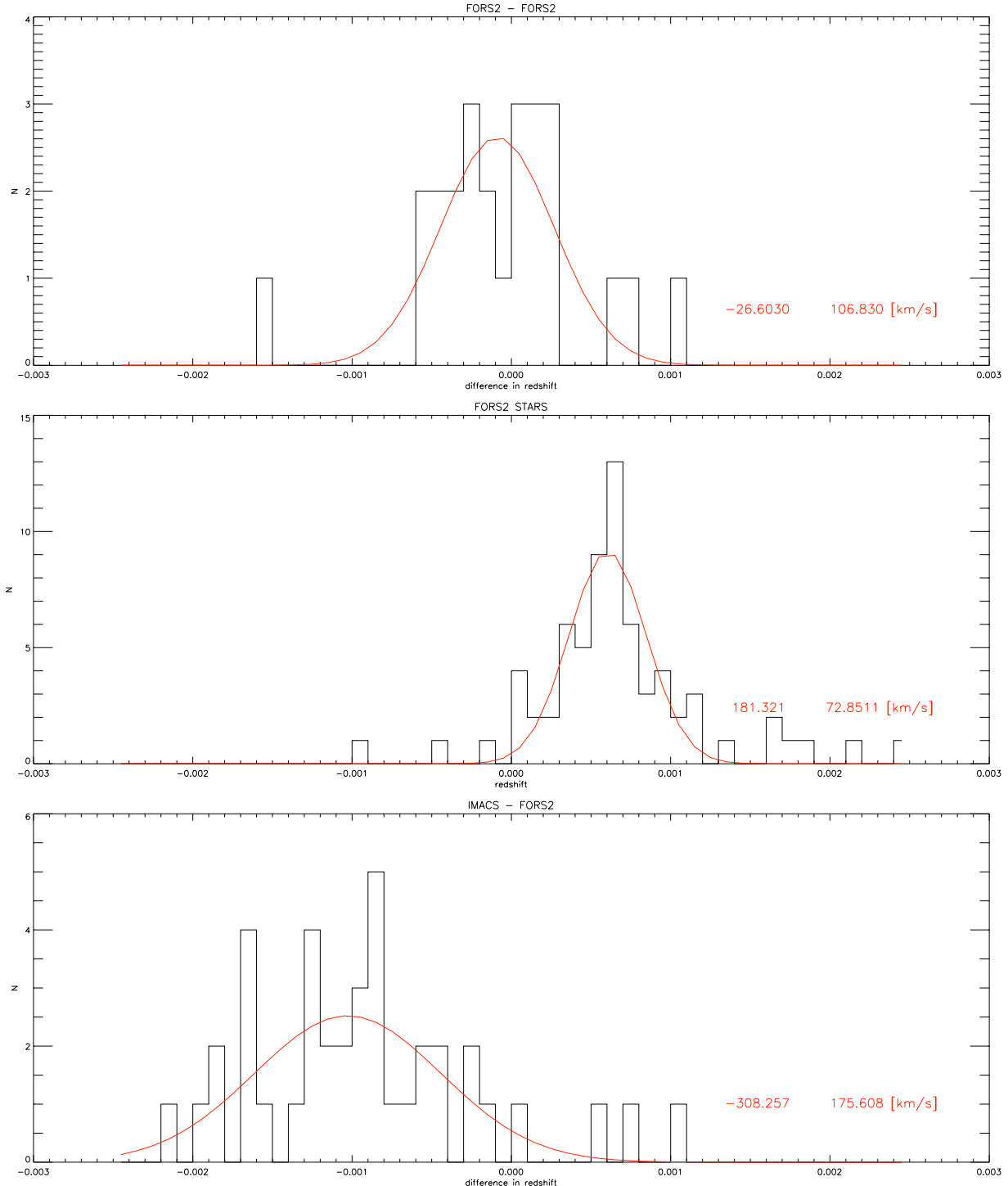


Figure 4.6: Redshift offset and error evaluation. The top panel compares objects with multiple FORS2 measurements. The middle shows stars. The bottom panel compares IMACS and FORS2 redshift measurements. Red lines indicate Gaussian fits with the center and standard deviation in km s^{-1} printed also in red.

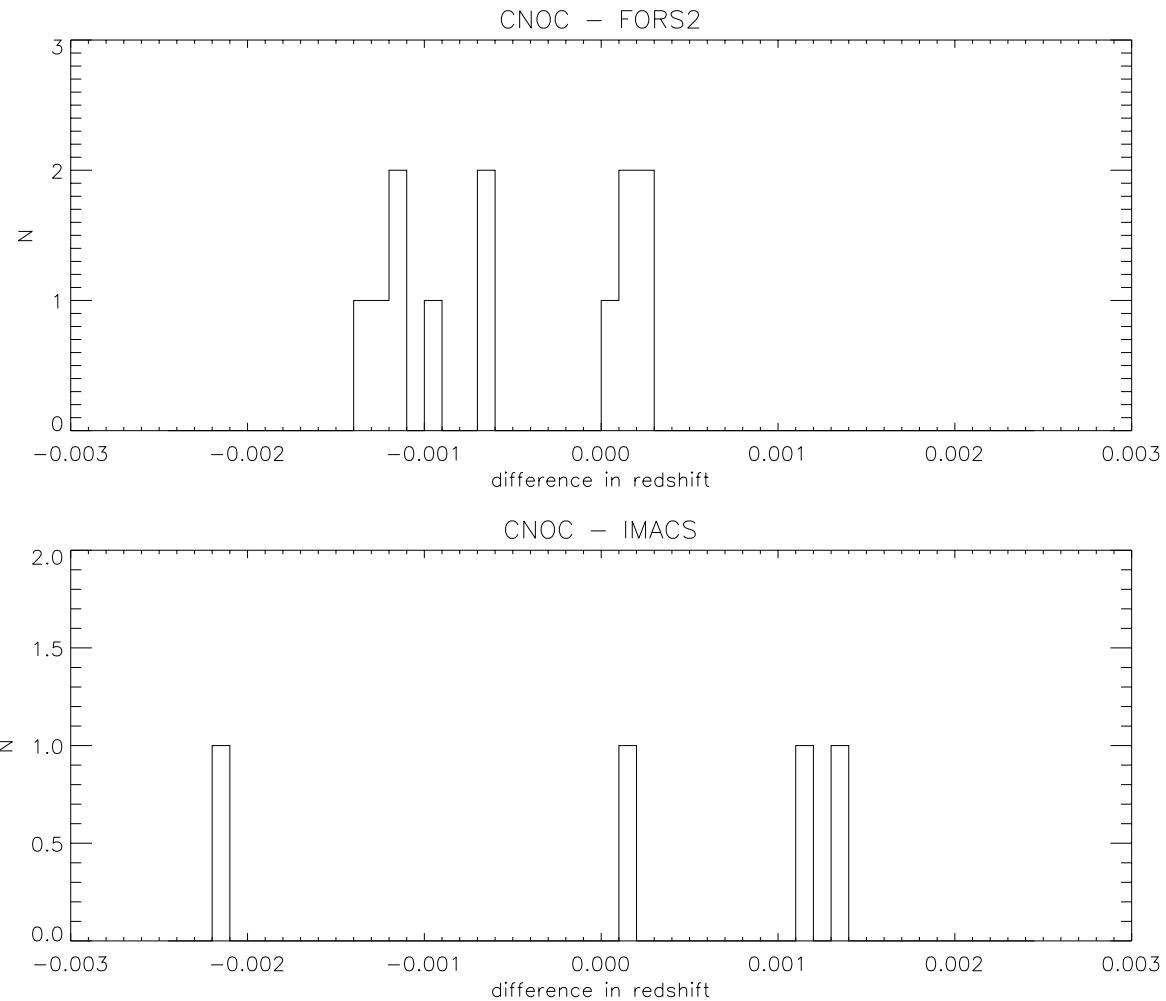


Figure 4.7: Redshift error evaluation continued. The top panel compares CNOC and FORS2 redshift measurements while the bottom shows CNOC and IMACS.

IMACS Data Reduction

IMACS data were reduced using the Carnegie Observatories System for MultiObject Spectroscopy (COSMOS[†]) package by Dr. John Mulchaey. The pipeline was designed specifically to efficiently process thousands of spectra with little to no intervention from the user. The reduction of data with COSMOS consists of three main steps: alignment of the slit mask, spectral map creation, and spectral reduction. In addition to the typical data frames (bias, flat field, arc lamp, and object spectra), three other input files are necessary. The first is a mask definition file, which was created by *maskgen*, describing the slit mask used. The second is a dewar offset file describing the positional zero-point of the particular mask + instrumental configuration which is necessary for the alignment process. The final is an observation definition file which includes the first two inputs and defines the observational setup, including instrument, camera, disperser element and tilt (if a grating was used).

Alignment of the slit mask is the first step in the reduction process and is necessary since the mounting of the masks and movement in the instrument introduce errors in the predicted positions of slit images. In this step, a mask image is used to correct for errors in x and y position, position angle, and scale of the mask image, by adjusting the values of these parameters in the dewar offset file. Next, spectral mapping, including calibration via the arc lamp images, is performed. The map ties locations in the 2D space of wavelength and location along the slit to the 2D space of CCD coordinates. Our wavelength calibrations were determined from He-NeAr arc exposures and the final spectral maps are typically accurate to 0.1 pixel. During the final step, overscan regions of the CCDs were used to measure and subtract the bias level, and dome-flat exposures taken during the night were used to flat-field the data. Then, sky subtraction was performed using the method outlined by Kelson (2003). The Kelson sky subtraction algorithm requires an accurate CCD-science coordinate system mapping to construct a median sky spectrum, cleaned of cosmic rays for each slit, which is subtracted from the slit image. Finally, individual 1D or 2D spectra are extracted from the combined and cosmic-ray cleaned science images.

IMACS Redshifts

Redshifts for the IMACS spectra were determined from cross-correlating the flux-calibrated object spectra with input model templates by Dr. John Mulchaey. The routine adopts SDSS spectral templates for early-type (SDSS template 24) and late-type (28) galaxies as input models and determines the best-fit redshift based on matching absorption and emission line features. The best-fit redshifts returned from the routine were then visually inspected to verify the object's redshift. For some objects, a good template fit was not found by the automatic routine, but spectral features were clearly visible in the galaxy spectrum. In these cases, we performed a manual cross-correlation to determine the redshift. In total, 865 high quality galaxy redshifts, with errors of 140 km s⁻¹ and systematic redshift offset of -0.0005 (-150 km s⁻¹), were obtained from the IMACS observations. The error was calculated by comparing IMACS redshifts to those from the 2dFGRS and SDSS and the offset calculated using IMACS observations of stars.

[†]<http://obs.carnegiescience.edu/Code/cosmos>

4.1.3 Additional Spectroscopy

Finally, a single group in the RA14h field (XR14h03) was recently targeted with GMOS-S as part of an ongoing study of galaxy groups within the redshift range $0.85 < z < 1$ (PI Balogh). Slit widths were set to $1''$ and an R600 grism with OG515 order blocking filter used. The spectroscopy was obtained in nod & shuffle mode (Glazebrook & Bland-Hawthorn, 2001), nodding the telescope by $\pm 0.725''$ from the center of the slit every 60 seconds with a total exposure time of two hours per group target. All observations were carried out and all data were reduced in IRAF, using the GEMINI packages with minor modifications, by collaborator Dr. Michael Balogh. See Balogh et al. (2011b) for further details of these observations and the data reduction. In total, 83 high quality galaxy redshifts with errors of 100 km s^{-1} were obtained. Ten groups (six in the RA14h field, and four in the RA21h) were observed with VLT-FORS2 in June and July of 2005. These data have recently been reduced by collaborator Robert Henderson and yielded 233 redshifts and a magnitude limit of $R = 23.2$. Observations and reductions were similar to that of our FORS2 data and details can be found in Henderson (2010).

Table 4.1: Summary of Supplemental Spectroscopy

	λ range [Å]	FOV [']	field	N_{masks}	N_{spec}	N_z
IMACS	5000-9500*	15.5 \square	RA14h	5	1197	553
			RA21h	2	551	312
FORS2	4300-7000	6.8 \square	RA14h	8	520	363
			RA21h	13	750	636
GMOS	5000-10000	5.5 \square	RA14h	3	125	115

* 4800-7800 for 3 of the RA14h field masks

Column description: Instrument (column 1), wavelength range (2), field of view (3), CNOC2 patch (4), number of masks (5), number of spectra (6), total number of redshifts (7). Note that for IMACS, the number of redshifts excludes stars.

4.1.4 Object Redshift Catalog

Beginning with a catalog produced by collaborator Dr. Michael Balogh which matches CFHT-MegaCam objects with those in the CNOC2 catalog, I created a master matched catalog including all IMACS and FORS2 targets. Because similar object positions in MegaCam and IMACS were not identical, matching was done by calculating spatial offsets. For FORS2, where object positions were in fact slit positions and thus often very difficult to cross-match correctly, matching was done manually by eye. The master matched catalog was then used first to check the magnitude and whether a redshift from another source (e.g. IMACS) already existed for those FORS2 objects with undetermined redshifts. If an object was within our magnitude limit and did not have a secure redshift, the FORS2 spectrum was revisited. Additionally, if such a FORS2 object was near an identified group, the group redshift was applied to see if that provided a good fit. Those objects with redshifts from the work of Balogh and Henderson which did not already have

a redshift in this master catalog were added. Finally, a high quality redshift catalog was created. Objects with multiple redshift (CNOC, IMACS, and/or FORS2) measurements were first checked for overall consistency and then their redshifts and errors averaged (the latter is added in quadrature). Additionally, corrections for systematic offsets in the FORS2 and IMACS redshifts (0.0006 and -0.0005 respectively) were applied. The final catalog of high quality redshifts is provided in the Appendix.

4.2 Measuring Group Properties

The fundamental group properties of the X-ray and optically selected groups are presented in Tables 4.2 and 4.3. Table 4.2 lists the group identification number for the X-ray system (column 1); redshift of group given a 1 Mpc radial cut (2); number of member galaxies within 1 Mpc (3); the radius in arcseconds of 1 Mpc (4); the velocity dispersion within a 1 Mpc cut (5); spectroscopic completeness (to $R < 22$) within a 1 Mpc cut (6); dynamical complexity within a 1 Mpc cut (7); redshift of group given a σ derived r_{200} ($r_{200,\sigma}$) (8); the number of member galaxies within $r_{200,\sigma}$ (9); the radius, $r_{200,\sigma}$, in arcseconds (10); the velocity dispersion within $r_{200,\sigma}$ (11); spectroscopic completeness (to $R < 22$) within $r_{200,\sigma}$ (12), dynamical complexity within $r_{200,\sigma}$ (13); redshift of group given an X-ray derived r_{200} (14); the number of member galaxies within an X-ray derived r_{200} (15); the radius, $r_{200,X}$, in arcseconds (16); velocity dispersion within $r_{200,X}$ (17); spectroscopic completeness (to $R < 22$) within $r_{200,X}$ (18); and the dynamical complexity within $r_{200,X}$ (19). Table 4.3 tabulates the optical groups and is similarly structured.

In total, the sample contains 39 high quality X-ray and 38 optical systems. Note that IAU names for several groups in the RA21h field have changed since the publication of Paper I as a result of improved centers due to the addition of XMM data in that field. Two of the high quality systems have low (< 1) X-ray significance (recall §3.2.2 and Tab. 3.1). The original significance of these systems was sufficient to occasion targeting for follow-up spectroscopy but was subsequently lessened with the addition of X-ray data and modifications to the X-ray reductions. As follow-up spectroscopy yielded groups with secure redshifts, these systems are included in the final sample, but their X-ray derived properties are *not* include in our analysis. 12 of our optically selected systems have significant X-ray emission when a fixed aperture is placed at the optical center. The following section describes the determination of redshifts for X-ray selected systems, and group membership assignment, centers, and radial cuts for both group samples.

4.2.1 X-ray Selected Group Redshifts

Initial group redshifts for X-ray systems were established by examining objects both within and around the immediate vicinity of the contours defining the extended X-ray sources. A clustering of galaxies in both redshift and projected spatial coordinates was often obvious and in some cases a prominent galaxy, possibly the BGG, exists near the X-ray center. Each group was assigned a redshift and a corresponding quality flag reflecting its plausibility. These quality flags are not related to those for individual galaxy redshifts and range from 1-3, from highest to lowest

quality. A quality of 1 reflects complete confidence in the redshift assignment and significant X-ray emission while a quality of 2 indicates a fairly confident redshift but low significance X-ray emission, weak multiple clustering (where one solution is preferred but others possible), or a highly incomplete region within the group (either an extended gap in the survey area or a few bright objects near the group center without redshifts). The quality flag 3 indicates a highly questionable redshift due to the projection of strong multiple clustering (more than one redshift at which galaxies are grouped), very low significance X-ray emission, or a dearth of objects with redshifts in the area. I add 0.5 to the quality flag of any group in regions of ‘confused’ emission: where X-ray contours overlap. This does *not* indicate a lesser certainty in the redshift / overall quality of the group. In this thesis I will often refer to subsets of X-ray systems as quality 1 and as quality 1 & 2, ignoring the 0.5 flag. This flag, and information about a system’s dynamical complexity (see §4.4), allows for the exploration of underlying reasons for outliers from the relations.

The process of group redshift evaluation is iterative, with each of the peaks in the redshift distribution of galaxies near the X-ray group center evaluated. In cases of more than one plausible group redshift, I apply our membership finding algorithm with all possible solutions to find the most self-consistent solution. The redshift distribution of galaxies near the X-ray center is evaluated and the velocity dispersion for a given solution examined. Additionally, the spatial position of galaxies is also inspected, with solutions with member galaxies within X-ray contours preferred. Recall that we are always examining projected X-ray emission and that, as in assigning X-ray emission to previously defined optical systems, assigning a group redshift and galaxy members to X-ray emission cannot be done with 100% confidence. The difficulty can be illustrated in part by the existence of such a large number of quality 3 groups in our sample, many of which are classified as such due to the presence of galaxy clustering at different redshifts. Figures 4.8 and 4.9 show an example of evaluation of an X-ray group redshift for a quality 1 group while 4.10 and 4.11 show that of a quality 3 system.

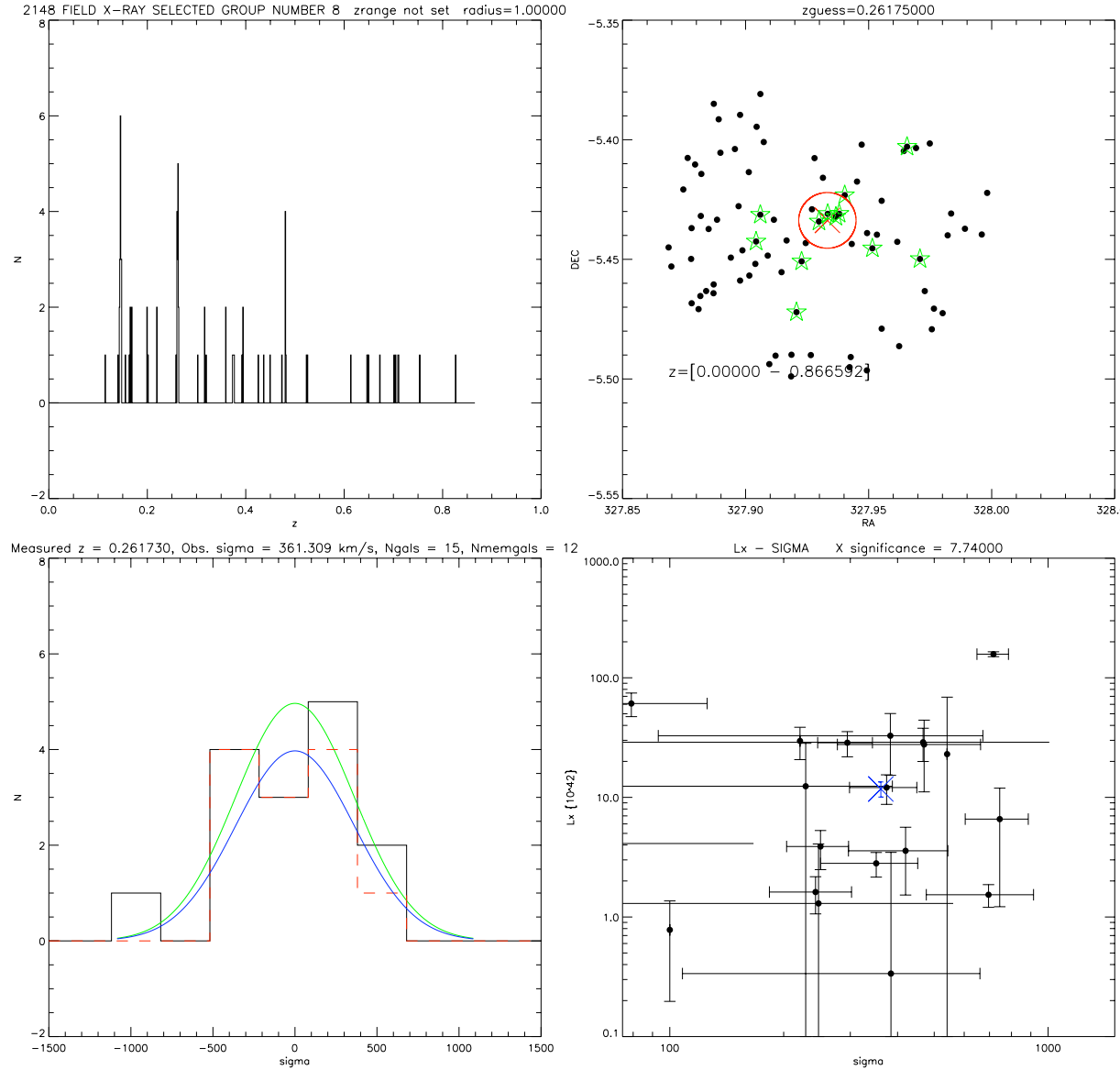


Figure 4.8: X-ray group redshift evaluation Q=1 group example: XR21h08. Top: Histogram of galaxy redshifts within a radius of 1 Mpc of group center (left) and spatial galaxy positions (black dots) with highlighting of objects assigned as group members in green and X-ray group center and ellipse marked in red (right). Galaxies within a given redshift range can also be highlighted to allow for easier location of galaxies in certain peaks of the redshift histogram. Bottom: Velocity distribution (left) and preliminary $L_x-\sigma$ relation with position of group being evaluated marked with blue ‘x’ (right). In the left panel, galaxies assigned as members (see §4.2.2) are shown as red dashed histograms, galaxies within 3σ are plotted in black and the velocity dispersion is used to overplot a normal distribution for members (blue) and galaxies within 3σ (green). In this case a redshift of ~ 0.26 is clearly preferred.

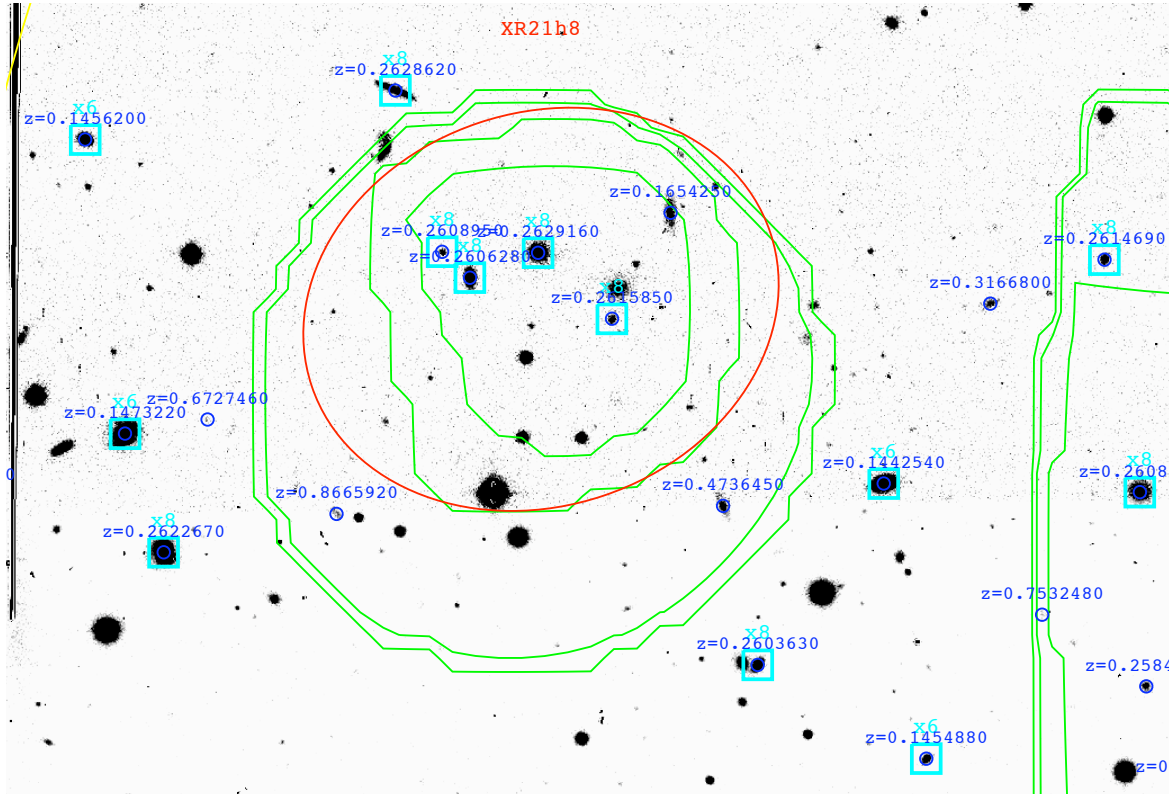


Figure 4.9: X-ray group redshift evaluation example continued: group XR21h08. Green contours mark X-ray emission while the red contour marks the X-ray group ellipse. Galaxies with redshifts are marked in blue and those assigned as members also denoted in cyan. In this case no radial cut is yet applied. Note the four galaxies at $z \sim 0.26$ all near the center of the X-ray emission.

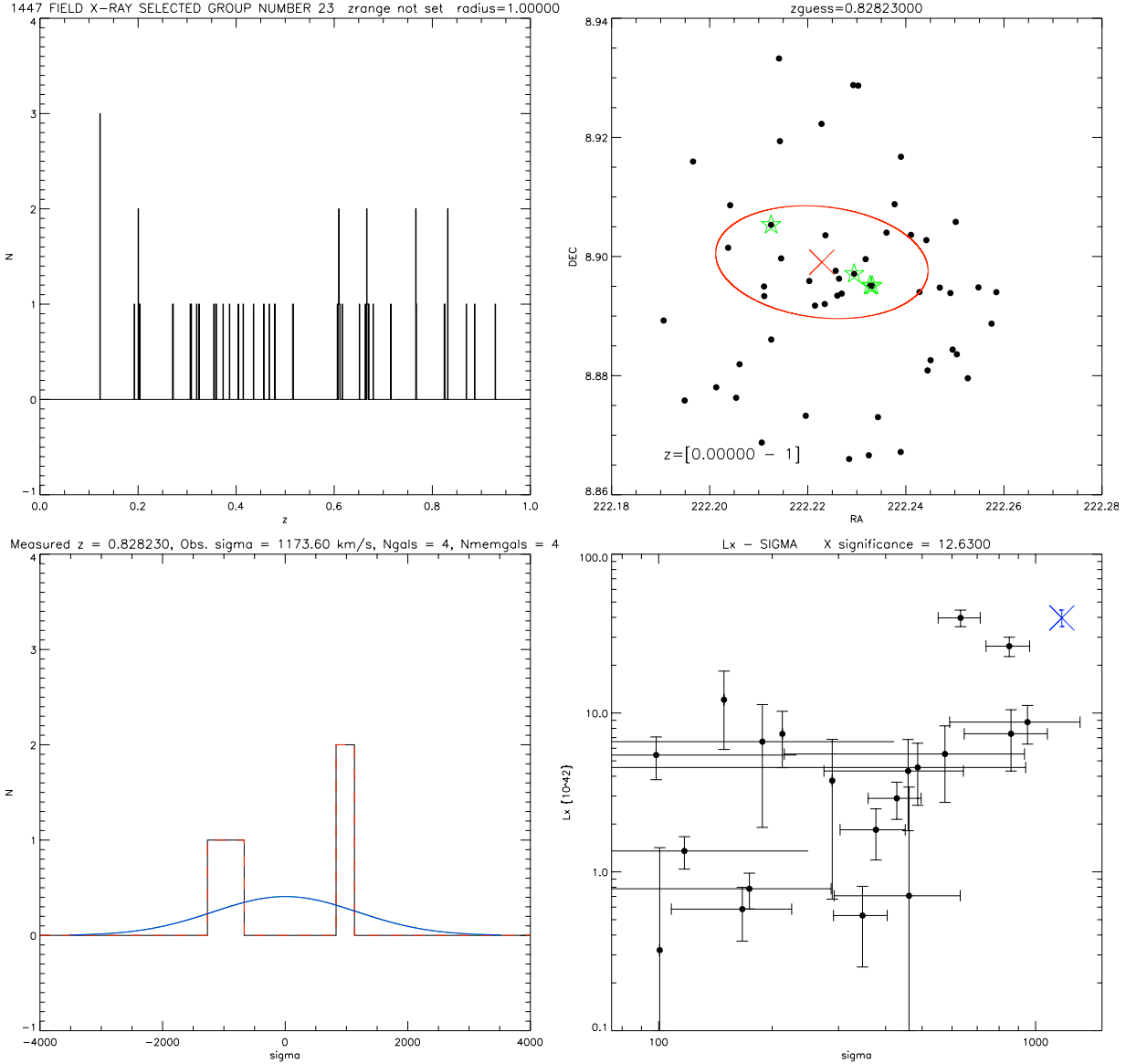


Figure 4.10: X-ray group redshift evaluation Q=3 group example: XR14h23. Top: Histogram of galaxy redshifts within a radius of 1 Mpc of group center (left) and spatial galaxy positions (black dots) with highlighting of objects within given redshift range in green and X-ray group center and ellipse marked in red (right). Bottom: Velocity distribution (left) and preliminary L_x - σ relation with position of group being evaluated marked with blue 'x' (right). In the left panel, galaxies assigned as members (see §4.2.2) are shown as red dashed histograms, galaxies within 3σ are plotted in black and the velocity dispersion is used to overplot a normal distribution for members (blue) and galaxies within 3σ (green). In this case, redshift solutions of $z=0.61, 0.66, 0.83$ are all possible.

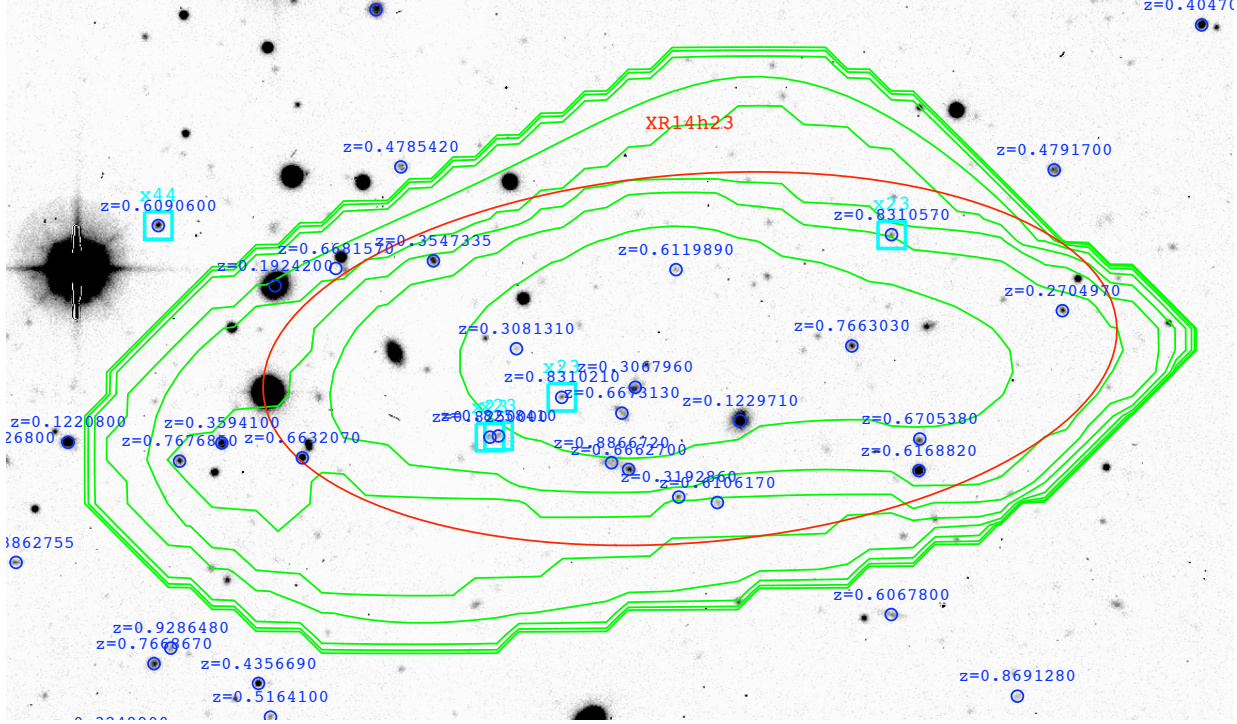


Figure 4.11: X-ray group redshift evaluation Q=3 group example continued: group XR14h23. Green contours mark X-ray emission while the red contour marks the X-ray group ellipse. Galaxies with redshifts are marked in blue and those assigned as members also denoted in cyan. In this case no radial cut is yet applied. Note several galaxies each at redshifts of z=0.61, 0.66, 0.83 all within the X-ray contours.

4.2.2 Group Membership

Details of the original membership finder algorithm are found in Wilman et al. (2005a) but a description, with changes made for the current analysis, follows. Beginning with the X-ray center and redshift for each group, an initial velocity dispersion of 500 km s^{-1} is assumed and a maximum redshift offset $\delta(z)_{max}$ calculated to clip members at $2 \times$ the velocity dispersion. This is then converted into a spatial offset $\delta(\theta)_{max}$ which is within 1/10 of the equivalent distance to $\delta(z)_{max}$ in the line-of-sight direction, and group members are selected by applying these redshift and spatial limits as follows:

$$\delta(r)_{max} = \frac{1}{10} \frac{\delta(z)_{max}}{h_{75}^{-1} \text{Mpc}} \quad (4.1)$$

$$\delta(\theta)_{max} = 206265'' \frac{\delta(r)_{max}}{h_{75}^{-1} \text{Mpc}} \left(\frac{D_\theta}{h_{75}^{-1} \text{Mpc}} \right)^{-1} \quad (4.2)$$

where 10 is the aspect ratio and the angular diameter distance D_θ is a function of redshift. Note that to tune this offset limit to the X-ray selected group sample, allowing for distinction between

adjacent systems while still obtaining stable membership solutions, I tighten it from the value of 5 used in Wilman et al. (2005a), choosing instead the aspect ratio of 10. This aspect ratio is applied to all systems, including those that are optically selected, and is closer to that implied by the virial theorem while the Wilman et al. value was motivated by the goal of studying radial trends in the galaxy population.

In order to obtain an accurate estimate for groups which have relatively few members, the galaxies within this radius are ordered sequentially by redshift and the observed velocity dispersion in the line-of-sight direction, $\sigma(v)_{obs}$, is then calculated using the Gapper algorithm (Beers et al., 1990, Eq. 3) as follows:

$$\sigma(v)_{obs} = 1.135c \left(\frac{\sqrt{\pi}}{n(n-1)} \sum_{i=1}^{n-1} w_i g_i \right) \quad (4.3)$$

where $w_i = i(n-1)$ and $g_i = z_{i+1} - z_i$ and the 1.135 multiplicative factor corrects for the 2σ clipping of a Gaussian velocity distribution.

This value is then shifted to a rest-frame velocity dispersion and, finally, the intrinsic velocity dispersion σ_{intr} is calculated by subtracting the combined error from the redshift measurements in quadrature. The mean redshift of the members and new velocity dispersion is then used to recompute the redshift (and, for optical groups, spatial) offsets and the entire process is repeated until a stable membership solution is attained. In cases where combined errors from the redshift measurements are larger than the measured rest-frame velocity dispersion of the group, a 1σ upper limit is placed on the intrinsic velocity dispersion using Monte-Carlo simulations. A simulated group is created having the same number of members and assuming an initial σ_{intr} in order to calculate a rest-frame velocity dispersion. 10,000 such groups are created, with initial intrinsic velocity dispersions ranging from 30–300 km s⁻¹ with a step size of 5 km s⁻¹. For all other groups, errors on the group velocity dispersion are calculated using the Jackknife technique (Efron, 1987). In the Jackknife technique, a velocity dispersion ($\sigma_{intr,Jack}$) is computed for the group excluding one group member. This calculation is repeated, each time excluding a different group member. The error on the velocity dispersion is then computed to be $[\sum(\delta_i^2)N_{tot}/N_{tot-1}]^{0.5}$ where $\delta_i = \sigma_{intr} - \sigma_{intr,Jack}$ and N_{tot} is the total number of known members. Note that the assumption of symmetric errors in this case can result in an error measurement larger than the velocity dispersion itself. Fig. 4.12

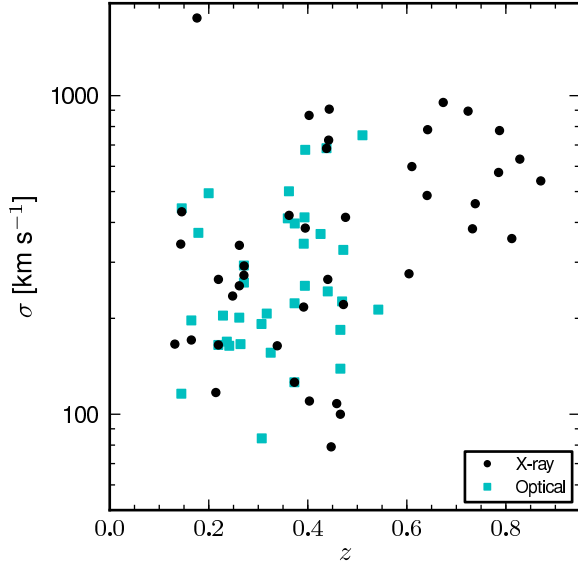


Figure 4.12: Velocity dispersion as a function of redshift given a σ based r_{200} radial cut (see §4.2.4 for details) for all X-ray and optical systems. Note that upper limits on velocity dispersion are not shown here.

shows the velocity dispersions for all systems as a function of redshift.

In the rare cases where the algorithm oscillates infinitely between two membership solutions, the solution with more members is chosen. Note that in such cases it is possible that a few member galaxies lie outside the final quoted $\delta(\theta)_{max}$ since this quantity is calculated from the final velocity dispersion of the group. To evaluate the results of the membership assignment, especially in cases with more than one possible group redshift, I examine both the imaging (X-ray and optical) and velocity distribution of the group members.

4.2.3 Group Centers

The process of assigning group membership is applied to both the X-ray and optically selected groups, using previously defined optical group centers for the latter. It is run twice, allowing for R-band luminosity-weighted recentering of the group in the second instance. Recall that X-ray centers are good to 10–30 arcseconds. The luminosity-weighted centers rely strongly on membership allocation and especially redshift completeness, and while the median off-centering value is $\sim 15''$, factor of three larger deviations are also predicted using mock catalogs (Wilman et al., 2009).

In Fig. 4.13 I compare the X-ray and luminosity-weighted centers for our X-ray groups. For the majority of systems, the center shifts $\leq 18''$ when luminosity re-centering is applied. Group membership and overall properties change very little using the luminosity-weighted center (see e.g. §5.1) and the ‘original’ centers - those found by the membership algorithm before any additional radial cut is applied (see the next subsection) - for these systems are adopted in all subsequent analysis.

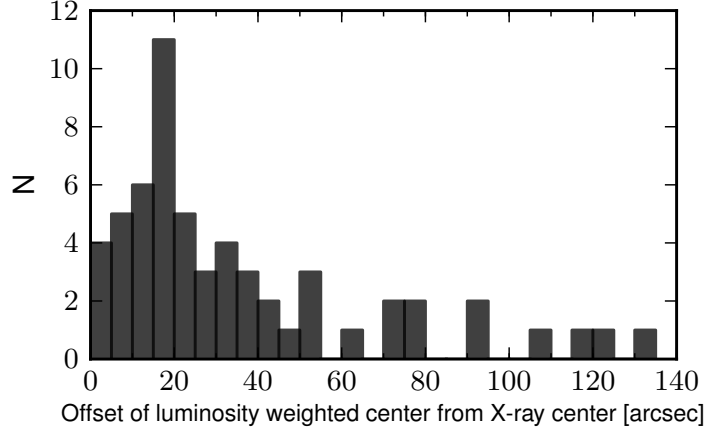


Figure 4.13: Histogram of offset between X-ray and luminosity weighted centers for all X-ray systems having significance ≥ 1 without a radial cut applied.

4.2.4 Radial Cuts

Once the best redshift and membership is determined, a radial cut must be chosen in order to sample analogous regions of each group. In the cluster regime, it is typical to use a radial cut of r_{500} or r_{200} , the radius at which the density of the system is 500 and 200 times the critical density respectively. The latter approximates the virial radius of the cluster. Though it is clear that the former radius is not ideal for significantly less dense systems like groups, the best definition of radius to use for groups is less clear. Here I test the effect of using three different cuts, applying a constant cut of 1 Mpc and two differently defined r_{200} measures.

The first r_{200} cut is X-ray based and is discussed in §3.2.2. Note that in the case of no X-ray detection, an upper limit on $r_{200,X}$ is used. The second r_{200} is derived using the velocity dispersion (σ_{intr}). I apply in this case the definition of r_{200} from Carlberg et al. (1997) as follows:

$$r_{200,\sigma} = \frac{\sigma_{intr}\sqrt{3}}{10H(z)}. \quad (4.4)$$

Using each of these radial cuts, the membership is redefined and a final σ computed. In the case of a velocity dispersion based r_{200} , the algorithm is allowed to iterate until a stable solution is found. Although these cuts often result in decreased membership, if the radial cut is larger than $\delta(\theta)_{max}$, as is often the case for the 1 Mpc cut, the membership of the group may increase.

For those groups that are adjacent both in position on the sky and in redshift space (e.g. XR21h06 and XR21h07), members may be shared across groups. As the original membership algorithm does *not* allow members to be in multiple groups and instead will merge such systems, discarding one group entirely, the discarded system in these adjacent groups will also have zero members given a $r_{200,\sigma}$ radial cut (see XR21h07 in Tab. 4.2 which is merged completely into XR21h06 by the original membership algorithm). Distinct X-ray groups may also be entirely stripped of members given a $r_{200,\sigma}$ if the initial velocity dispersion and subsequent iteration sufficiently reduces the redshift and spatial limits (see for example XR21h50, XR14h01, and OP21h101). This happens most commonly when group members are rather dispersed in projected position and have very similar velocities, causing the computed σ and $r_{200,\sigma}$ to be low and many, or all, of these members to be discarded, and is mainly a problem for Q=3 groups. Alternatively, a very large velocity dispersion can result in a great increase in members given an $r_{200,\sigma}$ radial cut as in XR32h27.

As group membership can change significantly given different definitions of group radius, the mean redshift of members may also change. The redshifts for each radial cut are listed in Tables 4.2 and 4.3 for reference. For the vast majority of systems, the redshift varies little, being stable at least to the third decimal place, and approaches ~ 0.003 only in the most extreme case. As the redshift of the group does not affect most quantities subsequently derived for the group, and those that are redshift-dependent are not significantly affected by differences at the level observed, I choose to apply a single redshift in all cases. X-ray properties (i.e. luminosity and mass) were calculated using the redshift of the group derived with the initial cut, as defined by Eq. 4.2, and this redshift is typically in very good agreement with those from the three radial cuts.

4.2 Measuring Group Properties

Table 4.2: Measured Properties of X-ray Selected Groups

XID	z	N	Radius [arcsec'']	σ [km s^{-1}]	completeness $R < 22$	dynamical complexity	z	N	Radius [arcsec'']	σ [km s^{-1}]	completeness $R < 22$	dynamical complexity	z	N	Radius [arcsec'']	σ [km s^{-1}]	completeness $R < 22$	dynamical complexity
XR14h02	0.1317	12	455.97	213±33	0.61	-	0.1315	7	164.88	166±58	0.63	-	0.1315	7	204.84	166±58	0.63	-
XR14h09	0.6431	15	155.01	850±112	0.67	AD	0.6424	20	196.65	782±88	0.67	AD,DS	0.6436	13	117.72	817±141	0.67	AD
XR14h10	0.7382	5	146.62	458±184	0.93	-	0.7382	5	103.01	458±184	0.94	-	0.7386	4	73.08	483±308	1.00	-
XR21h08	0.2619	14	263.99	262±38	0.37	-	0.2615	9	135.30	253±54	0.45	-	0.2618	11	147.96	280±46	0.41	-
XR21h10	0.3383	11	221.08	241±35	0.62	-	0.3390	4	70.40	164±190	0.67	-	0.3390	4	99.00	164±190	0.70	-
XR21h11	0.4762	14	179.72	374±75	0.61	AD	0.4761	11	133.64	415±86	0.68	-	0.4759	10	90.72	428±87	0.69	-
XR21h12	0.2195	37	301.07	255±32	0.58	-	0.2196	11	165.52	265±78	0.61	-	0.2196	11	126.72	265±78	0.62	-
XR21h14	0.4381	46	188.35	750±73	0.69	AD	0.4379	38	235.72	683±60	0.69	AD	0.4382	37	154.44	704±81	0.67	-
XR21h15	0.7326	4	147.04	382±289	0.61	-	0.7326	4	86.45	382±289	0.73	-	0.7326	4	74.16	382±289	0.75	-
XR21h60	0.3170	5	230.88	< 156	0.45	-	0.3166	0	-	-	0.3171	3	110.52	107±129	0.43	-
XR21h64	0.2483	5	274.42	179±52	0.45	-	0.2482	3	131.59	235±285	0.38	-	0.2482	3	146.88	235±285	0.38	-
XR21h69	0.2195	26	301.08	256±36	0.48	-	0.2195	10	102.92	165±34	0.72	-	0.2195	12	150.48	213±41	0.64	-
XR14h03	0.7882	7	143.21	860±213	0.79	-	0.7869	10	165.58	777±215	0.76	AD	0.7910	3	77.40	899±575	0.67	-
XR14h08	0.5070	7	173.75	104±126	0.70	-	0.5067	5	31.46	< 102	0.83	-	0.5070	6	102.60	98±133	0.70	-
XR14h18	0.3729	7	207.63	151±73	0.58	-	0.3730	4	49.79	126±144	0.80	-	0.3729	6	112.32	174±76	0.68	-
XR14h22	0.2715	20	257.20	382±42	0.73	DS	0.2715	9	151.65	292±76	0.85	-	0.2715	6	105.48	233±77	0.94	-
XR14h25	0.2706	22	257.82	267±43	0.55	DS	0.2708	13	141.65	273±56	0.67	-	0.2708	11	124.20	285±67	0.64	-
XR14h35	0.6402	6	155.32	557±153	0.64	-	0.6409	3	122.57	486±154	0.59	-	0.6409	3	81.36	486±454	0.79	-
XR14h40	0.6370	3	155.66	< 299	0.70	-	0.6370	3	75.64	< 298	0.88	-	0.6370	3	78.48	< 292	0.88	-
XR14h44	0.6102	11	158.66	599±91	0.70	AD,DS	0.6102	11	157.30	599±91	0.72	AD,DS	0.6120	5	72.00	426±423	0.92	-
XR21h06	0.1454	50	419.22	426±46	0.39	-	0.1454	49	389.95	432±46	0.40	-	0.1452	16	107.64	466±93	0.53	-
XR21h07	0.1454	46	419.27	443±47	0.40	-	0.1454	0	-	-	0.1453	40	313.56	473±49	0.46	-
XR21h13	0.2483	6	274.48	< 100	0.66	-	0.2483	5	55.95	< 100	0.86	-	0.2483	5	102.24	< 100	0.69	-
XR21h18	0.3913	11	201.48	244±53	0.59	AD	0.3912	0	-	-	0.3916	7	88.20	217±57	0.68	-
XR21h20	0.1454	17	424.23	362±70	0.49	-	0.1432	15	313.95	342±79	0.52	-	0.1433	≤ 5	< 168.84	164±119	0.64	-
XR21h23	0.3876	4	202.68	467±59	0.56	-	0.3866	0	-	-	0.3865	3	123.84	< 100	0.65	-
XR21h31	0.4581	7	183.63	127±33	0.38	-	0.4582	3	36.06	108±121	0.83	-	0.4584	5	74.52	66±100	0.60	-
XR21h32	0.7335	5	146.97	< 138	...	-	0.7336	2	52.54	< 232	...	-	0.7334	3	75.60	< 222	...	-
XR21h33	0.3916	8	201.40	198±58	0.60	-	0.3916	7	82.25	217±57	0.81	-	0.3916	7	95.40	217±57	0.78	-
XR21h37	0.4446	25	186.76	864±94	0.55	AD	0.4438	34	309.39	907±91	0.40	AD,DS	0.4453	17	88.20	917±118	0.81	-
XR21h42	0.4035	7	197.77	103±61	0.69	-	0.4033	4	41.00	110±120	1.00	-	0.4033	4	78.12	110±120	0.64	-
XR21h50	0.5678	8	164.11	470±192	0.57	-	0.5675	0	-	-	0.5681	4	83.16	201±223	0.63	-
XR21h55	0.2618	13	264.04	339±81	0.55	-	0.2619	10	181.54	339±101	0.63	-	0.2620	7	121.32	392±147	0.63	-
XR14h11	0.4717	18	180.65	331±55	0.78	AD,DS	0.4723	6	71.57	221±70	0.82	-	0.4723	6	87.12	221±70	0.75	-
XR14h12	0.1647	9	378.08	191±88	0.70	-	0.1650	5	138.25	171±188	0.74	-	0.1648	6	177.48	197±131	0.73	-
XR14h19	0.6376	2	155.59	< 194	...	-	0.6375	0	-	-	0.6376	2	93.96	< 194	...	-
XR14h29	0.3622	16	211.48	428±68	0.67	-	0.3623	15	170.58	421±73	0.74	-	0.3621	10	119.52	496±112	0.67	-
XR14h33	0.8120	3	141.78	356±318	0.71	-	0.8120	3	73.95	356±318	0.70	-	0.8120	≤ 3	< 84.24	356±318	0.67	-
XR21h27	0.1745	9	360.67	1199±282	0.37	-	0.1732	42	1350.54	1753±143	0.33	AD,DS	0.1763	7	172.08	695±219	0.47	-
XR14h50	0.3744	6	207.09	< 109	0.27	-	0.3741	0	-	-	0.3744	5	136.80	< 147	0.17	-
XR14h55	0.7853	4	143.39	574±359	0.64	-	0.7853	4	122.68	574±359	0.63	-	0.7872	2	72.72	634±...	...	-
XR14h07	0.5521	2	166.37	< 211	...	-	0.5521	2	60.21	< 211	...	-	0.5521	2	102.96	< 210	...	-
XR14h13	0.5580	1	165.50	-	0.5580	0	-	-	0.5580	1	87.12	-
XR14h23	0.8282	4	140.87	632±80	...	-	0.8282	4	129.22	632±80	...	-	0.8282	4	105.84	632±80	...	-
XR14h24	1.0114	2	133.33	205±...	...	-	1.0114	0	-	-	1.0114	2	69.48	205±...	...	-
XR14h26	0.7814	6	143.64	205±94	0.70	-	0.7807	0	-	-	0.7810	4	75.96	130±163	0.69	-
XR14h37	0.5567	8	165.69	461±169	0.59	-	0.5576	2	90.81	< 321	...	-	0.5569	≤ 3	< 88.92	295±352	0.60	-

XID	z	N	Radius [arcsec^2]	σ [km s^{-1}]	completeness $R < 22$	dynamical complexity	$r_{200,\sigma}$	z	N	Radius [arcsec^2]	σ [km s^{-1}]	completeness $R < 22$	dynamical complexity	$r_{200,X}$	z	N	Radius [arcsec^2]	σ [km s^{-1}]	completeness $R < 22$	dynamical complexity
XR14h38	0.2969	1	241.47	...	-	0.2969	0	-	0.2969	≤ 1	< 133.92	
XR14h39	0.2641	2	262.34	72±75	...	0.2639	0	-	0.2639	1	114.84	
XR14h41	0.8936	2	137.64	< 283	...	0.8936	2	54.44	< 283	-	0.8936	2	63.00	< 295	
XR14h47	0.4053	1	197.22	...	-	0.4053	0	-	0.4053	1	141.48	
XR21h16	0.3916	10	201.39	311±75	0.44	0.3912	0	-	0.3914	2	86.04	64±...	
XR21h17	0.7828	4	143.36	238±158	0.42	0.7820	0	-	0.7822	3	60.48	74±162	0.67	
XR21h19	0.5674	6	164.16	329±221	0.59	0.5672	0	-	0.5674	≤ 6	< 77.40	329±221	0.69	
XR21h21	0.4400	20	187.90	309±49	0.59	0.4402	9	91.22	265±40	0.64	-	0.4404	10	108.00	294±48	0.65		
XR21h30	0.3949	4	200.37	384±276	0.56	0.3949	4	144.46	384±276	0.61	-	0.3956	≤ 2	< 78.48	575±...		
XR21h40	0.6567	2	153.63	383±...	...	0.6556	0	-	0.6556	1	82.80	
XR21h41	0.8705	2	138.71	540±...	...	0.8705	2	106.14	540±...	-	0.8705	≤ 2	< 70.92	540±...	
XR21h43	0.6044	4	159.36	276±177	0.74	0.6044	4	73.20	276±177	0.90	-	0.6049	3	66.24	206±249	0.89		
XR21h48	0.2626	7	263.47	159±120	0.54	0.2618	2	75.97	< 142	-	0.2618	≤ 2	< 108.00	143	
XR21h49	0.4020	12	198.20	745±141	0.53	0.4026	26	320.96	867±99	0.60	AD	0.4015	1	79.92		
XR21h59	0.4423	10	187.32	689±136	0.68	0.4420	12	248.35	725±134	0.64	-	0.4426	4	97.92	798±369	0.76		
XR21h69	0.6745	4	151.92	952±498	0.46	0.6735	5	230.46	952±156	0.46	-	0.6737	1	92.52		
XR14h04	0.2145	6	306.54	156±49	0.67	0.2143	3	74.50	117±132	1.00	-	0.2143	3	158.04	117±132	0.68		
XR14h14	0.7237	8	147.72	951±360	0.62	0.7235	9	204.01	894±316	0.60	-	0.7249	5	85.68	761±281	0.63		
XR21h22	0.7574	2	145.24	533±...	...	0.7569	0	-	0.7590	1	75.24	
XR21h67	0.4470	6	186.20	80±68	0.43	0.4472	0	-	0.4472	4	121.32	79±46	0.54	

*Column description: group identification number for the X-ray system (column 1); redshift of the group given a 1 Mpc radial cut (2); number of member galaxies within 1 Mpc (3); the radius in arcseconds of 1 Mpc (4); the velocity dispersion within a 1 Mpc cut (5); spectroscopic completeness (to $R < 22$) within a 1 Mpc cut (6); dynamical complexity within a 1 Mpc cut (7); redshift of the group given a σ derived r_{200} radial cut (8) the number of member galaxies within $r_{200,\sigma}$ (9); the radius in arcseconds of $r_{200,\sigma}$ (10); the velocity dispersion within $r_{200,\sigma}$ (11); spectroscopic completeness (to $R < 22$) within $r_{200,\sigma}$ (12); dynamical complexity within $r_{200,\sigma}$ (13); redshift of the group given an X-ray derived r_{200} radial cut (14); the number of member galaxies within an X-ray derived r_{200} (15); the radius in arcseconds of an X-ray derived r_{200} (16); velocity dispersion within an X-ray derived r_{200} (17); spectroscopic completeness (to $R < 22$) within an X-ray derived r_{200} cut (18), and the dynamical complexity within an X-ray derived r_{200} cut (19)

4.2 Measuring Group Properties

65

Table 4.3: Measured Properties of Optically Selected Groups

OID	z	N	Radius	σ	completeness	dynamical	$r_{200,\sigma}$	σ	N	Radius	σ	completeness	dynamical	$r_{200,X}$	σ	N	Radius	σ	completeness	dynamical
	1Mpc	[$'$]	[$'$]	[km s^{-1}]	R<22	complexity	[$'$]	[km s^{-1}]	[$'$]	R<22	complexity	R<22	complexity	[$'$]	[km s^{-1}]	[$'$]	R<22	complexity	R<22	complexity
OP14h01	0.1647	9	378.08	191±88	0.70	-	0.1648	6	159.41	197±131	0.72	-	0.1648	7	165.96	174±112	0.72	-	-	
OP14h08	0.2284	8	292.19	159±101	0.59	-	0.2287	4	233.00	204±166	0.65	-	0.2287	< 4	< 115.92	204±166	0.60	-	-	
OP14h09	0.2616	10	264.17	168±55	0.58	-	0.2616	8	107.71	201±56	0.40	-	0.2616	< 8	< 100.08	201±56	0.43	-	-	
OP14h10	0.2709	16	257.58	367±59	0.72	DS	0.2709	11	152.08	293±68	0.83	-	0.2715	< 7	< 97.56	207±72	0.93	-	-	
OP14h11	0.2708	18	257.66	254±42	0.54	-	0.2710	15	134.54	259±50	0.75	-	0.2709	< 11	< 98.64	274±69	0.69	-	-	
OP14h15	0.3070	7	235.96	110±88	0.48	-	0.3069	6	39.56	84±110	0.70	-	0.3070	< 7	< 96.84	110±88	0.65	-	-	
OP14h16	0.3063	6	236.32	219±73	0.53	-	0.3065	5	89.54	192±158	0.73	-	0.3065	< 5	< 114.84	192±158	0.75	-	-	
OP14h19	0.3249	7	227.06	174±69	0.61	-	0.3251	5	69.16	156±182	0.47	-	0.3251	< 5	< 101.16	156±182	0.48	-	-	
OP14h24	0.3593	16	212.56	78±41	0.74	AD	0.3591	0	-	0.3593	< 14	< 89.64	87±43	0.94	AD	-	
OP14h25	0.3620	21	211.55	501±78	0.65	-	0.3620	21	202.95	501±78	0.66	-	0.3619	< 17	< 171.00	447±79	0.72	-	-	
OP14h27	0.3726	4	207.70	129±149	0.70	-	0.3729	3	77.43	< 196	0.92	-	0.3729	< 3	< 97.92	< 193	0.80	-	-	
OP14h28	0.3727	8	207.69	190±62	0.54	-	0.3730	4	49.79	126±144	0.89	-	0.3730	< 6	< 91.80	174±76	0.79	-	-	
OP14h29	0.3740	8	207.22	297±137	0.61	-	0.3737	5	156.52	397±205	0.71	-	0.3738	< 4	< 89.28	453±313	0.83	-	-	
OP14h30	0.3937	12	200.72	261±80	0.36	-	0.3942	6	95.45	253±222	0.52	-	0.3942	< 6	< 88.56	253±222	0.57	-	-	
OP14h31	0.3933	7	200.86	304±211	0.52	-	0.3935	5	156.57	415±252	0.62	-	0.3935	5	92.16	415±252	0.85	-	-	
OP14h32	0.3935	10	200.80	910±202	0.74	-	0.3941	17	254.65	676±150	0.73	DS	0.3930	< 7	< 83.88	822±108	0.86	-	-	
OP14h34	0.4658	6	181.92	139±31	0.67	-	0.4655	4	45.77	139±70	0.86	-	0.4658	< 6	< 144.72	139±31	0.79	-	-	
OP14h37	0.4716	20	180.68	328±46	0.77	DS	0.4714	13	106.66	328±64	0.83	AD	0.4714	< 13	< 75.96	414±98	0.95	-	-	
OP14h36	0.4693	6	181.16	183±202	0.70	-	0.4694	5	73.82	266±247	0.73	-	0.4693	< 6	< 81.36	183±202	0.67	-	-	
OP14h38	0.5102	22	173.19	737±57	0.76	AD	0.5104	26	228.15	751±52	0.74	AD	0.5087	10	78.12	673±142	0.57	AD	-	
OP14h40	0.5424	3	167.84	213±209	0.79	-	0.5424	3	61.72	213±209	1.00	-	0.5424	< 3	< 69.48	213±209	0.88	-	-	
OP21h101	0.1219	7	487.09	156±69	0.56	-	0.1214	0	-	0.1216	3	169.92	112±163	0.50	-	-	
OP22h102	0.1447	12	421.00	148±37	0.58	-	0.1445	5	105.69	116±61	0.50	-	0.1447	6	159.48	117±49	0.58	-	-	
OP22h104	0.1454	46	419.27	443±47	0.40	-	0.1454	46	400.49	443±47	0.41	-	0.1453	36	267.12	485±53	0.50	-	-	
OP22h111	0.1790	10	335.44	371±115	0.40	-	0.1790	10	371.99	371±115	0.37	-	0.1789	< 6	< 220.32	505±192	0.38	-	-	
OP22h113	0.1997	3	323.99	748±538	0.29	-	0.1998	6	334.91	494±192	0.28	-	0.2003	1	161.64	-	-	
OP22h117	0.2196	29	300.99	259±35	0.49	-	0.2195	10	102.92	165±34	0.68	-	0.2195	10	121.68	165±34	0.67	-	-	
OP22h119	0.2366	4	284.51	122±146	0.32	-	0.2365	3	98.99	169±139	0.61	-	0.2365	< 3	< 109.80	169±139	0.55	-	-	
OP22h120	0.2410	7	280.58	212±77	0.26	-	0.2414	5	94.51	164±50	0.30	-	0.2414	< 5	< 133.92	164±50	0.24	-	-	
OP22h123	0.2643	13	262.25	194±43	0.48	DS	0.2643	6	88.39	166±94	0.59	-	0.2643	< 6	< 99.00	166±94	0.55	-	-	
OP22h129	0.3171	10	230.80	207±85	0.66	AD	0.3171	10	94.05	207±85	0.79	AD	0.3171	< 10	< 86.40	207±85	0.81	AD	-	
OP22h132	0.3596	7	212.44	413±52	0.70	-	0.3599	6	167.82	412±126	0.71	-	0.3594	4	112.32	491±16	0.70	-	-	
OP22h133	0.3735	4	207.40	204±39	0.64	-	0.3733	3	88.04	203±277	0.53	-	0.3733	< 3	< 79.20	223±277	0.56	-	-	
OP22h134	0.3918	14	201.33	316±67	0.70	-	0.3918	12	129.98	343±73	0.80	-	0.3919	< 8	< 72.00	385±101	0.94	-	-	
OP22h137	0.4259	11	191.50	374±82	0.63	-	0.4257	8	130.14	368±128	0.71	-	0.4254	7	82.08	302±128	0.77	-	-	
OP22h138	0.4379	45	188.41	724±67	0.69	AD	0.4379	59	236.16	684±59	0.70	AD	0.4384	33	134.28	697±87	0.67	-	-	
OP22h139	0.4404	16	187.79	237±40	0.57	AD	0.4403	9	83.64	243±50	0.67	-	0.4405	10	97.56	273±54	0.69	-	-	
OP22h140	0.4658	5	181.91	108±82	0.61	-	0.4660	3	60.38	184±187	0.84	-	0.4659	< 4	< 74.88	144±81	0.76	-	-	

* Column description: group identification number for the optical system (column 1); redshift of the group given a 1 Mpc radial cut (2); number of member galaxies within 1 Mpc (3); radius in arcseconds of 1 Mpc (4); velocity dispersion within a 1 Mpc cut (5); spectroscopic completeness (to $R < 22$) within a 1 Mpc cut (6); dynamical complexity within a 1 Mpc cut (7); redshift of the group given a σ derived r_{200} (9); radius in arcseconds of a σ derived r_{200} (10); velocity dispersion within a σ derived r_{200} (11); spectroscopic completeness (to $R < 22$) within a σ derived r_{200} cut (12); dynamical complexity within a σ derived r_{200} (13); redshift of the group given an X-ray derived r_{200} (14); number of member galaxies within r_{200} (15); radius in arcseconds of r_{200} (16); velocity dispersion within r_{200} (17); spectroscopic completeness (to $R < 22$) within an $r_{200,X}$ cut (18); and dynamical complexity within an $r_{200,X}$ cut (19)

4.3 Matched X-ray - Optical Systems

Although the redshifts of both X-ray and optically selected groups are derived using galaxy redshifts, there are distinct differences in these two group selection procedures, allowing the X-ray and optically selected group samples to be treated as nearly independent. X-ray emission is proportional to density squared and is mainly detectable from cores of galaxy groups, occupying $\sim 10\%$ of the total group area. Such a small area has typically only a handful of galaxies and the primary goal of targeted spectroscopic identification is to increase the completeness, with the primary focus on the group X-ray center. Detection of optical systems on the other hand is entirely based on the depths and sampling of the spectroscopic survey, and typically associates galaxies at much larger separations compared to the size of the X-ray detection.

Examining the redshifts and proximity on the sky of groups in both samples, nine of the optically selected systems are associable with X-ray systems but five of these have an X-ray significance < 2 using the optical center and aperture. Several of the optically selected systems do have significant X-ray emission but are not readily matched to X-ray systems. Recall that the latter require a $\geq 4\sigma$ detection on the wavelet images in order to be identified. It is important to note that this is projected X-ray emission and thus absolute certainty in assigning X-ray emission to an optically detected system is not possible.

4.4 Dynamical Complexity

4.4.1 Descriptions of Tests

We search for dynamical complexity / substructure in our groups by applying the Dressler-Shectman (DS; Dressler & Shectman 1988) Test as in Hou et al., 2012. The DS Test uses both spatial and velocity information in order to identify substructure. A thorough discussion of this test and its application can be found in Hou et al., 2012 but a brief discussion of the methodology follows. We begin with the mean velocity and velocity dispersion (\bar{v}, σ) for each group having n member galaxies. Then for each galaxy i in the group, we select it and a number of its nearest neighbors, N_{nn} , and compute their mean velocity v_{local}^i and velocity dispersion σ_{local}^i . From these we compute

$$\delta_i^2 = \left(\frac{N_{nn} + 1}{\sigma^2} \right) [(\bar{v}_{local}^i - \bar{v})^2 + (\sigma_{local}^i - \sigma)^2], \quad (4.5)$$

where $1 \leq i \leq n_{members}$ and $N_{nn} = \sqrt{n_{members}}$. Note that N_{nn} is rounded/truncated to the nearest integer as appropriate. The Dressler-Shectman Δ statistic is then calculated as follows:

$$\Delta = \sum_{i=1}^N \delta_i, \quad (4.6)$$

where N is the total number of galaxies in the group.

100,000 Monte Carlo models are then run to calibrate the Δ statistic for each group. Each Monte Carlo model is made by randomly shuffling the velocities among the group galaxies. Then

a probability P is defined as the fraction of the total number of Monte Carlo models of the group that have Δ 's larger than the true value of the group. $P \sim 1.0$ means that the group contains no significant substructure, while $P \sim 0.0$ indicates that the group contains statistically significant substructure. For a group to be defined as having substructure, we require $P < 0.01$.

Another method of identifying dynamical complexity within groups is to search for deviations from a Gaussian velocity distribution. We use the Anderson-Darling (AD; Anderson & Darling 1952) Test to classify velocity distributions as non-Gaussian as in Hou et al. (2009), and show that the test is reliable and robust for group-sized systems. A detailed analysis of the AD test is given in Hou et al. (2009), but we give a brief description of the statistic here. The AD statistic is a goodness-of-fit test that compares the cumulative distribution function (CDF) of ordered data to a model empirical distribution function (EDF), which in our case is a Gaussian EDF. This comparison is done using the following computing formulae (D'Agostino & Stephens, 1986):

$$A^2 = -n - \frac{1}{n} \sum_{i=1}^n (2i - 1)(\ln \Phi(x_i) + \ln(1 - \Phi(x_{n+1-i}))), \quad (4.7)$$

$$A^{2*} = A^2 \left(1 + \frac{0.75}{n} + \frac{2.25}{n^2} \right) \quad (4.8)$$

where $x_i \leq x < x_{i+1}$, $\Phi(x_i)$ is the CDF of the hypothetical underlying distribution. Probabilities for the AD test are then computed using

$$\alpha = a \exp(-A^{2*}/b) \quad (4.9)$$

where $a = 3.6789468$ and $b = 0.1749916$, and both factors are determined via Monte Carlo methods (Nelson, 1998). A system is then considered to have a non-Gaussian velocity distribution, and therefore dynamical complexity, if its computed α value is less than 0.01, corresponding to a 99% confidence level.

Hou et al. find both tests to be reliable for groups with 10 or more members, thus we apply them only to those groups in our samples which meet this criterion. Tests using mock catalogs indicate that this criterion, combined with the requirement of a probability less than 0.01, results in a false positive rate of 1% and 5% for the AD and DS tests respectively.

4.4.2 Effect of Dynamical Complexity

Tab. 4.4 summarizes our results for both X-ray and optical groups, giving the number of systems where dynamical complexity was identified per the systems tested for each test and radial cut. In general, we find the least amount of dynamical complexity when we employ an X-ray based r_{200} cut to our systems. In fact the DS test fails to find significant substructure for any group with this radial cut applied. When we use the, normally larger, 1 Mpc and velocity dispersion based radial cuts we find significantly more dynamical complexity. The latter cut yields the highest fraction of both non-Gaussian (AD) and substructure (DS) groups. Recall that Tables 4.2 and 4.3 indicate whether dynamical complexity is detected for each X-ray and optical group respectively.

Table 4.4: Summary of Dynamical Complexity Test Results

	AD 1 Mpc	DS 1 Mpc	AD $r_{200,\sigma}$	DS $r_{200,\sigma}$	AD $r_{200,X}$	DS $r_{200,X}$
X-ray*	7 of 19	4 of 19	6 of 14	4 of 14	1 of 11	0 of 11
Optical	5 of 19	3 of 19	4 of 12	1 of 12	3 of 10	0 of 10

* quality 1 & 2 systems only

Column description: Number of systems meeting dynamical complexity criterion per total number tested for X-ray and optical systems in each radial cut.

Fig. 4.14 shows the results of both substructure tests for the X-ray selected system XR14h09. Substructure is detected in this group at all radial cuts by the AD test and for the $r_{200,\sigma}$ cut case according to the DS test. The top panel of Fig. 4.14 shows Dressler-Shectman ‘bubble-plots’ for this group for each of the three radial cuts. In a bubble-plot, each galaxy in the group is plotted at its spatial position and is represented by a symbol whose size scales with its δ_i value. Larger symbols indicate larger deviations in the local kinematics compared to the global values, and a ‘local grouping’ of galaxies with similarly large symbols may indicate a kinematically distinct system. The $r_{200,\sigma}$ cut plot shows such a congregation at a declination of $\sim 9.115^\circ$. Similar plots, showing the DS bubble-plots and histograms of the velocity distributions at each radial cut for all groups exhibiting substructure are provided in Fig. 4.15. Note that missing columns (e.g. OP14h37) occur where there are fewer than ten members.

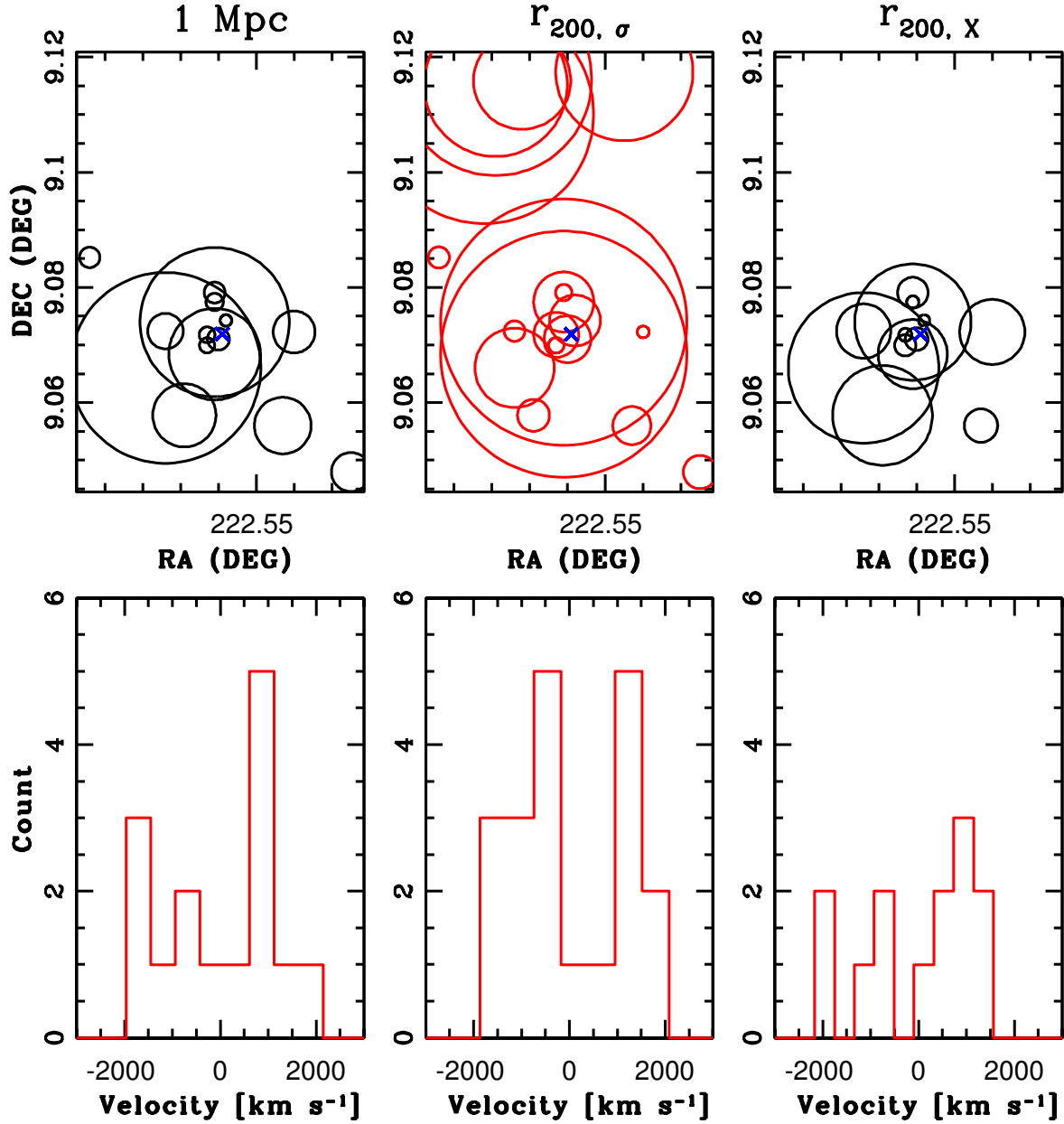


Figure 4.14: Results of dynamical complexity tests for group XR14h09. Top panel: Dressler & Shectman (1988) bubble-plots where the galaxy symbols scale with $\exp(\delta_i)$ for 1 Mpc, $r_{200,\sigma}$, and $r_{200,x}$ radial cuts. The DS test finds substructure only in the case of an $r_{200,\sigma}$ radial cut. Bottom panel: Histogram of the velocity distribution for the same radial cuts as above. Non-Gaussianity (dynamical complexity) is detected using the AD test at all radial cuts. Red indicates that for that radial cut and test, dynamical complexity is detected.

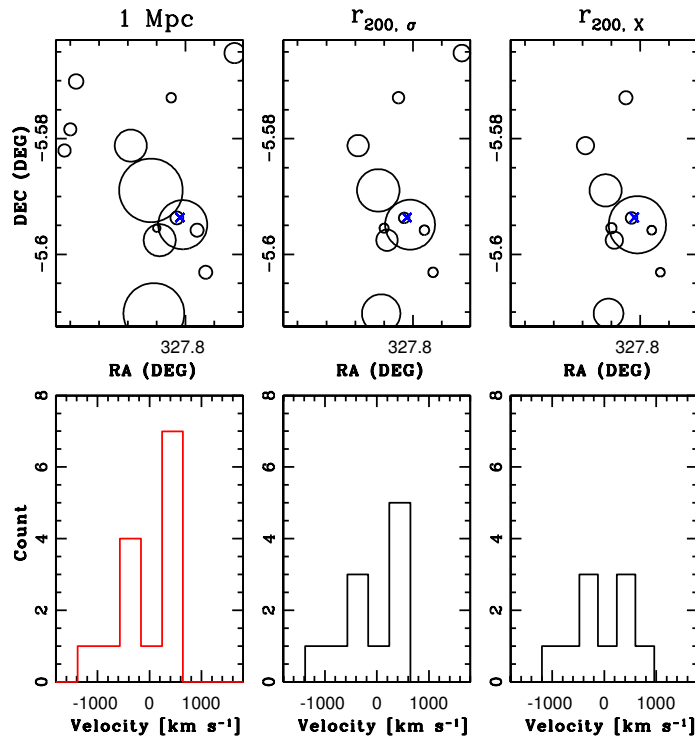


Figure 4.15: Systems with dynamical complexity. Top panels: Dressler & Shectman (1988) bubble-plots where the galaxy symbols scale with $\exp(\delta_i)$ for 1 Mpc, $r_{200,\sigma}$, and $r_{200,x}$ radial cuts. Bottom panels: Histogram of the velocity distribution for the same radial cuts as above. Red indicates that for that radial cut and test, dynamical complexity is detected. Group OP21h139.

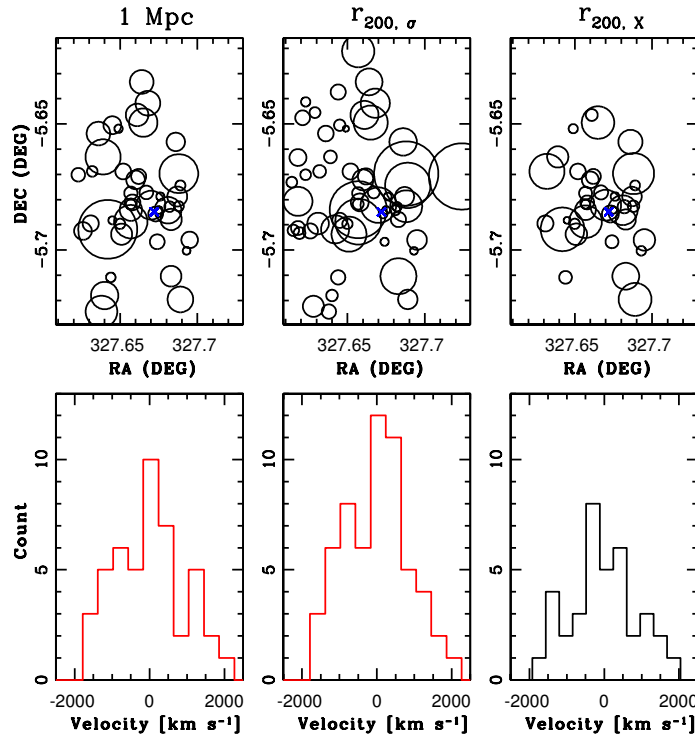


Figure 4.15: continued - XR21h14

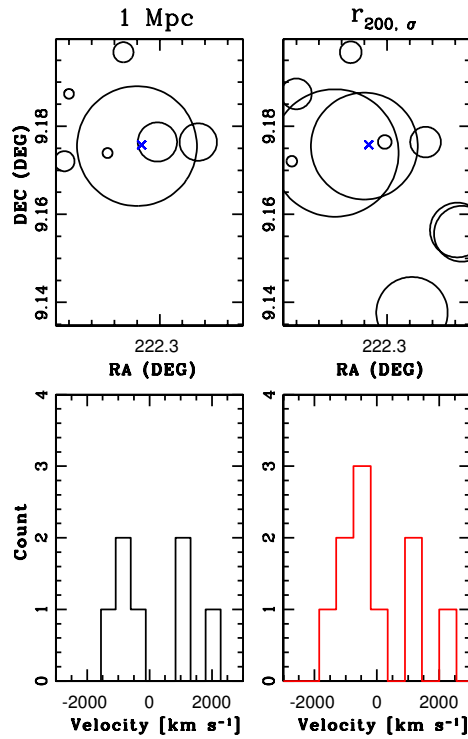


Figure 4.15: continued - XR14h03

4. Follow-up Spectroscopy and Measured Group Properties

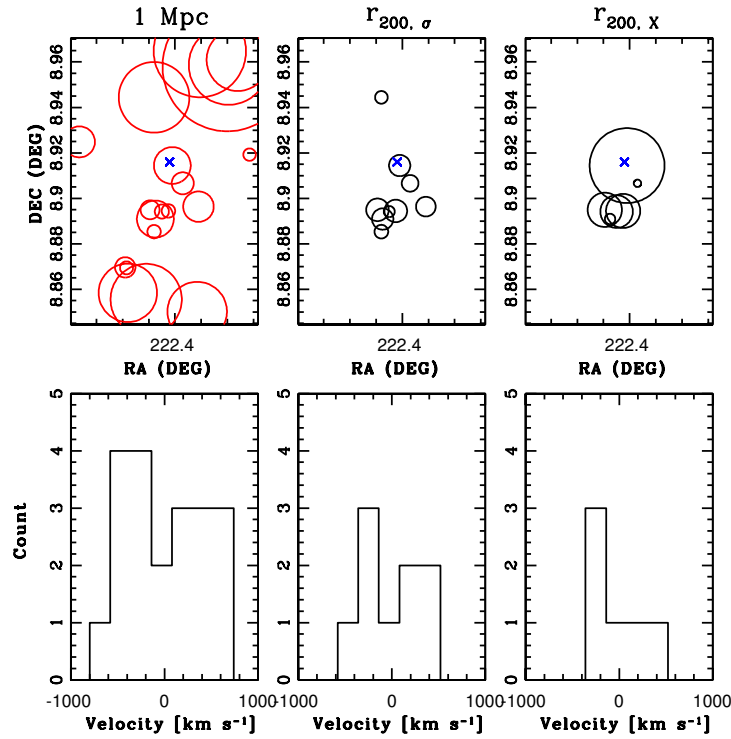


Figure 4.15: continued - XR14h22

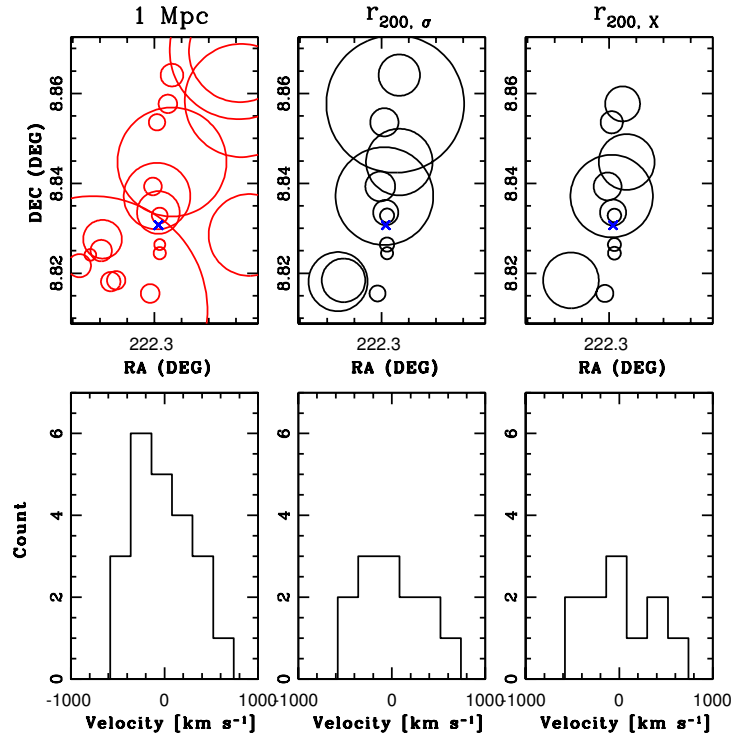


Figure 4.15: continued - XR14h25

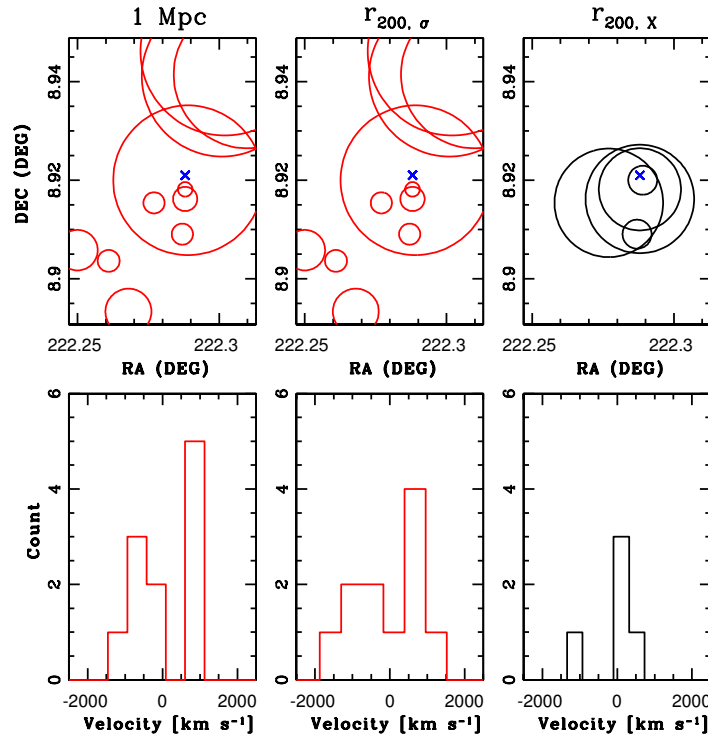


Figure 4.15: continued - XR14h44

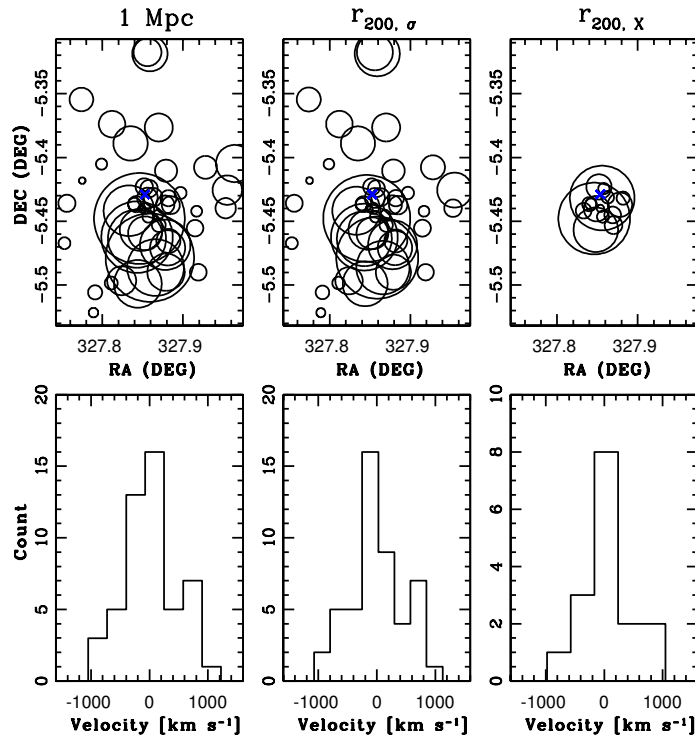


Figure 4.15: continued - XR21h06

4. Follow-up Spectroscopy and Measured Group Properties

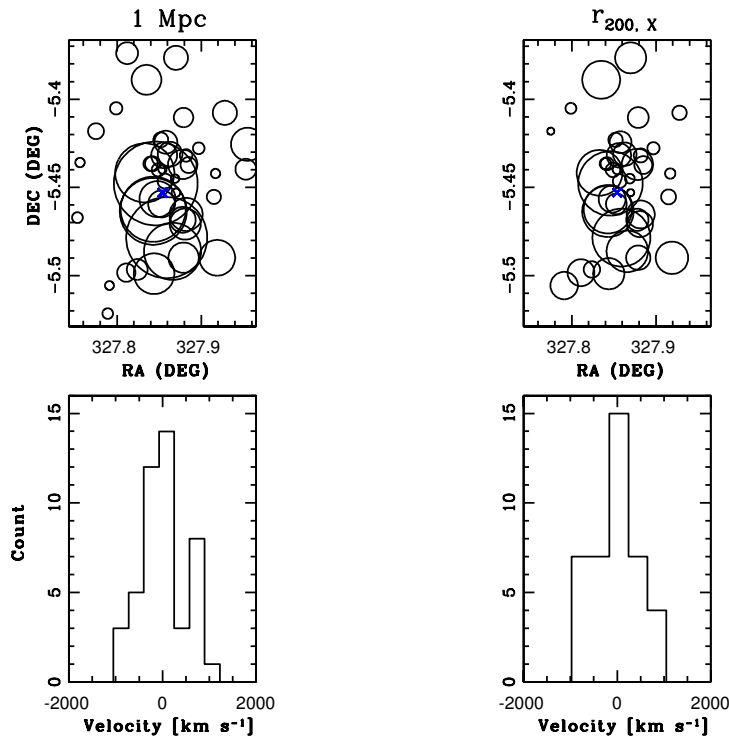


Figure 4.15: continued - XR21h7

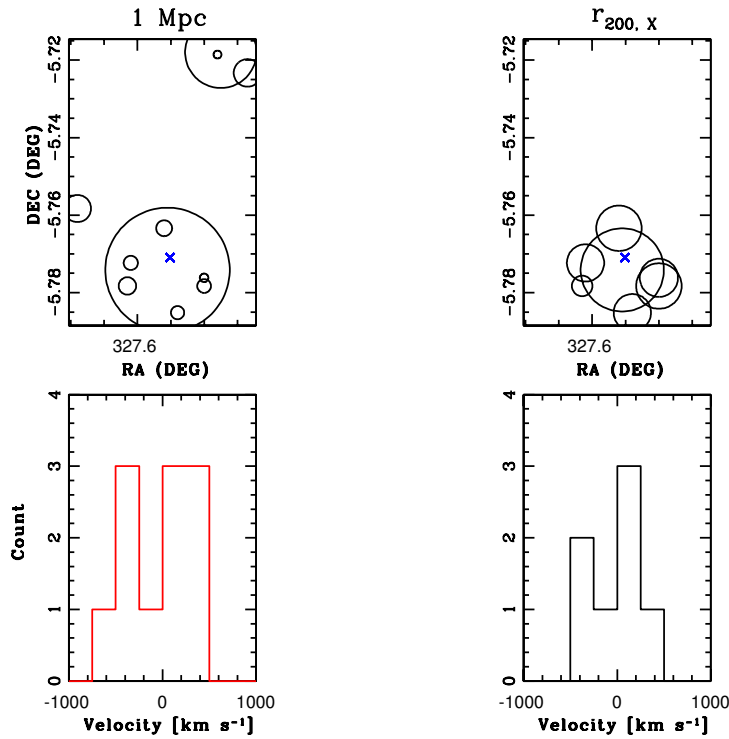


Figure 4.15: continued - XR21h18

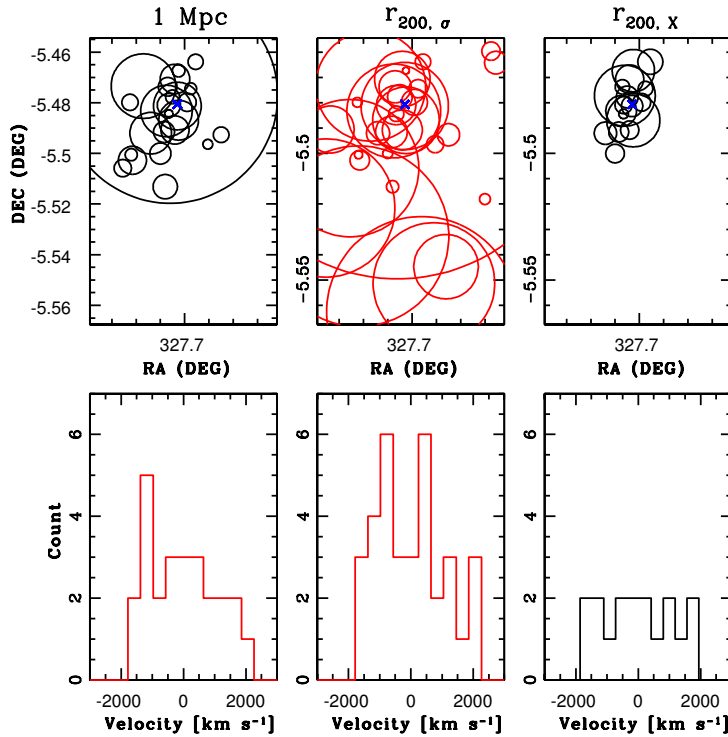


Figure 4.15: continued - XR21h37

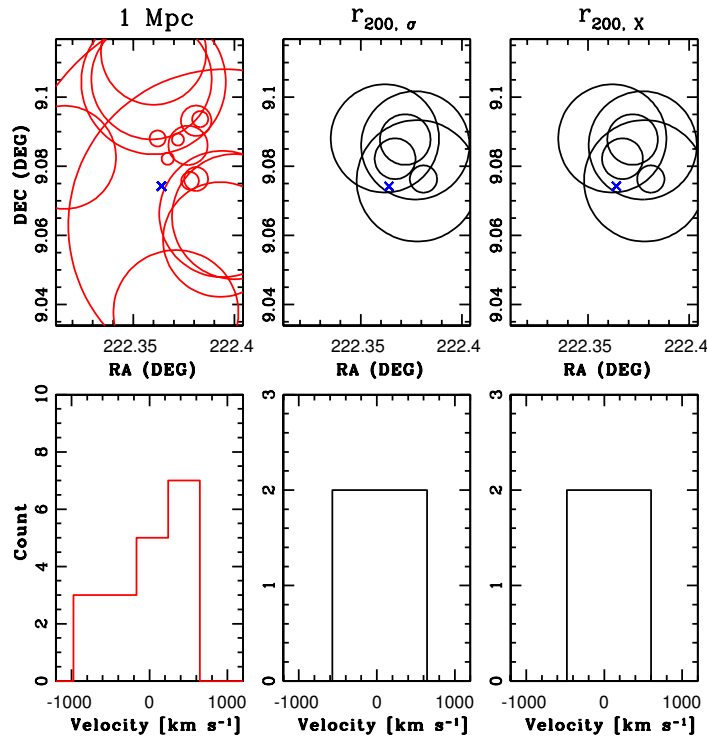


Figure 4.15: continued - XR14h11

4. Follow-up Spectroscopy and Measured Group Properties

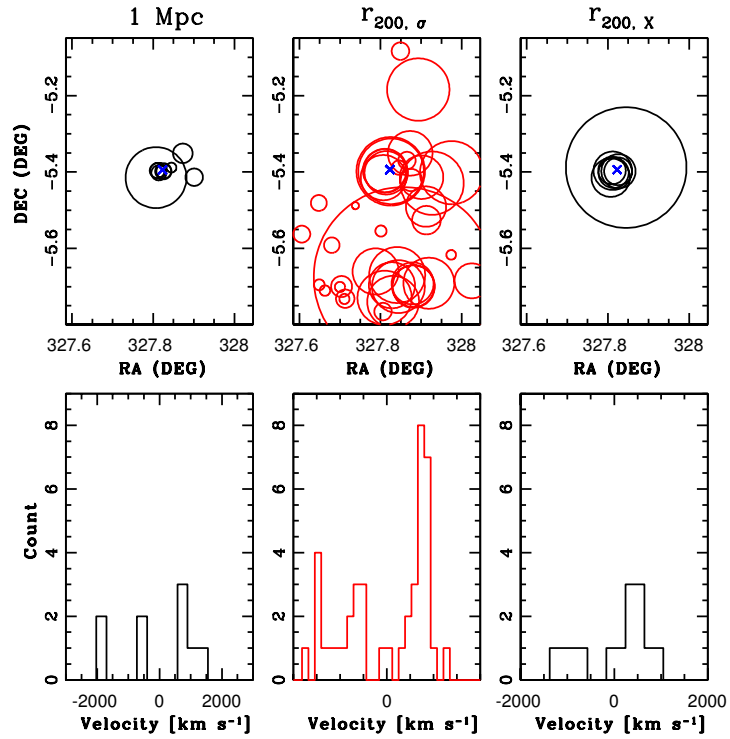


Figure 4.15: continued - XR21h27

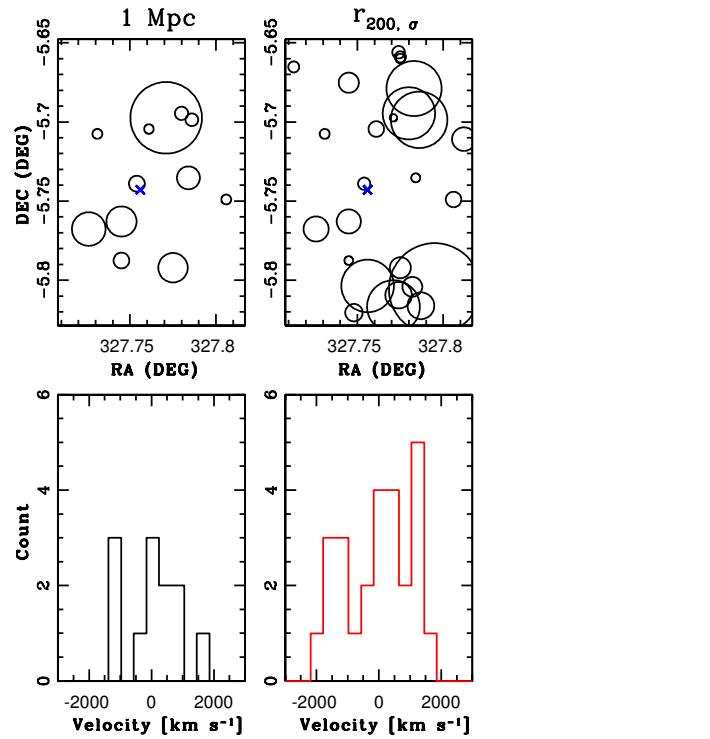


Figure 4.15: continued - XR21h49

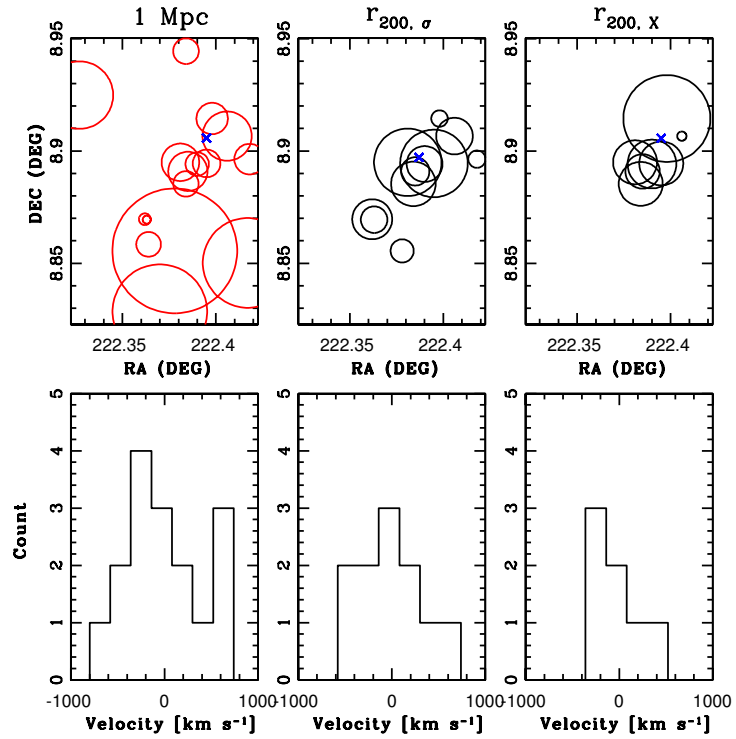


Figure 4.15: continued - OP14h10

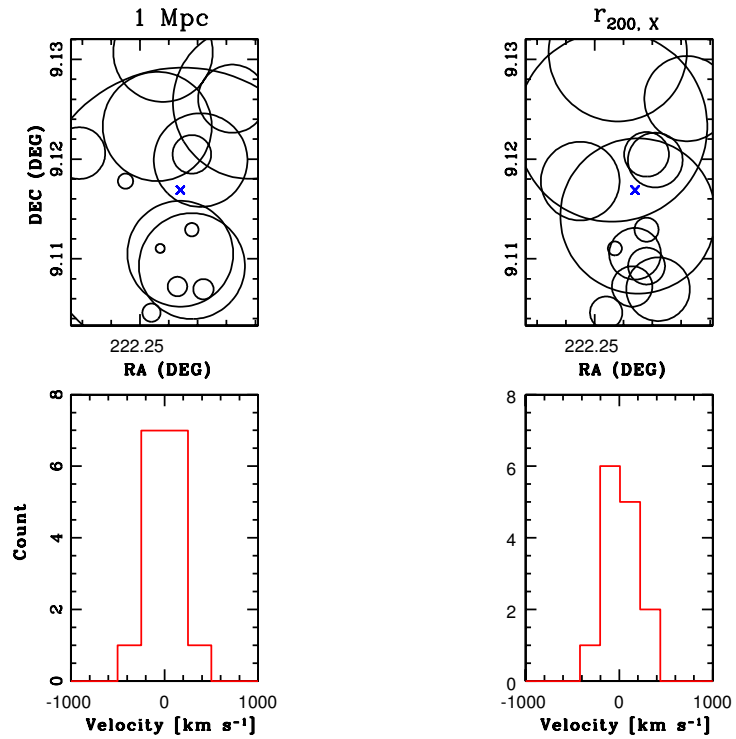


Figure 4.15: continued - OP14h24

4. Follow-up Spectroscopy and Measured Group Properties

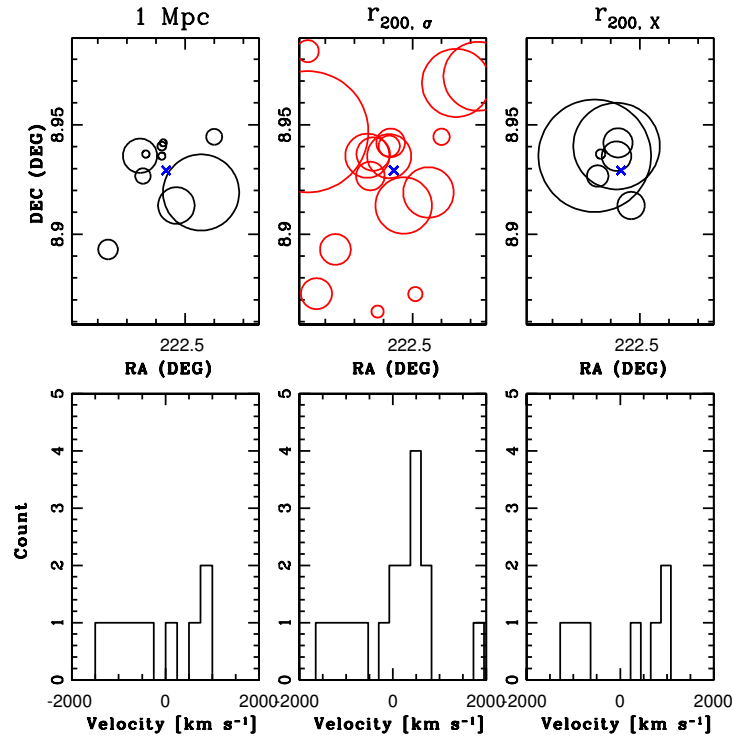


Figure 4.15: continued - OP14h32

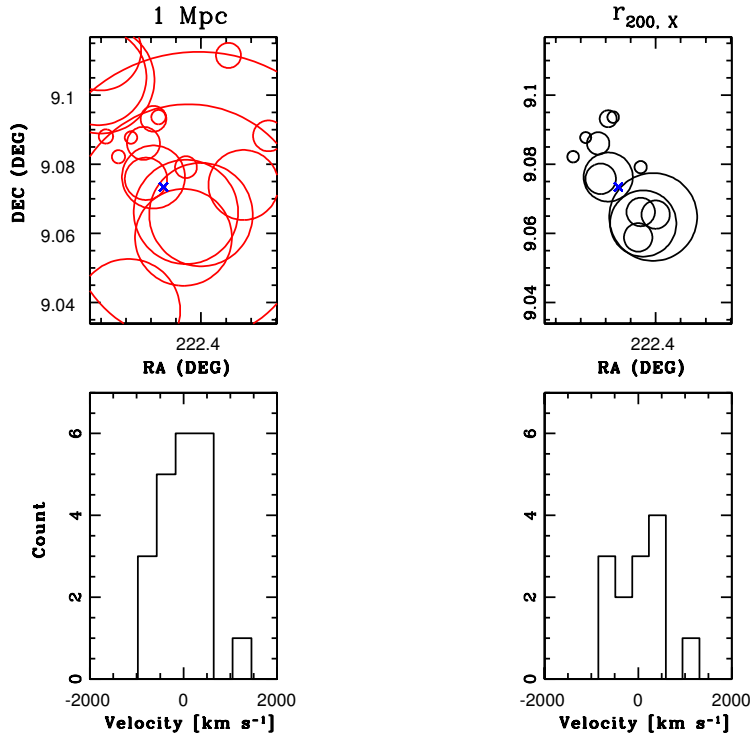


Figure 4.15: continued - OP14h37

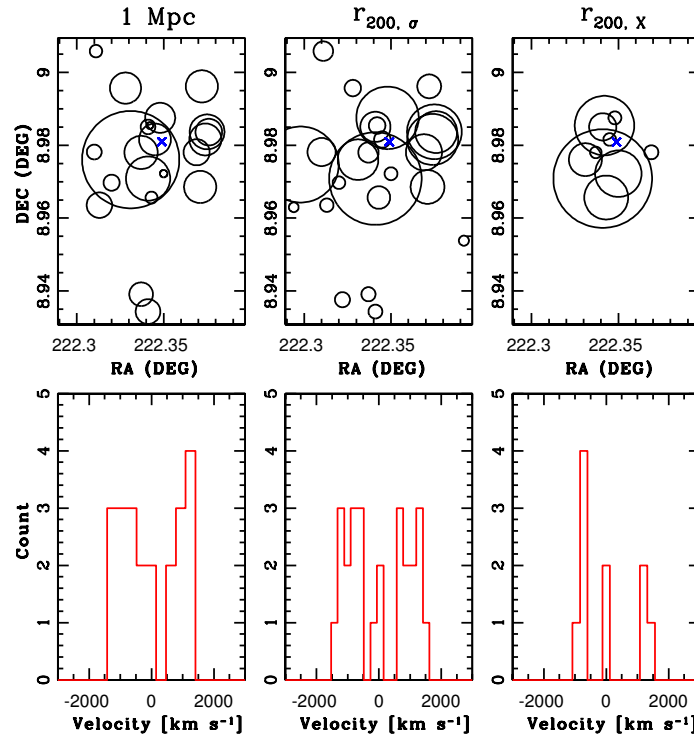


Figure 4.15: continued - OP14h38

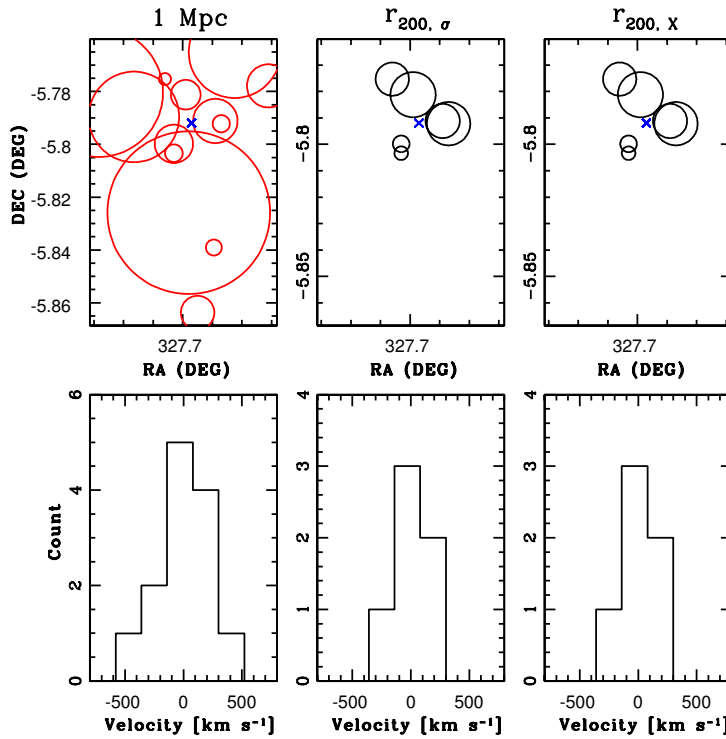


Figure 4.15: continued - OP21h123

4. Follow-up Spectroscopy and Measured Group Properties

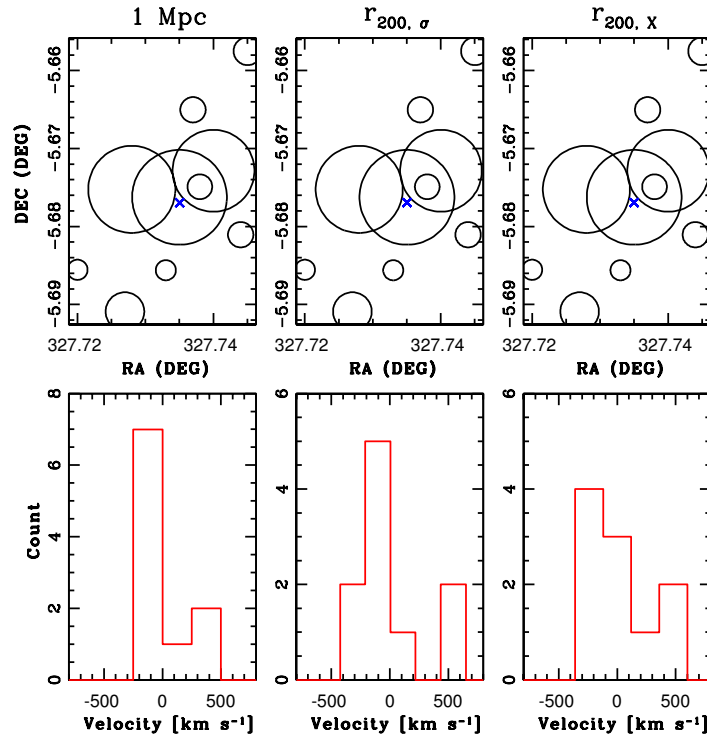


Figure 4.15: continued - OP21h129

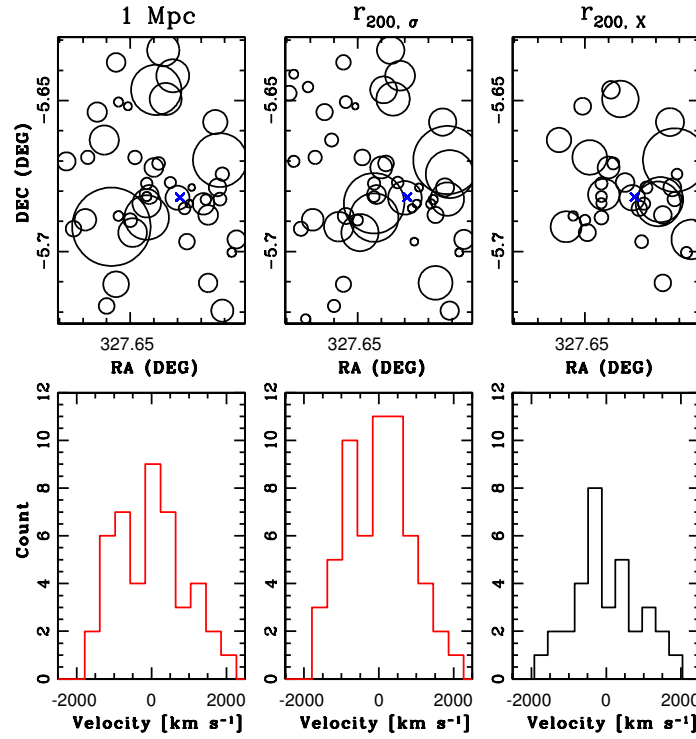


Figure 4.15: continued - OP21h138

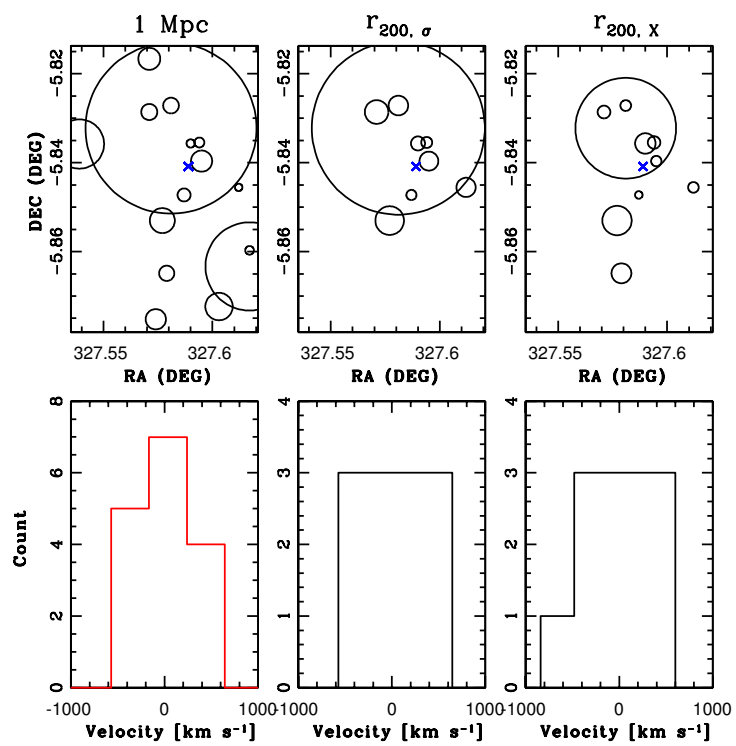


Figure 4.15: continued - OP21h139

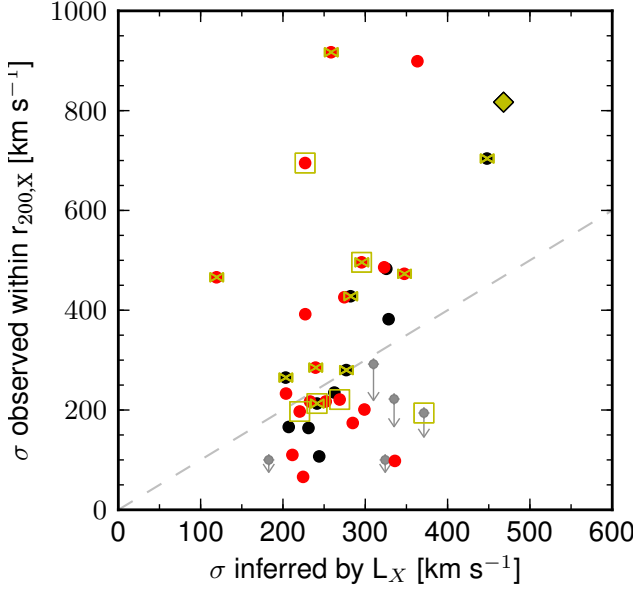


Figure 4.16: Velocity dispersions for quality 1 & 2 X-ray selected systems (black and red filled circles respectively) measured within $r_{200,X}$ and calculated as in Eq. 4.4 using $r_{200,X}$. Upper limits are shown in grey. Yellow bow-ties indicate systems tested for substructure. Filled yellow diamonds indicate systems with substructure according to the AD test. All substructure results shown here are for the $r_{200,X}$ radial cut case. Open yellow squares show groups in X-ray confused regions. A 1:1 line is shown in dashed grey.

The DS test fails to detect substructure for any group with an X-ray based r_{200} radial cut applied. Assuming substructure is preferentially located at the outskirts of groups, this supports the hypothesis that an X-ray based r_{200} cut is the one most likely to be tracing the virialized core of the system. Fig. 4.16 looks more closely at this $r_{200,X}$ cut, comparing the ‘real’ velocity dispersions *measured* for quality 1 & 2 X-ray systems within the X-ray defined r_{200} to the velocity dispersion for the same systems if σ were instead *computed* by substituting $r_{200,X}$ into Eq. 4.4 and rearranging to get σ . The latter results in a much tighter range in velocity dispersions. Very low velocity dispersions are not possible when inferred from L_X due to the X-ray detection limit but measured σ can also be much larger than that inferred from the X-ray measurements. This implies that dynamical complexity or non-virialized orbits may inflate velocity dispersion even within an X-ray derived r_{200} but this is confirmed by the AD test in only a single case.

The differences in σ – and thus dynamical mass – *measurements* within the different radial cuts are, however, small. Group stellar mass measurements may though be biased since larger radial cuts will always result in larger or equivalent stellar masses.

X-ray Substructure

Although our X-ray imaging may not be deep enough to detect X-ray substructure in the majority of our systems, a pair of X-ray detected systems, XR21h06 and XR21h07, does appear to constitute one clear case of this in the sample. These groups lie at essentially the same redshift of 0.145 and appear as two separate peaks within an area of overlapping X-ray emission. Fig. 4.17 shows these systems. The group XR21h07 corresponds to the center of optical group OP21h104. None of these groups has substructure detected using the AD or DS tests. This is especially surprising given a 1 Mpc radial cut as the membership overlaps so thoroughly in this case. If we relax our criterion to $P \approx 0.06$, XR21h06 would have substructure detected by the DS test in the case of all radial cuts and XR21h07 in the case of an X-ray based r_{200} cut. OP21h104 would also have

substructure detected via the DS test if the criterion was relaxed and an X-ray based r_{200} cut employed. If these groups are merging in the plane of the sky, it is doubtful substructure would be detected by the DS test. In this case we would, however, expect the AD test to find substructure as it is unlikely that the velocity distributions would combine to make a single Gaussian. Further discussion of false negatives for these tests and the effect of superposition for massive GEEC groups can be found in Hou et al. (2012).

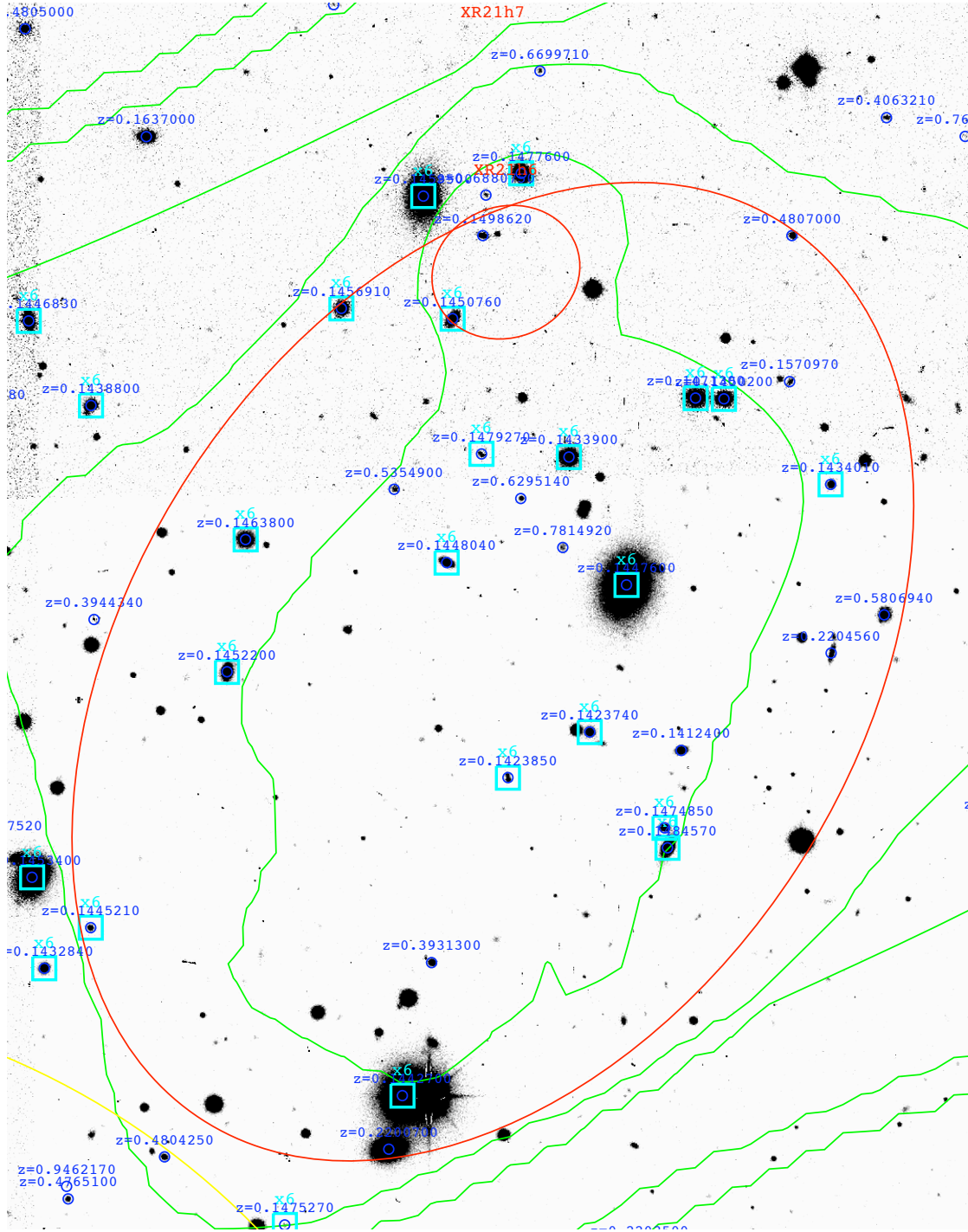


Figure 4.17: Optical (I-band) imaging of X-ray substructure groups XR21h06 and XR21h07 with X-ray contours overlaid. X-ray groups are marked by red ellipses (the larger being XR21h07). Green contours indicate X-ray emission from the wavelet map. All galaxies with redshifts are marked in blue while group members are marked in cyan. In this case no radial cut is yet applied and thus galaxies are assigned to only one group.

Chapter 5

L_X- σ Relation

As discussed in § 1.3, the X-ray luminosity and velocity dispersion of groups are predicted to correlate. In this chapter I first discuss the Bayesian best fit procedure used to evaluate the L_X- σ and subsequent relations before comparing my L_X- σ with those found for other samples and discussing scatter. Note that I apply E(z), the scaling factor of the Hubble parameter, to the X-ray luminosities. This is a customary choice, allowing rescaling of the data to the same redshift, and our value ($E_z^{-1} = [\Omega_M(1+z)^3 + \Omega_M]^{1/2}$) reflects a flat cosmology. The self-similar model of cluster formation predicts that the slopes of X-ray scaling relations are redshift-independent and the normalization evolves as E(z) due to the increasing density of Universe. As an example, the X-ray cluster at z=1 is approximately twice as luminous than one at z=0 for a given kT.

5.1 Bayesian Best Fits

In order to define the linear best fit for these relations while accounting for the errors in both L_X and σ , I chose a Bayesian approach as in Kelly (2007). Specifically, I use the LINMIX_ERR IDL code of Kelly (2007) to determine the slope m , intercept c , and intrinsic scatter s of the relation $\log(L_X) = m \times \log(\sigma) + c + \epsilon$, where ϵ is a random variable with variance equal to the square of the intrinsic scatter (s^2). The resultant slope, intercept, and intrinsic scatter, and their 1σ limits, are then used to search for changes in scatter between different samples as well as outliers from the relation, attempting to tie this to an observable property of the samples or outlying groups. This same approach is employed for subsequent scaling relations.

The Kelly method allows measurement errors to be treated as independent and log-normal and assumes that the intrinsic scatter in the dependent variable is Gaussian and the intrinsic distribution of the independent variables can be well approximated by a combination of Gaussians. This latter Gaussian approximation does not require the assumption of a uniform prior distribution on the independent variable (in this case, $\log(\sigma)$, where σ is the velocity dispersion) as in many commonly used χ^2 minimization techniques used to return best fits. The publicly available LINMIX_ERR code constructs Monte Carlo Markov Chains (MCMCs, Gilks et al., 1996; Christensen & Meyer, 2000) to draw random parameter sets from the probability distributions,

the maxima of the distributions of these draws representing the best fit values. The technique of random draws replaces direct computation of the probability (posterior) distribution, which is extremely computationally intensive. Note the probability distribution can be asymmetric. I compute 1σ uncertainties (15.9 and 85.1 percentile values) on all fit quantities.

The Kelly code provides two ways in which to create the Markov chains: the Gibbs Sampler and the Metropolis-Hastings Algorithm. I chose the latter, since this is recommended for samples which are small or where errors may dominate the scatter. I tested the effect of using a different number of Gaussians (from 1 to 4) and found that the resulting distributions were usually very similar, so one is used. Finally, the maximum number of iterations was varied, and the default value of 10^5 found to be sufficient.

For the X-ray groups, this best fit analysis is performed for quality 1 and 1 & 2 groups respectively and for each radial cut excluding those with upper limits on L_X and/or σ . Two examples of the distributions of m , c , and s can be seen in Fig. 5.1. As expected, the intrinsic scatter in the relation tends to increase with the addition of the poorer quality groups. Additionally, I examine the effect of luminosity-weighted recentering for X-ray systems by recomputing the membership and velocity dispersion and find little change in σ and thus little difference in the $L_X-\sigma$ relation. The best fit analysis is also performed for the optical systems for all radial cuts.

Table 5.1: $L_X-\sigma$ Relation Bayesian Best Fits

		m	c	s
X-ray Q=1	1Mpc	$2.5816 \pm^{0.4600}_{0.4435}$	$35.872 \pm^{1.1489}_{1.1891}$	$0.1884 \pm^{0.1286}_{0.0916}$
	$r_{200,\sigma}$	$2.3432 \pm^{0.5045}_{0.6154}$	$36.608 \pm^{1.4957}_{1.3824}$	$0.2592 \pm^{0.1781}_{0.1286}$
	$r_{200,X}$	$2.4044 \pm^{0.5879}_{0.6071}$	$36.341 \pm^{1.5298}_{1.5406}$	$0.2266 \pm^{0.1639}_{0.1126}$
X-ray Q=1 & 2	1Mpc	$1.1539 \pm^{0.3806}_{0.3793}$	$39.364 \pm^{0.9873}_{0.9635}$	$0.3703 \pm^{0.0654}_{0.0533}$
	$r_{200,\sigma}$	$0.6844 \pm^{0.3535}_{0.3491}$	$40.532 \pm^{0.9050}_{0.9149}$	$0.4303 \pm^{0.0821}_{0.0613}$
	$r_{200,X}$	$1.3529 \pm^{0.4249}_{0.4650}$	$38.839 \pm^{1.2093}_{1.0722}$	$0.3533 \pm^{0.0664}_{0.0548}$
Optical	1Mpc	$1.7125 \pm^{0.5883}_{0.5902}$	$37.769 \pm^{1.4878}_{1.5344}$	$0.3577 \pm^{0.1554}_{0.1034}$
	$r_{200,\sigma}$	$1.3628 \pm^{0.6351}_{0.6117}$	$38.691 \pm^{1.5328}_{1.6341}$	$0.3779 \pm^{0.1568}_{0.1081}$
	$r_{200,X}$	$1.7822 \pm^{0.6019}_{0.5350}$	$37.665 \pm^{1.3516}_{1.5601}$	$0.2994 \pm^{0.1614}_{0.1119}$

Column description: Bayesian best fit slope (m) and uncertainties (column 1); intercept (c) and uncertainties (2); and intrinsic scatter (s) and uncertainties (3) of the relation $\log(L_X) = m \times \log(\sigma) + c + \epsilon$, where ϵ is a random variable with variance equal to s^2 .

For a given radial cut, the $L_X - \sigma$ best fits for Q=1 & 2 X-ray and optically selected systems are relatively similar but the relation found for Q=1 X-ray systems is significantly steeper. For a fixed L_X , the range in σ is much larger for Q=2 than for Q=1 X-ray systems. Additionally, the higher σ Q=2 groups tend to lie well off the relation and exhibit dynamical complexity. The intrinsic scatter for the optical groups is larger than that found for the quality 1 X-ray groups, regardless of the quality cut applied, but generally comparable to or less than that for the quality

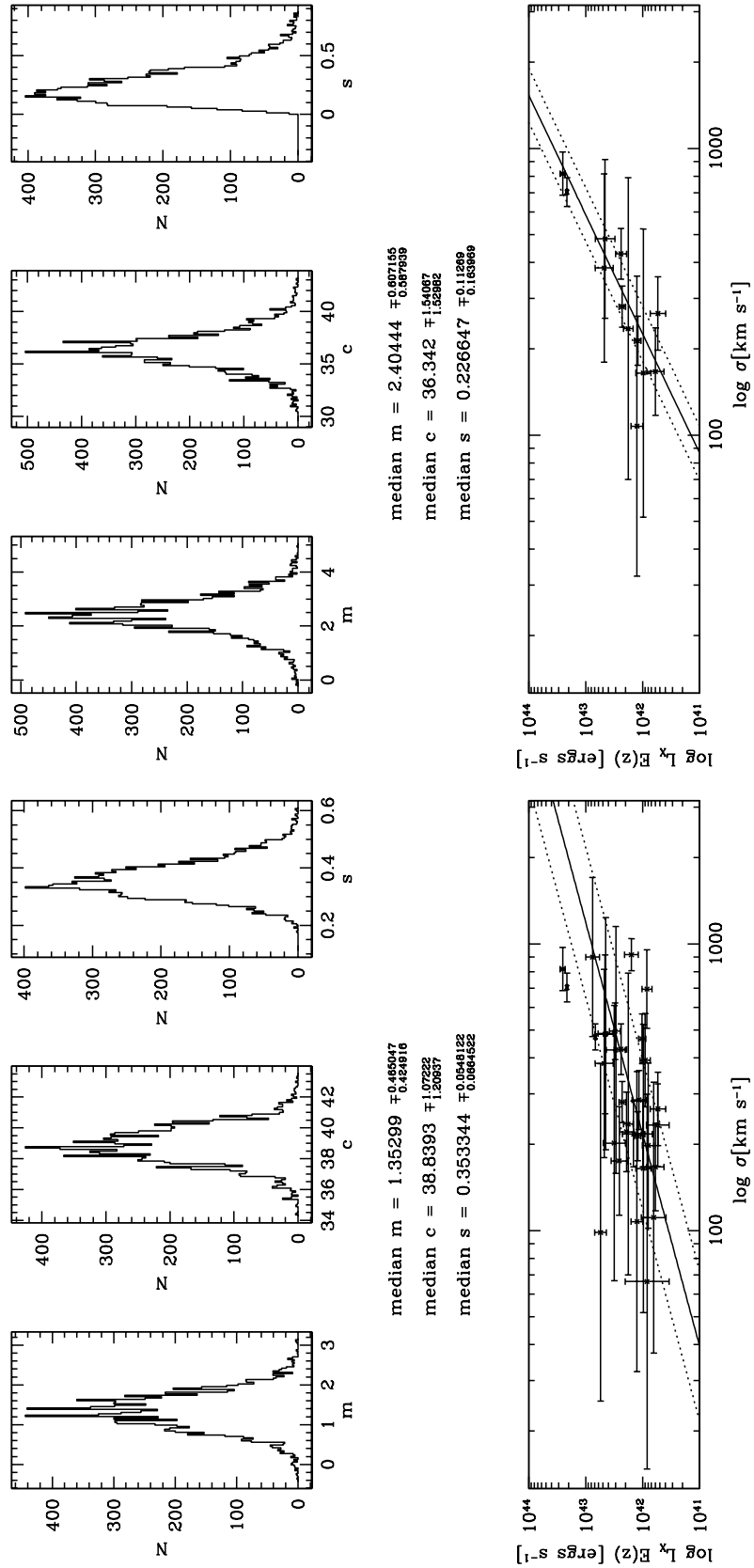


Figure 5.1: Example of evaluation of Kelly Bayesian best fit results. Distribution of m , c , and s (top), median and error values (middle), and L_x and σ relation with median best fit and scatter plotted as solid and dotted lines respectively (bottom) for only quality 1 X-ray groups (left) and quality 1 & 2 groups (right bottom) given an $r_{200,x}$ radial cut.

1 & 2 X-ray systems. Note that most optical systems are excluded from the fitting due to their L_X measurement limits. The $L_X\text{-}\sigma$ slope, intercept, and intrinsic scatter, and their uncertainties, are listed in Tab. 5.1 for the optical and high quality X-ray systems for each of the different radial cuts.

5.2 $L_X\text{-}\sigma$ Relation Results

The X-ray luminosity-velocity dispersion ($L_X\text{-}\sigma$) relation is shown in Fig. 5.2 for X-ray and optically selected groups with all radial cuts. I plot for comparison the $L_X\text{-}\sigma$ relation derived from two different samples: the Mulchaey et al. (2003) sample of groups at $z\approx 0$ and the Rykoff et al. (2008b) maxBCG sample of clusters at $0.1 \leq z \leq 0.3$. These comparisons are shown as dashed and dotted lines in Fig. 5.2 and find no evidence for deviation from the assumed evolution of this relation with redshift. The slope for our highest quality X-ray selected systems is very similar to the 2.56 ± 0.56 found by Osmond & Ponman for the GEMS group sample (Osmond & Ponman, 2004) and the slopes for our Q=1 & 2 X-ray systems and optical systems with an X-ray derived r_{200} are also in relatively good agreement with that of Jeltema et al. (2008, $m = 1.7 \pm 0.4$), though their relation is calculated within $r_{500,X}$ and the groups used are on average more massive than ours. Our work supports the findings that the $L_X\text{-}\sigma$ relation for groups is shallower than that for clusters (Mahdavi & Geller, 2001; Xue & Wu, 2000) where the relation has been found to agree well with the bolometric X-ray luminosity $\propto \sigma^4$ predicted by self-similar evolution (e.g. Horner, 2001; Zhang et al., 2011).

Note that several of the most significant outliers at high mass in these relations show substructure (marked as yellow diamonds and squares). Given a σ based r_{200} radial cut, all systems with a velocity dispersion greater than 500 km s^{-1} show dynamical complexity implying that these high values may be overestimated. This translates to a dynamical mass of $\sim 10^{14.1} M_\odot$.

High quality X-ray groups in X-ray confused regions (quality 1.5 or 2.5, shown as open yellow squares in Fig. 5.2) do not seem to be preferentially high in X-ray luminosity. For all systems (X-ray quality 1 and 1 & 2 and optical systems) the use of a σ derived r_{200} cut results in the largest scatter in the $L_X\text{-}\sigma$ relation and looks to be biased towards giving higher dispersions for dynamically complex systems. The X-ray derived r_{200} cut provides a relatively tight correlation even for optically selected systems. A 1 Mpc cut produces similarly tight fits for the good quality X-ray systems but is less well constrained than the X-ray radial cut for optical systems. This constant cut can extend beyond a physical r_{200} or lie within it and is biased large for low halo masses (and small for high halo masses reciprocally).

As velocity dispersions for systems with few members are less reliable (e.g. Zabludoff & Mulchaey, 1998; Girardi & Mezzetti, 2001), I perform additional Bayesian fitting to the $L_X\text{-}\sigma$ relation, further dividing the subsamples into those with $N_{mem} < 10$ and those with $N_{mem} \geq 10$ and tabulate the results in Tab. 5.2. Note that the latter subsample comprises all groups where dynamical complexity could be evaluated, thus marked by yellow bow-ties in Fig. 5.2. It is clear from Fig. 5.2 that, for X-ray selected groups, the low N_{mem} systems tend to have lower dispersion than the high N_{mem} groups at fixed L_X regardless of the radial cut applied. This indicates either that the dispersion and number of members correlate better with the group mass than L_X or that

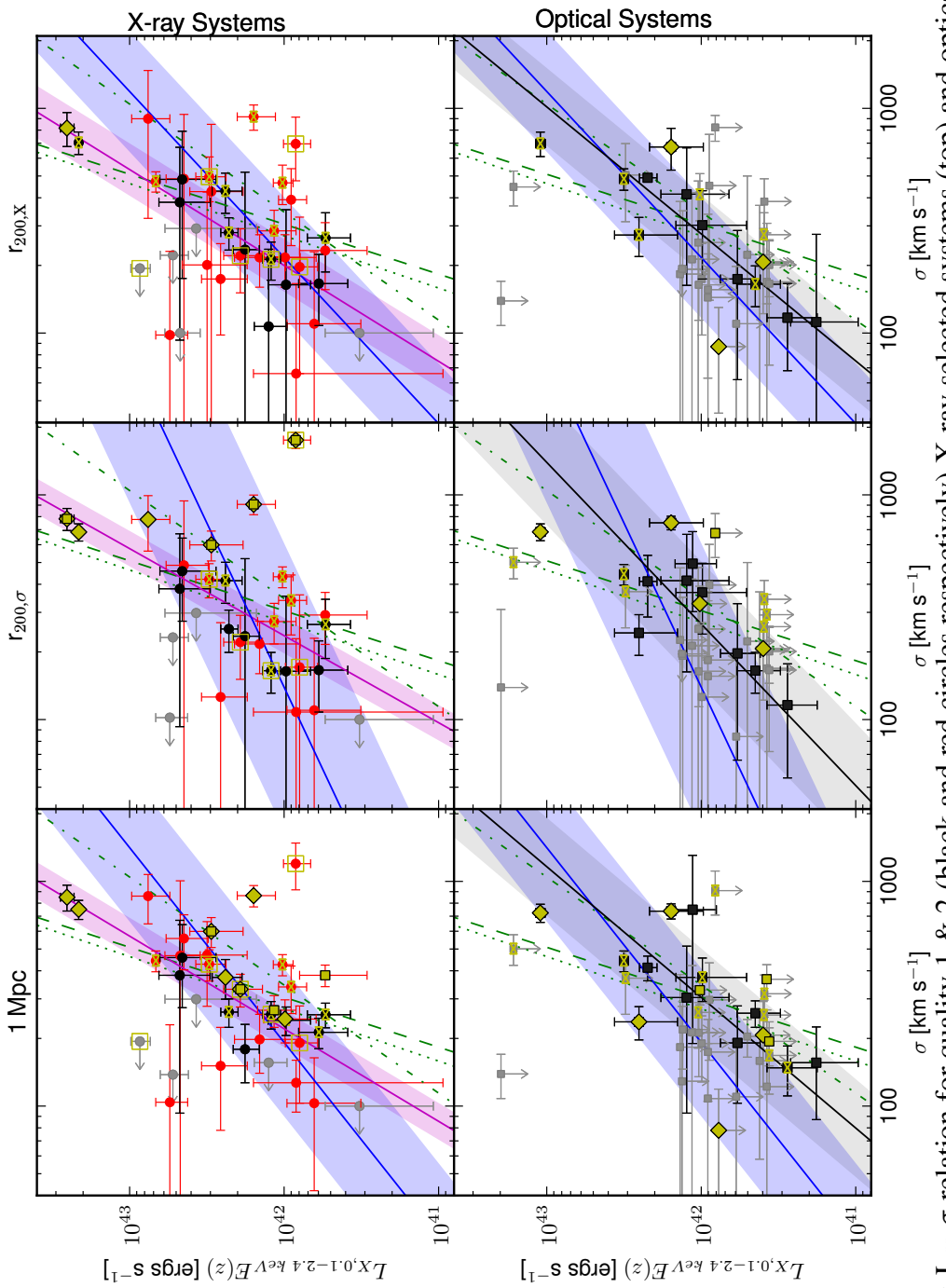


Figure 5.2: $L_X\text{-}\sigma$ relation for quality 1 & 2 (black and red circles respectively) X-ray selected systems (top) and optical systems (bottom) for all radial cuts. Dashed and dot-dashed green lines show $z\sim 0$ sample fits [Mulchaey et al. 2003] while the dotted line is a $z\sim 0.25$ sample [Rykoff et al. 2008b]. Bayesian best fits for quality 1 (magenta) and quality 1 & 2 (blue) X-ray and optical systems (black) are shown with filled regions representing the intrinsic scatter. Yellow bow-ties show systems tested for substructure. Filled yellow diamonds and squares indicate systems with substructure according to AD and DS Tests respectively. Open yellow squares show groups in X-ray confused regions.

the dispersion is typically estimated lower with fewer members. Nonetheless, the overall fits are similar to those found for the total population. Indeed, only in the case of quality 1 & 2 X-ray systems with a 1 Mpc radial cut applied is the difference between fitting significantly divergent for groups with fewer than ten members, being much shallower than that found for systems with at least ten members. As systems with few members also have large measurement errors in their velocity dispersions, they are consistent with a wide range of relations, while the high N_{mem} groups have smaller errors and thus import more stringent constraints on the best fit relation. In this light, it is not surprising that similar results are produced and I chose to include all group sample members, regardless of N_{mem} , in my analysis.

Table 5.2: $L_X-\sigma$ Relation Bayesian Best Fits with Groups Subdivided at $N_{mem} = 10$

	m		c		s	
	$N_{mem} \geq 10$	$N_{mem} < 10$	$N_{mem} \geq 10$	$N_{mem} < 10$	$N_{mem} \geq 10$	$N_{mem} < 10$
X-ray Q=1	1Mpc	2.7432 ± 0.4646	...	35.410 ± 1.1414	...	0.1970 ± 0.1726
	$r_{200,\sigma}$	2.6415 ± 3.1382	1.3271 ± 2.6441	35.715 ± 5.0870	39.005 ± 4.1871	0.9425 ± 3.2969
	$r_{200,X}$	2.7481 ± 1.2929	1.0101 ± 2.3692	35.446 ± 2.5106	39.823 ± 4.0695	0.4255 ± 0.6163
X-ray Q=1 & 2	1Mpc	1.8992 ± 0.5452	0.4102 ± 0.4228	37.382 ± 1.4192	41.365 ± 1.0160	0.3753 ± 0.0981
	$r_{200,\sigma}$	0.6790 ± 0.6856	1.3627 ± 2.8705	40.551 ± 1.7749	38.960 ± 12.436	0.5935 ± 0.1781
	$r_{200,X}$	1.6872 ± 0.9013	0.7869 ± 1.0804	37.982 ± 2.2048	40.305 ± 2.5923	0.5120 ± 0.1885
Optical	1Mpc	1.3423 ± 1.6965	1.6129 ± 1.5271	38.801 ± 4.6197	37.955 ± 2.9675	0.7150 ± 0.7264
	$r_{200,\sigma}$	1.1933 ± 1.4007	1.1905 ± 3.6719	39.256 ± 3.8189	38.973 ± 7.0081	0.6992 ± 0.7714
	$r_{200,X}$	1.6430 ± 1.1719	1.2470 ± 1.7510	38.067 ± 3.0628	38.922 ± 4.3277	0.5334 ± 0.5298

Column description: Bayesian best fit slope (m) and uncertainties (columns 1 & 2); intercept (c) and uncertainties (3 & 4); and intrinsic scatter (s) and uncertainties (5 & 6) of the relation $\log(L_X) = m \times \log(\sigma) + c + \epsilon$, where ϵ is a random variable with variance equal to s^2 . The first column of each quantity is for groups with at least ten members while the second only includes those with less than this amount. Note that in the case of the quality 1 X-ray groups with a 1 Mpc radial cut, there is an insufficient number of groups with less than ten members to perform robust fitting.

Chapter 6

Group Masses

6.1 NIR Photometry and Stellar Mass

6.1.1 NIR Observations

Details of the near infrared K_s observations of the CNOC2 fields from SOFI on the New Technology Telescope (NTT) and Ingrid on the William Herschel Telescope (WHT) can be found in Balogh et al. (2009). These observations however did not cover much of the area with X-ray coverage (in particular much of the RA21hr field) and so we have also obtained data with the WIRCam (Wide-field InfraRed Camera) on the Canadian France Hawaii Telescope (CFHT). This data is described by McGee et al. (2011) but a brief description follows here. Four pointings were made for each of the two fields with each pointing having 33 minutes of exposure time. Each pointing was dithered in a five point pattern to fill in the chip gaps and divided into 80 exposures of 25 seconds each. The resulting coverage area is $30' \times 30'$ per field. These data were subsequently reduced and processed by the Terapix pipeline.

6.1.2 Galaxy Stellar Masses

Stellar masses for our galaxies were computed by template-fitting their spectral energy distributions (SEDs), using available photometry, by a collaborator, Dr. Sean McGee. Details can be found in McGee et al. (2011) but a summary of this stellar mass derivation follows. The observed photometry, typically including K, i, r, g, u, GALEX NUV and FUV, was compared to a large grid of model SEDs constructed using the Bruzual & Charlot (2003) stellar population synthesis code and assuming a Chabrier initial mass function (Chabrier, 2003). This grid of models uniformly samples the allowed parameters of formation time, galaxy metallicity, and the dual component Charlot & Fall (2000) dust model and, as in Salim et al. (2007), the star formation history of a galaxy is assumed to be represented by an exponential model augmented with starbursts. Model magnitudes at nine redshift bins between 0.25 and 0.6 were derived by convolving these model SEDs with the observed photometric bandpasses. χ^2 is minimized while summing over all the models at the redshift of the galaxy and taking the observed uncertainty on each point

into account. Comparison to other estimates of stellar mass shows 1σ uncertainties of the order 0.15 dex.

6.2 Group Mass Estimates

Table 6.1 includes all three mass estimates (X-ray, dynamical, and stellar) for our X-ray selected systems, listing the group identification number for the X-ray system (column 1); rest-frame luminosity in the 0.1–2.4 keV band (2); estimates of a total mass, using X-ray luminosity as a mass proxy and a calibration of Leauthaud et al. (2010) (3); group stellar mass calculated using 1 Mpc, $r_{200,\sigma}$, and $r_{200,X}$ radial cuts (4, 5, & 6); and the dynamical (virial) mass for 1 Mpc, $r_{200,\sigma}$, and $r_{200,X}$ radial cuts (7, 8, & 9). Table 6.2 lists similar quantities for optically selected systems. In cases where there is no significant X-ray detection, I use the upper limit on $r_{200,X}$ in the mass estimates. Stellar masses are then less than or equal to the derived measurement. Dynamical masses however may be accurate but could also be under or overestimates as smaller radii could act to increase or decrease σ in this case.

6.2.1 Group Dynamical Mass

I estimate dynamical masses, $M_{dynamical}$ or M_{dyn} , for all groups from the velocity dispersion and radius as in Balogh et al. (2006) and Carlberg et al. (1999):

$$M_{dyn} = 3\sigma^2 r_{200}/G. \quad (6.1)$$

Note that the factor of three in this equation reflects the assumption of isotropic orbits and an isothermal potential, but is only weakly dependent on those assumptions (Łokas & Mamon, 2001). I calculate dynamical masses for groups having a minimum of three members. In cases where the velocity dispersion is an upper limit, dynamical masses are also treated as upper limits. When calculating errors in dynamical mass, no estimation of error in r_{200} is included. Large errors in velocity dispersion, which may result from the assumption of symmetric errors made via the Jackknife technique, can result in dynamical mass errors larger than the measure itself.

6.2.2 Group X-ray Mass

X-ray masses are estimated using the relation covering the same mass and redshift range of groups from Leauthaud et al. (2010). Standard evolution of the scaling relations, $M_{200}E_z = f(L_X E_z^{-1})$ where $E_z = (\Omega_M(1+z)^3 + \Omega_\Lambda)^{1/2}$, is assumed and these relations verified using a weak lensing calibration of X-ray groups in the COSMOS survey (Leauthaud et al., 2010). In order to use this calibration, a ‘concordance’ cosmology with $H_0 = 72 \text{ km s}^{-1} \text{ Mpc}^{-1}$, $\Omega_M = 0.25$, and $\Omega_\Lambda = 0.75$ is applied. X-ray mass limits quoted for X-ray and optically selected groups with low (<1 and <2 respectively) X-ray significance are 2σ upper limits.

6.2.3 Group Stellar Mass

In order to derive accurate total stellar masses for our groups, I must correct for incompleteness. The first major contribution to this incompleteness is the lack of spectra for *all* objects in our fields. To correct for this, I compute the fraction of objects with redshifts for each group within its radial cut as a function of R-band (used for spectroscopic selection) magnitude $f_z(R)$. I apply a small correction to this fraction to account for the fact that a small percentage of these objects are likely to be stars. This minor correction is itself a function of the R-band magnitude and star/galaxy classification. I then calculate the fraction of members, again as a function of R-band magnitude, by computing the number of known members and dividing this total by the fraction of galaxies having redshifts $f_{mem}(R) = N_{mem}(R)/N_z(R)$. Finally, the galaxy masses are weighted to correct for this incompleteness as a function of R-band magnitude: $\text{weight}_{mem}(R, M_{stellar}) = 1 + (1 - f_z(R))/f_z(R) \times f_{mem}(R)$.

The second major source of incompleteness results from the magnitude limit of our spectroscopy. I begin by recalling our overall R-band magnitude limit of 22. This limit means that low mass, faint galaxies will be missed. The mass at fixed magnitude is a function of mass-to-light (M/L) ratio. Therefore, in order to calculate the appropriate stellar mass limit for each group, I find the mass of a high M/L galaxy at the R=22 magnitude limit as a function of redshift. Fig. 6.1 shows the limit in stellar mass as a function of redshift. By examining the distribution of rest-frame U–R color as a function of redshift, I define a line separating the blue and red galaxy populations and categorize all galaxies with $U-R > (0.2 \times z) - 1.5$ as red and the rest as blue. In a given redshift bin, I calculate the mass each galaxy would have if it were observed at the magnitude limit of R=22 and with its own mass-to-light ratio in that band: $M_{stellar,R=22}(z) = M_{stellar}(z) \times 10^{-0.4(22.-R(z))}$. Finally, I compute the 90th percentile value of these mass estimates for the red galaxies in each redshift bin (these are the black diamonds in Fig. 6.1) and perform a simple linear fit to these values to define $M_{stellar_lim}(z)$, up to a maximum $z=0.6$ above which this completeness limit becomes unusefully high. This fit is comparable to what one would obtain from assuming a mass-to-light ratio of 12. Finally, I calculate a mass cutoff for each group, $M_{cut,group} = M_{stellar_lim}(z)$ using its redshift.

In order to extrapolate the mass below the limit at which we are complete, I first take the lowest redshift groups and fit a Schechter function. Using the parameters from this local Schechter function fit, I then extrapolate the stellar mass of each group below $M_{cut,group}$ down to a constant cutoff $M_{cut} = 10^{10} M_\odot$. I find that the parameters for a system with $\log(M_{halo}) = 13.64$ from Yang et al. (2009), with $\alpha = -1.22$ and $\log(M_*) = 11.122$, provide a reasonable fit for our local groups – these parameters are then used for the extrapolation. The final, corrected total group stellar mass is then summed down to our constant mass limit of $10^{10} M_\odot$. For groups at redshifts $z > 0.6$, Schechter function based extrapolation is not used and instead the total measured stellar mass of known members is considered a lower limit. Note that I calculate stellar masses only for groups with three or more members.

To calculate errors on the stellar mass determinations for our groups I account for the sampling error by bootstrapping the membership allocation above the mass limit at the group redshift, allowing the galaxies to be selected more than once. I also resample the fraction of galaxies with known redshifts which are members $f_{mem}(R)$ selecting from a binomial distribution. In cases

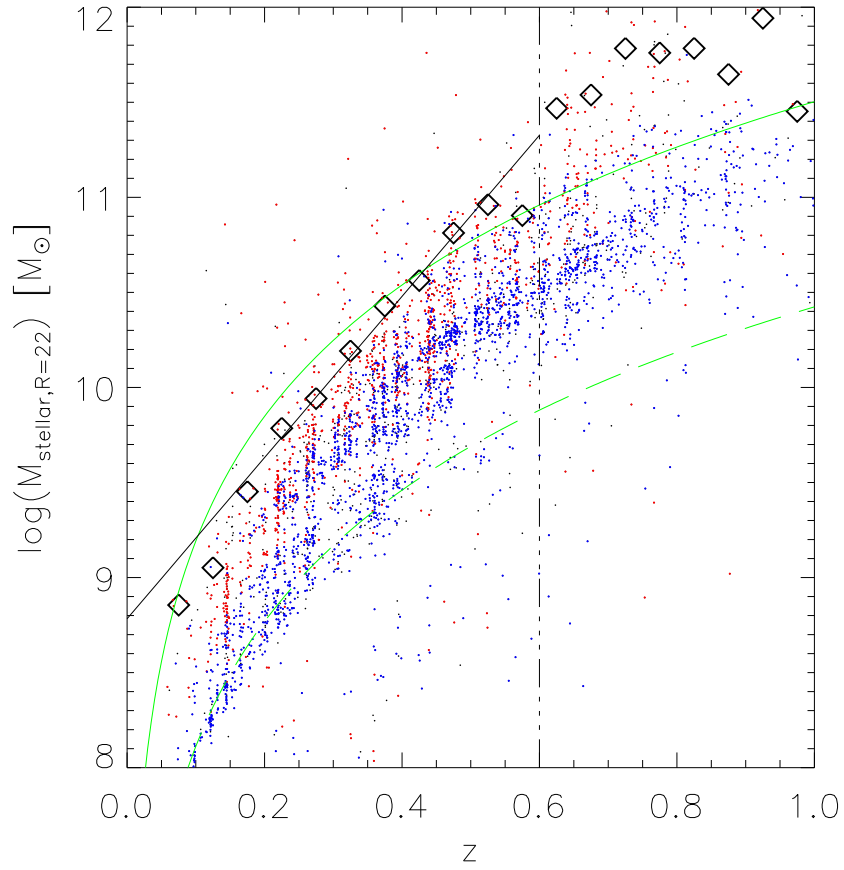


Figure 6.1: Stellar mass limit as a function of redshift. Red and blue dots, respectively, indicate red and blue galaxies, based on rest-frame U–R colors. Open black diamonds indicate the 90th percentile value of the mass estimates for a red galaxy with $R=22$, and the black solid line is a simple fit to these points for $z<0.6$. The vertical dot-dash line indicates $z=0.6$; no further extrapolation to lower mass is performed at $z>0.6$. Green solid and dashed lines represent a M/L ratio of 12 and 1 respectively.

where $f_{mem} = 0$ or 1 , I choose to binomially resample the fraction of members presuming that the true fraction is different from these extreme values by 0.5 times the resolution ($\langle f_{mem} \rangle = 0.5/N_z(R)$ or $1 - 0.5/N_z(R)$). For groups with $z < 0.6$ where $M_{cut,group} > 10^{10} M_\odot$, the extrapolation to lower mass (below the group mass limit) introduces additional uncertainty via the choice of the Schechter function parameters. To quantify this, I resample the correction randomly using the Schechter function parameters selected from the best fits to different halo mass bins in the range $13.05 < \log(M_{halo}) < 14.58$ from Yang et al. (2009, Tab. 4). To quantify the systematic errors associated with the individual galaxy stellar mass measurements, I calculate the group stellar masses using the 2.5 and 97.5 percentile masses from the probability distribution of SED fits to our galaxies and find total group stellar masses an average of 0.5 and 2.0 times those found using the median galaxy masses respectively regardless of the total group stellar mass.

Table 6.1: Masses of X-ray Selected Groups

XID	L_X 10^{42} ergs s $^{-1}$	M_X $10^{13} M_\odot$	$M_{stellar}(1\text{Mpc})$ $10^{11} M_\odot$	$M_{stellar}(r_{200},\sigma)$ $10^{11} M_\odot$	$M_{stellar}(r_{200,X})$ $10^{11} M_\odot$	$M_{dyn}(1\text{Mpc})$ $10^{13} M_\odot$	$M_{dyn}(r_{200},\sigma)$ $10^{13} M_\odot$	$M_{dyn}(r_{200,X})$ $10^{13} M_\odot$
XR14h02	0.62 \pm 0.22	1.38 \pm 0.29	1.04 $\pm^{0.48}_{0.55}$	0.87 $\pm^{0.49}_{0.49}$	0.89 $\pm^{0.48}_{0.49}$	3.170 \pm 1.001	0.700 \pm 0.492	0.869 \pm 0.612
XR14h09	34.6 \pm 3.55	11.8 \pm 0.76	> 21.5	> 30.6	> 20.3	50.50 \pm 13.36	54.09 \pm 12.25	35.38 \pm 12.28
XR14h10	6.55 \pm 2.64	3.74 \pm 0.90	> 4.69	> 4.76	> 3.31	14.68 \pm 11.80	10.32 \pm 8.297	8.135 \pm 10.37
XR21h08	2.54 \pm 0.32	3.07 \pm 0.24	2.87 $\pm^{0.71}_{0.78}$	2.27 $\pm^{0.56}_{0.60}$	2.54 $\pm^{0.54}_{0.63}$	4.815 \pm 1.415	2.286 \pm 0.992	3.078 \pm 1.017
XR21h10	1.12 \pm 0.34	1.72 \pm 0.32	6.23 $\pm^{3.46}_{3.73}$	4.14 $\pm^{2.87}_{2.88}$	4.14 $\pm^{2.88}_{2.88}$	4.052 \pm 1.205	0.602 \pm 1.395	0.846 \pm 1.963
XR21h11	2.98 \pm 0.66	2.85 \pm 0.39	11.2 $\pm^{2.52}_{2.97}$	10.1 $\pm^{2.01}_{2.47}$	9.51 $\pm^{1.83}_{2.00}$	9.766 \pm 3.945	8.949 \pm 3.737	6.474 \pm 2.641
XR21h12	0.59 \pm 0.18	1.24 \pm 0.23	5.31 $\pm^{0.84}_{0.89}$	1.06 $\pm^{0.20}_{0.21}$	1.08 $\pm^{0.20}_{0.19}$	4.570 \pm 1.144	2.705 \pm 1.601	2.071 \pm 1.226
XR21h14	26.1 \pm 0.99	11.8 \pm 0.28	12.2 $\pm^{1.80}_{1.93}$	21.2 $\pm^{3.16}_{3.61}$	8.20 $\pm^{1.74}_{1.97}$	39.24 \pm 7.647	40.77 \pm 7.241	28.41 \pm 6.542
XR21h15	6.77 \pm 2.52	3.84 \pm 0.86	> 11.5	> 12.9	> 14.5	10.21 \pm 15.46	6.008 \pm 9.090	5.154 \pm 7.797
XR21h60	1.44 \pm 0.34	2.05 \pm 0.30	2.48 $\pm^{1.97}_{1.99}$...	2.51 $\pm^{1.91}_{1.91}$	< 1.708	...	0.385 \pm 0.929
XR21h64	1.99 \pm 0.38	2.65 \pm 0.31	1.67 $\pm^{0.60}_{0.74}$	1.47 $\pm^{0.46}_{0.38}$	1.44 $\pm^{0.44}_{0.40}$	2.243 \pm 1.319	1.847 \pm 4.482	2.061 \pm 5.003
XR21h09	1.33 \pm 0.17	2.10 \pm 0.17	6.83 $\pm^{1.18}_{1.62}$	2.62 $\pm^{1.01}_{1.23}$	3.17 $\pm^{1.05}_{1.13}$	4.574 \pm 1.306	0.649 \pm 0.267	1.588 \pm 0.623
XR14h03	11.2 \pm 3.17	5.04 \pm 0.87	> 9.30	> 9.34	> 7.00	51.58 \pm 25.65	48.67 \pm 26.94	30.53 \pm 39.05
XR14h08	6.95 \pm 1.64	4.77 \pm 0.69	1.68 $\pm^{0.27}_{0.43}$...	1.87 $\pm^{0.34}_{0.39}$	0.759 \pm 1.843	< 0.133	0.399 \pm 1.083
XR14h18	3.04 \pm 1.01	3.15 \pm 0.63	3.51 $\pm^{0.90}_{1.10}$	1.82 $\pm^{0.58}_{0.56}$	3.02 $\pm^{0.83}_{0.81}$	1.597 \pm 1.542	0.266 \pm 0.608	1.154 \pm 1.006
XR14h22	0.60 \pm 0.28	1.22 \pm 0.34	4.41 $\pm^{1.13}_{1.39}$	2.39 $\pm^{1.20}_{1.21}$	2.28 $\pm^{0.98}_{1.02}$	10.19 \pm 2.290	3.529 \pm 1.854	1.554 \pm 1.029
XR14h25	1.30 \pm 0.36	1.99 \pm 0.34	4.50 $\pm^{0.83}_{0.84}$	1.99 $\pm^{0.35}_{0.43}$	1.79 $\pm^{0.33}_{0.40}$	4.998 \pm 1.622	2.858 \pm 1.186	2.737 \pm 1.292
XR14h35	6.05 \pm 1.87	3.88 \pm 0.73	> 1.83	> 0.94	> 0.94	21.65 \pm 11.95	13.03 \pm 24.34	8.652 \pm 16.16
XR14h40	5.03 \pm 3.04	3.46 \pm 1.22	> 2.26	> 2.05	> 2.73	< 6.265	< 3.025	< 3.007
XR14h44	3.96 \pm 1.52	3.04 \pm 0.70	> 13.2	> 13.2	> 4.41	25.09 \pm 7.646	24.88 \pm 7.580	5.770 \pm 11.45
XR21h06	1.08 \pm 0.15	1.94 \pm 0.17	7.38 $\pm^{1.63}_{2.31}$	6.13 $\pm^{1.53}_{1.86}$	2.54 $\pm^{0.69}_{0.77}$	12.66 \pm 2.755	12.11 \pm 2.598	3.893 \pm 1.559
XR21h07	7.17 \pm 0.15	6.51 \pm 0.09	6.85 $\pm^{1.74}_{2.33}$...	5.65 $\pm^{1.38}_{1.74}$	13.73 \pm 2.954	...	11.70 \pm 2.439
XR21h13	0.36 \pm 0.24	0.89 \pm 0.34	0.21 $\pm^{0.06}_{0.05}$	0.17 $\pm^{0.05}_{0.05}$	0.17 $\pm^{0.04}_{0.05}$	< 0.697	< 0.142	< 0.259
XR21h18	1.17 \pm 0.44	1.69 \pm 0.38	2.76 $\pm^{1.05}_{1.15}$...	1.92 $\pm^{0.57}_{0.56}$	4.175 \pm 1.816	...	1.440 \pm 0.763
XR21h20	< 0.37	< 0.98	0.41 $\pm^{0.12}_{0.14}$	0.39 $\pm^{0.10}_{0.14}$	$\leq 0.24 \pm^{0.10}_{0.12}$	9.142 \pm 3.535	6.065 \pm 2.826	0.749 \pm 1.085
XR21h23	5.59 \pm 1.45	4.60 \pm 0.73	0.42 $\pm^{0.08}_{0.09}$...	0.40 $\pm^{0.08}_{0.08}$	15.22 \pm 35.19	...	< 0.425
XR21h31	1.03 \pm 0.92	1.46 \pm 0.74	6.25 $\pm^{1.15}_{1.33}$	1.50 $\pm^{1.10}_{0.96}$	3.48 $\pm^{0.92}_{0.85}$	1.135 \pm 0.588	0.161 \pm 0.361	0.124 \pm 0.376
XR21h32	7.51 \pm 1.58	4.10 \pm 0.53	< 1.342	...	< 1.773
XR21h33	1.71 \pm 0.78	2.15 \pm 0.58	1.23 $\pm^{0.29}_{0.35}$	0.39 $\pm^{0.11}_{0.09}$	1.14 $\pm^{0.29}_{0.34}$	2.734 \pm 1.618	1.343 \pm 0.711	1.558 \pm 0.825
XR21h37	1.92 \pm 0.54	2.22 \pm 0.38	9.38 $\pm^{1.59}_{1.61}$	19.0 $\pm^{2.67}_{3.26}$	6.33 $\pm^{1.19}_{1.21}$	52.11 \pm 11.40	94.98 \pm 19.23	27.74 \pm 7.140
XR21h42	0.76 \pm 0.38	1.27 \pm 0.38	1.53 $\pm^{0.50}_{0.51}$	0.82 $\pm^{0.48}_{0.46}$	1.51 $\pm^{0.95}_{0.70}$	0.752 \pm 0.895	0.178 \pm 0.387	0.339 \pm 0.739
XR21h50	4.12 \pm 1.88	3.24 \pm 0.88	3.25 $\pm^{0.22}_{0.61}$...	3.20 $\pm^{0.44}_{0.74}$	15.41 \pm 12.64	...	1.440 \pm 3.186
XR21h55	1.00 \pm 0.20	1.70 \pm 0.21	1.61 $\pm^{0.39}_{0.47}$	1.34 $\pm^{0.37}_{0.43}$	0.97 $\pm^{0.37}_{0.44}$	8.056 \pm 3.856	5.543 \pm 3.299	4.947 \pm 3.716
XR14h11	2.38 \pm 0.68	2.48 \pm 0.43	18.1 $\pm^{3.17}_{3.07}$	4.69 $\pm^{0.92}_{0.91}$	4.55 $\pm^{0.99}_{0.99}$	7.641 \pm 2.544	1.350 \pm 0.863	1.644 \pm 1.050
XR14h12	0.84 \pm 0.20	1.64 \pm 0.23	0.87 $\pm^{0.32}_{0.42}$	0.50 $\pm^{0.26}_{0.27}$	0.52 $\pm^{0.25}_{0.29}$	2.565 \pm 2.375	0.754 \pm 1.651	1.283 \pm 1.704
XR14h19	11.6 \pm 1.71	5.92 \pm 0.54
XR14h29	3.58 \pm 0.80	3.53 \pm 0.48	8.05 $\pm^{3.16}_{3.53}$	7.28 $\pm^{3.21}_{3.61}$	2.13 $\pm^{0.53}_{0.62}$	12.79 \pm 4.102	10.01 \pm 3.505	9.698 \pm 4.409
XR14h33	< 19.2	< 6.98	> 0.85	> 0.85	≈ 0.85	8.839 \pm 15.82	4.610 \pm 8.251	5.252 \pm 9.400
XR21h27	0.90 \pm 0.18	1.69 \pm 0.21	...	2.13 $\pm^{0.53}_{0.53}$...	100.3 \pm 47.22	798.4 \pm 131.1	16.23 \pm 10.23
XR14h01	7.73 \pm 1.06	5.72 \pm 0.49	19.7 $\pm^{7.79}_{9.12}$...	52.6 $\pm^{23.8}_{23.2}$	< 0.836	...	< 1.003
XR14h05	8.36 \pm 2.85	4.18 \pm 0.86	23.04 \pm 28.81	19.71 \pm 24.64	...
XR14h07	9.89 \pm 2.95	5.75 \pm 1.04
XR14h13	4.78 \pm 1.61	3.59 \pm 0.73
XR14h23	60.1 \pm 4.75	14.2 \pm 0.71	27.87 \pm 7.123	25.57 \pm 6.534	20.94 \pm 5.352
XR14h24	19.7 \pm 5.00	5.93 \pm 0.92
XR14h26	9.97 \pm 4.82	4.71 \pm 1.35	> 2.78	...	> 0.59	2.953 \pm 2.703	...	0.624 \pm 1.568
XR14h37	< 5.19	< 3.79	20.4 $\pm^{4.78}_{8.40}$...	$\leq 5.84 \pm^{1.43}_{2.34}$	14.85 \pm 10.91	...	3.268 \pm 7.797
XR14h38	< 2.71	< 3.12
XR14h39	0.80 \pm 0.73	1.47 \pm 0.75
XR14h41	7.33 \pm 2.90	3.49 \pm 0.83
XR14h47	2.94 \pm 0.84	3.00 \pm 0.52
XR21h16	1.05 \pm 0.50	1.57 \pm 0.45	3.64 $\pm^{0.89}_{0.88}$	6.751 \pm 3.277
XR21h17	3.44 \pm 3.01	2.38 \pm 1.17	> 17.6	...	> 15.2	3.646 \pm 5.069	...	0.163 \pm 0.711
XR21h19	< 2.94	< 2.61	3.15 $\pm^{0.21}_{0.53}$...	$\leq 3.15 \pm^{0.21}_{0.94}$	7.592 \pm 10.20	...	3.579 \pm 4.812
XR21h21	4.95 \pm 0.96	4.07 \pm 0.49	11.4 $\pm^{2.16}_{2.68}$	6.25 $\pm^{2.17}_{2.42}$	7.17 $\pm^{2.19}_{2.43}$	6.664 \pm 2.145	2.390 \pm 0.731	3.482 \pm 1.150
XR21h30	< 0.73	< 1.24	0.88 $\pm^{0.14}_{0.17}$	0.95 $\pm^{0.20}_{0.20}$...	10.29 \pm 14.80	7.421 \pm 10.67	...
XR21h40	7.22 \pm 2.09	4.29 \pm 0.75
XR21h41	< 11.3	< 4.72
XR21h43	1.81 \pm 1.23	1.85 \pm 0.73	> 1.92	> 2.13	> 2.13	5.349 \pm 6.855	2.457 \pm 3.148	1.233 \pm 2.988
XR21h48	< 0.58	< 1.20	0.39 $\pm^{0.11}_{0.13}$	1.772 \pm 2.669

XID	L_X	M_X	$M_{stellar}(1\text{Mpc})$	$M_{stellar}(r_{200},\sigma)$	$M_{stellar}(r_{200,X})$	$M_{dyn}(1\text{Mpc})$	$M_{dyn}(r_{200},\sigma)$	$M_{dyn}(r_{200,X})$
XR21h49	0.84 ± 0.57	1.35 ± 0.53	$6.58 \pm^{1.54}_{1.92}$	$11.7 \pm^{1.78}_{1.88}$...	38.73 ± 14.68	85.07 ± 19.50	...
XR21h59	3.10 ± 0.72	3.01 ± 0.43	$4.74 \pm^{0.80}_{0.85}$	$6.49 \pm^{1.05}_{1.08}$	$2.42 \pm^{0.02}_{0.32}$	33.15 ± 13.15	48.68 ± 18.00	23.26 ± 21.52
XR21h69	13.5 ± 2.95	6.31 ± 0.85	> 2.52	> 4.32	...	63.25 ± 66.19	95.97 ± 31.57	...
XR14h04	1.50 ± 0.31	2.28 ± 0.29	$0.46 \pm^{0.14}_{0.16}$	$0.34 \pm^{0.14}_{0.12}$	$0.34 \pm^{0.14}_{0.12}$	1.704 ± 1.072	0.232 ± 0.524	0.492 ± 1.113
XR14h14	12.4 ± 2.39	5.74 ± 0.68	> 6.70	> 7.18	> 2.61	63.16 ± 47.81	76.99 ± 54.54	23.49 ± 17.36
XR21h22	8.47 ± 4.48	4.33 ± 1.35
XR21h67	9.11 ± 1.65	5.97 ± 0.67	$33.9 \pm^{28.5}_{28.5}$...	$32.8 \pm^{27.5}_{27.7}$	0.451 ± 0.773	...	0.284 ± 0.333

*Column description: group identification number for the X-ray system (column 1); rest-frame luminosity in the 0.1–2.4 keV band (2); estimates of a total mass, using X-ray luminosity as a mass proxy and a calibration of Leauthaud et al. (2010) (3); group stellar mass calculated using 1 Mpc, $r_{200,\sigma}$, and $r_{200,X}$ radial cuts (4, 5, & 6); and the dynamical (virial) mass for 1 Mpc, $r_{200,\sigma}$, and $r_{200,X}$ radial cuts (7, 8, & 9).

Table 6.2: Masses of Optically Selected Groups

OID	L_X 10^{42} ergs s $^{-1}$	M_X $10^{13} M_\odot$	$M_{stellar}(1\text{Mpc})$ $10^{11} M_\odot$	$M_{stellar}(r_{200,\sigma})$ $10^{11} M_\odot$	$M_{stellar}(r_{200,X})$ $10^{11} M_\odot$	$M_{dyn}(1\text{Mpc})$ $10^{13} M_\odot$	$M_{dyn}(r_{200,\sigma})$ $10^{13} M_\odot$	$M_{dyn}(r_{200,X})$ $10^{13} M_\odot$
OP14h01	0.62±0.18	1.34±0.23	0.87 $\pm^{0.33}_{0.41}$	0.52 $\pm^{0.28}_{0.28}$	0.53 $\pm^{0.27}_{0.30}$	2.565±2.375	1.153±1.530	0.928±1.200
OP14h08	< 0.46	< 1.05	0.77 $\pm^{0.19}_{0.21}$	0.46 $\pm^{0.12}_{0.13}$	$\leq 0.57 \pm^{0.10}_{0.10}$	1.781±2.253	1.230±2.007	1.159±1.891
OP14h09	< 0.40	< 0.95	1.32 $\pm^{0.46}_{0.49}$	1.37 $\pm^{0.38}_{0.45}$	$\leq 1.35 \pm^{0.39}_{0.42}$	1.983±1.304	1.154±0.641	1.073±0.596
OP14h10	< 0.42	< 0.96	3.74 $\pm^{1.08}_{1.19}$	2.90 $\pm^{1.03}_{1.16}$	$\leq 2.33 \pm^{1.15}_{1.06}$	9.425±2.824	3.540±1.652	1.142±0.800
OP14h11	< 0.44	< 0.99	2.80 $\pm^{0.41}_{0.50}$	2.24 $\pm^{0.35}_{0.41}$	$\leq 1.71 \pm^{1.71}_{0.42}$	4.509±1.503	2.453±0.952	2.011±1.012
OP14h15	< 0.67	< 1.27	3.64 $\pm^{1.49}_{1.71}$	1.40 $\pm^{0.35}_{0.34}$	$\leq 1.26 \pm^{0.36}_{0.45}$	0.859±1.377	0.084±0.219	0.352±0.565
OP14h16	< 1.50	< 2.12	1.67 $\pm^{0.59}_{0.75}$	1.44 $\pm^{0.73}_{0.64}$	$\leq 1.41 \pm^{0.72}_{0.77}$	3.367±2.261	0.975±1.605	1.250±2.059
OP14h19	< 1.04	< 1.65	4.20 $\pm^{1.11}_{1.13}$	3.15 $\pm^{0.51}_{0.51}$	$\leq 2.67 \pm^{0.64}_{0.62}$	2.124±1.689	0.517±1.213	0.756±1.774
OP14h24	< 0.90	< 1.46	5.04 $\pm^{1.18}_{0.98}$...	$\leq 3.69 \pm^{0.91}_{1.05}$	0.430±0.451	...	0.225±0.223
OP14h25	< 19.2	< 10.3	9.55 $\pm^{3.02}_{3.79}$	9.52 $\pm^{2.97}_{4.03}$	$\leq 8.83 \pm^{8.83}_{3.35}$	17.54±5.457	16.83±5.235	11.30±4.031
OP14h27	< 1.57	< 2.06	0.82 $\pm^{0.20}_{0.18}$	0.62 $\pm^{0.13}_{0.13}$	$\leq 0.67 \pm^{0.10}_{0.07}$	1.160±2.693	< 1.001	< 1.235
OP14h28	< 1.17	< 1.71	3.53 $\pm^{0.99}_{1.12}$	1.33 $\pm^{0.35}_{0.41}$	$\leq 2.55 \pm^{0.64}_{0.63}$	2.536±1.672	0.266±0.608	0.943±0.822
OP14h29	< 1.04	< 1.59	8.79 $\pm^{6.01}_{6.76}$	1.63 $\pm^{0.38}_{0.45}$	$\leq 1.08 \pm^{0.28}_{0.33}$	6.160±5.715	8.313±8.600	6.175±8.529
OP14h30	< 1.24	< 1.75	13.0 $\pm^{2.72}_{2.98}$	11.7 $\pm^{2.54}_{3.16}$	$\leq 11.7 \pm^{2.59}_{2.69}$	4.763±2.930	2.133±3.747	1.978±3.476
OP14h31	1.48±0.70	1.95±0.55	2.07 $\pm^{0.89}_{0.98}$	1.63 $\pm^{0.85}_{0.87}$	$1.56 \pm^{0.80}_{0.81}$	6.456±8.968	9.373±11.38	5.517±6.699
OP14h32	< 0.96	< 1.49	2.16 $\pm^{0.53}_{0.56}$	2.77 $\pm^{0.50}_{0.63}$	$\leq 1.40 \pm^{0.42}_{0.42}$	57.79±25.69	40.45±18	19.71±5.216
OP14h34	< 24.5	< 11.0	7.46 $\pm^{2.38}_{2.57}$	6.50 $\pm^{2.22}_{2.73}$	$\leq 7.36 \pm^{2.27}_{2.53}$	1.359±0.620	0.342±0.836	1.081±0.493
OP14h37	< 1.27	< 1.65	17.2 $\pm^{3.22}_{3.56}$	14.3 $\pm^{2.25}_{2.70}$	$\leq 13.2 \pm^{13.2}_{2.30}$	7.527±2.118	4.450±1.753	5.027±2.386
OP14h36	< 1.70	< 2.00	10.2 $\pm^{2.53}_{2.53}$	11.3 $\pm^{1.60}_{1.60}$	$\leq 11.3 \pm^{1.57}_{1.56}$	2.336±5.161	1.461±3.192	1.049±2.317
OP14h38	1.98±0.76	2.13±0.49	21.1 $\pm^{4.09}_{5.39}$	36.7 $\pm^{13.4}_{13.1}$	$15.6 \pm^{3.66}_{4.39}$	37.93±5.949	51.85±7.179	14.26±6.028
OP14h40	< 1.48	< 1.72	2.71 $\pm^{0.40}_{0.82}$	3.78 $\pm^{0.93}_{1.39}$	$\leq 3.63 \pm^{0.79}_{1.42}$	3.185±6.243	1.171±2.296	1.318±2.584
OP21h101	0.18±0.08	0.64±0.17	0.32 $\pm^{0.13}_{0.12}$...	$0.23 \pm^{0.07}_{0.07}$	1.712±1.527	...	0.306±0.893
OP21h102	0.29±0.10	0.84±0.18	1.15 $\pm^{0.42}_{0.49}$	0.95 $\pm^{0.37}_{0.37}$	$0.96 \pm^{0.96}_{0.44}$	1.548±0.789	0.237±0.251	0.362±0.308
OP21h104	3.36±0.16	4.01±0.12	6.81 $\pm^{1.62}_{2.08}$	6.86 $\pm^{1.68}_{2.16}$	$5.7 \pm^{5.7}_{2.07}$	13.73±2.914	13.11±2.822	10.48±2.299
OP21h111	< 3.32	< 3.88	1.04 $\pm^{0.28}_{0.28}$	0.80 $\pm^{0.25}_{0.28}$	$\leq 0.60 \pm^{0.24}_{0.30}$	9.646±6.011	7.589±4.729	11.08±8.430
OP21h113	1.23±0.37	2.03±0.37	0.54 $\pm^{0.49}_{0.48}$	0.54 $\pm^{0.48}_{0.50}$...	39.09±58.35	17.61±13.72	...
OP21h117	0.49±0.15	1.10±0.21	7.27 $\pm^{1.36}_{1.63}$	2.96 $\pm^{1.03}_{1.18}$	$2.96 \pm^{2.96}_{1.27}$	4.692±1.122	0.649±0.267	0.767±0.316
OP21h119	< 0.41	< 0.98	0.89 $\pm^{0.11}_{0.13}$	0.87 $\pm^{0.11}_{0.11}$	$\leq 0.87 \pm^{0.11}_{0.11}$	1.054±2.519	0.697±1.146	0.773±1.271
OP21h120	< 1.15	< 1.88	1.18 $\pm^{0.43}_{0.50}$	1.26 $\pm^{0.32}_{0.35}$	$\leq 1.23 \pm^{0.29}_{0.38}$	3.146±2.295	0.638±0.391	0.905±0.555
OP21h123	< 0.40	< 0.94	4.92 $\pm^{0.92}_{1.06}$	3.04 $\pm^{0.47}_{0.47}$	$\leq 3.57 \pm^{0.47}_{0.47}$	2.642±1.174	0.654±0.738	0.732±0.827
OP21h129	< 0.45	< 0.98	1.23 $\pm^{0.25}_{0.30}$	2.08 $\pm^{0.46}_{0.66}$	$\leq 1.97 \pm^{0.44}_{0.55}$	3.008±2.482	1.225±1.011	1.126±0.929
OP21h132	2.60±0.34	2.88±0.23	1.55 $\pm^{0.81}_{0.87}$	1.32 $\pm^{0.86}_{0.89}$	$1.20 \pm^{0.89}_{0.89}$	11.92±3.017	9.387±5.761	8.900±0.610
OP21h133	< 0.59	< 1.10	1.60 $\pm^{0.35}_{0.37}$	1.49 $\pm^{0.34}_{0.35}$	$\leq 1.49 \pm^{0.36}_{0.35}$	2.919±1.133	1.476±3.667	1.327±3.299
OP21h134	< 0.46	< 0.93	4.93 $\pm^{0.86}_{0.83}$	4.21 $\pm^{0.74}_{0.78}$	$\leq 2.80 \pm^{0.65}_{0.67}$	7.005±2.971	5.309±2.274	3.712±1.959
OP21h137	1.19±0.58	1.65±0.48	5.84 $\pm^{1.40}_{1.74}$	4.66 $\pm^{1.31}_{1.55}$	$4.65 \pm^{1.32}_{1.42}$	9.771±4.325	6.439±4.481	2.728±2.321
OP21h138	13.4±1.00	7.72±0.36	10.8 $\pm^{1.67}_{2.14}$	21.2 $\pm^{2.79}_{3.63}$	$7.19 \pm^{1.71}_{1.90}$	36.63±6.905	40.98±7.105	24.20±6.053
OP21h139	3.09±1.37	3.01±0.79	9.40 $\pm^{2.29}_{2.75}$	7.43 $\pm^{1.98}_{2.10}$	$8.32 \pm^{1.91}_{2.28}$	3.923±1.242	1.843±0.756	2.701±1.083
OP21h140	< 1.12	< 1.54	3.30 $\pm^{0.85}_{1.13}$	2.74 $\pm^{0.58}_{0.64}$	$\leq 3.50 \pm^{0.97}_{1.20}$	0.815±1.241	0.787±1.596	0.597±0.672

*Column description: group identification number for the optical system (column 1); rest-frame luminosity in the 0.1–2.4 keV band (2); estimates of a total mass, using X-ray luminosity as a mass proxy and a calibration of Leauthaud et al. (2010) (3); group stellar mass calculated using 1 Mpc, $r_{200,\sigma}$, and $r_{200,X}$ radial cuts (4, 5, & 6); and the dynamical (virial) mass for 1 Mpc, $r_{200,\sigma}$, and $r_{200,X}$ radial cuts (7, 8, & 9).

6.3 Total Mass Measurements

Fig. 6.2 presents the two ‘total’ mass measures for our samples: the X-ray and dynamical mass measures. In this figure I show an X-ray based r_{200} radial cut but, regardless of the radial cut applied, the disagreement between these measures increases for the average group, and the scatter decreases, with increasing dynamical mass. This is not unexpected, since the range in dynamical mass is much larger than in X-ray mass (recall Fig. 4.16). For σ and 1 Mpc radial cuts, the dynamical mass may be inflated by overestimates of velocity dispersion in systems with dynamical complexity. In general, X-ray masses are preferable, better discerning the virialized core of the system, but, for systems undetected in X-rays, this tracer of halo mass is unavailable. Girardi et al. (1998) find, for an inhomogeneous sample of clusters, good agreement between virial and X-ray masses. I show in Fig. 6.2 their weighted regression lines for comparison. I find our masses are less and less in agreement with decreasing total mass. As mass increases, our relation moves from something like a 1:1 relation, to something like the Girardi relation. Dynamical masses for massive systems might be improved with better dynamical modelling (e.g. ‘caustic masses’, e.g. Andreon, 2010; Serra et al., 2011, etc.), but such estimates are only possible when the number of spectroscopic galaxies in and around the group (cluster) is high.

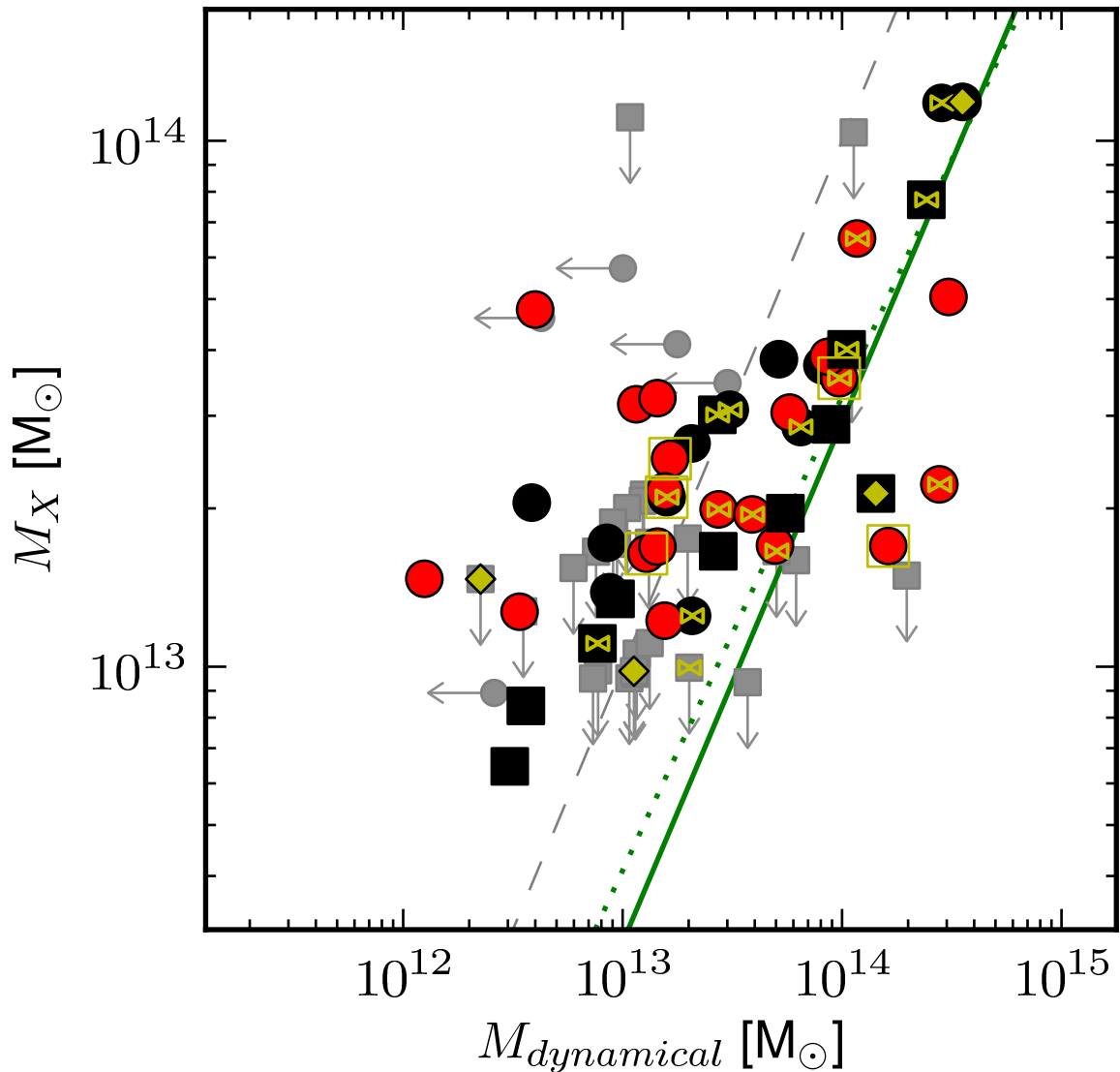


Figure 6.2: M_X - M_{dyn} relation for quality 1 & 2 X-ray (black and red circles respectively) and optical systems (black squares) within $r_{200,X}$. Grey arrows indicate limits. Yellow bow-ties show systems tested for substructure. Filled yellow diamonds indicate systems with substructure according to the AD test. Open yellow squares show groups in X-ray confused regions. A 1:1 line is shown in dashed grey. Girardi et al. (1998) weighted and bisecting regression lines are shown for comparison as green solid and dotted lines respectively.

6.4 Mass in Stars

6.4.1 $M_{stellar}$ - σ Relation

Fig. 6.3 shows the $M_{stellar}$ - σ relations for high quality X-ray and optically selected samples with a σ based radial cut applied. Again, I calculate the slope (m) and intercept (c), scatter (s) and uncertainties, for the optical and high quality X-ray systems [$\log(M_{stellar}) = m \times \log(\sigma) + c + \epsilon$ where ϵ is a random variable with variance equal to the square of the intrinsic scatter (s^2)] for each of the different radial cuts and present these in Tab. 6.3. As before, symmetric errors in stellar mass are produced by averaging the upper and lower errors on the stellar mass.

Fit solutions, including intrinsic scatter, between different subsets of groups (optical, $Q=1$, and $Q=1 \& 2$ X-ray systems) and radial cuts are relatively consistent for this relation. For all but an $r_{200,X}$ radial cut, substructure is found in all systems with $\sigma > 500 \text{ km s}^{-1}$ included on these relations.

Table 6.3: $M_{stellar}$ - σ Relation Bayesian Best Fits

		m	c	s
X-ray Q=1	1Mpc	$1.3531 \pm^{0.7749}_{0.7619}$	$8.3393 \pm^{1.8829}_{1.9215}$	$0.3295 \pm^{0.2397}_{0.1281}$
	$r_{200,\sigma}$	$1.8744 \pm^{0.8147}_{0.9284}$	$6.9124 \pm^{2.2699}_{2.0372}$	$0.3717 \pm^{0.2998}_{0.1803}$
	$r_{200,X}$	$1.2908 \pm^{0.7451}_{0.7473}$	$8.2511 \pm^{1.8616}_{1.8819}$	$0.3186 \pm^{0.2064}_{0.1282}$
X-ray Q=1 & 2	1Mpc	$1.2778 \pm^{0.4205}_{0.4102}$	$8.4293 \pm^{1.0116}_{1.0608}$	$0.3217 \pm^{0.0820}_{0.0653}$
	$r_{200,\sigma}$	$0.8514 \pm^{0.4103}_{0.3859}$	$9.2614 \pm^{0.9884}_{1.0289}$	$0.4349 \pm^{0.0965}_{0.0763}$
	$r_{200,X}$	$1.0376 \pm^{0.3359}_{0.3671}$	$8.8030 \pm^{0.9285}_{0.8493}$	$0.2125 \pm^{0.0641}_{0.0568}$
Optical	1Mpc	$0.8571 \pm^{0.3321}_{0.3373}$	$9.3296 \pm^{0.8372}_{0.8077}$	$0.3847 \pm^{0.0468}_{0.0421}$
	$r_{200,\sigma}$	$1.5866 \pm^{0.4309}_{0.4146}$	$7.4165 \pm^{1.0564}_{1.0726}$	$0.3467 \pm^{0.0609}_{0.0542}$
	$r_{200,X}$	$1.3612 \pm^{0.7977}_{0.8572}$	$8.0124 \pm^{2.1283}_{2.0479}$	$0.5186 \pm^{0.2551}_{0.1697}$

Column description: Bayesian best fit slope (m) and upper and lower errors (column 1); intercept (c) and upper and lower errors (2); and intrinsic scatter (s) and upper and lower errors (3) of the relation $\log(M_{stellar}) = m \times \log(\sigma) + c + \epsilon$, where ϵ is a random variable with variance equal to the square of the intrinsic scatter.

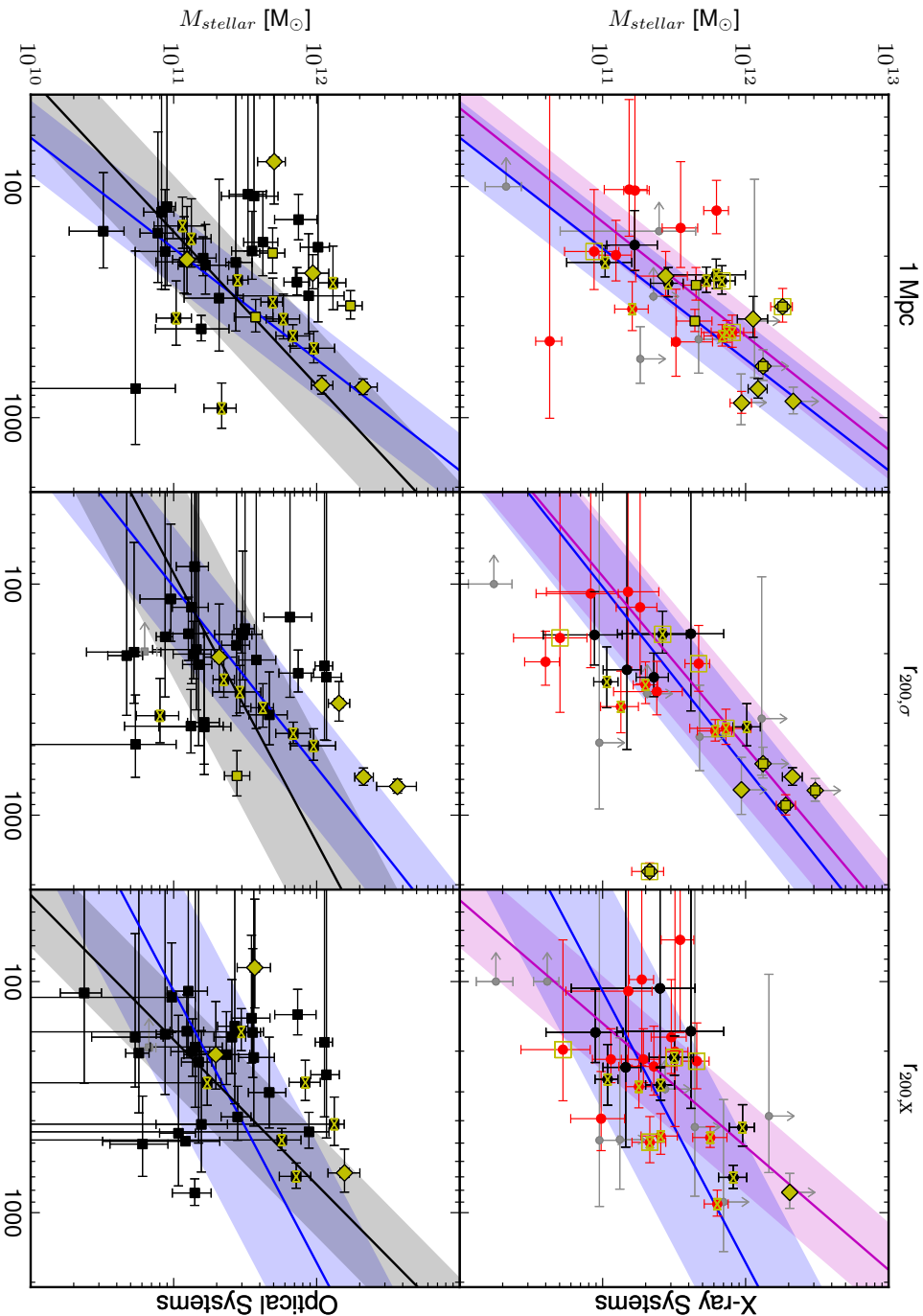


Figure 6.3: $M_{stellar}$ - σ relation for quality 1 & 2 (black and red circles respectively) X-ray selected systems (top) and optical systems (bottom) for all radial cuts. Grey arrows indicate limits. Bayesian best fits for quality 1 (magenta) and quality 1 & 2 (blue) X-ray and optical systems (black) are shown with filled region representing the scatter. Yellow bow-ties show systems tested for substructure. Filled yellow diamonds and squares indicate systems with substructure according to AD and DS Tests respectively. Open yellow squares show groups in X-ray confused regions.

6.4.2 Stellar Versus ‘Total’ Group Mass

The dynamical and group stellar masses are compared in Fig. 6.4. Stellar mass fractions for two different group halo masses from Andreon (2010) are overplotted for comparison. Our best fits are similar to the stellar mass fraction of 0.009 found by Andreon for a $10^{14.9} M_{\odot}$ halo. To derive total stellar masses, Andreon integrates the total luminosity function for all red galaxies in a cluster, assuming that, in the cluster regime, blue galaxies contribute little to the overall luminosity, and assumes a dynamical M/L from Cappellari et al. (2006). Our results are in good agreement with the average 1% stellar to dynamical mass fraction within r_{500} found by Balogh et al. (2011a) for a sample of low-mass nearby clusters.

Fig. 6.5 shows the stellar and X-ray masses of all of our systems. I compare relations found by Yang et al. (2009) for a low redshift sample of groups selected from SDSS, Giordini et al. (2009) for $0.1 \leq z \leq 1$ COSMOS X-ray detected groups, and Balogh et al. (2011a) for nearby clusters and find relatively good agreement. For the latter comparison, I shift the Giordini relation, which was computed for an r_{500} radial cut, assuming a simple conversion of $M_{200,X} \sim M_{500,X}/0.7$ and shifting by 0.25 dex to account for the difference in stellar mass due to the assumed IMFs (see Leauthaud et al., 2012). This shift is essential as assuming a Chabrier IMF (assumed in this work and by) instead of a Salpeter IMF (assumed by Giordini et al.) increases the M/L by $\sim 30\%$ (Longhetti & Saracco, 2009) and thus means an additional 30% in the stellar mass associated with galaxies. I shift also the Yang stellar mass values, derived using a Kroupa IMF, as $\log(M_{stellar,Kroupa}) = \log(M_{stellar,Chabrier}) + 0.05$. Note that Giordini et al. integrate down to a stellar mass limit of $10^8 M_{\odot}$ which, when compared to our limit of $10^{10} M_{\odot}$, means their total group stellar masses should be slightly higher. At lower X-ray mass, our derived best linear fit indicates significantly lower stellar masses than Yang or Giordini. However, the latter notes that, in this low X-ray mass region, their stellar masses can range by a factor of ten at a fixed total mass and that the logarithmic intrinsic scatter of their relation is of order 35%. The X-ray detection threshold of my sample also prevents robust comparison to these results at low X-ray masses. Like Giordini et al., I find significant scatter, with much higher $M_{stellar}$ at fixed M_X . The bayesian best fits well match the average 1% stellar to X-ray mass fraction found by Balogh et al. (2011a) for a sample of low-mass nearby clusters within r_{500} .

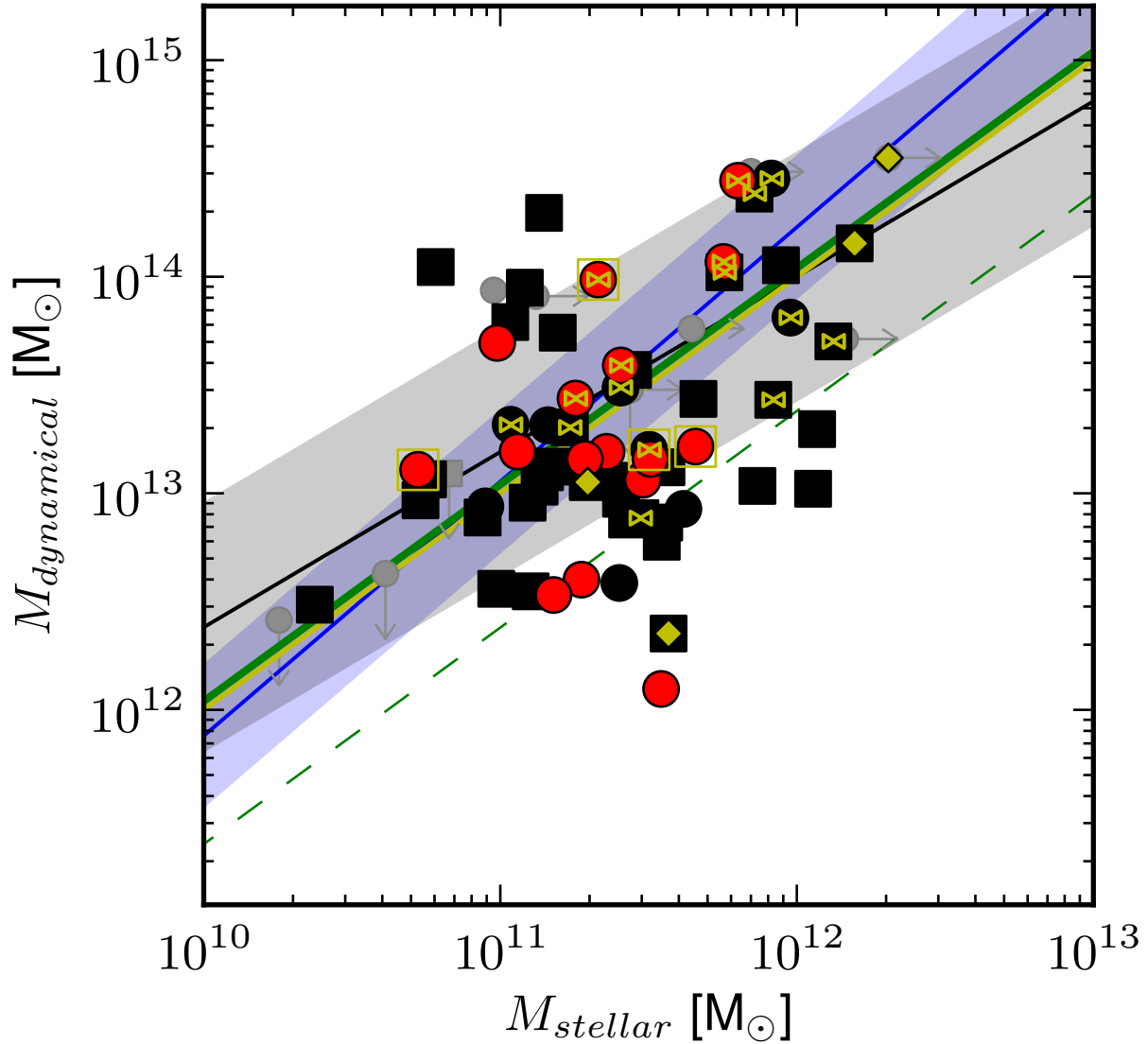


Figure 6.4: M_{dyn} - $M_{stellar}$ relation for quality 1 & 2 X-ray (black and red circles respectively) and optical systems (black squares) within $r_{200,X}$. Grey arrows indicate limits. Yellow bow-ties show systems tested for substructure. Filled yellow diamonds indicate systems with substructure according to the AD and DS test. Open yellow squares show groups in X-ray confused regions. Bayesian best fits for the X-ray systems (blue) and optical systems (black) are shown with the filled region representing the scatter. Constant stellar mass fractions of 0.009 and 0.042 are shown in green solid and dashed lines respectively and correspond to the fractions found for M_{200} halo masses of 14.9 and 13.7 M_\odot by Andreon (2010). The average 1% fraction found by Balogh et al. (2011a) within r_{500} for nearby low-mass clusters is shown in yellow.

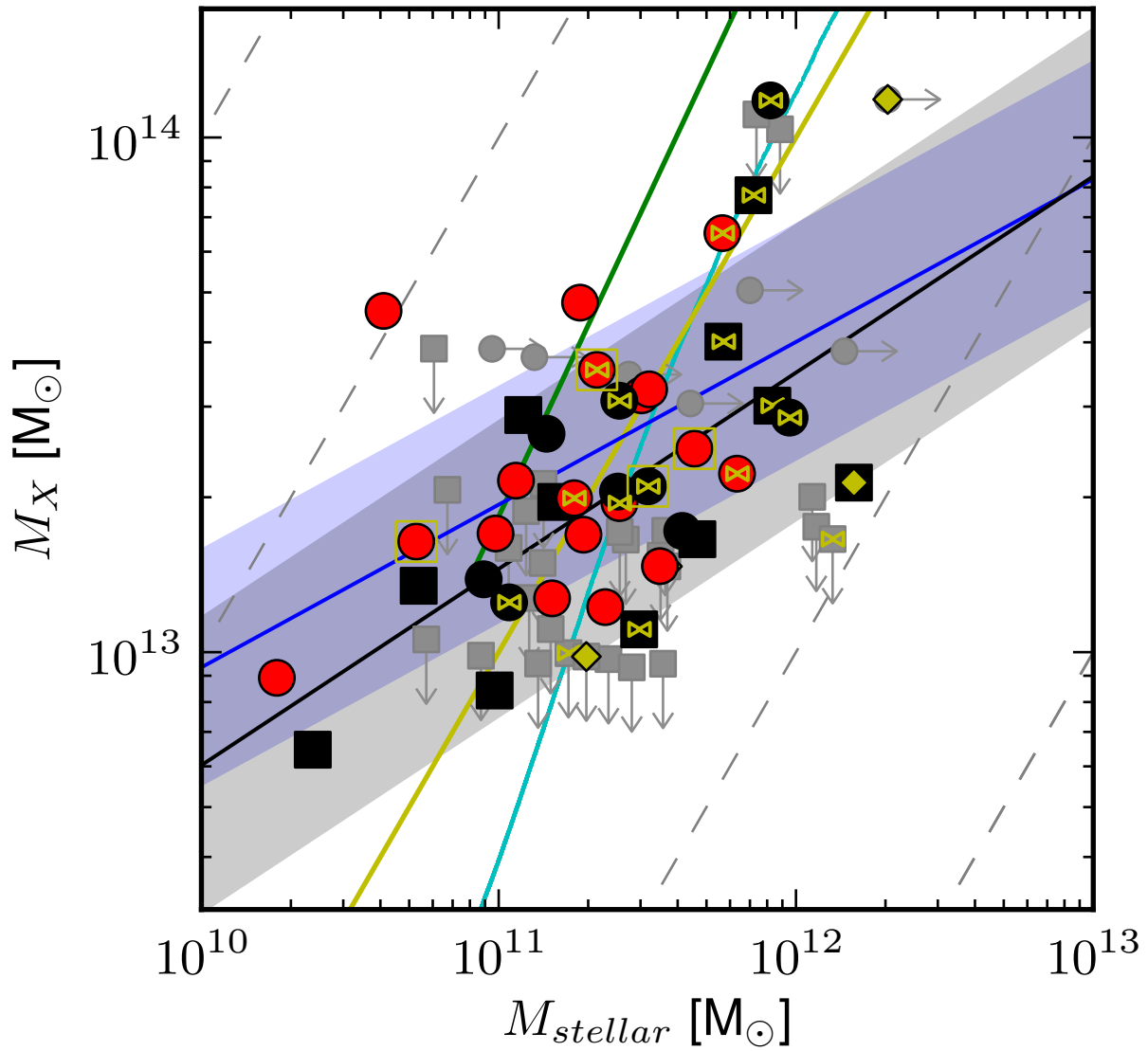


Figure 6.5: M_X - $M_{stellar}$ relation for quality 1 & 2 X-ray (black and red circles respectively) systems within $r_{200,X}$. Grey arrows indicate limits. Yellow bow-ties show systems tested for substructure. Filled yellow diamonds indicate systems with substructure according to the AD tests. Open yellow squares show groups in X-ray confused regions. Bayesian best fits for the X-ray systems (blue) and optical systems (black) are shown with filled region representing the scatter. Yang et al. (2009) data are over-plotted in cyan, Giodini et al. (2009) relation is shown in green, and the average 1% fraction found within r_{500} for nearby low-mass clusters by Balogh et al. (2011a) shown in yellow. Lines of constant mass are shown as grey dashed lines.

Table 6.4: M_{dyn} - $M_{stellar}$ Relation Bayesian Best Fits

		m	c	s
X-ray Q=1	1Mpc	0.9870 ± 0.5806	2.2493 ± 6.5824	0.3435 ± 0.2213
	$r_{200,\sigma}$	1.1365 ± 0.4680	0.4003 ± 5.4586	0.4935 ± 0.4133
	$r_{200,X}$	1.0838 ± 0.6199	1.0920 ± 7.2696	0.4791 ± 0.3384
X-ray Q=1 & 2	1Mpc	0.7090 ± 0.2633	5.5576 ± 3.1089	0.3338 ± 0.0846
	$r_{200,\sigma}$	1.0066 ± 0.4630	2.1746 ± 4.7953	0.8001 ± 0.1830
	$r_{200,X}$	1.1745 ± 0.3737	0.1341 ± 4.1988	0.3181 ± 0.1059
Optical	1Mpc	0.4360 ± 0.1618	8.7538 ± 1.9372	0.3861 ± 0.0587
	$r_{200,\sigma}$	0.7723 ± 0.1940	4.8051 ± 2.3556	0.4814 ± 0.0803
	$r_{200,X}$	0.8660 ± 0.5078	3.6283 ± 5.4831	0.5620 ± 0.2483

Column description: Bayesian best fit slope (m) and upper and lower errors (column 1); intercept (c) and upper and lower errors (2); and intrinsic scatter (s) and upper and lower errors (3) of the relation $\log(M_{dyn}) = m \times \log(M_{stellar}) + c + \epsilon$, where ϵ is a random variable with variance equal to s^2 .

Table 6.5: M_X - $M_{stellar}$ Relation Bayesian Best Fits

		m	c	s
X-ray Q=1	1Mpc	0.4379 ± 0.4648	8.2571 ± 5.0432	0.3409 ± 0.1702
	$r_{200,\sigma}$	0.5384 ± 0.2135	7.2254 ± 2.8646	0.2508 ± 0.1549
	$r_{200,X}$	0.5800 ± 0.3261	6.7669 ± 3.8182	0.2828 ± 0.1300
X-ray Q=1 & 2	1Mpc	0.1580 ± 0.1218	11.552 ± 1.4383	0.2454 ± 0.0476
	$r_{200,\sigma}$	0.3124 ± 0.0911	9.7752 ± 1.0656	0.1814 ± 0.0389
	$r_{200,X}$	0.3161 ± 0.1343	9.8088 ± 1.5718	0.2254 ± 0.0440
Optical	1Mpc	0.3278 ± 0.1866	9.5392 ± 1.9961	0.2887 ± 0.1022
	$r_{200,\sigma}$	0.2930 ± 0.1670	9.9691 ± 1.9516	0.2661 ± 0.1094
	$r_{200,X}$	0.3956 ± 0.1830	8.7837 ± 2.1637	0.2807 ± 0.1096

Column description: Bayesian best fit slope (m) and upper and lower errors (column 1); intercept (c) and upper and lower errors (2); and intrinsic scatter (s) and upper and lower errors (3) of the relation $\log(M_X) = m \times \log(M_{stellar}) + c + \epsilon$, where ϵ is a random variable with variance equal to s^2 .

Both the M_{dyn} - $M_{stellar}$ and M_X - $M_{stellar}$ relations show a wide range in stellar mass for a given ‘total’ mass, especially considering the limits. With a σ derived r_{200} , the M_{dyn} - $M_{stellar}$ relation *appears* an improvement over that obtained with $r_{200,X}$. However, this is merely due to the increased range in velocity dispersion and thus M_{dyn} with most high σ groups exhibiting dynamical complexity (recall Fig. 5.2). This drives up M_{dyn} but can also increase $M_{stellar}$ due to the increased membership resulting from larger r_{200} . Therefore I choose not to show the σ derived r_{200} cut version of this relation as its relative tightness is misleading due to this covariance. The M_X - $M_{stellar}$ relations behave similarly when comparing the differently defined radial cuts.

To determine if the scatter in $M_{stellar}$ given fixed total mass may be related to the dominance of the most massive galaxy (MMG), I first identify the MMG in each group and examine the offset of this galaxy from the group center. Fig. 6.6 shows the histogram of offsets and the offset versus the total (X-ray) system mass. The MMG generally lies near the group center regardless of whether an X-ray or luminosity-weighted center is used. With the exception of a single system, groups with higher X-ray mass ($M_X \gtrsim 3.5 \times 10^{13} M_\odot$) have the MMG within the inner third of the X-ray derived r_{200} . This corresponds to a distance of less than 200 kpc of the group center (nearer allowing for centering accuracy, see Fig. 4.13). For lower mass systems, there is a much greater scatter in the offset of the MMG. The group with its MMG at greatest offset from the center is XR21h14 (OP21h138), a massive group with two bright stars near the (projected) center. It is likely that the complication introduced to the photometry in this area due to the presence of these stars may be obscuring the actual MMG for this group.

The stellar mass contributed by the most massive galaxies does decrease with increasing total stellar mass, regardless of radial cut or choice of group center from an average fraction of 0.6 at $10^{10.5} M_\odot$ to 0.2 at $10^{12.2} M_\odot$. In the cluster regime, Sanderson et al. (2009) found that the offset of the BCG relates both to activity in that galaxy and to the dynamical state of the cluster itself. A full study of our BGGs (or MMGs) which includes correlation of offsets with emission properties as in Sanderson and also exploration of issues such as multiple component BGGs (as in Jeltema et al., 2007) would be an

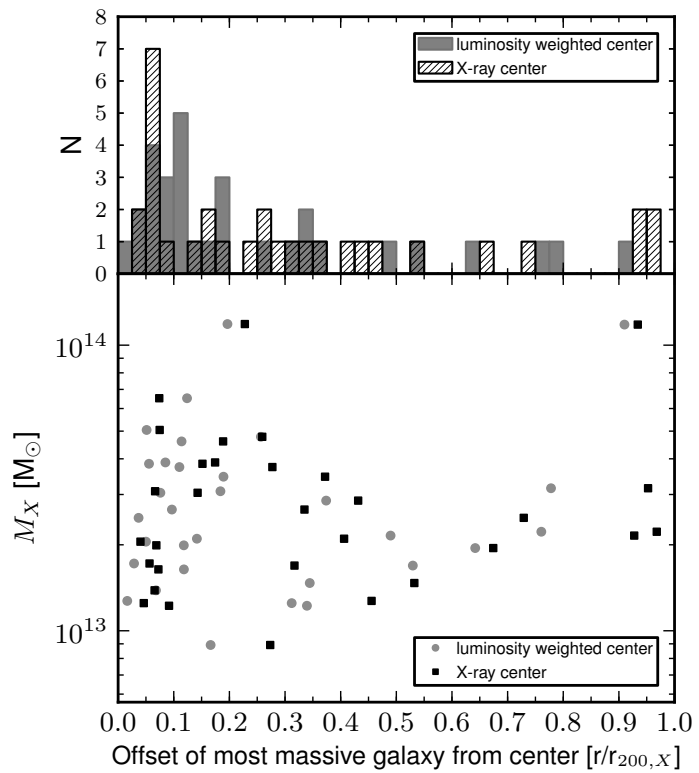


Figure 6.6: Histogram of the offset of the most massive galaxy from the group center (top) and versus total (X-ray) group mass (bottom). Offsets from X-ray centers are shown as black hashed histogram and black squares and luminosity weighted centers are shown as grey histogram and circles.

interesting addition to future work on galaxy properties.

6.4.3 Stellar Mass Fractions

Using the X-ray mass to represent the total halo mass, our best fits for both the high quality X-ray and optically selected systems indicate almost constant fractions ($M_{stellar}/M_X$) of ~ 0.011 , independent of halo mass (M_X). This is different from the *mean* fraction (for high quality systems and excluding limits) $M_{stellar}/M_X \sim 0.014$ with logarithmic standard deviation of 0.398. This fraction is closer to 0.0099 when limits are included. Recall that stellar mass is integrated down to $10^{10} M_\odot$. Using dynamical mass instead as the total group mass results in a mean fraction of ~ 0.022 . Examining the M_{dyn} - $M_{stellar}$ best fits, the fraction is similar to the ~ 0.009 found by Andreon for a $10^{14.9} M_\odot$ halo. Giordini et al. (2009) find that the stellar mass fraction associated with galaxies within r_{500} decreases with increasing total mass as $M_{500}^{-0.26 \pm 0.04}$. I do not find a similar relation but note that the relation found by Giordini et al. breaks down when clusters are excluded.

Fig. 6.7 shows the stellar mass fraction versus the total (X-ray) system mass given an X-ray based r_{200} cut for the total stellar mass and mass of the most massive galaxy. The mean contribution of the most massive galaxy to the total system mass ($M_{stellar}^{MMG}/M_X$) including both quality 1 & 2 X-ray and optically selected systems is ~ 0.004 (0.0033 when limits are included). Recall that though the overall group stellar mass is corrected for incompleteness, the individual mass of the MMG is not. In addition to constant lines approximating our mean stellar mass fractions for an X-ray based halo mass, the fractions found by Giordini et al. (2009) for their COSMOS sample of groups, Balogh et al. (2011a) within r_{500} for their nearby low-mass galaxy clusters, the Leauthaud et al. (2012) $z \sim 0.37$ COSMOS derived sample of groups and clusters, and the fraction including intracluster light (ICL) within r_{500} from the Gonzalez et al. (2007) cluster sample are all shown. The Giordini relation is again shifted to account for a difference in IMF. Additionally, the fractions found by Leauthaud by dividing the group population into central and satellite galaxies are shown.

In the cluster regime, stellar mass fractions are not universal, but generally decrease with increasing cluster mass (e.g. Ramella et al., 2004; Eke et al., 2005; Giordini et al., 2009). I find our fraction to be significantly lower than the fraction including ICL found by Gonzalez et al. (2007) with this divergence increasing with decreasing X-ray mass. I find many more systems at lower stellar mass fractions than do Giordini et al. Our spectroscopic selection results in a larger scatter in the stellar mass fraction.

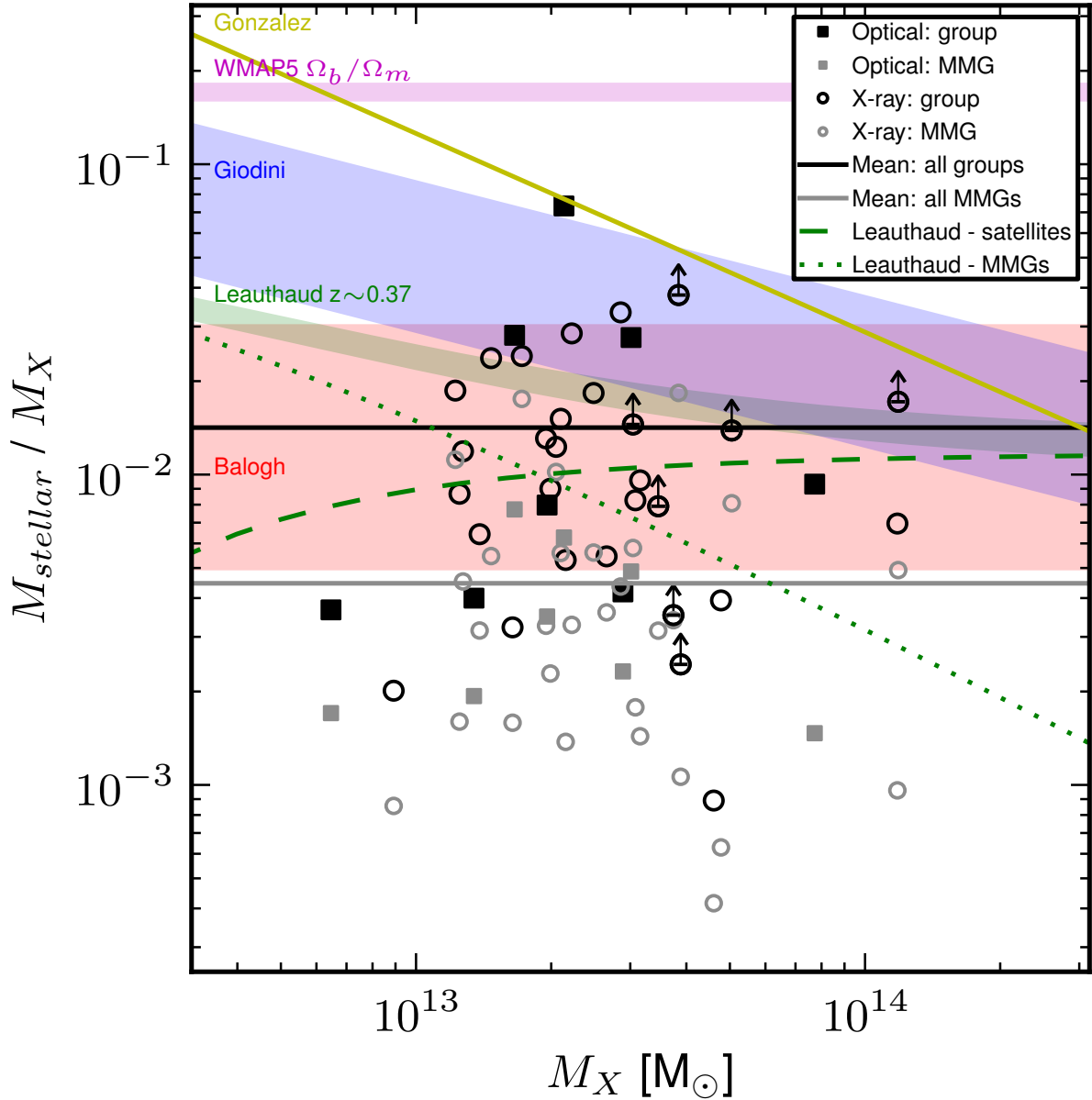


Figure 6.7: Stellar mass fraction versus total mass. Black and grey circles indicate total and most massive galaxy fractions respectively for X-ray systems while squares indicate similar quantities for optical systems. The mean stellar mass fraction for our entire sample (high quality X-ray and optical samples) is indicated by a black solid line and that of the MMG in grey. The Leauthaud et al. (2012) $z \sim 0.37$ stellar mass fraction is shown in green with dotted green line indicating central and dashed green line indicating the contribution from satellite galaxies. The Giordini et al. (2009) COSMOS sample stellar mass fraction and its intrinsic scatter is shown in blue. The Balogh et al. (2011a) fraction measured within r_{500} is shown in red and the Gonzalez et al. (2007) in yellow. The baryon fraction from WMAP5 (Dunkley et al., 2009) is plotted in magenta.

Chapter 7

Exploring Stellar Mass and X-ray Brightness: Underluminous Groups

To explore the correlation between X-ray luminosity and stellar mass, I use the Kelly Bayesian fitting code with the relation $\log(L_X) = m \times \log(M_{stellar}) + c + \epsilon$ for the optical and high quality X-ray systems for each of the different radial cuts. The best fit L_X - $M_{stellar}$ slope, intercept, and scatter and their associated errors are presented in Tab. 7.1. Note that positive and negative errors in stellar mass are averaged in order to produce symmetric errors for input into the Kelly Bayesian best fit procedure. The best fit solutions for X-ray systems vary significantly between the quality 1 and quality 1 & 2 systems and between different radial cuts. Considering only the quality 1 X-ray systems, the 1 Mpc radial cut produces a much shallower L_X - $M_{stellar}$ relation but with a very large intrinsic scatter. Comparing the quality 1 & 2 X-ray systems to that for the optical groups and taking the standard deviations into account, the best fit to the relations for both samples are very similar. Recall though that upper limits are not included in these fits. If the limits were included, assuming the luminosity is the value of the limit, the optical groups would be on average comparatively *underluminous* in X-rays. Fig. 7.2 (top panel) shows the $M_{stellar}$ - L_X relations for X-ray and optical groups respectively with an X-ray based r_{200} cut applied.

A fit to the relation *including* the optical systems with upper limits on X-ray luminosity, assuming the luminosity is the value of the limit (i.e. the maximum value possible), can be seen in magenta in the top right panel of Fig. 7.2 and is also included (in its reciprocal form) in Tab. 7.1. Using this best fit, I split the entire population of groups, including all optical systems and Q = 1 & 2 X-ray systems, into three parts: ‘underluminous’, ‘normal’, and ‘overluminous’ groups. I define X-ray under- and overluminous groups as those which have lower/higher L_X than the best fit value (including upper limits), minus/plus half the scatter (0.5s). Those groups that are underluminous, having higher stellar masses and lower luminosities than the fit even including half the scatter, are marked by open magenta squares while the overluminous systems are marked similarly in cyan. Note that while groups with upper limits in X-ray luminosity are included in the underluminous group population, I exclude these from the overluminous subset as they may in fact be consistent with the relation.

Several of the outliers to the $M_{stellar}$ - L_X relation, including an underluminous optical and

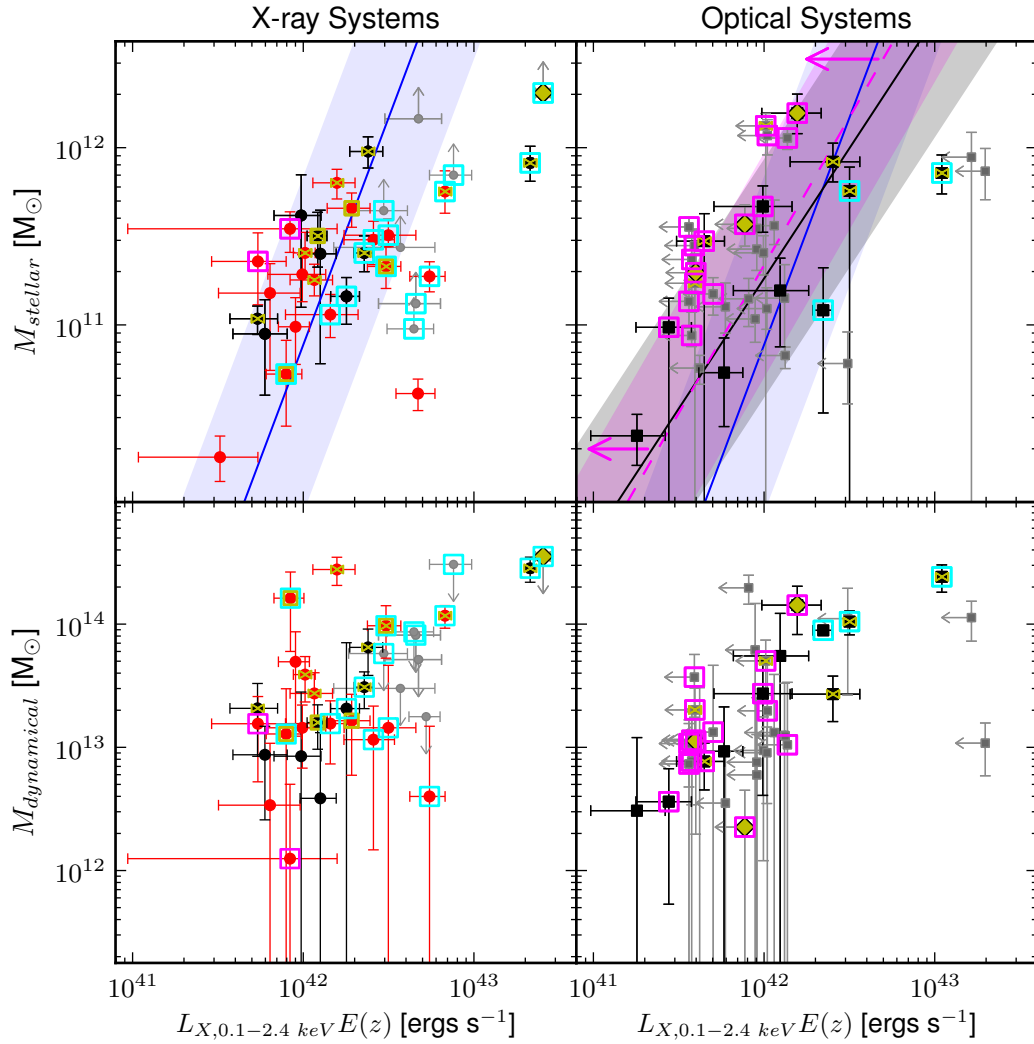


Figure 7.1: TOP: $M_{stellar}$ - L_X relation for X-ray selected systems (left) and optical systems (right) with X-ray based r_{200} cut applied. Bayesian best fits are shown in blue and black (X-ray and optical fits respectively) with filled regions representing the scatter. Bayesian best fit for optical systems where upper limits on X-ray luminosity have been treated as detections is shown in magenta with filled region representing the scatter and magenta arrows reflecting that this relation is in reality likely shifted to lower X-ray luminosities. BOTTOM: M_{dyn} - L_X relation for X-ray (left) and optically (right) selected systems with X-ray based r_{200} cut applied. Quality 1 & 2 X-ray selected systems are shown as black and red circles respectively while optical systems are shown as black squares. Grey arrows indicate limits. Yellow bow-ties show systems tested for substructure. Filled yellow diamonds and squares indicate systems with substructure according to AD and DS Tests respectively. Open yellow squares show groups in X-ray confused regions. Open magenta and cyan squares indicate X-ray underluminous and overluminous systems respectively.

Table 7.1: L_X - $M_{stellar}$ Relation Bayesian Best Fits

		m	c	s
X-ray Q=1	1Mpc	$0.2506 \pm^{0.9341}_{0.8836}$	$39.184 \pm^{10.542}_{11.047}$	$0.6271 \pm^{0.3061}_{0.1676}$
	$r_{200,\sigma}$	$1.0128 \pm^{0.4214}_{0.3992}$	$30.463 \pm^{4.6178}_{4.9364}$	$0.3981 \pm^{0.2403}_{0.1378}$
	$r_{200,X}$	$1.0659 \pm^{0.7493}_{0.7725}$	$29.847 \pm^{8.8896}_{8.7808}$	$0.5017 \pm^{0.2429}_{0.1500}$
X-ray Q=1 & 2	1Mpc	$0.1636 \pm^{0.1822}_{0.1759}$	$40.301 \pm^{2.0875}_{2.1560}$	$0.4057 \pm^{0.0761}_{0.0582}$
	$r_{200,\sigma}$	$0.4285 \pm^{0.1563}_{0.1564}$	$37.197 \pm^{1.8092}_{1.8303}$	$0.3228 \pm^{0.0694}_{0.0552}$
	$r_{200,X}$	$0.3903 \pm^{0.1779}_{0.1748}$	$37.749 \pm^{1.9910}_{2.0485}$	$0.3625 \pm^{0.0647}_{0.0544}$
Optical	1Mpc	$0.5915 \pm^{0.3093}_{0.2970}$	$35.288 \pm^{3.4474}_{3.5627}$	$0.4661 \pm^{0.1646}_{0.1085}$
	$r_{200,\sigma}$	$0.5266 \pm^{0.2603}_{0.2653}$	$36.093 \pm^{3.0918}_{3.0718}$	$0.4010 \pm^{0.1570}_{0.1014}$
	$r_{200,X}$	$0.7034 \pm^{0.2943}_{0.3040}$	$34.042 \pm^{3.4661}_{3.3378}$	$0.4459 \pm^{0.1849}_{0.1188}$
Optical with upper limits	1Mpc	$0.5161 \pm^{0.1802}_{0.1841}$	$36.081 \pm^{2.1159}_{2.0891}$	$0.3870 \pm^{0.0648}_{0.0521}$
	$r_{200,\sigma}$	$0.5198 \pm^{0.1678}_{0.1658}$	$36.089 \pm^{1.9194}_{1.9111}$	$0.3640 \pm^{0.0679}_{0.0566}$
	$r_{200,X}$	$0.5956 \pm^{0.1754}_{0.1789}$	$35.243 \pm^{2.0368}_{1.9962}$	$0.3691 \pm^{0.0687}_{0.0545}$

Column description: Bayesian best fit slope (m) and lower and upper errors (column 1); intercept (c) and lower and upper errors (2); and intrinsic scatter (s) and lower and upper errors (3) of the relation $\log(L_X) = m \times \log(M_{stellar}) + c + \epsilon$, where ϵ is a random variable with variance equal to s^2 .

the most overluminous X-ray group – which are also the systems with the highest stellar mass – show substructure. However, some of the groups with ≥ 10 members (marked as yellow bowties) do not show evidence of substructure from either the AD or DS test and are among the most significant outliers from this relation.

7.1 X-ray Underluminous Groups

The bottom panel of Fig. 7.2 shows the M_{dyn} - L_X relations for X-ray and optical groups respectively with an X-ray based r_{200} cut applied. Examining the positions of the underluminous systems, indicated by open magenta squares, their dynamical masses are not unusually low, spanning a wide range in M_{dyn} . Further, the majority of these underluminous groups do not exhibit significant dynamical complexity which would lead to elevated velocity dispersions and thus overestimation of dynamical and group stellar mass. So, given their dynamical mass, these groups appear to be genuinely X-ray underluminous. This may be evidence for a population of dynamically young groups which are just in the process of collapse. It is possible, however, that the effect seen is *not* a deviance in L_X but rather a result of scatter in the stellar mass.

Next I examine the median contribution of the MMG to the total group stellar mass ($M_{stellar}^{MMG}/M_{stellar}$).

Recall that $M_{stellar}$ for all groups has had substantial incompleteness corrections applied. In order to best determine the contribution from the MMG, I re-calculate the group stellar mass *excluding* the MMG, and use the difference between this value and that found for the group including all members to characterize the fraction $M_{stellar}^{MMG}/M_{stellar}$. For underluminous systems, the median contribution of the MMG to the total group stellar mass ($M_{stellar}^{MMG}/M_{stellar}$) is lower ($\sim 36\%$) than that found for all systems ($\sim 42\%$) with the most underluminous systems having less of their mass contributed from this member. Fig. 7.2 shows the histograms of $M_{stellar}^{MMG}/M_{stellar}$ for all, overluminous, and underluminous systems.

To test the significance of the difference in the contribution of the MMG to the total stellar mass between underluminous and the total population of groups, I first create a sample matched in mass to our underluminous groups from the complete sample of X-ray and optical systems. I repeat this process 10,000 times, calculating $M_{stellar}^{MMG}/M_{stellar}$ for each group in each sample. Finally I calculate for each sample the number of systems having $M_{stellar}^{MMG}/M_{stellar} < 40\%$ (above the peak of the underluminous distribution, see Fig. 7.2). For the underluminous groups, this is 80% of 15 groups. Only 89 of the 10,000 matched samples meet this criterion – i.e. having $\geq 80\%$ of groups with $M_{stellar}^{MMG}/M_{stellar} < 40\%$ – indicating that the difference is indeed significant. The cumulative distribution of the fraction of matched sample groups having $M_{stellar}^{MMG}/M_{stellar} < 40\%$ is shown in Fig. 7.3. This may imply that in the underluminous systems less IGM is available from relatively equal mass progenitors (which leads to the group not having a single dominant galaxy). The existence and possible origins of X-ray underluminous or ‘dark’ systems remains a topic of vigorous debate even in the cluster regime where X-ray and spectroscopic data are abundant. A recent study of an X-ray bright subsample of the maxBCG clusters by the Planck Collaboration (2011) finds evidence for a possible X-ray underluminous population which shows a low Sunyaev-Zel’dovich signal normalization, while Andreon & Moretti (2011) find no evidence for a significant population of underluminous systems in a study of X-ray luminosity in color selected clusters.

The overall fraction of gas scales with halo mass, with clusters having a higher gas mass fraction than groups (e.g. Sun et al., 2009; Pratt et al., 2009; Giordini et al., 2009; Peebles & Shankar, 2011). To explore why groups with similar total stellar mass may have lower gas mass and a lower contribution of stellar mass from the most massive member, I contrast two modes of group assembly. In the first scenario, the group begins with a massive galaxy and accretes mass smoothly. In the second, roughly equivalent mass ‘subgroups’ (clumps) comprised of similar mass / luminosity galaxies merge. The former case would result in a group with a both

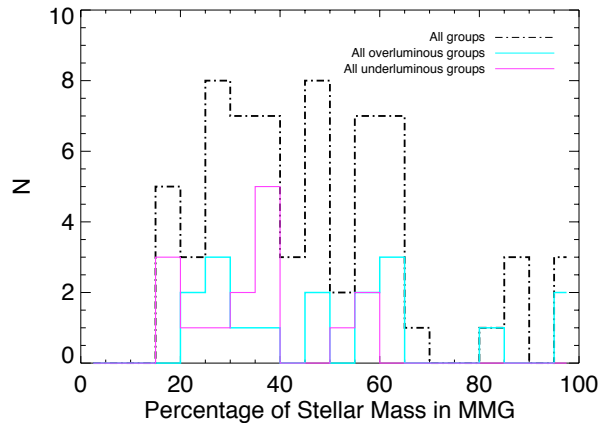


Figure 7.2: Histograms of $M_{stellar}^{MMG}/M_{stellar}$ for all (black dash-dot), overluminous (cyan), and underluminous (magenta) groups. Note the distribution of underluminous groups peaks at $\sim 40\%$ while the overluminous distribution is much flatter.

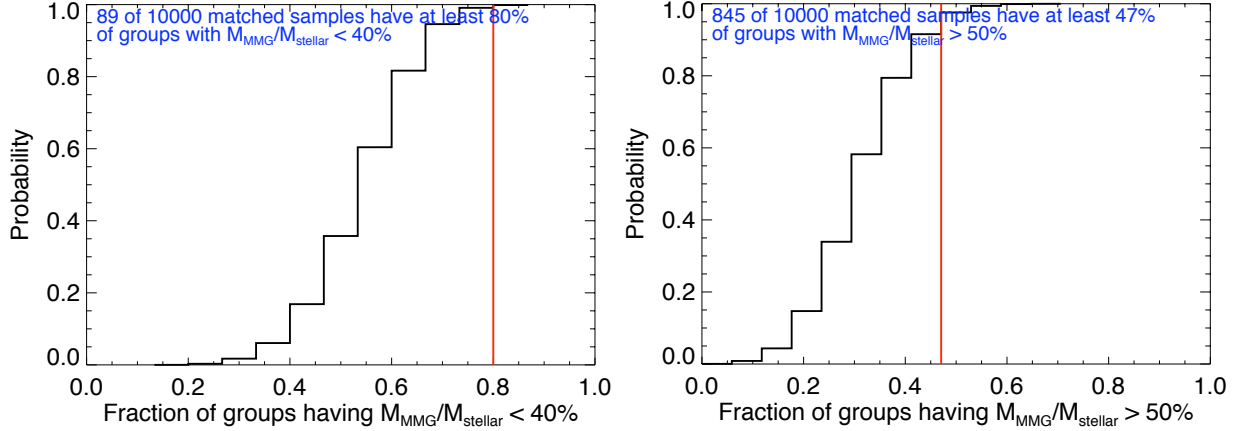


Figure 7.3: Cumulative distribution of the fraction of matched sample groups having $M_{MMG}/M_{stellar} < 40\%$. Red solid line indicates the fraction of underluminous groups which have less than 40% of their stellar mass contributed by the MMG.

Figure 7.4: Cumulative distribution of the fraction of matched sample groups having $M_{MMG}/M_{stellar} > 50\%$. Red solid line indicates the fraction of overluminous groups which have more than 50% of their stellar mass contributed by the MMG.

a higher gas fraction and a more massive central galaxy. I posit this may be one explanation for the observed correlation between the fraction of mass in the most massive galaxy, and the relative X-ray luminosity. The Rykoff et al. (2008b) comparison of X-ray and optically selected clusters suggests there is a wide range of L_X at fixed mass, and that X-ray selection simply picks off the more X-ray luminous part of the population. Popesso et al. (2007a) use an optically selected cluster sample to explore the nature of underluminous systems, finding evidence that these systems are undergoing a phase of mass accretion and are still accreting intracluster gas or in the process of merging. It would be interesting to examine the galaxy population in these groups to examine the role of the X-ray emitting hot medium in driving galaxy evolution in our groups in the future.

7.2 X-ray Overluminous Groups

Examining the positions of the optically and X-ray selected overluminous systems on the M_{dyn} - L_X relation (bottom panel of Fig. 7.2), indicated by open cyan squares, the dynamical masses of the former are all very high ($\gtrsim 10^{14} M_\odot$) while the latter span the entire range in M_{dyn} . The median contribution of the MMG to the total group stellar mass ($M_{MMG}/M_{stellar}$) is higher ($\sim 47\%$) for overluminous systems than for all systems ($\sim 42\%$). As for the underluminous groups, I test the significance of this difference in the relative contribution from the MMG by creating a sample matched in mass to our overluminous groups from the complete sample of X-ray and optical systems. In this case, I calculate for each sample the number of systems having $M_{MMG}/M_{stellar} > 50\%$. For the overluminous groups, this is 47% of 17 groups. 845 of the 10,000 matched samples meet this criterion, having $\geq 47\%$ of groups with $M_{MMG}/M_{stellar} > 50\%$, indicating that this

difference is not as significant as that found for underluminous systems.

Note that to further ensure the robustness of these results, the under- and overluminous groups were also defined relative to the best fit based on the *X-ray* ($Q=1 \& 2$) systems and, though specific numbers changed, all qualitative results remained consistent. The specific characterization of the relation is, however, of paramount importance to these results. For example, using only the $Q=1$ groups for either of the r_{200} based cuts would result in a much shallower slope of the L_X - $M_{stellar}$ relation (top left panel of Fig.) and thus a significant difference in the population of groups defined as under- or overluminous. Note that this slope is much more cluster-like.

Chapter 8

Conclusions

Two group samples at $0.12 < z < 0.79$ have been defined in the same fields, one containing 39 high quality X-ray selected systems and the other 38 optically selected systems, in order to study groups spanning a significant mass and evolutionary range. Group membership was assigned and I applied three different radial cuts: r_{200} cuts based on the X-ray emission and velocity dispersion of the systems, and a constant 1 Mpc cut. Group masses were estimated from X-ray luminosity ('X-ray mass'), velocity dispersion ('dynamical mass'), and stellar content of group galaxies ('group stellar mass') – the latter two within the differing radial cuts. Dynamical complexity and substructure was explored using the Anderson-Darling and Dressler-Shectman tests and the shape of X-ray emission. I presented the $L_X - \sigma$ relation for our systems, which is similar to that found for nearby groups, and discussed the effects of centering, radial cuts and dynamical complexity/substructure in regards to outliers in this, and other scaling relations. Best fits to the $L_X - \sigma$ and $L_X - M_{stellar}$ relations for different group samples and radial cuts, were presented. Stellar mass fractions were estimated using the X-ray and dynamical mass as proxies for the group halo mass. Finally, a population of systems relatively underluminous in X-rays given their stellar and dynamical mass was defined and discussed. My main conclusions are as follows:

- X-ray wavelet decomposition technique:

Given sufficiently deep exposures and careful data reduction, this method can successfully be employed to detect low mass systems even at moderate redshift.

- Confusion:

Confusion exists both in matching galaxies to extended X-ray emission and matching X-ray emission to already identified optical systems. Until X-ray spectroscopy is available to measure the redshift of the X-ray emitting gas, completely confident matching will not be possible. Splitting systems into X-ray detected and undetected systems designates the problem, not the solution. These difficulties in matching make cosmological studies using groups difficult.

- X-ray apertures for optically detected groups:

A constant aperture, based on the confusion limit, enables direct comparison of X-ray properties (and limits) across these disparately selected systems.

- **Dynamical complexity:**

Dynamical complexity/substructure in a system *can* work to inflate velocity dispersion and stellar mass and may explain the position of certain outliers in the scaling relations explored and introduce scatter in scaling relations. The tests we are using are orbit-dependent and can only be confidently applied to systems with at least ten members.

- **Overlap of X-ray and optically selected samples:**

Nine optical systems are associateable with X-ray systems. A lack in overlap between these spatially coincident but disparately selected samples implies that neither technique can recover all groups. Similarities in group properties, however, indicate that given sufficient spectral coverage and X-ray depth, samples defined in these ways can be fairly compared.

- **Radial cuts:**

Applying X-ray based r_{200} radial cuts usually produces the tightest scaling relations. The good correlation between L_X and σ and the lack of dynamical complexity found for systems using this radius implies that it is isolating the virialized part of the group. Velocity dispersion based and constant cuts generally result in larger radii and more members, and include more substructure/non-Gaussianity. This acts to increase scatter and inflate both velocity dispersion and stellar mass. However, as some systems are not X-ray detected and using X-ray limits is less than ideal, such cuts are the only options.

- **Stellar mass fraction:**

I find a mean stellar mass fraction for high quality systems of ~ 0.014 within an X-ray based r_{200} treating the X-ray mass as the total mass of the system and excluding limits. This is comparable to those found by Giordini et al. (2009), Balogh et al. (2011a), and Leauthaud et al. (2012) but significantly lower than that found by Gonzalez et al. (2007). The mean contribution of the most massive galaxy is ~ 0.004 . Using a total mass based on dynamical mass would result in different fractions due to significant disagreement between M_X and M_{dyn} for many of the systems.

- **Total mass measures:**

The differences in mean total mass measures (M_X and M_{dyn}) tend to increase, and the scatter to decrease, as X-ray mass increases.

- **X-ray underluminous groups:**

I define a sample of systems as X-ray underluminous given their stellar mass, the majority of which are optically selected. Not all such systems show dynamical complexity and the stellar mass fraction in the most massive galaxy of these systems is on average less than that found for the total population of groups. This may indicate that less IGM is being contributed from the

progenitor halo containing the most massive member and I posit that differences in accretion (a continuous smooth accretion of galaxies from the field verses the merging of similar mass ‘sub-groups’) may be one explanation for the observed correlation between the fraction of mass in the most massive galaxy and the relative X-ray luminosity.

Further Lines of Inquiry

With the global group properties of a relatively large sample of groups defined and explored in this thesis and a multiwavelength dataset already assembled for these systems, characterizing the galaxy populations and investigating possible correlations between the global properties of the host groups and those of the members may be readily accomplished. I propose here three such topics that the combination of global group properties with galaxy colors, morphologies, star formation rates, masses, and AGN classification would enable.

- Evolution of brightest group galaxies:

Locally, brightest group galaxies tend to be found in the center of the X-ray emission and are massive galaxies similar to those found in the center of clusters. However, studies show BGGs are strongly evolving via mergers, morphological transformation, and dynamical relaxation at intermediate redshift (Jeltema et al., 2008; Tran et al., 2008). A cursory investigation of our sample shows that the frequency of BGGs is low and that galaxy clustering is often not peaked at the center of the X-ray emission (recall Fig. 6.6).

- Mass & age of groups – distinguishing effects of mass, age, and the IGM on galaxy properties: X-ray data can be used to distinguish old, relaxed groups from young, dynamically active groups, still in the processes of virializing. X-ray bright galaxy clusters show good correlations between X-ray properties (temperature and luminosity) and optical properties (total optical/NIR luminosity or stellar mass) with system mass. Popesso et al. (2005) show that the correlation of cluster mass with total optical luminosity is better than that with X-ray luminosity. In these systems, the mass or/and X-ray brightness correlates with properties of the galaxy population such as the morphological composition, the fraction of blue galaxies, or the AGN fraction (Osmond & Ponman, 2004; Balogh et al., 2002; Popesso & Biviano, 2006; Popesso et al., 2007a). However, clusters also exist which are underluminous in X-rays with respect to their optical properties or mass (Gilbank et al., 2004). Popesso et al. (2007b) show that for a sample of X-ray Underluminous Abell clusters, the fraction of blue galaxies is higher than in clusters which fall on the usual relations. They infer that these clusters are still in formation. This indicates clearly that an offset from X-ray-optical scaling relations traces the evolutionary phase or age of a system. In groups these offsets are much more common (Popesso et al., 2004), since the cores of more massive systems formed earlier, on average. Combining my X-ray and optically selected group samples will populate the old and younger group regimes, which can also be separated by group substructure, galaxy composition, and dynamical segregation of different galaxy types and allow

us to differentiate between the effects of age, mass, and the IGM on observed galaxy properties.

- Star formation rate (SFR) density in groups

Studies of the global star formation rate show a significant decline (factor of 3-10) since the peak of star formation at $z = 1.2$ (Lilly et al., 1995; Madau et al., 1998; Glazebrook et al., 1999; Wilson et al., 2002). The cause of this downturn in the cosmic star formation rate is unclear, but two main hypotheses exist. First, that the decline is a result of galaxies running out of a supply of material for star formation. This is intrinsic to the galaxy population. In the second scenario, the downturn is a result of the growth of structure in the Universe. In other words, it is caused by the changing environments of galaxies. Since most galaxies are found in groups, understanding the effects of the group environment is essential to understanding the evolution of the cosmic star formation rate. Comparing the SFR density in our groups to the local value will allow us to see to what extent these systems impact the global evolution of SFR density.

Appendix: Spectroscopic Redshifts

Table 1: Spectroscopic Redshifts

RA J2000	Dec J2000	z	source	1 Mpc Group Member	$r_{200,\sigma}$ Group Member	$r_{200,X}$ Group Member
221.927383	9.147980	0.5685	GMOS
221.941650	9.159590	0.8850	GMOS
221.959946	9.192980	0.8497	GMOS
221.963501	9.136121	0.8112	GMOS
221.964722	9.137767	0.8116	GMOS
221.981888	9.151252	0.7233	GMOS
221.993881	9.211152	0.7040	GMOS
222.003189	9.144666	0.8836	GMOS
222.014923	9.215993	0.7014	GMOS
222.019150	8.903519	0.3581	CNOC2
222.019943	9.196466	0.7638	GMOS
222.021164	8.918481	0.4938	CNOC2
222.021225	8.825347	0.2036	CNOC2
222.023453	8.860129	0.2039	CNOC2
222.024719	8.884596	0.6732	CNOC2
222.025604	8.836168	0.1669	CNOC2
222.025650	9.211432	0.4669	GMOS
222.027191	9.146202	0.8832	GMOS
222.027298	8.901578	0.4144	CNOC2
222.027679	8.863700	0.5261	CNOC2
222.028992	8.903384	0.1848	CNOC2
222.031784	8.775932	0.4638	CNOC2
222.031967	8.845531	0.3562	CNOC2
222.034225	8.774302	0.4652	CNOC2
222.034760	8.835194	0.3084	CNOC2
222.036774	8.905704	0.4017	CNOC2
222.037567	8.906237	0.4085	CNOC2
222.039490	8.828058	0.2708	CNOC2
222.041458	8.863553	0.5261	CNOC2
222.042374	8.919587	0.3539	CNOC2
222.042999	8.788318	0.3082	CNOC2
222.043701	8.821358	0.3097	CNOC2
222.044968	8.883969	0.2362	CNOC2
222.045288	8.933855	0.3534	CNOC2
222.045746	8.870946	0.4821	CNOC2
222.048584	8.860609	0.2365	CNOC2
222.049988	8.916006	0.3239	CNOC2
222.051758	8.921947	0.2246	CNOC2
222.053574	8.931828	0.3245	CNOC2
222.053909	8.842780	0.4664	CNOC2
222.054123	8.930885	0.3240	CNOC2
222.056961	8.875625	0.4553	CNOC2
222.057114	8.927853	0.2281	CNOC2
222.057251	9.143275	0.7053	GMOS
222.058533	9.159166	0.7932	GMOS
222.058838	8.932894	0.2227	CNOC2
222.059860	8.808464	0.1966	CNOC2
222.060898	8.842739	0.1970	CNOC2
222.062256	8.914667	0.6053	CNOC2
222.063034	8.897182	0.4787	CNOC2
222.064880	8.874642	0.4560	CNOC2
222.064911	8.928461	0.3221	CNOC2
222.065399	8.792393	0.1156	CNOC2
222.065964	8.775584	0.2035	CNOC2
222.067566	8.859791	0.2365	CNOC2
222.068634	8.937251	0.3533	CNOC2
222.068939	8.886365	0.2366	CNOC2
222.071014	8.848438	0.4624	CNOC2
222.073868	8.940305	0.2037	CNOC2
222.074768	8.798632	0.4609	CNOC2
222.075531	8.832848	0.4644	CNOC2
222.075684	8.853609	0.2708	CNOC2
222.076019	8.940099	0.3528	CNOC2
222.076401	8.884063	0.4619	CNOC2
222.076462	8.909295	0.2283	CNOC2
222.078918	8.801896	0.3751	CNOC2
222.078949	8.855593	0.2704	CNOC2
222.079254	8.941572	1.7700	CNOC2

RA	Dec	z	source	l Mpc	$r_{200,\sigma}$	$r_{200,X}$
222.082123	8.805657	0.6517	CNOC2
222.082489	8.905748	0.4695	CNOC2
222.084122	8.910165	0.2277	CNOC2
222.084351	8.884232	0.2376	CNOC2
222.085770	8.905604	0.2273	CNOC2
222.086273	8.827558	0.5138	CNOC2
222.088593	8.891824	0.2701	CNOC2
222.088699	8.817811	0.3072	CNOC2
222.090408	8.942347	0.1936	CNOC2
222.090897	8.824166	0.4090	CNOC2
222.090927	9.172957	0.7384	GMOS
222.091278	9.178577	0.7860	GMOS
222.092987	8.942700	0.1937	CNOC2
222.093063	8.812249	0.2703	CNOC2
222.093918	8.944454	0.1932	IMACS
222.093979	8.929597	0.7365	IMACS
222.094467	8.815980	0.4643	CNOC2
222.096130	8.783916	0.3096	CNOC2
222.096848	8.884443	0.3082	CNOC2
222.097244	8.910457	0.4699	CNOC2
222.097855	8.942586	0.9985	IMACS
222.098038	8.811475	0.4641	CNOC2
222.098801	9.209483	0.6910	GMOS
222.099091	8.901239	0.2359	CNOC2
222.100433	8.887013	0.4554	CNOC2
222.100739	8.927544	0.3086	IMACS
222.100906	8.781972	0.3104	CNOC2
222.101318	8.784624	0.3106	CNOC2
222.103180	8.851841	0.4640	CNOC2
222.104279	8.804113	0.2704	CNOC2
222.104813	8.880278	0.7700	CNOC2
222.105087	8.941574	0.2273	CNOC2
222.105637	8.922588	0.2373	IMACS
222.105652	8.824803	0.6525	CNOC2
222.105820	8.893362	0.2375	CNOC2
222.105972	8.905978	0.8106	IMACS
222.107086	8.884840	0.5268	IMACS
222.107285	8.773086	0.5042	LDSS2
222.108032	8.805390	0.4647	CNOC2
222.108826	8.901307	0.1846	CNOC2
222.111130	8.898141	0.1845	CNOC2
222.111786	8.859863	0.4633	CNOC2
222.112640	8.802913	0.6338	CNOC2
222.116882	8.812265	0.6547	CNOC2
222.118149	8.926601	0.4687	CNOC2
222.119904	8.906499	0.3894	CNOC2
222.120636	8.823205	0.4474	CNOC2
222.120895	8.900317	0.8121	IMACS
222.121399	8.914010	0.4793	CNOC2
222.122391	8.936090	0.4704	CNOC2
222.122635	9.216505	0.3611	GMOS
222.122711	8.874545	0.6094	CNOC2
222.124908	8.814411	0.4466	CNOC2
222.125137	8.863828	0.2243	CNOC2
222.126129	8.907748	0.3228	CNOC2
222.126404	8.793371	0.2725	CNOC2
222.126678	9.186406	0.6078	GMOS
222.127899	8.942175	0.6487	CNOC2
222.129196	8.878336	0.6091	CNOC2
222.129456	8.927191	0.5309	IMACS
222.129578	9.148497	0.8119	GMOS
222.130722	9.140047	0.6074	GMOS
222.130951	8.907487	0.7347	IMACS
222.131943	8.835113	0.5316	CNOC2
222.132660	8.925350	0.7663	IMACS
222.133682	8.812096	0.3856	CNOC2
222.133972	8.836501	0.4467	CNOC2
222.134857	8.894422	0.4622	CNOC2
222.136581	9.171988	0.4231	GMOS
222.136887	8.828555	0.4075	CNOC2
222.138443	8.869699	0.4781	CNOC2
222.140152	8.808433	0.2705	CNOC2
222.140427	8.916725	0.2715	CNOC2
222.140976	8.807593	0.3857	CNOC2
222.141037	8.896926	0.7693	CNOC2
222.141937	9.199562	0.7656	GMOS
222.143051	8.799981	0.6537	CNOC2
222.144943	8.934057	0.7376	IMACS
222.145004	8.922487	0.2375	CNOC2
222.145386	8.895625	0.4087	CNOC2
222.145538	8.889994	0.3083	IMACS
222.146149	8.856542	0.0658	CNOC2
222.146332	8.922687	0.2703	CNOC2
222.147095	8.925745	0.4082	CNOC2
222.149261	8.876601	0.5550	CNOC2
222.150345	8.916539	0.5058	CNOC2
222.152283	8.845948	0.6528	CNOC2

RA	Dec	z	source	l Mpc	$r_{200,\sigma}$	$r_{200,X}$
222.152557	8.842437	0.4662	CNOC2
222.152679	9.206910	0.7006	GMOS
222.152817	8.899772	0.0875	CNOC2
222.154099	8.776782	0.3105	CNOC2
222.154129	8.857385	0.4466	CNOC2
222.154312	8.931884	0.4073	IMACS
222.157043	8.873466	0.6821	IMACS
222.157135	8.932751	0.4029	CNOC2
222.157654	8.939324	0.4019	CNOC2
222.158524	8.912645	0.7674	IMACS
222.158737	8.880896	0.5538	CNOC2
222.159698	8.875638	0.5444	CNOC2
222.160049	8.848881	0.6813	IMACS
222.160736	8.820871	0.4066	IMACS
222.160797	8.934812	0.0060	CNOC2
222.161392	8.914151	0.7558	FORS2
222.162369	8.810489	0.2707	CNOC2
222.162384	8.884173	0.4471	CNOC2
222.162628	8.857023	0.4654	CNOC2
222.163162	8.937333	0.7557	IMACS+FORS2
222.163910	9.194970	0.5104	GMOS
222.164597	8.885272	0.4149	CNOC2
222.166672	8.785604	0.3762	CNOC2
222.166901	8.788022	0.2702	CNOC2
222.166901	8.832489	0.5669	CNOC2
222.167480	8.855910	0.4473	IMACS
222.168335	8.918101	0.4619	CNOC2
222.168686	8.907840	0.8701	IMACS
222.169006	8.860918	0.8072	IMACS
222.169952	8.905677	0.4662	CNOC2
222.169998	8.813510	0.2632	CNOC2
222.170975	9.219070	0.6240	GMOS
222.171219	8.880983	0.6820	FORS2
222.171387	8.902526	0.4561	IMACS
222.171509	8.925439	0.1807	CNOC2
222.171722	8.920381	0.6822	IMACS
222.171783	8.923467	0.2365	CNOC2
222.172806	8.782291	0.6661	CNOC2
222.173004	9.059504	0.4760	CNOC2
222.173431	8.881822	0.6820	FORS2
222.173538	8.852532	0.4666	CNOC2
222.173660	8.817430	0.0798	CNOC2
222.173676	8.850183	0.1273	IMACS
222.173737	9.133977	0.7866	GMOS
222.173828	8.854190	0.5320	IMACS
222.174088	9.029489	0.3593	CNOC2
222.174225	9.012068	0.4609	IMACS
222.174301	9.061087	0.4696	IMACS
222.174423	8.869074	0.2838	CNOC2
222.174423	8.916541	0.2412	CNOC2
222.174820	8.908166	0.4664	IMACS
222.174850	8.943486	0.2618	IMACS
222.174866	9.014757	0.3537	IMACS
222.175491	8.899057	0.3074	CNOC2
222.175690	8.880870	0.5532	FORS2
222.175919	8.977683	0.4615	CNOC2
222.176636	8.859960	0.4650	CNOC2
222.176666	8.825929	0.3204	IMACS
222.176682	9.036731	0.1312	CNOC2
222.176682	9.046879	0.9297	IMACS
222.176743	8.870021	0.8059	IMACS
222.177185	8.977679	0.2720	CNOC2
222.177612	8.830968	0.6825	IMACS
222.177765	8.885782	0.8917	IMACS+FORS2
222.177811	9.142787	0.1847	IMACS
222.177948	8.826077	0.6006	CNOC2
222.178253	8.874579	0.4033	CNOC2
222.178299	8.910164	0.6810	IMACS
222.178635	8.915078	0.5611	CNOC2
222.178879	8.822914	0.4079	CNOC2
222.178894	8.817614	0.3201	IMACS
222.178909	8.897865	1.0732	FORS2
222.179016	9.122180	0.5090	IMACS
222.179153	9.192177	0.7950	GMOS
222.179520	8.854868	0.3076	CNOC2
222.179794	9.124189	0.5444	CNOC2
222.180084	8.858018	0.4651	CNOC2
222.180740	8.854699	0.3060	CNOC2
222.182312	8.884371	0.5534	FORS2
222.182388	9.049950	0.3535	IMACS
222.182648	9.151045	0.5928	IMACS
222.182693	8.882808	0.8936	IMACS
222.182770	9.179016	0.1989	CNOC2
222.182922	8.939084	0.1889	CNOC2
222.183136	8.883332	0.4770	CNOC2
222.183136	8.887851	0.1376	IMACS
222.183151	8.883950	0.4764	FORS2

RA	Dec	z	source	l Mpc	$r_{200,\sigma}$	$r_{200,X}$
222.183167	8.822246	0.6837	IMACS
222.183212	8.864369	0.4076	CNOC2
222.183258	8.972871	0.0919	CNOC2
222.183838	9.120731	0.5146	CNOC2
222.184235	8.842810	0.3222	CNOC2
222.184494	8.816932	0.6134	CNOC2
222.184525	8.888362	0.6101	CNOC2
222.184982	8.917034	0.3087	CNOC2
222.185074	8.934668	0.8077	FORS2
222.185455	8.959918	0.4612	CNOC2
222.185684	9.035859	0.6921	IMACS
222.186066	8.972129	0.0931	CNOC2
222.186752	8.841579	0.7054	IMACS
222.187210	8.980124	0.6505	IMACS
222.187592	9.131219	0.7287	IMACS
222.187637	8.971086	0.6386	IMACS
222.187912	8.873365	0.8955	FORS2
222.187927	9.012451	0.8711	IMACS
222.188248	9.098611	0.5144	IMACS
222.188492	9.155569	0.8959	IMACS
222.188766	9.166511	0.6444	CNOC2
222.188904	9.004075	0.1673	CNOC2
222.189346	9.114197	0.3243	CNOC2
222.189346	9.130722	0.7238	IMACS
222.189743	9.008673	0.9176	IMACS
222.189896	9.128983	0.5129	CNOC2
222.189941	8.926884	0.2033	CNOC2
222.190445	8.857313	0.4664	CNOC2
222.190613	8.889252	0.6095	FORS2
222.191833	9.053389	0.3526	CNOC2
222.192307	8.983098	0.5636	IMACS
222.192398	9.002891	0.7057	IMACS
222.192551	9.090387	0.5438	CNOC2
222.192963	8.865202	0.4049	CNOC2
222.193024	8.849782	0.8069	IMACS
222.193115	8.853235	0.3082	CNOC2
222.193344	9.128616	0.4682	CNOC2
222.194122	9.144702	0.7059	IMACS
222.194717	8.809758	0.8719	IMACS
222.194901	8.875822	0.2009	FORS2
222.194992	9.182595	0.3542	CNOC2
222.195251	8.856229	0.4071	CNOC2
222.195267	8.954683	0.3073	IMACS
222.195511	8.985126	0.3728	IMACS
222.195816	9.084979	0.3076	IMACS
222.196243	8.961057	0.3070	CNOC2
222.196457	9.159102	0.2617	CNOC2
222.196609	8.915950	0.4047	CNOC2
222.196671	8.968378	0.3068	IMACS
222.196915	8.944765	0.5616	IMACS
222.197128	9.151291	0.3574	CNOC2
222.197235	9.181221	0.8237	IMACS
222.197342	8.953718	0.1928	IMACS
222.197372	9.011305	0.3526	CNOC2
222.197433	8.868369	0.5274	CNOC2
222.197754	8.962750	0.3075	IMACS
222.197891	9.011380	0.3531	CNOC2
222.198242	9.097924	0.3910	CNOC2
222.198441	9.004166	0.5073	IMACS
222.198547	8.928186	0.4702	CNOC2
222.198776	9.141904	0.5140	IMACS
222.199356	9.208499	0.7143	IMACS
222.199402	9.043610	0.7241	IMACS
222.199799	9.040490	0.8182	FORS2
222.199860	8.848786	0.6090	CNOC2
222.199921	8.964623	0.3850	IMACS
222.200943	9.204609	0.1562	CNOC2
222.201340	8.878038	0.7154	FORS2
222.201660	8.941230	0.2615	CNOC2
222.202133	9.152305	0.6771	CNOC2
222.202332	8.958585	0.6568	IMACS
222.202606	8.961629	0.6908	IMACS
222.202652	8.963228	0.5285	CNOC2
222.202957	9.065994	0.6682	CNOC2
222.202988	8.942918	0.6804	IMACS
222.203430	9.157626	0.7363	IMACS
222.203751	8.963174	0.3066	CNOC2
222.203766	8.901469	0.2705	FORS2
222.204178	8.908607	0.4792	CNOC2
222.204712	9.024413	0.6571	FORS2
222.204987	8.862645	0.5640	CNOC2
222.205399	8.876283	0.2011	CNOC2
222.205566	9.169603	0.8122	GMOS
222.205826	8.966437	0.3060	CNOC2
222.205933	9.063980	0.6698	IMACS
222.206085	8.881911	0.8691	FORS2
222.206421	9.063125	0.6704	CNOC2

RA	Dec	z	source	l Mpc	$r_{200,\sigma}$	$r_{200,X}$
222.207123	9.030962	0.2722	CNOC2
222.207306	8.852566	0.3854	FORS2
222.208145	8.831158	0.6699	IMACS
222.208344	8.864155	0.5639	CNOC2
222.208801	8.808737	0.5836	IMACS
222.208847	9.050218	0.7695	FORS2
222.209320	9.165730	0.7871	IMACS
222.210114	9.053653	0.3595	FORS2
222.210129	9.134468	0.7299	IMACS
222.210388	9.108767	0.5145	CNOC2
222.210587	9.037852	1.0190	CNOC+IMACS
222.210617	8.868763	0.2004	CNOC2
222.210632	9.138011	0.3577	IMACS
222.210663	8.939602	0.5953	CNOC2
222.211090	8.894965	0.6705	IMACS
222.211136	8.893357	0.6169	IMACS
222.211411	8.940229	0.5927	IMACS
222.211655	8.810207	1.0716	CNOC2
222.212463	9.084748	0.3587	CNOC2
222.212524	8.905321	0.8311	FORS2
222.212555	8.886061	0.6068	CNOC2
222.212860	8.942201	0.2702	CNOC2
222.213501	9.022103	0.4352	FORS2
222.214142	8.933246	0.4567	IMACS
222.214172	8.862802	0.1504	CNOC2
222.214203	8.835660	0.4473	CNOC2
222.214325	8.919368	0.6519	FORS2
222.214569	8.899681	0.7663	IMACS
222.215225	9.213845	0.6441	IMACS
222.215607	8.833772	0.3070	CNOC2
222.216949	8.937035	0.2621	CNOC2
222.217026	8.964893	0.3078	IMACS
222.218323	9.155907	0.7332	IMACS
222.218536	9.133560	0.4595	CNOC2
222.219543	9.038826	0.7226	FORS2
222.219589	8.873257	0.2710	CNOC2
222.219910	9.139568	0.4073	CNOC2
222.219986	8.986948	0.1652	CNOC2
222.220306	8.895889	0.1230	FORS2
222.220810	8.966935	0.6797	IMACS
222.220932	9.068513	0.3077	CNOC2
222.221085	9.081325	0.1205	FORS2
222.221283	9.116539	0.5673	CNOC2
222.221313	9.074634	0.2316	IMACS
222.221329	8.810707	0.2235	CNOC2
222.221329	9.134104	0.2021	CNOC2
222.221344	9.153931	0.2298	CNOC2
222.221451	9.023150	0.7065	FORS2
222.221481	8.891750	0.6106	FORS2
222.221970	9.052009	0.4086	FORS2
222.222809	8.922272	0.5155	CNOC2
222.223465	8.892023	0.3193	IMACS
222.223587	9.139963	0.8759	IMACS
222.223602	8.903562	0.6120	FORS2
222.223907	8.987459	0.1667	CNOC2
222.224640	9.044268	0.4933	FORS2
222.225632	9.033276	1.0726	IMACS
222.225693	8.897595	0.3068	FORS2
222.225891	9.002251	0.1813	CNOC2
222.225922	8.854437	0.2605	CNOC2
222.226028	8.893428	0.6663	CNOC2
222.226303	8.955104	0.5344	CNOC2
222.226379	8.896279	0.6673	IMACS
222.226791	9.033025	0.7280	FORS2
222.226913	8.893772	0.8867	IMACS
222.227066	9.104980	0.6687	CNOC2
222.227371	9.173508	0.6920	IMACS
222.227524	9.018654	0.3719	CNOC2
222.227737	9.046182	0.7300	IMACS
222.228439	8.866000	0.6668	FORS2
222.228867	9.053742	0.4055	CNOC2
222.229004	9.184777	0.2687	IMACS
222.229080	9.052999	0.7559	FORS2
222.229279	8.928778	0.6800	CNOC2
222.229462	8.897093	0.8310	IMACS
222.229462	9.120601	0.3598	CNOC2
222.229660	9.190325	0.5575	IMACS
222.230286	8.928688	0.3733	CNOC2
222.230347	9.139621	0.2288	CNOC2
222.230682	9.075714	0.2431	CNOC2
222.230789	9.193625	0.6944	GMOS
222.231094	8.975649	0.5107	CNOC2
222.231323	9.105711	0.6679	FORS2
222.231506	9.151150	0.3246	CNOC2
222.231750	9.025369	0.5157	CNOC2
222.231796	8.899561	0.3081	FORS2
222.231949	9.086425	0.3074	FORS2_HENDERSON

RA	Dec	z	source	l Mpc	$r_{200,\sigma}$	$r_{200,X}$
222.232269	8.971932	0.5095	IMACS
222.232422	9.033834	0.2709	CNOC2
222.232452	8.866629	0.2032	CNOC2
222.232544	8.945625	0.2611	CNOC2
222.232544	9.025254	0.5153	CNOC2
222.232712	8.895131	0.8258	FORS2
222.233154	8.895067	0.8250	FORS2
222.233795	9.158057	0.3247	CNOC2
222.233963	8.926050	1.5585	IMACS
222.233978	8.991438	0.2225	IMACS
222.233994	9.128579	0.3925	CNOC2
222.234146	9.174767	0.2728	CNOC2
222.234177	9.140695	0.3067	CNOC2
222.234314	8.873032	0.4671	CNOC2
222.234421	8.945989	0.2628	CNOC2
222.234589	8.958534	0.2610	IMACS
222.234802	9.017558	0.7554	IMACS
222.234940	9.088565	0.7696	FORS2,HENDERSON
222.235077	9.147455	1.0099	IMACS
222.235931	9.054012	0.5104	IMACS
222.236053	8.904008	0.3547	IMACS+FORS2
222.236130	9.110028	0.2717	CNOC2
222.236252	9.113665	0.6897	IMACS
222.236267	9.047453	0.7223	FORS2
222.237091	9.106041	0.7256	CNOC2
222.237274	8.842222	0.1506	CNOC2
222.237396	9.108104	0.1152	IMACS
222.237473	9.104942	0.8473	IMACS
222.237518	8.940283	0.3553	CNOC2
222.237717	8.908780	0.4785	FORS2
222.237946	9.208837	1.9650	CNOC2
222.237976	8.832352	0.5655	CNOC2
222.238312	8.864402	0.4145	IMACS
222.238922	9.107951	0.2732	IMACS
222.238953	8.867181	0.4145	IMACS
222.238998	8.916744	0.3551	CNOC2
222.239594	8.985734	0.4249	CNOC2
222.239777	8.863800	0.2610	CNOC2
222.239944	9.093210	0.3534	CNOC2
222.240280	9.131831	0.9618	FORS2
222.240326	9.130331	0.3476	CNOC2
222.240463	9.107469	0.5114	CNOC2
222.240555	9.143895	0.7846	FORS2
222.240570	9.031194	0.0662	CNOC2
222.240662	9.019794	0.4072	FORS2
222.240921	8.954865	0.2617	CNOC2
222.241013	9.055608	0.7218	FORS2
222.241052	8.903635	0.6682	FORS2
222.241867	9.162212	0.6261	FORS2
222.241943	9.014669	0.1079	FORS2
222.242783	8.894027	0.6632	IMACS
222.242889	9.159016	0.6031	FORS2
222.243347	9.052748	1.0722	FORS2
222.243622	8.842918	0.6377	CNOC2
222.243683	9.123655	0.8878	IMACS
222.243729	9.115744	0.9743	IMACS
222.243790	9.124579	0.4662	CNOC2
222.244110	9.128202	0.4655	CNOC2
222.244186	8.902751	0.1924	CNOC2
222.244232	8.948930	0.6828	IMACS
222.244431	8.880876	0.5164	FORS2
222.244553	9.123167	0.7246	FORS2,HENDERSON
222.244675	8.960745	0.2605	CNOC2
222.244843	9.052055	1.0721	IMACS
222.244888	8.821686	0.2701	CNOC2	XR14h25,OP14h11,OP14h12
222.244904	9.095343	0.7365	CNOC2
222.244980	9.146265	0.2283	CNOC2
222.245041	8.882588	0.4357	IMACS
222.245071	9.026488	1.0016	IMACS
222.245132	9.117789	0.3604	IMACS
222.245178	9.029249	1.0731	FORS2
222.245896	9.124956	0.7238	IMACS+FORS2
222.245911	9.159219	0.8423	FORS2
222.246017	9.163512	0.8724	FORS2
222.246262	9.113774	0.6055	FORS2
222.246368	9.162789	0.8716	IMACS
222.246445	9.202171	0.4901	IMACS
222.246552	9.196494	0.2385	CNOC2
222.246674	8.951415	0.2625	CNOC2
222.246918	8.894777	0.3594	CNOC2
222.246964	9.149017	0.8430	FORS2
222.247070	9.137438	0.5197	FORS2
222.247345	9.046425	1.2490	FORS2
222.248108	9.008388	1.0784	FORS2
222.249084	8.893864	0.7677	FORS2
222.249146	9.062271	0.6696	FORS2
222.249542	8.884375	0.9286	IMACS

RA	Dec	z	source	l Mpc	$r_{200,\sigma}$	$r_{200,X}$
222.249649	9.167595	0.8732	FORS2
222.250076	8.809224	1.1651	CNOC2
222.250168	8.905810	0.6091	CNOC2
222.250397	8.883586	0.7669	FORS2
222.250610	8.973826	0.6646	CNOC2
222.251495	9.036728	0.7046	FORS2
222.251678	9.125627	0.5563	CNOC2+FORS2
222.251984	8.826203	0.7055	IMACS
222.252228	9.150984	0.6039	CNOC2
222.252441	9.073886	0.7145	IMACS+FORS2
222.252640	8.879565	0.3250	CNOC2
222.252747	8.975509	0.5140	IMACS
222.253082	8.868390	0.3734	FORS2
222.253113	9.207394	0.3965	GMOS
222.253494	8.824102	0.2722	CNOC2	XR14h25,OP14h11,OP14h12
222.254120	9.104597	0.3591	CNOC2
222.254379	8.863515	0.4459	FORS2
222.254547	8.826755	0.3735	CNOC2
222.254562	8.811690	0.2699	IMACS	XR14h25,OP14h11,OP14h12
222.254807	8.894818	0.1221	CNOC2
222.254868	8.966076	0.2310	CNOC2
222.255142	8.824746	0.3737	IMACS
222.255325	9.189733	0.3928	GMOS
222.256058	8.944957	0.3910	CNOC2
222.256485	9.123270	0.3591	CNOC2
222.256546	9.111038	0.3588	CNOC2
222.257095	9.128016	0.5220	IMACS+FORS2
222.257278	8.835176	0.1837	CNOC2
222.257385	9.067975	0.5109	CNOC2
222.257477	8.888723	0.3863	FORS2+FORS2
222.257584	9.157787	0.8714	IMACS
222.257629	9.172064	0.7912	IMACS
222.257782	9.103523	0.7058	IMACS
222.258316	9.130725	0.3594	CNOC2
222.258362	9.069006	0.4564	IMACS
222.258453	8.894013	0.1227	CNOC2
222.259583	9.106329	0.7241	FORS2
222.259598	9.156620	0.2040	CNOC2
222.259735	8.827057	0.2744	CNOC2
222.259750	9.130545	0.8400	FORS2_HENDERSON
222.260193	8.981993	0.4062	CNOC2
222.260223	8.836234	0.4063	IMACS
222.260284	9.187358	0.7831	GMOS
222.260300	9.055388	0.7266	FORS2
222.260406	9.106243	0.7462	CNOC2
222.260864	8.825043	0.2715	CNOC2	XR14h25,OP14h11,OP14h12
222.260992	8.903643	0.6103	FORS2
222.261047	8.814938	0.2736	IMACS
222.261322	8.910309	0.7338	IMACS
222.261353	9.114691	0.3623	IMACS
222.261581	8.883760	0.4054	CNOC2
222.261597	9.110366	0.2721	FORS2
222.262238	8.827571	0.2709	CNOC2	XR14h25,OP14h11,OP14h12
222.262329	9.043614	0.6112	CNOC2
222.262482	8.917667	0.3735	FORS2
222.262817	9.107225	0.3590	CNOC2
222.262970	9.069317	0.6103	IMACS
222.263184	9.072916	0.7456	IMACS
222.263275	9.052189	0.8553	FORS2
222.263626	9.046697	0.0907	FORS2
222.263657	9.205411	0.3004	IMACS
222.263824	9.175605	0.2281	CNOC2
222.264420	9.110502	0.3601	CNOC2
222.264526	8.948439	0.5528	CNOC2
222.264908	9.057024	0.7461	FORS2
222.264999	8.885559	0.4053	CNOC2
222.265106	8.824416	0.7805	IMACS
222.265167	9.114296	0.3591	FORS2
222.266102	8.813136	0.3893	FORS2
222.266205	9.066159	0.3260	FORS2_HENDERSON
222.266418	9.193402	0.3230	CNOC2
222.266516	8.812305	0.6831	IMACS
222.266861	9.042432	0.1130	IMACS
222.266907	9.109499	0.1076	FORS2
222.267014	9.046988	0.3282	CNOC2
222.267517	8.818145	0.2714	CNOC2+FORS2	XR14h25,OP14h11,OP14h12	XR14h25,OP14h11	...
222.267731	9.112919	0.3596	FORS2
222.267776	9.120475	0.3598	CNOC2
222.267944	9.079436	0.7215	FORS2_HENDERSON
222.267960	9.109269	0.3589	CNOC2
222.267975	8.893336	0.6124	FORS2
222.268127	9.061093	0.3723	FORS2
222.268311	9.088237	0.7653	IMACS
222.268433	9.147175	0.3075	CNOC2
222.268478	9.096628	0.7413	IMACS
222.268784	8.978954	0.5075	CNOC2
222.268860	8.812845	0.4439	CNOC2

RA	Dec	z	source	l Mpc	$r_{200,\sigma}$	$r_{200,X}$
222.269043	9.151514	0.5565	FORS2,HENDERSON
222.269821	8.932162	0.6665	FORS2
222.269974	9.104242	0.1963	CNOC2
222.270660	8.966984	0.2612	CNOC2
222.270676	8.812028	0.6829	IMACS
222.270782	8.859092	0.4146	CNOC2
222.271011	9.164037	0.6149	FORS2,HENDERSON
222.271179	9.119898	0.3594	FORS2,HENDERSON
222.271408	9.056388	0.6671	FORS2
222.271439	8.997154	0.6811	IMACS
222.272095	9.190977	0.3232	CNOC2
222.272156	8.925324	0.5095	CNOC2
222.272430	8.818433	0.2718	CNOC2	XR14h25,OP14h11,OP14h12	XR14h25,OP14h11	XR14h25,OP14h12
222.272491	9.106946	0.3585	FORS2
222.272522	9.097917	0.4555	CNOC2
222.272568	9.145982	0.3735	IMACS
222.272903	9.098201	0.6665	CNOC2
222.273026	9.002645	0.7035	FORS2
222.273056	9.063896	0.6669	FORS2,HENDERSON
222.273270	9.097246	0.7386	FORS2
222.273544	9.092203	0.7389	IMACS+FORS2
222.273804	9.184624	0.4760	GMOS
222.274139	9.104429	0.5506	CNOC2
222.274185	9.191609	0.3241	FORS2
222.274216	9.100537	0.3294	FORS2
222.274277	9.137749	0.5315	IMACS
222.274506	8.845294	0.1301	IMACS
222.274979	9.088628	1.2600	FORS2
222.275009	9.097221	0.7357	CNOC2
222.275696	8.896801	0.2006	CNOC2
222.276428	8.932095	0.6832	IMACS+FORS2
222.276596	9.173922	0.7914	FORS2
222.276642	9.154059	0.8116	IMACS
222.276779	9.131864	0.5925	FORS2
222.276794	8.942210	0.1510	CNOC2
222.277115	8.915423	0.6128	IMACS
222.277252	8.922175	0.3737	CNOC2
222.277298	8.800950	0.3742	FORS2
222.277618	9.030077	0.5108	CNOC2
222.277924	9.212028	0.5287	GMOS
222.277954	9.011007	0.5107	CNOC2
222.278214	9.046559	0.7740	IMACS
222.278320	8.904261	0.6821	IMACS
222.278473	9.060783	0.6690	CNOC2
222.278549	9.106930	0.6148	FORS2
222.278763	8.839302	0.5558	CNOC2
222.280273	8.956167	0.6803	IMACS
222.280304	8.971218	0.2729	CNOC2
222.280441	9.092066	0.4838	CNOC2
222.280670	8.827098	0.8702	IMACS
222.280823	8.882748	0.7391	FORS2
222.281021	9.057775	0.8773	FORS2
222.281372	8.899079	0.7368	FORS2
222.281403	9.058700	0.6910	FORS2
222.281540	9.217107	2.0200	CNOC2
222.281738	8.895695	0.7367	FORS2
222.282089	9.126063	0.3597	CNOC2
222.282181	9.051158	0.4055	CNOC2
222.282471	8.913059	0.6836	IMACS
222.282898	9.093715	0.6449	FORS2
222.283925	9.174814	0.8246	IMACS+FORS2
222.283966	8.814435	0.6324	CNOC2
222.283981	9.159891	0.7321	FORS2
222.284103	9.072812	0.7840	IMACS+FORS2
222.284103	9.213796	0.2277	CNOC2
222.284164	9.196806	0.7847	CNOC2
222.284180	8.921095	0.6833	IMACS
222.285065	9.119657	0.7634	CNOC2
222.285080	9.042720	0.1893	CNOC2
222.285309	8.895571	0.7330	IMACS
222.285934	8.823910	0.5568	CNOC2
222.286301	8.826134	0.5564	IMACS
222.286484	9.046614	0.3976	CNOC2
222.286652	8.883921	0.0401	CNOC2
222.287170	8.892442	0.8098	FORS2
222.287170	9.017780	0.7673	IMACS
222.287201	8.945724	0.7039	IMACS
222.287277	9.057951	0.3724	CNOC2
222.287338	8.909056	0.6128	IMACS
222.287766	9.167438	1.0890	GMOS
222.287994	9.125701	0.3591	CNOC2
222.288132	8.783913	0.7655	FORS2
222.288177	8.916215	0.6124	IMACS
222.288208	8.918160	0.6138	IMACS
222.288330	9.149747	0.7043	FORS2,HENDERSON
222.288605	8.796601	0.3556	FORS2
222.288879	9.083202	0.6133	CNOC2

RA	Dec	z	source	l Mpc	$r_{200,\sigma}$	$r_{200,X}$
222.288925	8.920014	0.6081	CNOC2
222.289383	9.179708	0.7039	FORS2
222.290375	9.131387	0.6445	IMACS
222.290421	8.822159	0.6834	FORS2
222.290421	9.175499	0.7867	CNOC2
222.291061	8.870423	0.4667	CNOC2
222.291183	9.048149	0.3974	CNOC2
222.291428	8.861707	0.6920	IMACS
222.291626	8.820546	0.5557	FORS2
222.292023	8.869231	0.4466	FORS2
222.292099	8.823580	0.0449	CNOC2
222.292099	9.185936	0.6068	GMOS
222.292206	8.870881	0.4673	CNOC2+FORS2
222.292236	8.824364	0.0448	CNOC2
222.292511	8.829349	0.6829	IMACS
222.292557	8.879371	0.2980	CNOC2
222.293076	8.885097	0.7649	FORS2
222.293472	9.153410	0.4692	CNOC2+FORS2
222.293625	8.962991	0.5153	CNOC2
222.294037	9.113104	0.5566	CNOC2
222.294769	9.200303	0.2279	CNOC2
222.294968	8.862334	0.8123	FORS2
222.294983	9.195661	0.5311	CNOC2
222.295166	8.821897	0.3560	IMACS
222.295197	8.862885	0.8095	FORS2
222.295227	9.130626	0.6234	CNOC2
222.295609	8.917067	0.3083	CNOC2
222.295715	8.793310	0.6015	FORS2
222.295898	8.996163	0.3909	CNOC2
222.296799	8.815510	0.2696	FORS2	XR14h25,OP14h11,OP14h12	XR14h25,OP14h11	XR14h25,OP14h12
222.297638	9.060338	0.3724	CNOC2
222.298279	8.974724	0.5080	CNOC2
222.298386	9.011944	0.4078	CNOC2
222.298904	8.874625	0.6918	FORS2
222.299057	9.176435	0.7948	FORS2
222.299088	9.030520	0.6076	IMACS
222.299225	9.199642	0.7653	IMACS
222.299408	8.839320	0.2728	FORS2	XR14h25,OP14h11,OP14h12	XR14h25,OP14h11	XR14h25,OP14h12
222.299637	9.189580	0.3962	CNOC2
222.299713	8.981148	0.1212	IMACS
222.299835	8.923107	0.3913	CNOC2
222.299988	9.178743	0.1663	FORS2
222.300186	9.110021	0.2286	FORS2
222.300323	9.190220	0.5309	CNOC2
222.300446	9.122556	0.5988	FORS2
222.300537	9.186589	0.1127	CNOC2
222.300644	8.844523	0.7370	FORS2
222.300812	8.923785	0.2704	IMACS
222.300919	9.004849	0.1951	CNOC2
222.301270	8.941137	0.6075	IMACS
222.301346	9.204906	0.2278	CNOC2
222.301636	8.912092	0.2363	CNOC2
222.301636	8.946222	0.6076	IMACS
222.301758	8.885394	0.2694	FORS2	XR14h25,OP14h11,OP14h12	XR14h25,OP14h11	XR14h25,OP14h12
222.301773	8.825053	0.5422	IMACS
222.301895	9.122047	0.3900	CNOC2
222.302307	9.077075	0.4577	FORS2_HENDERSON
222.302338	8.837167	0.2708	CNOC2	XR14h25,OP14h11,OP14h12	XR14h25,OP14h11	XR14h25,OP14h12
222.302612	9.169748	0.2890	FORS2_HENDERSON
222.302795	9.065173	0.1951	CNOC2
222.303207	8.833523	0.2720	IMACS	XR14h25,OP14h11,OP14h12	XR14h25,OP14h11	XR14h25,OP14h12
222.303314	8.826045	0.5430	FORS2
222.303467	8.829941	0.5427	FORS2
222.303528	9.059092	0.6367	CNOC2
222.303528	9.066189	0.3239	FORS2
222.303635	8.834722	0.7458	IMACS
222.303787	8.832851	0.2713	CNOC2	XR14h25,OP14h11,OP14h12	XR14h25,OP14h11	XR14h25,OP14h12
222.303925	8.826388	0.2705	CNOC2	XR14h25,OP14h11,OP14h12	XR14h25,OP14h11	XR14h25,OP14h12
222.304047	8.824470	0.2702	IMACS+FOR2	XR14h25,OP14h11,OP14h12	XR14h25,OP14h11	XR14h25,OP14h12
222.304123	8.845627	0.5123	FORS2
222.304504	9.107413	0.2719	CNOC2
222.305054	9.168987	0.8118	IMACS
222.305252	9.020595	0.7993	IMACS
222.305267	8.855733	0.4677	FORS2
222.305389	8.848171	0.1970	FORS2
222.306122	8.911522	0.3741	IMACS
222.306351	8.920591	0.1228	CNOC2
222.306625	8.948765	0.4402	FORS2_HENDERSON
222.306793	9.090408	0.4706	IMACS
222.306870	9.214215	0.7014	GMOS
222.306992	8.979200	0.6759	CNOC2
222.307053	9.096579	0.3730	CNOC2
222.307236	9.094345	0.6383	IMACS
222.307449	9.195963	0.8497	FORS2
222.307724	9.138002	0.6995	FORS2_HENDERSON
222.308044	9.139635	0.6079	CNOC2
222.308212	9.182461	0.8698	GMOS

RA	Dec	z	source	l Mpc	$r_{200,\sigma}$	$r_{200,X}$
222.308472	9.044571	0.2046	CNOC2
222.309174	8.894652	0.7678	FORS2
222.309418	8.924674	0.1233	CNOC2
222.309464	8.946467	0.4148	IMACS
222.309631	8.978157	0.5129	CNOC2
222.309662	8.941477	0.6057	IMACS
222.309860	8.857689	0.2706	CNOC2	XR14h25,OP14h11,OP14h12	XR14h25,OP14h11	...
222.310287	8.875787	0.7493	IMACS
222.310486	8.961434	0.5646	CNOC2
222.310562	9.005863	0.5144	CNOC2
222.310577	9.136050	0.3243	CNOC2
222.310883	9.137680	0.7853	CNOC2
222.311462	8.804592	0.4902	FORS2
222.311615	8.840489	0.3550	FORS2
222.311722	9.208491	0.7051	IMACS+FORS2
222.311935	9.124514	0.8717	IMACS
222.311951	9.059591	0.3727	IMACS
222.312012	9.186824	0.3928	CNOC2
222.312073	9.190141	0.8106	IMACS
222.312271	9.192825	0.8493	IMACS
222.312515	8.963562	0.5149	CNOC2
222.312531	9.042291	0.6964	IMACS
222.312622	9.015954	0.1993	CNOC2
222.312668	8.827275	1.2372	FORS2
222.312759	9.014580	0.6073	IMACS
222.312897	8.949209	0.5642	CNOC2
222.312927	9.135723	0.7394	CNOC2	XR14h25,OP14h11,OP14h12	XR14h25,OP14h11	...
222.312958	8.844748	0.2699	CNOC2
222.313049	8.916136	0.7397	IMACS
222.313202	8.794576	0.5184	FORS2
222.313446	8.864077	0.2698	CNOC2	XR14h25,OP14h11,OP14h12
222.314529	9.039508	0.6792	IMACS
222.314636	9.100773	0.6070	CNOC2
222.314896	9.193680	0.6942	IMACS
222.315002	9.126187	0.6671	IMACS
222.315063	9.005832	0.2637	CNOC2
222.315094	9.189501	0.3920	CNOC2
222.315231	8.961954	0.8935	IMACS
222.315231	9.061241	0.3729	IMACS
222.315247	8.842328	0.8695	FORS2
222.315506	9.185944	0.6069	FORS2
222.315613	9.082608	0.4707	IMACS
222.315796	8.947769	0.6920	CNOC2
222.315887	9.188810	0.4635	FORS2
222.315918	9.130322	0.6444	IMACS
222.316193	8.860279	0.7651	FORS2
222.316254	9.003922	0.2637	CNOC2
222.316254	9.181342	0.6072	CNOC2
222.316376	8.959778	0.8360	IMACS
222.316422	9.090228	0.2285	CNOC2
222.316559	8.990728	0.5853	IMACS
222.316833	9.176409	0.7856	IMACS+FORS2
222.317276	9.012713	0.3746	CNOC2
222.317352	9.059492	0.3066	CNOC2
222.317566	8.873166	0.8096	FORS2
222.317703	8.787795	0.5866	FORS2
222.317764	9.038797	0.7826	IMACS
222.317780	9.131174	0.7891	CNOC2
222.317856	8.864001	1.0122	IMACS+FORS2
222.317963	9.097066	0.5121	CNOC2
222.318222	9.029824	0.5565	IMACS
222.318420	9.216498	0.5562	IMACS
222.319153	9.189860	0.3939	FORS2
222.319397	8.966394	0.8938	IMACS
222.319641	9.208099	0.7076	CNOC2
222.320023	9.189780	0.3926	IMACS
222.320053	8.828805	0.2876	IMACS
222.320068	8.969729	0.5085	FORS2,HENDERSON
222.320145	8.852457	1.0107	FORS2
222.320557	8.822059	0.5565	CNOC2
222.320847	9.183854	0.3249	CNOC2
222.320862	9.054163	0.3287	CNOC2
222.321030	9.096949	0.3944	CNOC2
222.321121	8.900763	0.4758	CNOC2
222.321121	9.003052	0.0411	CNOC2
222.321304	9.182591	0.3062	CNOC2
222.321823	8.937614	0.5142	CNOC2
222.322205	9.138993	0.3927	CNOC2
222.322296	8.998018	0.3731	CNOC2
222.322433	8.999312	0.3741	CNOC2
222.323151	9.203436	0.9041	CNOC2
222.323486	8.882640	0.4548	CNOC2
222.323746	9.176188	0.4641	CNOC2
222.323944	9.214511	0.7043	IMACS
222.324371	9.177833	0.6072	CNOC2
222.324387	8.826750	0.3897	CNOC2
222.324432	9.058495	0.6928	IMACS

RA	Dec	z	source	l Mpc	$r_{200,\sigma}$	$r_{200,X}$
222.324829	9.176183	0.4650	GMOS
222.324982	9.041898	0.7370	IMACS
222.325134	8.974451	0.4593	FORS2_HENDERSON
222.325241	8.932414	0.2038	FORS2_HENDERSON
222.325455	9.051585	0.2710	CNOC2
222.325500	8.857442	0.1949	FORS2
222.326004	9.157025	0.6468	CNOC2
222.326080	9.160384	0.6077	FORS2
222.326126	9.180217	0.6073	IMACS
222.326172	8.957099	0.3526	CNOC2
222.326523	8.924858	0.2733	IMACS	XR14h22,OP14h10,OP14h13
222.326523	9.093162	0.2614	CNOC2
222.327438	9.040149	0.6253	IMACS
222.327759	9.185867	0.3232	CNOC2
222.327820	8.813732	0.3026	IMACS
222.327850	9.188036	0.3260	CNOC2
222.327972	8.952249	0.6932	FORS2_HENDERSON
222.328125	9.146202	0.6072	IMACS
222.328186	8.995716	0.5130	CNOC2
222.328293	8.853438	1.5249	IMACS
222.328506	9.195058	0.5097	FORS2
222.329086	9.740898	0.2305	CNOC2
222.329330	9.194369	0.5384	CNOC2
222.329453	9.022181	0.6374	CNOC2
222.330093	9.740592	0.4167	CNOC2
222.330856	9.156437	0.7841	CNOC2
222.330994	8.842752	0.6167	IMACS
222.331085	8.883386	0.8707	FORS2
222.331146	9.034634	0.5405	CNOC2
222.331177	8.828408	0.4065	IMACS
222.331299	8.976072	0.5063	CNOC2
222.331635	9.158670	0.8689	GMOS
222.331863	9.178950	0.6063	GMOS
222.332642	9.155592	0.7826	IMACS
222.332733	8.987241	0.4601	FORS2_HENDERSON
222.332901	9.203149	0.3607	CNOC2
222.333420	9.005701	0.3524	FORS2_HENDERSON
222.333618	9.523591	0.5836	CNOC2
222.334213	9.473379	0.1655	CNOC2
222.334290	9.043526	0.4588	CNOC2
222.334305	9.090546	0.3617	IMACS
222.334549	9.062172	0.2352	IMACS
222.334579	8.910266	0.7471	IMACS
222.334854	9.728400	0.1976	CNOC2
222.335617	8.954273	1.2854	FORS2
222.335739	9.681327	0.1313	CNOC2
222.336243	9.479238	0.5379	CNOC2
222.336395	8.999467	0.8786	IMACS
222.336578	9.655559	0.4844	CNOC2
222.336670	8.845733	0.2041	IMACS
222.336716	9.410271	0.3250	CNOC2
222.336853	9.093370	0.6370	CNOC2
222.337173	8.946265	0.4008	FORS2
222.337250	8.964071	0.6135	IMACS
222.337280	8.978045	0.5067	CNOC2
222.337341	9.373013	0.5073	CNOC2
222.337357	8.939104	0.5142	IMACS
222.337402	9.051526	0.2290	CNOC2
222.337448	8.848129	0.3021	IMACS
222.337463	8.888930	0.3227	IMACS
222.337830	9.197186	0.3217	CNOC2
222.337875	9.757017	0.3799	CNOC2
222.338745	9.222256	0.5565	CNOC2
222.338760	9.017178	0.8763	IMACS
222.338882	9.465571	0.3542	CNOC2
222.339050	8.968216	0.6125	IMACS
222.339157	9.025633	0.2714	CNOC2
222.339188	8.977236	0.2645	CNOC2
222.339417	9.487593	0.5343	FORS2_HENDERSON
222.339539	8.986378	0.2630	CNOC2
222.339539	9.564185	0.5444	CNOC2
222.339813	9.474667	0.1643	CNOC2
222.339828	8.932009	0.2612	IMACS+FORS2
222.339905	9.467453	0.3543	CNOC2
222.340195	9.284084	0.2826	CNOC2
222.340561	9.269243	0.1975	CNOC2
222.340622	8.934341	0.5145	FORS2
222.340714	9.328347	0.4371	CNOC2
222.340805	9.377315	0.3221	CNOC2
222.341095	8.970867	0.5134	IMACS+FORS2
222.341324	8.985067	0.5087	CNOC2
222.341385	9.030391	0.5819	IMACS
222.341660	8.918587	0.5416	CNOC2
222.342255	8.983171	0.6931	IMACS
222.342255	9.042350	0.1999	FORS2_HENDERSON
222.342300	9.033284	0.3073	CNOC2
222.342316	8.985434	0.5057	CNOC2

RA	Dec	z	source	l Mpc	$r_{200,\sigma}$	$r_{200,X}$
222.342880	9.747797	0.2981	CNOC2
222.343094	9.793854	0.2005	CNOC2
222.343231	8.965660	0.5066	FORS2
222.343536	9.030851	0.8769	IMACS
222.343933	8.840231	0.5428	CNOC2
222.344116	8.918572	0.5422	CNOC2
222.344543	9.146198	0.6072	GMOS
222.345093	9.178470	0.5124	CNOC2
222.345261	8.981601	0.5126	CNOC2
222.345383	8.990660	0.4600	CNOC2
222.345535	9.233995	0.4411	CNOC2
222.346405	9.693359	0.3469	CNOC2
222.346466	9.627476	0.1970	CNOC2
222.346481	9.151392	0.8838	IMACS
222.346481	9.191544	0.7414	IMACS
222.346512	9.730286	0.2484	CNOC2
222.346786	9.030651	0.8151	IMACS
222.347122	9.129575	0.6441	CNOC2
222.347565	8.976203	0.6929	IMACS
222.347595	9.005067	0.6400	IMACS
222.347626	9.107655	0.8719	IMACS
222.347885	9.254054	0.1660	CNOC2
222.347992	8.987536	0.5123	CNOC2
222.348099	9.454446	0.5463	CNOC2
222.348251	9.099609	0.5409	FORS2,HENDERSON
222.348480	9.409741	0.5702	CNOC2
222.348740	9.116754	0.6810	IMACS
222.348770	8.931328	0.3075	IMACS
222.348816	8.891711	0.4754	CNOC2
222.348907	9.031704	0.3242	FORS2,HENDERSON
222.348953	9.028274	0.2287	CNOC2
222.349106	9.245433	0.6634	CNOC2
222.349182	8.931726	0.3084	CNOC2
222.349228	8.990904	0.3730	CNOC2
222.349274	8.849147	0.6088	IMACS
222.349289	9.192777	0.7411	IMACS
222.349579	9.337120	0.2292	CNOC2
222.349594	8.937975	0.2366	FORS2,HENDERSON
222.350021	9.520896	0.5110	FORS2,HENDERSON
222.350327	9.098439	0.5392	CNOC2
222.350372	9.735682	0.2487	CNOC2
222.350418	8.972203	0.5062	CNOC2
222.350479	9.034642	0.3247	CNOC2
222.350586	9.473404	0.5369	CNOC2
222.350815	9.620244	0.6382	CNOC2
222.351410	9.529976	0.2606	CNOC2
222.351425	9.485249	0.5384	CNOC2
222.351486	9.100082	0.5399	CNOC2
222.351944	9.334068	0.3060	CNOC2
222.351959	8.978385	0.6208	CNOC2
222.352066	9.470175	0.5091	FORS2,HENDERSON
222.352158	9.791671	0.3697	CNOC2
222.352188	9.385375	0.3113	CNOC2
222.352188	9.462588	0.5559	CNOC2
222.352432	9.304772	0.5084	CNOC2
222.352509	8.813448	0.6835	IMACS
222.352631	9.164150	0.6781	IMACS
222.352737	9.149533	0.3616	CNOC2
222.353043	9.742728	0.4740	CNOC2
222.353500	8.883855	0.1315	CNOC2
222.353806	9.127769	0.3515	IMACS
222.354019	9.117123	0.5120	IMACS
222.354095	9.497470	0.5339	CNOC2
222.354111	9.446424	0.3523	CNOC2
222.354660	8.929237	0.3635	FORS2,HENDERSON
222.354660	9.447141	0.3534	CNOC2
222.354706	9.660241	0.1851	CNOC2
222.354813	9.212790	3.1700	CNOC2
222.355042	9.074556	0.4108	CNOC2
222.355148	8.987292	0.8855	IMACS
222.355209	9.033450	0.3063	CNOC2
222.355347	9.117347	0.3742	CNOC2
222.355362	9.486117	0.3775	CNOC2
222.355408	9.509809	0.3526	CNOC2
222.355667	9.612704	0.2780	CNOC2
222.355728	9.213263	0.5924	IMACS
222.355820	9.049846	0.2291	IMACS
222.356018	9.301228	0.3244	CNOC2
222.356369	9.336162	0.2290	CNOC2
222.356415	9.494324	0.2981	CNOC2
222.356552	8.927071	0.5435	CNOC2
222.356628	9.519347	0.4070	FORS2,HENDERSON
222.356644	8.847940	0.6070	CNOC2
222.357162	9.094097	0.5689	IMACS
222.357376	9.127218	0.8513	IMACS
222.357452	9.020370	0.4708	LDSS2
222.357574	9.788733	0.2011	CNOC2

RA	Dec	z	source	l Mpc	$r_{200,\sigma}$	$r_{200,X}$
222.357666	9.510591	0.3512	CNOC2
222.357834	8.936098	0.5654	FORS2
222.357834	9.146313	0.2237	FORS2,HENDERSON
222.357941	8.824694	0.3758	CNOC2
222.358063	9.166571	0.4690	IMACS
222.358109	9.368428	0.3542	CNOC2
222.358154	8.837587	0.6833	IMACS
222.358368	9.524487	0.5439	CNOC2
222.358612	9.053067	0.2725	FORS2,HENDERSON
222.358841	9.179770	0.9190	IMACS
222.358871	9.105269	0.4738	FORS2,HENDERSON	XR14h11,OP14h35,OP14h37
222.358902	9.357954	0.4097	CNOC2
222.359039	9.108908	0.3668	FORS2,HENDERSON
222.359222	9.559881	0.5447	CNOC2
222.359299	9.117584	0.3740	FORS2,HENDERSON
222.359375	9.484564	0.3856	CNOC2
222.359589	9.028276	0.3507	CNOC2
222.359589	9.591772	0.3246	CNOC2
222.359741	9.104443	0.4726	CNOC2	XR14h11,OP14h35,OP14h37
222.359818	9.113042	0.4732	FORS2,HENDERSON	XR14h11,OP14h35,OP14h37
222.359848	9.648274	0.5348	CNOC2
222.360046	9.482778	0.3850	CNOC2
222.360245	9.156972	0.4615	GMOS
222.360382	8.891242	0.5054	CNOC2
222.360504	8.944313	0.3634	CNOC2
222.360519	9.244989	0.3024	CNOC2
222.360565	9.122648	0.3778	CNOC2
222.360580	9.499488	0.5904	CNOC2
222.360870	8.971139	0.0407	IMACS
222.361038	8.841831	0.6071	CNOC2
222.361053	9.278512	0.4049	CNOC2
222.361130	9.358991	0.4082	CNOC2
222.361282	9.033383	0.5564	FORS2,HENDERSON
222.361343	8.997274	0.6818	FORS2,HENDERSON
222.361475	8.976319	0.8865	FORS2
222.361664	9.619443	0.7010	CNOC2
222.361694	9.484247	0.6144	FORS2,HENDERSON
222.361710	9.441237	0.0295	CNOC2
222.361816	9.683558	0.2789	CNOC2
222.362015	9.088082	0.4723	FORS2	XR14h11,OP14h35,OP14h37	XR14h11,OP14h35	...
222.362122	8.869619	0.2700	CNOC2	XR14h22,XR14h25,OP14h10,OP14h13
222.362167	9.086471	0.7149	FORS2
222.362167	9.535335	0.7368	CNOC2
222.362213	9.055022	0.8716	IMACS
222.362213	9.124052	0.3736	CNOC2
222.362503	9.175923	0.4536	CNOC2
222.362885	8.869418	0.2693	CNOC2	XR14h22,XR14h25,OP14h10,OP14h13
222.363358	9.570778	0.1315	CNOC2
222.363434	9.653768	0.2569	CNOC2
222.363480	9.479258	0.4064	CNOC2
222.363495	9.520526	0.3517	CNOC2
222.363617	9.767238	0.2797	CNOC2
222.363632	9.481307	0.5475	FORS2,HENDERSON
222.363892	8.923414	1.0223	IMACS
222.363892	8.945040	0.4289	CNOC2
222.364014	8.858439	0.2698	IMACS	XR14h22,XR14h25,OP14h10,OP14h13
222.364120	8.981481	0.3736	FORS2+FORS2
222.364182	9.001575	0.4070	CNOC2
222.364288	8.958459	0.7676	FORS2
222.364578	8.965006	0.8791	CNOC2
222.364670	9.166435	0.4641	IMACS
222.364685	9.207498	0.4063	CNOC2
222.364746	8.879570	0.3236	CNOC2
222.364746	9.396131	0.3267	CNOC2
222.364792	9.493841	0.5350	CNOC2
222.364853	9.479757	0.5449	CNOC2
222.364929	9.044064	0.5416	FORS2,HENDERSON
222.365082	9.290483	0.1982	CNOC2
222.365372	9.684708	0.2032	CNOC2
222.365448	9.093954	0.3064	FORS2,HENDERSON
222.365448	9.160232	0.0302	CNOC2
222.365753	9.490579	0.5335	CNOC2
222.365768	9.608572	0.4593	CNOC2
222.365814	9.403427	0.3860	CNOC2
222.366089	8.960384	0.7679	FORS2
222.366135	8.963510	0.8572	FORS2
222.366394	8.944322	0.5925	CNOC+IMACS
222.366409	8.957043	0.3253	CNOC2
222.366531	9.694608	0.2013	CNOC2
222.366684	9.691989	0.2037	CNOC2
222.366882	9.082216	0.4734	IMACS+FORS2	XR14h11,OP14h35,OP14h37	XR14h11,OP14h35	XR14h11,OP14h37
222.367279	9.083441	0.3526	FORS2,HENDERSON
222.367310	9.182412	0.3788	IMACS
222.367340	9.734321	0.3307	CNOC2
222.367386	9.639885	0.5362	CNOC2
222.367554	8.843743	0.3732	CNOC2
222.367676	9.340596	0.2818	CNOC2

RA	Dec	z	source	l Mpc	$r_{200,\sigma}$	$r_{200,X}$
222.367706	8.989010	0.8825	IMACS
222.367828	9.482464	0.6836	FORS2_HENDERSON
222.367828	9.483197	0.5106	CNOC2
222.367859	9.109814	0.7360	IMACS
222.367996	9.091662	0.3063	CNOC2
222.368027	9.139951	0.3695	CNOC2
222.368256	9.201168	0.3710	CNOC2
222.368439	9.031586	0.6399	CNOC2
222.368713	8.978093	0.5085	CNOC2
222.368851	9.557802	0.6987	CNOC2
222.368866	8.955852	0.8547	FORS2
222.368896	9.104669	0.8130	IMACS
222.369232	8.811412	0.3612	IMACS
222.369385	8.954130	0.5640	CNOC2
222.369629	9.559412	0.6395	CNOC2
222.369644	9.515061	0.2593	CNOC2
222.369751	9.783391	0.3067	CNOC2
222.369873	9.086797	0.6377	IMACS
222.370026	8.812956	0.3239	CNOC2
222.370102	9.148552	0.4688	CNOC2
222.370102	9.149803	0.7039	GMOS
222.370163	9.657371	0.5356	CNOC2
222.370300	9.317238	0.5073	CNOC2
222.370453	8.828517	0.2689	CNOC2	XR14h25,OP14h10
222.370453	8.880660	0.4006	CNOC2
222.370453	9.094371	0.2095	CNOC2
222.370499	9.004635	0.1250	CNOC2
222.370499	9.028434	0.7517	IMACS
222.370544	8.927020	0.8572	FORS2_HENDERSON
222.370560	9.507362	0.5832	CNOC2
222.370575	8.951005	0.6921	FORS2
222.370575	9.473776	0.3769	CNOC2
222.370704	9.074867	0.7146	IMACS
222.370704	9.074867	0.7149	IMACS
222.370728	8.949153	0.3590	FORS2
222.370834	9.093440	0.2435	CNOC2
222.370865	8.994757	0.8558	FORS2_HENDERSON
222.370911	9.524443	0.3817	CNOC2
222.370987	9.037671	0.4731	FORS2_HENDERSON	XR14h11,OP14h35,OP14h37
222.371140	9.508233	0.5859	CNOC2
222.371216	8.968572	0.5077	FORS2
222.371262	8.895011	0.8542	IMACS
222.371353	8.835675	0.7665	IMACS
222.371582	9.087767	0.4732	CNOC2	XR14h11,OP14h35,OP14h37	XR14h11,OP14h35	XR14h11,OP14h37
222.372009	8.996197	0.5068	CNOC2
222.372147	9.196576	0.5928	CNOC2
222.372223	9.721295	0.0940	CNOC2
222.372253	8.857992	0.6924	IMACS
222.372253	9.079287	0.0374	IMACS
222.372299	9.486117	0.6691	CNOC2
222.372635	8.957850	0.5641	CNOC2
222.372864	9.427739	0.1983	CNOC2
222.372864	9.491362	0.6703	CNOC2
222.372986	9.621835	0.1201	CNOC2
222.373138	9.511602	0.5363	CNOC2
222.373291	9.638330	0.3257	CNOC2
222.373474	9.500017	0.5348	CNOC2
222.373734	9.494206	0.5473	CNOC2
222.373871	8.939367	0.3739	CNOC2
222.373871	9.251151	0.5487	CNOC2
222.373886	9.213441	0.7046	GMOS
222.373932	8.882259	0.8124	IMACS
222.373962	8.844997	0.3236	CNOC2
222.374039	8.966748	0.8310	FORS2
222.374069	8.981606	0.5103	FORS2_HENDERSON
222.374084	8.887262	0.8120	IMACS
222.374268	9.015936	0.0417	IMACS
222.374283	9.271475	0.5359	CNOC2
222.374619	9.751428	0.2012	CNOC2
222.374725	9.019725	0.8089	CNOC2
222.374832	8.949535	0.1970	IMACS
222.374924	9.442546	0.4932	CNOC2
222.374939	8.983698	0.5105	CNOC2
222.374969	9.497063	0.5473	FORS2_HENDERSON
222.375015	9.008368	0.8922	IMACS
222.375137	9.061196	0.4650	CNOC2
222.375168	9.014181	0.5915	FORS2
222.375168	9.151171	0.4713	CNOC2
222.375565	9.702394	0.2025	CNOC2
222.375671	9.726456	0.5327	CNOC2
222.375809	8.983632	0.5095	FORS2
222.376099	9.486867	0.5387	CNOC2
222.376144	8.834670	0.8868	IMACS
222.376160	9.371986	0.2139	CNOC2
222.376511	9.638413	0.6458	CNOC2
222.376617	8.959996	0.6149	CNOC2
222.376648	8.944116	0.5192	CNOC2

RA	Dec	z	source	l Mpc	$r_{200,\sigma}$	$r_{200,X}$
222.376785	9.157826	0.4688	CNOC2
222.376984	9.086080	0.4709	CNOC2	XR14h11,OP14h35,OP14h37	XR14h11,OP14h35	XR14h11,OP14h37
222.377136	9.452144	0.5479	CNOC2
222.377380	9.153053	0.4685	CNOC2
222.377563	9.511185	0.3493	CNOC2
222.377594	9.471457	0.3773	CNOC2
222.377747	9.458837	0.1192	CNOC2
222.377863	9.053655	0.3889	IMACS
222.377884	9.154553	0.6786	IMACS
222.378052	9.120239	0.5912	IMACS
222.378159	9.461782	0.4077	CNOC2
222.378418	9.075829	0.4725	FORS2,HENDERSON	XR14h11,OP14h35,OP14h37	XR14h11,OP14h35	XR14h11,OP14h37
222.378479	9.392574	0.2295	CNOC2
222.378494	8.855543	0.2703	CNOC2	XR14h22,OP14h10,OP14h13
222.378738	8.859530	0.5117	IMACS
222.378876	9.019322	0.6377	CNOC2
222.379211	9.143377	0.7667	IMACS
222.379227	8.821489	0.4143	CNOC2
222.379227	9.125862	0.1796	FORS2,HENDERSON
222.379272	9.513233	0.3509	CNOC2
222.379456	9.146265	0.6428	IMACS
222.379486	9.515528	0.5369	CNOC2
222.379532	9.391973	0.3264	CNOC2
222.379715	9.057875	0.6411	IMACS
222.379745	9.151896	0.4694	IMACS
222.379745	9.505703	0.3493	CNOC2
222.380127	9.501211	0.5407	CNOC2
222.380402	9.600052	0.1988	CNOC2
222.380432	8.968531	0.3640	CNOC2
222.380936	8.894957	0.2708	CNOC2	XR14h22,OP14h10,OP14h13	XR14h22,OP14h10	XR14h22,OP14h10,OP14h13
222.380966	8.970289	0.3629	CNOC2
222.381104	9.191277	0.3930	CNOC2
222.381180	9.205163	0.4044	CNOC2
222.381226	9.093199	0.4713	CNOC2	XR14h11,OP14h35,OP14h37
222.381332	9.076344	0.4714	CNOC2	XR14h11,OP14h35,OP14h37	XR14h11,OP14h35	XR14h11,OP14h37
222.381439	9.057708	0.6383	CNOC2
222.381714	9.710075	0.2018	CNOC2
222.381836	9.514408	0.2802	CNOC2
222.381866	9.125593	0.1800	IMACS
222.381927	9.528150	0.0658	CNOC2
222.382187	9.763776	0.2793	CNOC2
222.382294	9.443293	0.0684	CNOC2
222.382446	9.498665	0.4900	CNOC2
222.382507	9.650256	0.6258	CNOC2
222.382629	9.093676	0.4724	CNOC2	XR14h11,OP14h35,OP14h37
222.382645	9.307147	0.3255	CNOC2
222.382675	9.096362	0.2229	CNOC2
222.382889	8.814248	0.3744	CNOC2
222.383255	8.868430	0.7685	IMACS
222.383545	9.165316	0.3124	CNOC2
222.383575	9.179373	0.5914	IMACS
222.383636	9.062786	0.6395	CNOC2
222.383682	8.986242	0.6473	CNOC2
222.383881	9.173826	0.9344	IMACS
222.384064	8.984193	0.4583	CNOC2
222.384079	8.967666	0.6150	IMACS
222.384140	9.077651	0.6812	IMACS
222.384216	8.885349	0.2715	FORS2	XR14h22,OP14h10,OP14h13	XR14h22,OP14h10	...
222.384262	9.465632	0.5460	CNOC2
222.384293	8.953696	0.8820	FORS2,HENDERSON
222.384308	9.031693	0.6796	IMACS
222.384323	8.944430	0.2730	FORS2	XR14h22,OP14h10,OP14h13
222.384384	8.926899	1.1774	CNOC2
222.384537	9.022704	0.8721	FORS2
222.384552	8.890911	0.2729	CNOC2	XR14h22,OP14h10,OP14h13	XR14h22,OP14h10	XR14h22,OP14h10,OP14h13
222.384567	9.003645	0.6375	FORS2
222.384674	9.203407	0.5919	IMACS
222.384842	9.731083	0.2717	CNOC2
222.385147	9.358582	0.3223	CNOC2
222.385223	9.511390	0.5362	CNOC2
222.385239	8.961690	0.6129	FORS2
222.385757	9.071322	0.6054	CNOC2
222.385788	9.702389	3.0800	CNOC2
222.385834	9.452614	0.5467	CNOC2
222.385849	9.465046	0.5475	CNOC2
222.385941	8.899872	0.0396	FORS2
222.386093	8.830906	0.4147	IMACS
222.386307	8.890004	0.9457	IMACS
222.386490	8.944269	0.3231	CNOC2
222.386551	9.704535	0.2932	CNOC2
222.386566	9.468649	0.3567	CNOC2
222.386719	9.181724	0.2142	CNOC2
222.386719	9.753515	0.2013	CNOC2
222.386780	8.967999	0.6157	CNOC2
222.386780	9.197035	0.5572	CNOC2
222.386810	9.120833	0.3875	CNOC2
222.386826	8.926143	0.1921	CNOC2

RA	Dec	z	source	l Mpc	$r_{200,\sigma}$	$r_{200,X}$
222.386902	9.466800	0.3777	CNOC2
222.387375	8.974049	0.6140	IMACS
222.387375	9.474099	0.3770	CNOC2
222.387512	9.072821	0.8433	FORS2
222.387619	8.854472	0.4939	CNOC2
222.388031	8.821105	0.3718	CNOC2
222.388123	9.525550	0.1194	CNOC2
222.388687	9.730426	0.3309	CNOC2
222.388779	9.277402	0.5553	CNOC2
222.388794	9.685103	0.1998	CNOC2
222.388870	8.949339	0.3933	CNOC2
222.388962	9.180982	0.2139	CNOC2
222.388992	9.591178	0.1756	CNOC2
222.389191	9.560826	0.1648	CNOC2
222.389374	9.306622	0.4891	CNOC2
222.389603	9.430657	0.3762	CNOC2
222.389618	9.176581	0.2149	IMACS
222.389664	8.975078	0.7653	IMACS
222.389923	8.956077	0.6503	IMACS
222.389984	9.407313	0.3219	CNOC2
222.390137	8.894200	0.2718	FORS2	XR14h22,OP14h10,OP14h13	XR14h22,OP14h10	XR14h22,OP14h10,OP14h13
222.390213	8.998174	1.1026	FORS2
222.390676	9.230011	0.7333	IMACS
222.390732	8.999925	0.6370	FORS2
222.391006	9.526929	0.2792	CNOC2
222.391052	9.483143	0.4060	CNOC2
222.391068	9.120131	0.7597	CNOC2
222.391159	9.528342	0.2786	CNOC2
222.391403	8.914117	0.7532	FORS2
222.391464	8.908100	0.8102	IMACS
222.391632	9.173983	0.5922	IMACS
222.391739	9.140117	0.4753	CNOC2
222.391785	8.996256	0.2301	CNOC2
222.391953	9.421391	0.2289	CNOC2
222.392090	9.633573	0.0489	CNOC2
222.392105	8.859750	0.2816	CNOC2
222.392258	9.033655	0.2297	IMACS
222.392319	8.953813	0.5076	CNOC2
222.392334	8.861710	0.8090	IMACS
222.392426	9.362847	0.3246	CNOC2
222.392488	8.915643	0.8089	FORS2
222.392609	9.750752	0.3281	CNOC2
222.392639	9.292605	0.1733	CNOC2
222.392654	9.445078	0.4061	CNOC2
222.393021	9.058864	0.4691	FORS2	XR14h11,OP14h35,OP14h37
222.393097	8.901115	0.3075	FORS2
222.393341	8.978626	0.5929	CNOC2
222.393341	9.266839	0.3611	FORS2_HENDERSON
222.393356	9.503927	0.5344	FORS2_HENDERSON
222.393448	8.918548	0.4388	CNOC+IMACS
222.393646	8.912328	0.6629	FORS2
222.393768	9.181217	0.3239	CNOC2
222.393814	9.580525	0.5440	CNOC2
222.394012	9.427922	0.4279	CNOC2
222.394119	9.177626	0.3928	FORS2_HENDERSON
222.394119	9.709440	0.2938	CNOC2
222.394135	9.485471	0.4064	CNOC2
222.394211	9.329861	0.6636	CNOC2
222.394287	9.079202	0.4753	CNOC2
222.394333	9.052559	0.4335	CNOC2
222.394363	9.066229	0.4693	CNOC2	XR14h11,OP14h35,OP14h37
222.394531	8.916479	0.3229	IMACS+FORS2+FORS2
222.394547	8.829945	0.5574	CNOC2
222.394653	8.973996	0.4671	CNOC2
222.394882	8.894463	0.2710	FORS2	XR14h22,OP14h10,OP14h13	XR14h22,OP14h10	XR14h22,OP14h10,OP14h13
222.394928	9.484369	0.3771	FORS2_HENDERSON
222.394928	9.495228	0.1311	CNOC2
222.395340	9.677412	0.0460	CNOC2
222.395355	9.062888	0.4710	CNOC2	XR14h11,OP14h35,OP14h37
222.395386	9.755167	0.2602	CNOC2
222.395615	8.917859	0.7531	IMACS
222.395691	9.578675	0.5423	CNOC2
222.395785	8.918144	0.7522	FORS2
222.395844	9.376817	0.3017	CNOC2
222.396200	8.917868	0.7532	FORS2+FORS2
222.396207	8.892596	0.4688	FORS2
222.396210	8.921775	0.4008	CNOC2
222.396210	9.183994	0.5935	IMACS
222.396225	8.924942	0.2294	FORS2
222.396317	9.617513	0.1478	CNOC2
222.396454	9.054172	0.1646	CNOC2	XR14h12,OP14h1	XR14h12,OP14h1	XR14h12,OP14h1
222.396698	9.040722	0.4821	CNOC2
222.396912	9.754384	0.1977	CNOC2
222.396973	8.892628	0.4691	IMACS
222.397217	8.926862	0.7668	IMACS+FORS2
222.397522	9.330994	0.6444	CNOC2
222.397614	8.921166	0.4002	FORS2+FORS2

RA	Dec	z	source	l Mpc	$r_{200,\sigma}$	$r_{200,X}$
222.397873	9.358285	0.3224	CNOC2
222.397995	9.203946	0.3654	FORS2_HENDERSON	XR14h29,OP14h25,OP14h26	XR14h29,OP14h25	...
222.398010	8.914443	0.2722	CNOC2	XR14h22,OP14h10,OP14h13	XR14h22,OP14h10	XR14h22,OP14h10,OP14h13
222.398071	9.533717	0.1662	CNOC2
222.398178	9.229929	0.6095	IMACS
222.398193	9.190322	1.0821	GMOS
222.398514	8.897165	0.5438	IMACS+FORS2
222.398621	9.630656	0.2272	CNOC2
222.398666	9.121091	0.5658	FORS2_HENDERSON
222.398773	8.889330	0.6808	FORS2
222.398849	8.979612	0.4589	FORS2
222.398849	9.229314	0.3599	CNOC2	XR14h29,OP14h25,OP14h26	XR14h29,OP14h25	XR14h29,OP14h26
222.398941	9.080023	0.0492	CNOC2
222.399048	9.063887	0.2043	FORS2_HENDERSON
222.399124	9.064783	0.4715	CNOC2	XR14h11,OP14h35,OP14h37
222.399124	9.678420	0.5882	CNOC2
222.399323	8.911016	0.6821	IMACS
222.399536	8.830047	0.4004	CNOC2
222.399560	8.913704	0.6820	FORS2
222.399567	9.608076	0.5091	CNOC2
222.399758	9.077731	0.2659	IMACS
222.399758	9.077731	0.2664	IMACS
222.399811	9.254197	0.2231	CNOC2
222.399902	9.106347	0.2291	CNOC2
222.399918	9.262626	0.5566	CNOC2
222.399963	9.511945	0.5316	FORS2_HENDERSON
222.400085	9.065469	0.4693	IMACS	XR14h11,OP14h35,OP14h37
222.400192	9.698186	0.3219	CNOC2
222.400223	9.445758	0.1998	CNOC2
222.400253	9.080367	0.1548	CNOC2
222.400269	8.974069	0.1243	CNOC2
222.400482	9.244475	0.3243	CNOC2
222.400497	8.899073	0.5430	CNOC2
222.400665	8.910044	0.8098	FORS2
222.400772	9.302561	0.4884	CNOC2
222.401031	9.404826	0.5298	CNOC2
222.401154	8.982760	0.4589	CNOC2
222.401199	9.355223	0.3201	CNOC2
222.401428	9.434574	0.2238	CNOC2
222.401535	9.111577	0.5651	IMACS
222.401764	8.905634	0.7659	IMACS+FORS2+FORS2
222.402023	9.133994	0.8125	IMACS
222.402100	8.995957	0.8099	FORS2
222.402176	9.366074	0.2715	CNOC2
222.402481	8.974692	0.1212	IMACS
222.402512	9.290631	0.1981	CNOC2
222.402710	9.040167	0.8781	FORS2_HENDERSON
222.402802	9.466676	0.3783	CNOC2
222.402817	8.890570	0.6828	CNOC2
222.402908	9.256039	0.4624	FORS2_HENDERSON
222.403061	8.820659	0.3746	CNOC2	XR14h1,OP14h29
222.403366	9.091579	0.2450	CNOC2
222.403503	8.934368	0.2292	IMACS
222.403687	9.064570	0.1645	FORS2	XR14h12,OP14h1	XR14h12,OP14h1	XR14h12,OP14h1
222.403839	9.095807	0.6383	CNOC2
222.404068	9.166448	0.1647	CNOC2
222.404083	8.819450	0.3750	IMACS	XR14h1,OP14h29
222.404129	9.507219	0.5352	CNOC2
222.404190	9.269412	0.4636	CNOC2
222.404465	8.927326	0.2644	FORS2
222.404465	9.039081	0.8772	FORS2
222.404663	9.212902	0.6489	IMACS
222.404663	9.623924	0.2300	CNOC2
222.404800	8.942227	0.2297	CNOC2
222.404831	8.969608	0.1226	CNOC2
222.405029	9.133443	0.8135	IMACS
222.405090	9.380740	0.1989	CNOC2
222.405136	9.663723	0.3712	CNOC2
222.405182	8.903123	0.5443	FORS2
222.405411	9.503231	0.7028	FORS2_HENDERSON
222.405457	9.704166	0.2998	CNOC2
222.405594	8.987166	0.0399	CNOC2
222.405685	8.906623	0.2706	CNOC2	XR14h22,OP14h10,OP14h13	XR14h22,OP14h10	XR14h22,OP14h10,OP14h13
222.406067	9.343163	0.2719	CNOC2
222.406464	8.916459	0.6409	FORS2
222.406525	9.749781	0.3249	CNOC2
222.406662	9.477400	0.3771	CNOC2
222.406738	9.580714	0.5433	CNOC2
222.407074	9.465585	0.6757	FORS2_HENDERSON
222.407089	9.090946	0.9366	FORS2_HENDERSON
222.407150	8.857246	0.3732	CNOC2
222.407257	9.272445	0.1860	CNOC2
222.407455	9.611336	0.2720	CNOC2
222.407501	9.149826	0.2873	CNOC2
222.407562	9.678461	0.2724	CNOC2
222.407715	9.044764	0.2179	CNOC2
222.407715	9.059119	0.5567	IMACS

RA	Dec	z	source	l Mpc	$r_{200,\sigma}$	$r_{200,X}$
222.407959	9.000338	0.8124	CNOC2
222.407990	8.912503	0.1956	CNOC2
222.407990	8.948162	0.3228	FORS2
222.408188	9.081319	1.1291	FORS2_HENDERSON
222.408401	8.980691	0.3072	CNOC2
222.408539	9.050125	0.1652	CNOC2	XR14h12,OP14h1	XR14h12,OP14h1	XR14h12,OP14h1
222.408722	8.994943	0.8116	FORS2
222.408752	8.942078	0.7095	FORS2
222.408997	9.198163	0.3927	FORS2_HENDERSON
222.409286	8.999597	0.3959	IMACS
222.409531	8.840926	0.5116	CNOC2
222.409592	9.476283	0.4072	CNOC2
222.409668	9.134365	0.8100	IMACS
222.409836	9.355311	0.5712	CNOC2
222.409958	8.941607	0.6824	IMACS
222.410339	9.605372	0.2276	CNOC2
222.410446	9.579455	0.5431	CNOC2
222.410645	9.152355	0.3710	CNOC2
222.410660	9.111541	0.4709	CNOC2
222.410828	9.044642	0.3282	CNOC2
222.410843	9.198738	0.6687	IMACS
222.410904	9.170492	0.4894	CNOC2
222.411113	9.090547	0.7246	IMACS
222.411209	8.887400	0.6816	FORS2
222.411316	9.491929	0.5101	CNOC2
222.411484	8.892068	0.3800	IMACS
222.411667	9.037273	0.3054	FORS2_HENDERSON
222.412033	9.421573	0.3232	CNOC2
222.412140	9.059652	0.3243	CNOC2
222.412140	9.246499	0.3783	CNOC2
222.412247	8.878260	0.8695	FORS2
222.412292	9.491855	0.5103	CNOC2
222.412369	8.904343	0.3568	CNOC2
222.413025	8.931781	0.6660	CNOC2
222.413147	9.689635	0.3792	CNOC2
222.413223	9.084035	0.2668	CNOC2
222.413391	9.103965	0.6648	IMACS
222.413589	8.922102	0.7832	FORS2+FORS2
222.413742	9.784928	0.3294	CNOC2
222.413834	8.811278	0.3741	CNOC2	XR14h1,OP14h29
222.413834	9.069249	0.2036	CNOC2
222.413910	8.878592	0.6084	CNOC2
222.414093	8.875899	0.8708	FORS2
222.414200	9.697568	0.1647	CNOC2
222.414383	9.083970	0.2665	CNOC2
222.414627	9.569745	0.3517	CNOC2
222.414825	9.405349	0.2810	CNOC2
222.414902	9.642013	0.2009	CNOC2
222.414932	8.877445	0.3813	FORS2+FORS2
222.415085	9.253172	0.3042	CNOC2
222.415283	9.138901	0.7861	GMOS
222.415283	9.784152	0.3399	CNOC2
222.415390	9.188462	0.0201	CNOC2
222.415497	9.031860	0.4069	IMACS
222.415573	9.778868	0.3395	CNOC2
222.415634	9.025848	0.2334	FORS2
222.415710	8.874304	0.7661	FORS2
222.415771	8.842548	0.7665	IMACS
222.416031	9.070701	0.3240	FORS2
222.416046	9.300147	0.1195	CNOC2
222.416168	9.225331	0.2614	CNOC2
222.416214	9.040423	0.3594	CNOC2
222.416534	9.107148	0.7344	IMACS
222.416595	9.135741	0.3589	FORS2_HENDERSON
222.416656	9.364509	0.1972	CNOC2
222.416702	9.274804	0.3585	CNOC2
222.416748	9.033266	0.6374	FORS2
222.416763	9.035514	0.2700	FORS2
222.416855	9.473008	0.4620	CNOC2
222.416901	9.074050	0.4706	FORS2
222.416916	9.022501	0.4332	IMACS
222.416931	8.797172	0.3741	IMACS
222.416931	9.517712	0.5088	CNOC2
222.417084	8.850195	0.2699	CNOC2	XR14h22,OP14h10,OP14h13
222.417160	9.043494	0.8795	FORS2
222.417343	9.038791	0.3726	CNOC2
222.417419	9.445869	0.6053	CNOC2
222.417572	8.869072	0.4557	FORS2
222.418152	8.896358	0.2696	IMACS	XR14h22,OP14h10,OP14h13	XR14h22,OP14h10	...
222.418274	9.502267	0.2475	CNOC2
222.418304	9.126416	0.2050	CNOC2
222.418503	9.062051	0.6431	FORS2
222.418655	9.284237	0.4623	FORS2_HENDERSON
222.418716	9.054066	0.3591	FORS2
222.418808	9.395975	0.3217	CNOC2
222.418808	9.472131	0.2300	FORS2_HENDERSON
222.418915	9.125413	0.4714	IMACS

RA	Dec	z	source	l Mpc	$r_{200,\sigma}$	$r_{200,X}$
222.419373	9.049986	0.1646	CNOC2	XR14h12,OP14h1	XR14h12,OP14h1	XR14h12,OP14h1
222.419403	8.880552	0.6081	FORS2+FORS2
222.419495	8.945872	0.1470	CNOC2
222.419495	8.964758	0.2737	CNOC2	XR14h22,OP14h13
222.419540	8.821800	0.8116	IMACS
222.419678	9.097046	0.0300	CNOC2
222.419724	9.778922	0.2548	CNOC2
222.419937	9.164671	0.2852	CNOC2
222.420120	9.649726	0.2290	CNOC2
222.420593	9.100770	0.7178	FORS2_HENDERSON
222.420639	9.376654	0.2875	CNOC2
222.420822	9.524755	0.6655	CNOC2
222.420898	9.037032	2.5284	IMACS
222.421219	8.851039	0.2435	CNOC2
222.421265	9.197965	0.5360	CNOC2
222.421524	9.437892	0.1651	CNOC2
222.421951	8.964076	0.8885	IMACS
222.421967	9.066178	0.5684	CNOC2
222.422073	9.229736	0.2151	CNOC2
222.422089	9.102500	0.5694	FORS2_HENDERSON
222.422134	9.270273	0.6433	CNOC2
222.422165	9.084416	0.6392	IMACS
222.422302	8.868617	0.3083	CNOC2
222.422531	9.664759	0.3394	CNOC2
222.422699	8.905263	0.6056	CNOC2
222.422699	8.935594	0.6446	FORS2
222.422760	8.976742	0.5639	CNOC2
222.422882	9.632322	0.2007	CNOC2
222.422974	8.821333	0.4536	CNOC2
222.423004	9.097258	0.6425	FORS2_HENDERSON
222.423325	9.373224	0.1963	CNOC2
222.423386	9.582798	0.2336	CNOC2
222.423706	9.038786	0.3097	IMACS
222.423752	9.687074	0.5092	CNOC2
222.423859	8.922494	0.7645	IMACS
222.423874	9.475951	0.5362	FORS2_HENDERSON
222.424301	9.355751	0.1187	CNOC2
222.424362	9.093156	0.3718	CNOC2
222.424454	9.222839	0.3618	CNOC2	XR14h29,OP14h25,OP14h26	XR14h29,OP14h25	XR14h29,OP14h26
222.424530	8.908784	0.7539	FORS2
222.424545	9.067428	0.6819	FORS2_HENDERSON
222.424698	9.041905	0.6809	FORS2
222.424759	9.494059	0.5103	CNOC2
222.424911	9.049926	0.3730	FORS2
222.425049	9.207799	0.7447	IMACS
222.425110	9.239239	0.4296	FORS2_HENDERSON
222.425201	9.260273	0.3602	CNOC2	XR14h29,OP14h25,OP14h26
222.425262	9.237127	0.4281	CNOC2
222.425308	9.443804	0.6055	CNOC2
222.425476	9.118150	0.2047	CNOC2
222.425873	9.201037	0.3637	IMACS	XR14h29,OP14h25,OP14h26	XR14h29,OP14h25	XR14h29,OP14h26
222.426025	9.677179	0.2989	CNOC2
222.426437	9.237379	0.4699	CNOC2
222.426590	9.088255	0.4702	IMACS
222.426605	8.827866	0.1838	CNOC2
222.426987	9.485096	0.5096	CNOC2
222.427032	8.897156	0.6363	FORS2
222.427185	9.132521	0.4703	CNOC2
222.427292	9.520879	0.8213	FORS2_HENDERSON
222.427460	8.838903	0.4290	CNOC2
222.427597	9.242868	0.2124	CNOC2
222.427734	9.289245	0.4899	FORS2_HENDERSON
222.428284	8.946815	0.3958	CNOC2
222.428436	8.983689	0.3950	FORS2
222.428741	9.533516	0.3519	FORS2_HENDERSON
222.428772	9.334576	0.5264	CNOC2
222.428818	8.897777	0.8118	FORS2
222.428833	9.236934	0.3633	CNOC2	XR14h29,OP14h25,OP14h26	XR14h29,OP14h25	...
222.428970	9.033959	0.3732	CNOC2
222.429260	9.087296	0.6418	IMACS
222.429565	9.060142	0.8744	FORS2
222.429581	9.221740	0.3619	CNOC2	XR14h29,OP14h25,OP14h26	XR14h29,OP14h25	XR14h29,OP14h26
222.429596	9.029179	0.9151	FORS2
222.429642	9.293570	0.3599	CNOC2
222.429703	9.035983	0.3296	IMACS
222.430069	8.994627	0.6150	CNOC2
222.430283	8.991124	0.7367	FORS2
222.430603	9.239438	0.3636	CNOC2	XR14h29,OP14h25,OP14h26	XR14h29,OP14h25	...
222.430618	9.224586	0.5211	CNOC2
222.430634	9.521452	0.8160	FORS2_HENDERSON
222.430786	9.087743	0.1640	CNOC2	XR14h12,OP14h1	...	XR14h12,OP14h1
222.431107	8.904506	0.5415	CNOC2
222.431122	9.237673	0.5935	FORS2_HENDERSON
222.431259	8.940920	0.3805	CNOC2
222.431290	9.605306	0.1657	CNOC2
222.431305	9.232803	0.3602	CNOC2	XR14h29,OP14h25,OP14h26	XR14h29,OP14h25	XR14h29,OP14h26
222.431458	9.031833	0.2869	CNOC2

RA	Dec	z	source	l Mpc	$r_{200,\sigma}$	$r_{200,X}$
222.431641	9.109920	0.5614	IMACS
222.431656	8.990150	0.6143	FORS2
222.431778	9.210372	0.3798	CNOC2
222.431793	8.864114	0.3641	CNOC2
222.431961	9.130026	0.5694	CNOC2
222.432022	8.988098	0.7363	FORS2
222.432022	9.208799	2.1174	IMACS
222.432068	8.895226	0.6365	FORS2
222.432373	9.226692	0.4683	CNOC2
222.432526	8.850794	0.5907	IMACS
222.432617	9.371918	0.1970	CNOC2
222.432861	9.217021	0.3623	CNOC2	XR14h29,OP14h25,OP14h26	XR14h29,OP14h25	XR14h29,OP14h26
222.432877	9.529524	0.2302	FORS2_HENDERSON
222.433029	8.830052	0.5150	CNOC2
222.433563	9.157431	0.6068	GMOS
222.433701	8.912812	0.5882	CNOC2
222.433960	9.151555	0.5481	CNOC2
222.433960	9.206060	0.6427	FORS2_HENDERSON
222.434036	8.872794	0.3950	FORS2
222.434158	9.305675	0.4289	CNOC2
222.434158	9.331150	0.4046	CNOC2
222.434219	9.233360	0.2230	CNOC2
222.434525	9.478110	0.2292	CNOC2
222.434937	9.769217	0.4873	CNOC2
222.434982	9.475759	0.3775	CNOC2
222.435104	9.183152	0.3252	FORS2_HENDERSON
222.435272	9.212815	0.3605	CNOC2	XR14h29,OP14h25,OP14h26	XR14h29,OP14h25	XR14h29,OP14h26
222.435410	9.473693	0.3765	CNOC2
222.435760	9.607385	0.2038	CNOC2
222.435760	9.706777	0.3303	CNOC2
222.435959	9.476919	0.6057	CNOC2
222.436066	9.460355	0.5096	FORS2_HENDERSON
222.436142	9.162194	0.5692	IMACS
222.436172	9.356189	0.3541	CNOC2
222.436401	8.922961	0.7809	FORS2
222.436508	8.990635	0.2639	CNOC2
222.436798	9.235086	0.4730	FORS2_HENDERSON
222.436890	9.516201	0.8156	CNOC2
222.437149	9.286306	0.5721	FORS2_HENDERSON
222.437225	9.301193	0.3644	CNOC2
222.437363	9.219418	0.9760	IMACS
222.437668	9.217221	0.6255	IMACS
222.437668	9.512278	0.3513	CNOC2
222.437866	9.203400	0.0300	CNOC2
222.437881	9.685556	0.3472	CNOC2
222.438019	8.837836	0.1311	CNOC2
222.438019	9.496522	0.4408	FORS2_HENDERSON
222.438110	8.831256	0.3999	CNOC2
222.438110	9.112114	0.5083	CNOC2
222.438141	9.673012	0.5652	CNOC2
222.438202	8.917443	0.7821	FORS2
222.438278	9.617315	0.3567	CNOC2
222.438293	9.212467	0.5377	FORS2_HENDERSON
222.438293	9.404750	0.5704	CNOC2
222.438629	8.975186	0.5316	IMACS
222.438629	9.234768	0.4714	CNOC2
222.438675	9.073899	0.2264	CNOC2
222.438675	9.602811	0.1660	CNOC2
222.438889	9.279433	0.2160	CNOC2
222.439056	9.321742	0.1198	CNOC2
222.439194	9.214429	0.4837	CNOC2
222.439514	8.921355	0.7802	FORS2
222.439789	9.478908	0.2814	FORS2_HENDERSON
222.439865	9.462898	0.3771	CNOC2
222.439972	9.528531	0.3502	CNOC2
222.440353	9.343742	0.3699	CNOC2
222.440445	8.958014	0.2720	CNOC2	XR14h22,OP14h13
222.440582	9.158323	0.2339	CNOC2
222.440628	9.087533	0.3881	CNOC2
222.440704	9.384203	0.3015	CNOC2
222.440720	9.116069	0.1636	CNOC2	XR14h12,OP14h1
222.440903	8.851721	0.2034	CNOC2
222.440933	9.005273	0.7821	FORS2
222.441010	9.052343	0.2432	CNOC2
222.441040	9.280614	1.0746	CNOC2
222.441147	9.172672	0.8843	IMACS
222.441193	9.165727	0.5562	CNOC2
222.441193	9.763604	0.4914	CNOC2
222.441238	9.210783	0.2590	FORS2_HENDERSON
222.441483	8.958667	0.2729	CNOC2	XR14h22,OP14h13
222.441605	9.512797	0.2285	CNOC2
222.441635	8.897103	0.8125	FORS2
222.441910	8.850114	0.3757	CNOC2
222.441971	8.986803	0.3255	CNOC2
222.442093	9.046871	0.5376	CNOC2
222.442230	9.615219	0.3692	CNOC2
222.442734	9.519230	0.2289	CNOC2

RA	Dec	z	source	l Mpc	$r_{200,\sigma}$	$r_{200,X}$
222.442993	9.142099	0.5691	CNOC2
222.443085	9.128250	0.8161	IMACS
222.443115	9.499991	0.4622	CNOC2
222.443176	9.516578	0.3496	CNOC2
222.443573	9.662189	0.2036	CNOC2
222.443893	8.961029	0.5108	IMACS
222.443985	8.916448	0.5882	FORS2
222.444061	9.766217	0.2923	CNOC2
222.444138	9.363022	0.3966	CNOC2
222.444214	8.992121	0.6667	IMACS
222.444244	9.218546	0.3605	CNOC2	XR14h29,OP14h25,OP14h26	XR14h29,OP14h25	XR14h29,OP14h26
222.444351	9.253934	0.4623	FORS2_HENDERSON
222.444427	9.679092	0.3565	CNOC2
222.444534	9.092855	0.5596	FORS2
222.444763	9.364121	0.5651	CNOC2
222.444824	8.939769	0.3098	CNOC2
222.445023	9.583202	0.5674	CNOC2
222.445099	9.326261	0.3220	CNOC2
222.445511	9.222978	0.3623	CNOC2	XR14h29,OP14h25,OP14h26	XR14h29,OP14h25	...
222.445541	9.364085	0.3751	CNOC2
222.445694	9.195285	0.3648	CNOC2	XR14h29,OP14h25,OP14h26	XR14h29,OP14h25	XR14h29,OP14h26
222.445770	8.978835	0.3808	CNOC2
222.445786	9.038720	0.6156	CNOC2
222.445984	9.524385	0.2301	FORS2_HENDERSON
222.446030	9.016739	0.5678	IMACS
222.446167	9.522959	0.2005	CNOC2
222.446213	8.981436	0.3798	CNOC2
222.446243	8.898722	0.5194	CNOC2
222.446335	8.906397	0.7807	IMACS
222.446518	9.406995	0.0293	CNOC2
222.446640	9.038836	0.6148	CNOC2
222.446655	8.851397	0.7662	IMACS
222.446930	8.893023	0.3915	CNOC2
222.447189	9.098240	0.4695	CNOC2
222.447327	9.192253	0.5919	CNOC2
222.447403	8.835546	0.7370	IMACS
222.447601	9.015210	0.5070	CNOC2
222.447601	9.715080	0.4788	CNOC2
222.447617	9.438800	0.5100	CNOC2
222.447662	9.444822	0.0733	CNOC2
222.447800	8.856583	0.6840	IMACS
222.447968	9.192823	0.5647	FORS2_HENDERSON
222.448105	9.034621	0.5373	CNOC2
222.448120	8.960960	0.2737	CNOC2
222.448273	8.912448	0.5862	FORS2
222.448364	9.760910	0.6514	CNOC2
222.448380	9.262901	0.3580	CNOC2
222.448608	9.064921	0.3247	CNOC2
222.448685	9.397602	0.1560	CNOC2
222.448822	8.862394	0.3715	CNOC2
222.448914	8.842367	0.3742	CNOC2	XR14h1,OP14h29
222.449203	9.255622	0.3638	CNOC2
222.449387	9.209356	0.1643	CNOC2
222.449402	9.287073	0.1475	CNOC2
222.449463	9.144224	0.1317	CNOC2
222.449570	9.651316	0.4863	CNOC2
222.449677	9.237661	0.3635	CNOC2	XR14h29,OP14h25,OP14h26	XR14h29,OP14h25	...
222.449890	9.652208	0.2008	CNOC2
222.449997	8.816850	0.4060	CNOC2
222.450287	9.320201	0.2242	CNOC2
222.450409	8.906246	0.7604	FORS2
222.450409	9.325556	0.4520	CNOC2
222.450760	8.973070	0.1650	CNOC2	XR14h12,OP14h1
222.450958	9.471232	0.0299	CNOC2
222.450974	9.230338	0.5923	CNOC2
222.450989	9.037720	0.1661	CNOC2	XR14h12,OP14h1	XR14h12,OP14h1	XR14h12,OP14h1
222.451019	9.583242	0.5733	CNOC2
222.451096	8.902583	1.0250	IMACS
222.451126	9.489906	0.2291	CNOC2
222.451370	9.155305	0.4299	CNOC2
222.451477	9.104499	0.4682	CNOC2
222.451950	9.269966	0.4680	CNOC2
222.451965	9.200392	0.2136	CNOC2
222.452042	9.174516	0.7929	GMOS
222.452667	9.179477	0.2725	CNOC2
222.452774	9.199192	0.2150	CNOC2
222.453110	9.183429	0.1325	CNOC2
222.453262	8.981124	0.5314	IMACS
222.453629	8.957729	0.1246	CNOC2
222.453888	8.919769	0.2641	CNOC2
222.453888	9.239667	0.3076	CNOC2
222.453964	8.825655	0.3999	CNOC2
222.453964	9.067151	0.5103	CNOC2
222.454559	9.018740	0.5076	IMACS
222.455124	9.211564	0.5636	CNOC2
222.455307	8.962423	0.2404	CNOC2
222.455383	9.225722	0.3618	CNOC2	XR14h29,OP14h25,OP14h26	XR14h29,OP14h25	...

RA	Dec	z	source	l Mpc	$r_{200,\sigma}$	$r_{200,X}$
222.455658	9.096693	0.4688	IMACS
222.455780	9.017777	0.7539	IMACS
222.455872	9.243095	0.4717	FORS2_HENDERSON
222.455933	9.496131	0.2284	CNOC2
222.456406	9.002075	0.5375	IMACS
222.456482	9.506647	0.0949	CNOC2
222.456787	9.053790	0.6528	CNOC2
222.456787	9.202479	0.2847	FORS2_HENDERSON
222.456909	9.280635	0.2237	FORS2_HENDERSON
222.456940	8.863431	0.5081	IMACS
222.457153	8.916067	0.2359	CNOC2
222.457153	9.268185	0.2167	CNOC2
222.457428	8.919233	0.2715	FORS2	XR14h22,OP14h13
222.457474	8.891496	0.3813	CNOC2
222.457672	8.835778	0.6363	CNOC2
222.457687	9.271077	0.1324	CNOC2
222.457855	8.996322	0.9036	IMACS
222.458054	9.013816	0.1546	CNOC2
222.458359	8.971778	0.4744	CNOC2
222.458405	8.906033	0.7557	IMACS
222.458542	8.854037	0.6025	IMACS
222.458649	9.751391	0.2798	CNOC2
222.458679	9.447747	0.4261	CNOC2
222.458817	9.183968	0.1308	CNOC2
222.459091	8.908353	0.5117	CNOC2
222.459229	8.874081	0.6080	IMACS
222.459274	8.849282	0.8729	IMACS
222.459305	9.174426	0.3101	CNOC2
222.459503	8.877094	0.9363	FORS2
222.459564	9.214058	0.5630	CNOC2
222.459595	9.116788	0.3256	CNOC2
222.459641	8.979782	0.5693	IMACS
222.459656	8.974922	0.5311	CNOC2
222.459885	9.341332	0.3212	CNOC2
222.459976	9.515932	0.5382	CNOC2
222.460358	9.257124	0.2225	CNOC2
222.460602	9.083058	0.7363	IMACS
222.460953	9.635483	0.2011	CNOC2
222.460953	9.665284	0.2011	CNOC2
222.460999	9.389810	0.0286	CNOC2
222.461014	9.306455	0.0484	CNOC2
222.461349	9.285531	0.4691	CNOC2
222.461685	9.179467	0.7865	CNOC2
222.461700	9.460970	0.0572	CNOC2
222.461975	8.990886	0.7622	IMACS
222.462128	8.908375	0.6424	CNOC2
222.462158	9.247938	0.5379	CNOC2
222.462219	8.815693	0.6835	IMACS
222.462372	8.973774	0.5523	CNOC2
222.462479	9.025238	0.3291	CNOC2
222.462723	9.173552	0.1320	CNOC2
222.462753	9.187313	0.5063	FORS2_HENDERSON
222.462845	9.351514	0.4035	CNOC2
222.462982	8.928813	0.7816	IMACS+FORS2
222.463135	9.117210	0.3255	CNOC2
222.463196	9.645966	0.3486	CNOC2
222.463272	9.184860	0.1311	IMACS
222.463287	8.902855	0.3642	CNOC2
222.464142	8.908189	0.6449	IMACS+FORS2
222.464203	9.109259	0.0606	CNOC2
222.464355	9.199092	0.4086	CNOC2
222.464417	9.443978	0.2716	CNOC2
222.464600	9.280410	0.2466	CNOC2
222.464691	8.993132	0.5536	IMACS
222.464905	8.887153	0.4164	IMACS
222.464905	9.003712	0.3806	CNOC2
222.465363	8.839773	0.6841	IMACS
222.465591	9.140076	0.7001	IMACS
222.466064	8.996166	0.3800	CNOC2
222.466064	9.413903	0.6063	CNOC2
222.466095	9.217740	0.2054	CNOC2
222.466141	8.840422	0.3932	CNOC2
222.466202	8.894201	0.5121	CNOC2
222.466568	9.768685	0.4076	CNOC2
222.466797	9.092253	0.6662	IMACS
222.466827	9.005326	0.3812	CNOC2
222.466949	8.865202	0.3740	CNOC2
222.467148	9.066203	0.8826	IMACS
222.467194	9.491825	0.3568	CNOC2
222.467697	9.058046	0.4800	CNOC2
222.467728	9.693773	0.3313	CNOC2
222.467834	8.958932	0.8142	CNOC2
222.467957	9.663155	0.4331	CNOC2
222.467972	8.860948	0.8637	FORS2
222.468140	9.119680	0.6403	CNOC2
222.468506	8.942227	0.2380	CNOC2
222.468582	8.935863	0.3905	CNOC2

RA	Dec	z	source	l Mpc	$r_{200,\sigma}$	$r_{200,X}$
222.468674	9.341063	0.3194	CNOC2
222.468933	9.287327	0.1328	CNOC2
222.469162	9.071260	0.6662	CNOC2
222.469574	8.936674	0.5887	FORS2
222.469772	9.488465	0.5860	CNOC2
222.470047	9.432928	0.5295	CNOC2
222.470108	8.926303	0.3025	CNOC2
222.470184	9.317521	0.3279	CNOC2
222.470398	9.026424	0.5693	CNOC2
222.470413	9.503346	0.1491	CNOC2
222.470596	9.079230	0.0874	IMACS
222.470657	8.942153	0.5869	CNOC2
222.470810	9.044783	0.1649	CNOC2	XR14h12,OP14h1
222.470871	9.263085	0.4571	CNOC2
222.470886	8.926587	0.3890	FORS2
222.470963	9.738208	0.3789	CNOC2
222.471039	9.154402	0.7880	IMACS
222.471634	9.460917	0.2290	CNOC2
222.472183	8.894128	0.1654	CNOC2
222.472229	8.896425	0.2860	CNOC2
222.472473	9.525628	0.2787	CNOC2
222.472748	8.936637	0.3895	IMACS
222.472763	9.138159	0.1318	CNOC2
222.472794	9.209158	0.3263	CNOC2
222.472809	9.683585	0.2287	CNOC2
222.472839	9.367142	0.3202	CNOC2
222.473328	8.876123	0.1306	FORS2
222.473541	9.188393	0.1308	IMACS
222.473679	8.955150	0.1316	CNOC2
222.473801	9.209350	0.5130	CNOC2
222.474030	8.889300	0.3022	CNOC2
222.474031	9.011789	0.6385	IMACS
222.474091	9.178580	1.0051	IMACS
222.474335	8.846030	0.3914	CNOC2
222.474365	9.062794	1.0931	IMACS
222.474503	9.150453	0.4733	IMACS
222.474518	9.149204	0.4743	CNOC2
222.474548	9.507011	0.1194	CNOC2
222.475174	9.063723	0.4226	CNOC2
222.475449	8.967440	0.2289	CNOC2
222.475632	9.004067	0.3076	IMACS
222.475647	9.558561	0.5579	CNOC2
222.475693	9.049941	0.3303	IMACS
222.475708	8.858243	0.7254	IMACS
222.475723	9.089277	0.7390	IMACS
222.475830	9.431997	0.1653	CNOC2
222.475922	8.884990	0.3027	CNOC2
222.475937	9.780955	0.1975	CNOC2
222.476013	8.864609	0.3937	FORS2
222.476120	9.646112	0.3487	CNOC2
222.476181	9.589283	0.2291	CNOC2
222.476212	9.262562	0.6419	FORS2_HENDERSON
222.476364	9.323856	0.3282	CNOC2
222.476776	9.247907	0.2247	FORS2_HENDERSON
222.476883	9.505202	0.3771	CNOC2
222.476913	9.260915	0.3264	CNOC2
222.476913	9.447604	0.5356	CNOC2
222.476959	9.045617	0.6392	IMACS
222.477097	8.819544	0.8130	IMACS
222.477219	9.050563	0.6433	IMACS
222.477509	9.328310	0.3267	CNOC2
222.478119	9.048125	0.7870	IMACS
222.478267	8.919364	0.3807	IMACS+FORS2
222.478317	9.345057	0.1728	CNOC2
222.478439	8.823463	0.2724	CNOC2
222.478775	8.908179	0.3433	CNOC2
222.478928	9.212050	0.6363	CNOC2
222.478973	9.645472	0.3496	CNOC2
222.479065	8.966022	0.2288	CNOC2
222.479095	9.751957	0.1414	CNOC2
222.479156	9.275212	0.3258	CNOC2
222.479263	8.933274	0.8319	IMACS
222.479370	9.645793	0.3489	CNOC2
222.479706	9.134855	0.7476	GMOS
222.480057	9.036742	0.5062	IMACS
222.480148	9.019273	0.2696	IMACS
222.480240	8.823657	0.7673	IMACS
222.480301	9.049852	0.6401	CNOC2
222.480545	9.648580	0.3474	CNOC2
222.480896	9.125986	0.8453	IMACS
222.481171	9.696217	0.2336	CNOC2
222.481461	9.173423	0.4726	CNOC2
222.481583	9.308982	0.1308	CNOC2
222.481857	9.214152	0.4067	CNOC2
222.481949	9.107505	0.7310	IMACS
222.482300	9.600576	0.3951	CNOC2
222.482605	9.205526	0.3637	CNOC2

RA	Dec	z	source	l Mpc	$r_{200,\sigma}$	$r_{200,X}$
222.482651	9.446763	0.2707	CNOC2
222.482697	8.880375	0.5414	FORS2
222.482910	8.851983	0.2964	CNOC2
222.482956	9.123878	1.0692	IMACS
222.483292	9.610356	0.2007	CNOC2
222.483414	9.213846	0.3937	CNOC2
222.483475	9.054384	0.5478	CNOC2
222.483505	9.489789	0.6067	CNOC2
222.483643	8.940269	0.3941	CNOC2
222.483643	9.324723	0.3275	CNOC2
222.483948	9.053366	0.2044	IMACS
222.484283	8.834771	0.3943	CNOC2
222.484283	8.935688	0.3961	CNOC2
222.484344	8.966979	0.2288	CNOC2
222.484375	9.102031	0.6409	IMACS
222.484451	9.389988	0.5936	CNOC2
222.484665	9.517373	0.2636	CNOC2
222.484726	9.180815	0.4714	CNOC2
222.484863	9.306934	0.3250	CNOC2
222.484940	9.161481	0.1213	CNOC2
222.485107	9.011841	0.6431	IMACS
222.485321	8.941764	0.3964	FORS2
222.485565	8.909641	0.7654	IMACS
222.485733	8.926921	0.9430	IMACS
222.485733	9.522500	0.2704	CNOC2
222.485809	9.702349	0.2989	CNOC2
222.485992	9.646603	0.3482	CNOC2
222.486008	8.881758	0.4059	CNOC2
222.486435	9.300802	0.3225	CNOC2
222.486481	9.474588	0.2303	CNOC2
222.486710	9.182787	0.6655	IMACS
222.486816	8.919604	0.1644	CNOC2
222.487122	9.043075	0.5083	IMACS
222.487183	9.072749	0.5634	CNOC2
222.487198	9.065497	1.0715	IMACS
222.487259	9.093497	0.4211	IMACS
222.487610	9.093987	0.3421	IMACS
222.487610	9.215459	0.3925	CNOC2
222.488068	8.824035	0.3951	CNOC2
222.488144	8.828086	0.3949	IMACS
222.488220	9.081169	0.8773	IMACS
222.488846	9.078117	0.5580	IMACS
222.488983	9.531026	0.2212	CNOC2
222.489090	8.842174	0.5452	CNOC2
222.489334	9.006036	0.5635	CNOC2
222.489487	8.826548	0.0295	CNOC2
222.489624	9.038913	0.8717	IMACS
222.489685	9.031465	0.7374	IMACS
222.489868	9.099193	0.6693	IMACS
222.490143	9.462139	0.4591	CNOC2
222.490295	9.179063	0.6059	CNOC2
222.490372	8.892682	0.2312	CNOC2
222.490555	9.167543	0.1213	IMACS
222.490570	9.457220	0.2287	CNOC2
222.491577	9.151110	0.6418	IMACS
222.491669	9.074175	0.2029	CNOC2
222.491699	8.980208	0.6372	IMACS
222.491913	9.043763	0.7948	IMACS
222.492020	8.876143	0.2694	FORS2
222.492172	9.011717	0.7117	IMACS
222.492584	8.989640	0.6373	CNOC2
222.493561	8.843946	0.1217	CNOC2
222.493988	8.986678	0.7900	CNOC2
222.494064	9.206497	0.3631	CNOC2
222.494110	8.886263	0.5704	FORS2
222.494156	8.913108	0.3955	CNOC+IMACS
222.494354	8.988018	0.4450	CNOC2
222.494492	9.176686	0.6915	GMOS
222.494614	9.073611	0.3270	IMACS
222.494858	8.913234	0.4831	FORS2
222.495010	8.815746	0.5196	CNOC2
222.495239	8.971782	0.9446	IMACS
222.495438	8.973402	0.3750	CNOC2
222.495956	8.980692	0.6364	IMACS
222.496506	9.162332	0.8720	GMOS
222.496613	9.157431	0.2628	CNOC2
222.497681	8.952163	0.9447	IMACS
222.498108	8.810451	0.3942	CNOC2
222.498108	9.159541	0.4714	CNOC2
222.498123	9.017103	0.3295	CNOC2
222.498230	8.915027	0.2989	CNOC2
222.498291	9.067399	0.4722	IMACS
222.498398	9.130288	0.3719	IMACS
222.498459	9.124555	0.8471	IMACS
222.499146	9.068032	0.4720	CNOC2
222.499603	8.805259	0.0588	CNOC2
222.500137	9.138039	0.1217	IMACS

RA	Dec	z	source	l Mpc	$r_{200,\sigma}$	$r_{200,X}$
222.500183	8.915935	0.1926	CNOC2
222.500427	9.160734	0.4699	IMACS
222.500549	8.925512	0.5056	IMACS
222.501175	9.140379	0.3713	CNOC2
222.501633	9.109631	0.4724	IMACS
222.501724	9.079787	0.4718	CNOC2
222.501785	9.019277	0.7626	IMACS
222.501953	8.828082	0.3950	CNOC2
222.502090	8.872620	0.3939	IMACS
222.502121	8.975670	0.7827	IMACS
222.502228	8.829670	0.6374	IMACS
222.502548	9.143524	0.7338	IMACS
222.502548	9.171809	0.4714	CNOC2
222.503082	9.194154	0.6684	CNOC2
222.503250	9.165938	0.7869	GMOS
222.503830	8.861730	0.4552	CNOC2
222.503967	8.950000	0.7837	IMACS
222.503998	8.911888	0.3725	FORS2
222.504364	8.811071	0.6443	CNOC2
222.505066	9.065948	0.2267	CNOC2
222.505188	8.920795	0.2960	FORS2
222.505219	9.137864	0.5076	IMACS
222.505295	9.054594	0.5475	IMACS
222.505493	9.060535	0.2263	CNOC2
222.505859	9.085209	0.6369	IMACS
222.505966	8.905300	0.4559	CNOC2
222.506149	9.211967	0.3035	CNOC2
222.506805	8.964201	0.4721	IMACS
222.506912	9.133632	0.1984	CNOC2
222.507050	8.946021	0.3562	IMACS
222.507126	8.977222	0.1241	CNOC2
222.507141	8.919190	0.5052	CNOC2
222.507278	8.885160	0.1316	CNOC2
222.507828	9.121011	0.6415	IMACS
222.508026	8.839962	0.4934	IMACS
222.508240	9.126836	0.1657	IMACS
222.508682	8.914779	0.5071	CNOC2
222.509445	8.818540	0.5621	CNOC2
222.510056	9.075122	0.4093	CNOC2
222.510208	9.075834	0.4087	FORS2
222.510422	8.906375	0.2365	CNOC2
222.510498	8.851654	0.3939	IMACS
222.510574	9.105722	0.4711	IMACS
222.510818	9.164583	0.4539	CNOC2
222.511002	8.926359	0.5058	CNOC2
222.511169	8.871686	0.5400	CNOC2
222.511169	9.136008	0.7341	IMACS
222.511322	9.075026	0.5936	CNOC2
222.511490	8.919073	0.3919	CNOC2
222.511566	8.944886	0.3641	IMACS
222.511917	9.095955	0.4833	CNOC2
222.512283	8.816993	0.4002	CNOC2
222.512375	9.116865	0.1323	IMACS
222.512421	9.049739	0.5385	FORS2
222.512634	8.813422	0.3919	CNOC2
222.513245	8.880117	0.2618	CNOC2
222.513474	8.964907	0.5562	CNOC2
222.514847	9.118891	0.3064	CNOC2
222.516006	9.062073	0.2264	CNOC2
222.516556	9.052450	0.5633	CNOC2
222.517838	9.110097	0.6408	IMACS+FORS2
222.518112	9.215463	0.3133	CNOC2
222.518372	8.879121	0.3239	CNOC2
222.519928	8.944520	0.4002	CNOC2
222.519989	9.003700	0.3225	CNOC2
222.520401	8.903693	0.1924	CNOC2
222.520584	9.115200	0.6387	IMACS
222.521133	9.116112	0.6404	FORS2
222.522018	8.943753	0.3740	CNOC2
222.522903	8.843051	0.4710	CNOC2
222.523087	8.956767	0.3663	CNOC2
222.523117	8.897111	0.4725	IMACS
222.523193	8.949381	0.3751	IMACS
222.523193	8.992319	0.2285	CNOC2
222.523468	9.113453	0.4649	CNOC2
222.523514	9.197895	0.3638	CNOC2
222.523819	9.186359	0.5575	GMOS
222.524445	9.198959	0.3646	CNOC2
222.524597	9.085831	0.4649	CNOC2
222.524628	8.842210	0.2229	CNOC2
222.524673	9.063101	0.5370	CNOC2
222.525644	9.107663	0.5067	FORS2
222.525742	9.107378	0.5071	IMACS
222.526123	8.867325	0.1677	CNOC2
222.526138	9.072417	0.6462	FORS2
222.526291	9.066025	0.6370	IMACS
222.526596	9.119422	0.5977	CNOC2

RA	Dec	z	source	l Mpc	$r_{200,\sigma}$	$r_{200,X}$
222.526718	8.887124	0.9226	IMACS
222.526779	8.996935	0.2969	CNOC2
222.527374	9.175581	0.4298	CNOC2
222.527618	9.115900	0.6399	FORS2
222.527802	9.190662	0.5647	CNOC2
222.527893	8.841700	0.6018	CNOC2
222.528732	8.923615	0.3662	CNOC2
222.528915	8.934220	0.0502	CNOC2
222.529083	8.817507	0.3932	CNOC2
222.529633	8.877323	0.5406	CNOC2
222.529938	9.164508	0.6442	GMOS
222.529968	8.969152	0.3954	CNOC2
222.530014	9.045897	1.0787	FORS2
222.530029	9.049381	0.5076	CNOC2
222.530106	9.153217	1.0939	GMOS
222.530182	9.059349	0.2439	CNOC2
222.530518	9.115658	0.5062	IMACS
222.530548	8.986906	0.7819	IMACS
222.531342	9.109343	0.5068	IMACS
222.531403	9.057777	0.6458	FORS2
222.531509	8.886512	0.3750	CNOC2
222.531967	9.122278	0.5083	FORS2
222.532410	8.885594	0.2303	CNOC2
222.533005	8.933106	0.5470	CNOC2
222.533112	9.114538	0.3719	FORS2
222.533173	9.105393	0.3053	CNOC2
222.533447	9.079434	0.0501	CNOC2
222.534027	8.812301	0.6377	CNOC2
222.534729	8.990645	0.2967	IMACS
222.535065	8.926132	0.4794	CNOC2
222.535614	9.107406	0.2609	CNOC2
222.535998	8.907102	0.6971	IMACS
222.536713	9.069940	0.6474	CNOC2
222.536758	9.071763	0.6461	FORS2
222.537445	9.106316	0.3120	IMACS
222.537811	9.073785	0.8109	IMACS
222.537933	8.834916	0.2350	CNOC2
222.538513	9.077472	0.6408	FORS2
222.538559	9.073983	0.6396	FORS2
222.538605	9.132678	0.3937	GMOS
222.538864	9.068413	0.6377	FORS2
222.538940	9.079111	0.6467	FORS2
222.539062	9.110384	1.0025	IMACS
222.539169	9.077331	0.4153	IMACS
222.539230	9.144795	0.3713	CNOC2
222.539536	9.071018	0.6442	IMACS
222.540298	9.076675	0.3246	CNOC2
222.540344	8.864315	0.3946	CNOC2
222.540344	9.185494	0.3638	CNOC2
222.540405	8.883438	0.3746	CNOC2
222.540619	9.153672	0.3716	CNOC2
222.541199	9.126184	0.7919	FORS2
222.541367	9.076563	0.3248	CNOC2
222.541504	9.074266	0.6456	FORS2
222.541504	9.211551	0.0295	CNOC2
222.542084	9.091720	0.1306	FORS2
222.542191	9.018005	0.5544	CNOC2
222.542313	8.863245	0.3945	CNOC2
222.542419	9.047344	0.5900	FORS2
222.542740	9.078856	0.6651	IMACS
222.542816	9.035723	0.5069	CNOC2
222.543320	8.935141	0.1844	CNOC2
222.543961	9.065157	0.2299	CNOC2
222.544693	8.972191	0.3953	CNOC2
222.545181	8.936421	0.2849	IMACS
222.545380	9.187670	0.8410	CNOC2
222.545441	9.083262	0.1211	FORS2
222.545700	9.107443	0.5068	CNOC2
222.546951	8.897032	0.0913	CNOC2
222.548264	8.872400	0.3949	CNOC2
222.548264	8.961906	0.3253	CNOC2
222.548355	9.145017	0.7884	FORS2
222.549026	8.814595	0.3724	CNOC2
222.549103	8.949309	0.3258	CNOC2
222.549881	9.110718	0.4849	CNOC2
222.550018	9.011369	0.5573	CNOC2
222.550217	9.008090	0.1654	CNOC2
222.550262	9.033541	0.7249	FORS2
222.550659	9.142403	0.5979	FORS2
222.550964	9.099162	0.1986	FORS2
222.551025	8.923948	0.4666	CNOC2
222.551300	8.805300	0.4316	CNOC2
222.551498	8.959273	0.3252	IMACS
222.552536	9.194278	0.2697	CNOC2
222.552872	9.169277	0.8502	GMOS
222.552963	9.105472	0.4829	CNOC2
222.553299	9.045760	0.5103	FORS2

RA	Dec	z	source	l Mpc	$r_{200,\sigma}$	$r_{200,X}$
222.553329	8.872980	0.4554	CNOC2
222.553726	8.910730	0.5397	CNOC2
222.553741	9.160946	0.4980	CNOC2
222.553818	8.933040	0.5327	CNOC2
222.554337	8.854388	0.5407	CNOC2
222.554901	8.876593	0.4553	CNOC2
222.554916	9.133171	0.4651	CNOC2
222.555496	9.117406	0.6413	FORS2
222.556183	8.860175	0.3727	CNOC2
222.556366	8.920246	0.4349	CNOC2
222.557053	8.975259	0.3958	FORS2_HENDERSON
222.557297	9.056007	0.6409	FORS2
222.557404	9.017416	0.5545	CNOC2
222.557617	8.962554	0.3238	CNOC2
222.557709	9.014171	0.5554	CNOC2
222.558014	9.202101	0.3444	CNOC2
222.558395	9.036587	0.7617	FORS2
222.558960	9.023330	0.3103	CNOC2
222.559387	9.041681	0.5072	FORS2
222.560379	8.837495	0.2657	CNOC2
222.560455	9.072266	0.6486	CNOC2
222.560638	9.132533	0.4719	CNOC2
222.560699	9.096246	0.7259	IMACS
222.561386	9.201862	0.1309	CNOC2
222.561783	8.868800	0.4900	CNOC2
222.562790	9.087409	0.7269	FORS2
222.564117	9.032243	0.5857	CNOC2
222.564377	8.982782	0.7656	IMACS
222.564545	8.942033	0.5622	CNOC2
222.565018	8.888652	0.0464	CNOC2
222.565613	9.045707	0.2489	FORS2_HENDERSON
222.565796	8.899766	0.3943	CNOC2
222.565887	8.966945	0.1243	CNOC2
222.565903	8.964637	0.3254	CNOC2
222.566299	9.039569	0.5657	CNOC2
222.566391	8.991670	0.8118	IMACS
222.566452	8.850476	0.6057	CNOC2
222.566650	8.998949	0.5574	IMACS
222.566727	9.071264	0.1316	CNOC2
222.566772	9.063414	0.3895	FORS2_HENDERSON
222.566864	8.988677	0.7020	IMACS
222.567032	9.104086	0.5579	FORS2
222.567108	9.044617	0.4835	FORS2
222.567276	8.993977	1.1200	CNOC2
222.567703	8.839999	0.5411	CNOC2
222.567719	8.993370	0.5386	IMACS
222.567917	9.143655	0.3650	FORS2
222.568237	9.107720	0.4832	CNOC2
222.568283	9.068760	0.2232	CNOC2
222.568604	9.141425	0.5927	FORS2
222.568634	8.967660	0.3714	FORS2_HENDERSON
222.568710	8.995540	0.5385	CNOC2
222.568832	8.930542	0.3746	CNOC2
222.569046	8.999531	0.5578	CNOC2
222.569154	9.008864	0.5310	IMACS
222.569641	9.006486	0.4561	CNOC2
222.569977	9.031723	0.7531	IMACS
222.570969	9.072920	0.5579	FORS2
222.571991	9.014560	0.6410	CNOC2
222.572021	8.915190	0.2738	CNOC2
222.572098	9.145943	0.6452	CNOC2
222.573181	9.090501	0.2693	CNOC2
222.573227	9.102321	0.3052	CNOC2
222.573502	9.115385	0.5522	FORS2
222.573990	8.814628	0.4260	CNOC2
222.574371	9.114183	0.5520	FORS2
222.574478	8.944852	0.3728	CNOC2
222.574692	9.047944	0.6425	CNOC2
222.576157	8.837264	0.2729	CNOC2
222.576553	8.887792	0.4534	CNOC2
222.576797	9.011673	0.6427	CNOC2
222.576965	9.137628	0.0978	CNOC2
222.577652	9.188700	0.3074	CNOC2
222.577805	9.078977	0.5583	FORS2_HENDERSON
222.577988	9.030208	0.3735	CNOC2	XR14h18,OP14h28	...	XR14h18,OP14h28
222.578506	9.010100	0.3952	CNOC2
222.578720	9.060375	0.3235	CNOC2
222.578979	9.078709	0.6032	CNOC2
222.579041	8.871013	0.3736	CNOC2
222.579254	9.077228	0.5586	FORS2_HENDERSON
222.579529	8.984745	0.3248	FORS2_HENDERSON
222.579651	9.127204	0.5832	FORS2
222.579681	8.828502	0.5560	CNOC2
222.579987	8.943248	0.3747	CNOC2
222.580002	8.927050	0.2298	CNOC2
222.580017	9.100762	0.3069	CNOC2
222.580383	9.103647	0.3065	FORS2

RA	Dec	z	source	l Mpc	$r_{200,\sigma}$	$r_{200,X}$
222.580978	8.973690	0.4662	FORS2_HENDERSON
222.581192	9.010556	0.2206	CNOC2
222.581757	9.008717	0.2198	FORS2_HENDERSON
222.581955	8.895792	0.3932	CNOC2
222.582504	8.827776	0.5575	CNOC2
222.582794	9.182864	0.5255	CNOC2
222.583176	8.817195	0.2649	CNOC2
222.583298	9.063388	0.6796	CNOC2
222.584503	9.024202	0.5624	LDSS2
222.584503	9.112470	0.6706	FORS2
222.584518	8.920540	0.4579	CNOC2
222.584961	8.986273	0.4312	FORS2_HENDERSON
222.585312	9.089431	0.5260	CNOC2
222.585602	8.830007	0.2648	CNOC2
222.586136	9.125572	0.5900	CNOC2
222.586456	8.906567	0.3075	CNOC2
222.587097	9.065287	0.7256	CNOC2
222.587326	9.176878	0.5065	CNOC2
222.587646	9.154843	0.8711	GMOS
222.587845	8.945109	0.5584	CNOC2
222.587860	8.913287	0.3719	CNOC2
222.587967	9.043379	0.5228	FORS2_HENDERSON
222.588486	9.011948	0.7251	CNOC2
222.588577	9.117682	0.7935	FORS2
222.588852	8.888771	0.5580	CNOC2
222.589462	9.156439	0.3710	CNOC2
222.589966	9.061827	0.5871	FORS2_HENDERSON
222.590393	8.840720	0.6494	CNOC2
222.590607	9.169849	0.4650	CNOC2
222.590683	9.019964	0.3738	CNOC2	XR14h18,OP14h28	XR14h18,OP14h28	XR14h18,OP14h28
222.591095	9.106431	0.3066	CNOC2
222.591705	8.999443	0.6026	CNOC2
222.591827	8.822332	0.2695	CNOC2
222.592056	9.035869	0.3988	CNOC2
222.592361	9.126782	0.5064	FORS2
222.593613	9.059511	0.4541	FORS2_HENDERSON
222.593719	9.173856	0.5077	CNOC2
222.593750	8.875839	0.1168	CNOC2
222.593933	9.218342	0.6953	GMOS
222.594086	8.895952	0.1460	CNOC2
222.594101	8.966411	0.3081	CNOC2
222.594223	9.026244	0.6421	CNOC2
222.594315	9.023224	0.3725	CNOC2	XR14h18,OP14h28	XR14h18,OP14h28	XR14h18,OP14h28
222.594955	8.825332	0.3476	CNOC2
222.595001	9.135692	0.5371	FORS2
222.595901	8.957505	0.5564	CNOC2
222.595963	9.055884	1.0509	FORS2
222.596085	9.191118	0.2821	CNOC2
222.596115	8.822730	0.5592	CNOC2
222.596558	9.026876	0.3241	FORS2_HENDERSON
222.596588	9.072724	0.1460	CNOC2
222.596649	9.021311	0.3731	CNOC2	XR14h18,OP14h28	XR14h18,OP14h28	XR14h18,OP14h28
222.597183	9.019692	0.3725	CNOC2	XR14h18,OP14h28	XR14h18,OP14h28	XR14h18,OP14h28
222.597336	9.105988	0.3878	CNOC2
222.598434	9.109883	0.3882	FORS2
222.598465	8.938559	0.3954	CNOC2
222.598465	9.196171	0.2839	CNOC2
222.598724	8.872776	0.3939	CNOC2
222.599350	8.852836	0.2353	CNOC2
222.599899	8.895073	0.3468	CNOC2
222.600525	9.076789	0.1466	CNOC2
222.600632	9.078253	0.2666	CNOC2
222.600922	9.067594	1.0911	FORS2_HENDERSON
222.601212	9.015361	0.5608	CNOC2
222.601227	9.167992	0.6096	CNOC2
222.601318	8.966010	0.5884	FORS2_HENDERSON
222.601440	9.191316	0.2820	CNOC2
222.601852	9.111825	0.3878	CNOC2
222.601959	8.952083	0.2824	CNOC2
222.602097	9.091367	0.3074	CNOC2
222.602905	8.887497	0.6385	CNOC2
222.602951	8.998738	0.2834	CNOC2
222.603638	8.939502	0.3727	CNOC2
222.604065	9.163897	0.2974	CNOC2
222.604095	9.162630	0.1460	CNOC2
222.604202	9.105908	0.2034	FORS2
222.604385	9.050425	0.5910	CNOC2
222.604980	8.996541	0.3717	CNOC2	XR14h18,OP14h28	XR14h18,OP14h28	XR14h18,OP14h28
222.605026	8.940618	0.1461	CNOC2
222.605530	9.109116	0.5887	CNOC2
222.606461	8.940038	0.1461	CNOC2
222.606567	8.888137	0.4720	CNOC2
222.607162	8.993628	0.1667	CNOC2
222.607498	9.077894	0.0860	CNOC2
222.607681	8.842250	0.1922	CNOC2
222.607681	9.111353	0.9801	FORS2
222.607880	9.006866	0.2849	FORS2_HENDERSON

RA	Dec	z	source	l Mpc	$r_{200,\sigma}$	$r_{200,X}$
222.608215	9.179019	0.5065	CNOC2
222.608887	8.877481	0.3734	CNOC2
222.609085	8.939877	0.5565	CNOC2
222.609192	9.035116	0.3470	FORS2_HENDERSON
222.609207	9.075847	0.2837	CNOC2
222.609436	8.988700	0.2839	CNOC2
222.609665	9.116414	0.3880	CNOC2
222.609879	9.211247	0.2043	CNOC2
222.610306	8.978142	0.3239	CNOC2
222.610336	9.074375	0.2200	CNOC2
222.610840	9.050097	0.1664	CNOC2
222.611954	9.032533	0.3930	FORS2_HENDERSON
222.612244	9.141618	0.3127	CNOC2
222.612259	9.075988	0.5365	FORS2_HENDERSON
222.612442	9.191520	0.3649	CNOC2
222.612930	8.806551	0.5585	CNOC2
222.613159	8.805031	0.2736	CNOC2
222.613632	9.185518	0.2810	CNOC2
222.614059	8.866777	0.2734	CNOC2
222.614136	9.086158	0.4832	CNOC2
222.614609	8.989527	0.2834	CNOC2
222.614731	8.922318	0.0471	CNOC2
222.615250	8.896260	0.4716	CNOC2
222.615356	9.189672	0.4661	CNOC2
222.615372	9.116423	0.5898	CNOC2
222.616470	9.052368	0.6476	FORS2_HENDERSON
222.616684	8.810848	0.1314	CNOC2
222.616928	8.871877	0.5270	CNOC2
222.618240	8.970612	0.3278	CNOC2
222.618347	9.023225	0.5362	FORS2_HENDERSON
222.618469	9.016522	0.2052	CNOC2
222.618927	9.072391	0.6714	FORS2_HENDERSON
222.619217	9.208602	0.5925	CNOC2
222.619278	8.908108	0.4908	CNOC2
222.620102	8.818010	0.2727	CNOC2
222.620895	8.819423	0.5594	CNOC2
222.621246	8.808441	0.1221	CNOC2
222.621460	8.878851	0.2223	CNOC2
222.621506	8.933670	0.4627	CNOC2
222.621552	9.034015	0.2203	FORS2_HENDERSON
222.621933	9.144367	0.4661	CNOC2
222.622482	8.993811	0.0408	CNOC2
222.622681	8.914182	0.1458	CNOC2
222.622879	9.001278	0.4787	FORS2_HENDERSON
222.623123	8.953616	0.3777	CNOC2
222.623291	9.200397	0.6394	CNOC2
222.623566	9.016610	0.3943	CNOC2
222.623932	9.012471	1.1150	CNOC2
222.625885	9.183664	0.2829	CNOC2
222.625977	9.034364	0.5073	CNOC2
222.626038	9.084239	0.2843	CNOC2
222.626083	9.029060	0.6041	CNOC2
222.626434	9.018952	0.7246	CNOC2
222.627029	9.015146	0.7221	CNOC2
222.627686	8.847371	0.0925	CNOC2
222.627716	9.019593	0.3236	FORS2_HENDERSON
222.628311	9.106522	0.0982	CNOC2
222.628601	9.012626	0.2829	CNOC2
222.628983	9.205021	0.2706	CNOC2
222.629242	8.912642	0.1311	CNOC2
222.630661	8.999299	0.2479	FORS2_HENDERSON
222.631210	9.002728	0.3103	CNOC2
222.631500	8.860120	0.1230	CNOC2
222.632095	9.126066	0.2491	CNOC2
222.632614	9.007695	0.6046	CNOC2
222.632706	8.960676	0.2313	CNOC2
222.634476	9.021501	0.7750	FORS2_HENDERSON
222.634766	9.040492	0.4382	FORS2_HENDERSON
222.635132	9.046939	0.3729	FORS2_HENDERSON	XR14h18,OP14h28
222.657669	9.198235	0.7062	GMOS
222.675903	9.192427	0.8486	GMOS
222.689850	9.179928	0.7903	GMOS
222.707916	9.160279	0.6072	GMOS
222.732895	9.215728	0.3225	GMOS
222.743378	9.178808	0.7375	GMOS
222.752975	9.167306	0.9681	GMOS
222.760269	9.205818	0.3948	GMOS
222.804413	9.155382	0.7848	GMOS
222.821915	9.151824	0.7660	GMOS
222.828629	9.157336	0.4682	GMOS
222.836441	9.194131	0.5376	GMOS
222.864838	9.188330	0.9926	GMOS
222.880859	9.208191	0.7054	GMOS
222.894211	9.179840	0.6069	GMOS
327.144928	-5.999311	0.3952	CNOC2
327.156799	-6.039863	0.3715	CNOC2
327.161835	-5.943105	0.3341	CNOC2

RA	Dec	z	source	l Mpc	$r_{200,\sigma}$	$r_{200,X}$
327.163208	-5.913837	0.3588	CNOC2
327.164551	-5.923813	0.2181	CNOC2
327.165924	-5.985393	0.5103	CNOC2
327.168091	-6.043636	0.5316	CNOC2
327.169128	-5.988082	0.5562	CNOC2
327.174286	-5.983690	0.5572	CNOC2
327.176056	-5.998526	0.3579	CNOC2
327.182281	-6.049038	0.5066	CNOC2
327.182831	-5.986391	0.3950	CNOC2
327.183746	-5.949133	0.5476	CNOC2
327.186127	-5.965920	0.2570	CNOC2
327.186371	-5.967335	0.3950	CNOC2
327.190613	-5.928857	0.2575	CNOC2
327.191376	-5.916413	0.1527	CNOC2
327.191956	-6.016929	0.1532	CNOC2
327.192505	-5.929845	0.3560	CNOC2
327.196838	-5.985358	0.5573	CNOC2
327.197174	-6.032071	0.2718	CNOC2
327.197998	-5.958980	0.2576	CNOC2
327.198578	-5.929388	0.1528	CNOC2
327.198578	-5.982383	0.5567	CNOC2
327.199829	-5.983895	0.1525	CNOC2
327.200500	-5.916395	0.3601	CNOC2
327.202850	-5.935238	0.3154	CNOC2
327.204376	-5.932755	0.1522	CNOC2
327.204559	-6.029070	0.3939	CNOC2
327.205109	-6.025856	0.3954	CNOC2
327.207001	-5.920506	0.4687	CNOC2
327.210205	-5.930406	0.3572	CNOC2
327.211548	-6.031823	0.3931	CNOC2
327.213165	-5.956962	0.2145	CNOC2
327.216187	-5.992719	0.3562	CNOC2
327.218781	-6.001753	0.6232	CNOC2
327.218964	-5.932134	0.3959	CNOC2
327.219147	-6.022416	0.2013	CNOC2
327.221497	-5.934201	0.6645	CNOC2
327.222534	-6.019383	0.3563	CNOC2
327.227478	-5.975981	0.5135	CNOC2
327.228973	-6.034412	0.2714	CNOC2
327.229828	-5.922841	0.3574	CNOC2
327.231537	-6.032939	0.3928	CNOC2
327.232880	-5.950029	0.3937	CNOC2
327.236755	-5.980959	0.5265	CNOC2
327.241028	-6.002577	0.5274	CNOC2
327.241852	-5.942997	0.3161	CNOC2
327.245117	-5.966631	0.1546	CNOC2
327.247711	-6.024193	0.2718	CNOC2
327.248230	-6.024088	0.6058	CNOC2
327.248596	-5.912336	0.4389	CNOC2
327.250549	-6.037920	0.6353	CNOC2
327.256744	-5.989762	0.0615	CNOC2
327.257904	-5.985114	0.6227	CNOC2
327.262665	-5.979711	0.5109	CNOC2
327.268005	-5.964984	0.2142	CNOC2
327.268738	-5.920068	0.3155	CNOC2
327.269257	-5.988906	0.6361	CNOC2
327.269379	-6.037994	0.5135	CNOC2
327.270691	-5.910816	0.3985	CNOC2
327.271606	-5.928284	0.1532	CNOC2
327.273132	-6.006653	0.1544	CNOC2
327.276703	-5.914512	0.5264	CNOC2
327.279724	-5.968575	0.3961	CNOC2
327.284546	-6.002820	0.3601	CNOC2
327.285736	-5.919997	0.1779	CNOC2
327.286835	-5.932099	0.2306	CNOC2
327.297363	-5.936588	0.2519	CNOC2
327.301758	-6.007174	0.5067	CNOC2
327.312744	-6.042396	0.6390	CNOC2
327.316406	-5.953771	0.1535	CNOC2
327.317810	-5.938707	0.3128	CNOC2
327.318085	-5.975606	0.1162	CNOC2
327.323792	-6.005826	0.5386	CNOC2
327.325256	-5.925936	0.3128	CNOC2
327.326782	-6.044148	0.6040	CNOC2
327.327423	-5.978844	0.3122	CNOC2
327.328583	-5.981282	0.3133	CNOC2
327.331512	-5.973482	0.3130	CNOC2
327.332184	-6.036611	0.1025	CNOC2
327.333893	-5.974921	0.3120	CNOC2
327.336670	-5.929099	0.3592	CNOC2
327.341888	-5.966646	0.3575	CNOC2
327.343842	-6.030993	0.6039	CNOC2
327.344391	-6.031076	0.5968	CNOC2
327.345184	-6.007125	0.2576	CNOC2
327.345551	-5.952711	0.5826	CNOC2
327.345917	-6.006844	0.5751	CNOC2
327.347565	-5.923097	0.2071	CNOC2

RA	Dec	z	source	l Mpc	$r_{200,\sigma}$	$r_{200,X}$
327.348206	-5.934424	0.4774	CNOC2
327.349121	-5.973751	0.6111	CNOC2
327.351013	-6.015833	0.4422	CNOC2
327.356232	-5.900491	0.4090	CNOC2
327.357391	-5.972800	0.4146	CNOC2
327.357880	-5.967173	0.6401	CNOC2
327.359558	-5.945218	0.0606	CNOC2
327.359772	-5.969895	0.2012	CNOC2
327.360413	-6.031665	0.3752	CNOC2
327.364929	-5.987643	0.2009	CNOC2
327.368195	-5.940081	0.1777	CNOC2
327.372894	-6.041994	0.3396	CNOC2
327.374878	-5.983222	0.1441	CNOC2
327.374969	-6.030879	0.5353	CNOC2
327.375885	-5.958749	0.2258	CNOC2
327.378754	-5.969237	0.3966	CNOC2
327.378845	-6.043862	0.3931	CNOC2
327.382050	-6.015186	0.3752	CNOC2
327.383148	-5.913882	0.5932	CNOC2
327.386047	-5.934900	0.0709	CNOC2
327.389008	-5.912051	0.2183	CNOC2
327.392242	-5.942732	0.3394	CNOC2
327.396515	-5.914208	0.0713	CNOC2
327.399567	-5.945548	0.1559	CNOC2
327.402435	-6.004158	0.6378	CNOC2
327.407471	-6.000445	0.3125	CNOC2
327.407532	-5.944469	0.3971	CNOC2
327.408661	-5.909382	0.3569	CNOC2
327.413452	-5.919359	0.4160	CNOC2
327.416168	-6.007090	0.2341	CNOC2
327.418335	-6.001434	0.1531	CNOC2
327.423431	-5.991836	0.0864	CNOC2
327.427429	-5.973999	0.6654	CNOC2
327.428040	-5.946134	0.5993	CNOC2
327.428497	-6.033247	0.5475	CNOC2
327.431000	-5.997768	0.2783	CNOC2
327.431976	-5.986361	0.6025	CNOC2
327.432556	-5.958654	0.8022	FORS2
327.436371	-5.916791	0.0587	CNOC2
327.437103	-5.953950	0.2510	FORS2
327.439453	-5.995386	0.2063	FORS2
327.439758	-5.976099	0.3572	CNOC2
327.441172	-5.982069	0.2788	FORS2
327.443787	-5.965607	0.6737	FORS2
327.446006	-5.958819	0.6954	FORS2
327.447662	-5.949981	0.6989	FORS2
327.451202	-5.938292	0.7877	FORS2
327.452362	-6.013668	0.0557	CNOC2
327.453339	-5.975839	0.6658	FORS2
327.453918	-5.841236	0.5672	CNOC2
327.453949	-5.985736	0.1977	CNOC2
327.454895	-5.922038	0.3389	FORS2
327.455536	-5.828373	0.4776	CNOC2
327.455963	-6.008651	0.3187	CNOC2
327.457214	-5.974533	0.1588	FORS2
327.458374	-6.001944	0.1537	CNOC2
327.458588	-5.970465	0.7879	FORS2
327.459686	-5.839136	0.6803	IMACS
327.459747	-5.762829	0.2575	CNOC2
327.459900	-5.829337	0.4782	CNOC2
327.460480	-5.918552	0.2160	FORS2
327.460541	-5.934174	0.0596	CNOC2
327.460876	-5.827439	0.4236	CNOC2
327.462189	-6.012956	0.1538	CNOC2
327.462189	-6.031535	0.3071	CNOC2
327.462341	-5.963610	0.9820	FORS2
327.463440	-5.984083	0.6232	CNOC2
327.463898	-6.004564	0.1591	CNOC2
327.464813	-5.984246	0.6217	FORS2
327.465118	-5.971355	0.0602	CNOC2
327.465149	-5.937919	0.3864	CNOC2
327.466553	-5.759420	0.3501	CNOC2
327.467224	-5.956101	0.1534	FORS2
327.467255	-5.880782	0.3607	CNOC2
327.468201	-6.007307	0.2586	CNOC2
327.468475	-5.928714	0.5245	CNOC2
327.468719	-5.782619	0.6556	CNOC2
327.468781	-5.966963	0.4152	FORS2
327.469421	-5.808183	0.6444	CNOC2
327.469666	-5.965041	0.0553	CNOC2
327.470276	-5.994945	0.2591	CNOC2
327.470581	-5.869341	0.2583	CNOC2
327.470886	-5.922665	0.8029	FORS2
327.471784	-5.922536	0.8005	FORS2
327.472260	-6.022965	0.2172	CNOC2
327.472290	-5.772703	0.7011	IMACS
327.473358	-5.855938	0.6028	CNOC2

RA	Dec	z	source	l Mpc	$r_{200,\sigma}$	$r_{200,X}$
327.474030	-5.799614	0.2435	CNOC2
327.474121	-5.790354	0.5250	CNOC2
327.474579	-5.906761	0.6398	IMACS
327.474609	-5.999510	0.6656	FORS2
327.475525	-5.871991	0.4322	CNOC2
327.475922	-6.021649	0.1532	CNOC2
327.476776	-5.992619	0.4810	FORS2
327.477539	-5.826885	0.2790	CNOC2
327.478180	-5.877640	0.3600	CNOC2
327.478302	-5.834221	0.2173	CNOC2
327.478424	-5.976770	0.3600	CNOC2
327.478546	-5.947020	0.3864	CNOC2
327.478577	-5.942009	0.4372	FORS2
327.479370	-5.790761	0.0726	CNOC2
327.479523	-5.895323	0.5240	CNOC2
327.480072	-5.960276	0.3865	CNOC2
327.480438	-5.933692	0.5874	FORS2
327.480499	-5.785216	0.1581	CNOC2
327.480652	-5.792387	0.4410	IMACS
327.480927	-6.007205	0.3066	CNOC2
327.481232	-5.954775	0.3753	CNOC2
327.481842	-5.916569	0.7341	FORS2
327.482574	-5.839870	0.2790	CNOC2
327.483643	-5.858103	0.6702	IMACS
327.485199	-5.982993	0.0589	CNOC2
327.486359	-5.909124	0.5985	CNOC2
327.486450	-6.043008	0.5258	CNOC2
327.486755	-5.906772	0.5665	IMACS
327.488190	-5.803462	0.5243	CNOC2
327.488373	-5.773171	0.5826	IMACS
327.488953	-5.896403	0.7776	IMACS
327.489166	-5.955799	0.2590	CNOC2
327.490936	-5.951362	0.6580	FORS2
327.491516	-5.964822	0.1734	CNOC2
327.491638	-5.949228	0.5668	FORS2
327.492310	-5.950220	0.3926	CNOC2
327.492828	-6.046749	0.7483	CNOC2
327.493256	-5.890742	0.3057	CNOC2
327.494019	-5.835363	0.2173	CNOC2
327.495300	-5.981768	0.3191	CNOC2
327.495758	-5.955232	0.1412	FORS2
327.495941	-5.767486	0.7484	CNOC2
327.496094	-5.847031	0.5321	CNOC2
327.496887	-5.966532	0.6697	CNOC2
327.496918	-5.982747	0.1980	CNOC2
327.498535	-6.035837	0.2595	CNOC2
327.499023	-5.779294	0.3713	CNOC2
327.499786	-5.768972	0.7844	IMACS
327.499817	-5.908885	0.5676	CNOC2
327.500305	-5.837625	0.2586	CNOC2
327.501312	-5.853511	0.0906	CNOC2
327.502228	-5.807728	0.4420	CNOC2
327.502899	-5.932645	0.7865	FORS2
327.504150	-5.939791	0.3929	IMACS
327.504333	-5.770599	0.7830	IMACS
327.504486	-5.965847	0.0742	CNOC2
327.504517	-5.818873	0.2722	CNOC2
327.505737	-5.953944	0.3179	CNOC2
327.506073	-5.998912	0.1437	CNOC2
327.506378	-5.834097	0.0617	CNOC2
327.507080	-5.864250	0.5658	CNOC2
327.507874	-5.826459	0.6450	IMACS
327.508453	-5.958614	1.0253	FORS2
327.509583	-5.982652	0.3609	CNOC2
327.509979	-6.035100	0.3957	CNOC2
327.511372	-5.906135	0.8046	IMACS
327.511780	-6.009690	0.2594	CNOC2
327.513062	-5.957436	0.0606	CNOC2
327.513245	-5.937835	0.3707	CNOC2
327.513702	-5.951990	0.1411	FORS2
327.515411	-5.885372	0.4375	CNOC2
327.515778	-5.821793	0.8038	IMACS
327.517181	-6.000585	0.3176	CNOC2
327.517426	-5.935174	0.0738	CNOC2
327.517792	-5.857457	0.5069	CNOC2
327.518799	-5.789330	0.4769	IMACS
327.518829	-5.790602	0.0724	CNOC2
327.519745	-5.825654	0.5063	CNOC2
327.520172	-5.981211	0.3713	CNOC2
327.521790	-5.812490	0.5421	CNOC2
327.522034	-5.772711	0.7820	IMACS
327.522217	-5.936286	0.5019	FORS2
327.522430	-5.763238	0.2157	CNOC2
327.523773	-6.012485	0.3863	CNOC2
327.523955	-5.916925	0.5662	FORS2
327.524109	-5.922280	0.7903	IMACS
327.524170	-5.819167	0.0335	CNOC2

RA	Dec	z	source	l Mpc	$r_{200,\sigma}$	$r_{200,X}$
327.524414	-5.927843	0.5653	CNOC2
327.524689	-5.796862	0.4770	IMACS
327.525330	-5.990482	0.8945	FORST
327.525604	-5.759762	0.1189	CNOC2
327.526093	-5.891527	0.4641	CNOC2
327.527679	-5.946021	1.0103	FORST
327.528229	-5.826377	0.4385	CNOC2
327.528870	-5.795937	0.6825	IMACS
327.528900	-5.850119	0.6672	CNOC2
327.529724	-5.962896	0.8953	FORST
327.529877	-5.946057	0.3610	CNOC2
327.530365	-6.013089	0.6359	CNOC2
327.531586	-5.778159	0.7816	IMACS
327.531647	-5.950190	0.6774	FORST
327.532104	-6.024581	0.5864	CNOC2
327.532349	-5.905479	0.7338	IMACS
327.532654	-5.977012	0.3908	CNOC2
327.533356	-5.922307	0.6977	FORST
327.534943	-5.907655	0.3927	IMACS
327.535309	-5.864164	0.6722	CNOC2
327.535706	-5.815460	0.4856	CNOC2
327.535858	-5.962352	0.7111	FORST
327.535950	-5.864101	0.6735	CNOC2
327.536713	-5.827752	0.4394	CNOC2
327.536835	-6.017464	0.2563	CNOC2
327.537170	-5.917187	0.7540	CNOC2
327.538757	-5.965037	0.7103	FORST
327.539093	-5.835792	0.4399	IMACS	XR21h21,OP21h139		...
327.539307	-6.046411	0.1696	CNOC2
327.539612	-5.973933	0.1227	CNOC2
327.541016	-5.878691	0.8688	IMACS
327.541260	-5.964254	0.3068	FORST
327.542358	-5.986564	0.2597	CNOC2
327.542786	-5.778170	0.4046	IMACS
327.543427	-5.807813	0.6442	CNOC2
327.543549	-5.929098	0.6992	FORST
327.545166	-5.880009	0.5273	CNOC2
327.545685	-5.958223	0.7287	FORST
327.546478	-5.759743	0.4774	CNOC2
327.546478	-5.797078	0.6556	IMACS+FORST
327.546722	-6.034032	0.6403	CNOC2
327.546936	-5.925677	0.5678	CNOC2
327.547119	-5.990167	0.3993	FORST
327.548035	-5.823634	0.3903	CNOC2
327.548553	-6.035389	0.3864	CNOC2
327.548920	-5.913638	0.6781	IMACS
327.548981	-5.888425	0.3922	CNOC2
327.549652	-5.866183	0.4538	FORST,HENDERSON
327.550049	-5.984236	0.2426	CNOC2
327.550079	-5.988224	0.5993	CNOC2
327.550476	-5.791817	0.8023	IMACS
327.550476	-5.933677	0.5976	IMACS
327.551154	-5.803708	0.3603	FORST
327.551910	-5.772762	0.3717	CNOC2
327.552795	-6.029037	0.2974	CNOC2
327.553375	-5.891837	0.6305	CNOC2
327.554016	-5.848967	0.1449	CNOC2
327.554291	-5.857008	0.4008	FORST
327.554779	-5.850004	0.3647	FORST
327.555359	-5.885882	0.5261	FORST,HENDERSON
327.556458	-5.830273	1.0465	FORST
327.556793	-5.924452	0.1975	CNOC2
327.556915	-5.789651	0.3017	CNOC2
327.557068	-5.803049	0.1073	CNOC2
327.557159	-5.919333	0.1419	CNOC2
327.557434	-5.965846	0.3330	CNOC2
327.558014	-5.838163	0.2305	FORST,HENDERSON
327.558655	-5.821641	0.3387	CNOC2
327.558990	-5.763128	0.3166	CNOC2
327.559662	-5.755053	0.4011	FORST
327.560974	-5.918042	0.5175	IMACS
327.561035	-5.767749	0.1210	IMACS
327.561920	-5.851121	0.3563	CNOC2
327.562225	-5.969802	0.2657	CNOC2
327.562286	-5.832472	1.1714	FORST
327.562317	-5.808894	0.3168	FORST,HENDERSON
327.562439	-5.931238	0.5244	CNOC2
327.562592	-5.829040	0.3923	CNOC2
327.562592	-5.881642	0.5268	CNOC2
327.562744	-5.853415	0.0903	CNOC2
327.563019	-6.033626	0.2425	CNOC2
327.563110	-6.005845	0.2352	CNOC2
327.563354	-5.777236	0.3176	IMACS
327.563873	-5.891018	0.8722	IMACS
327.564117	-5.879279	0.5248	FORST,HENDERSON
327.564240	-5.876442	0.4686	FORST,HENDERSON
327.564453	-5.880125	0.5255	CNOC2

RA	Dec	z	source	l Mpc	$r_{200,\sigma}$	$r_{200,X}$
327.565277	-5.919050	0.2890	CNOC2
327.565582	-6.023357	0.2161	CNOC2
327.566010	-5.963133	0.5236	CNOC2
327.566284	-5.820730	0.9915	IMACS
327.566406	-5.973833	0.2184	CNOC2
327.567963	-5.854951	0.3712	CNOC2
327.568115	-5.905117	0.2403	IMACS
327.568146	-5.879948	0.5255	CNOC2
327.568207	-5.693364	0.2663	FORS2
327.568573	-5.734774	0.2998	FORS2
327.568695	-5.762324	0.5066	CNOC2
327.569122	-5.762661	0.5060	CNOC2
327.569733	-5.788578	0.4375	FORS2
327.570068	-5.926533	0.6737	CNOC2
327.570160	-5.825455	0.3669	FORS2_HENDERSON
327.570648	-6.015345	0.6791	CNOC2
327.570770	-5.816627	0.4389	FORS2	XR21h21,OP21h139
327.570892	-5.916332	0.3372	CNOC2
327.571228	-5.828591	0.4411	CNOC2	XR21h21,OP21h139	XR21h21,OP21h139	XR21h21,OP21h139
327.571411	-5.839127	0.8884	IMACS
327.571533	-5.993534	0.0666	CNOC2
327.571686	-5.823875	0.6426	FORS2
327.571686	-5.836184	0.3921	CNOC2
327.572388	-5.692481	0.4299	FORS2
327.573975	-5.818294	0.6717	FORS2_HENDERSON
327.574066	-5.818743	0.6708	IMACS
327.574066	-5.875210	0.4412	CNOC2	XR21h21,OP21h139
327.574127	-5.843597	0.6040	CNOC2
327.574158	-5.706975	0.3874	FORS2
327.574554	-5.681901	0.6055	FORS2
327.574829	-5.843495	0.6037	CNOC2
327.575134	-6.009092	0.4279	CNOC2
327.575500	-5.686359	0.3644	FORS2
327.575714	-5.930507	3.1954	CNOC2
327.575989	-5.845150	0.3894	FORS2
327.576447	-5.684931	0.7623	FORS2
327.576782	-6.016286	0.4734	CNOC2
327.577179	-5.768411	0.3170	CNOC2
327.577301	-5.853014	0.4401	CNOC2	XR21h21,OP21h139	XR21h21,OP21h139	XR21h21,OP21h139
327.577850	-5.685856	0.3635	FORS2
327.578430	-5.923440	0.3636	CNOC2
327.578538	-5.726297	0.3720	FORS2
327.578797	-5.834750	0.6032	CNOC2
327.578979	-5.864875	0.4422	CNOC2	XR21h21,OP21h139	XR21h21,OP21h139	XR21h21,OP21h139
327.579407	-5.778475	0.4374	CNOC2
327.579407	-5.814732	0.2033	FORS2_HENDERSON
327.579437	-6.011482	0.2638	CNOC2
327.579926	-5.710092	0.3716	FORS2
327.580017	-5.822113	0.6577	FORS2
327.580933	-5.832228	0.4393	CNOC2	XR21h21,OP21h139	XR21h21,OP21h139	XR21h21,OP21h139
327.581085	-5.827142	0.4413	FORS2_HENDERSON	XR21h21,OP21h139	XR21h21,OP21h139	XR21h21,OP21h139
327.581207	-5.944838	0.5661	CNOC2
327.581879	-5.758294	0.3918	CNOC2
327.582092	-5.819688	0.2194	CNOC2
327.582428	-5.729632	0.3729	FORS2
327.582947	-5.786881	0.1444	CNOC2
327.583130	-5.692256	0.1755	FORS2
327.583252	-5.899006	0.6687	IMACS
327.583679	-5.844075	0.8336	FORS2_HENDERSON
327.583729	-5.804173	0.2235	IMACS
327.583984	-5.887668	0.3904	FORS2_HENDERSON
327.584869	-5.800255	0.5912	FORS2
327.585358	-5.777548	0.3751	CNOC2
327.585419	-5.701294	0.7075	FORS2
327.585999	-6.020699	0.1898	CNOC2
327.586029	-5.890072	0.6696	CNOC2
327.586182	-5.697506	0.4376	FORS2
327.586365	-5.853677	0.4445	FORS2_HENDERSON
327.586823	-5.847251	0.4386	FORS2_HENDERSON	XR21h21,OP21h139	XR21h21,OP21h139	XR21h21,OP21h139
327.587583	-5.989296	0.2652	CNOC2
327.588013	-5.685601	0.7527	FORS2
327.588633	-5.812550	0.5667	IMACS
327.588715	-5.689463	0.3912	FORS2	XR21h16,OP21h134
327.589661	-5.835659	0.4417	CNOC2	XR21h21,OP21h139	XR21h21,OP21h139	XR21h21,OP21h139
327.590729	-5.674082	0.7207	FORS2+FORS2
327.591125	-6.004372	0.0678	CNOC2
327.591827	-5.812830	0.1450	CNOC2
327.592957	-5.687461	0.0934	FORS2+FORS2
327.592987	-5.858854	0.0915	CNOC2
327.593018	-5.786121	0.3169	FORS2
327.593781	-5.839716	0.9685	LDSS2
327.594116	-5.969288	0.4614	CNOC2
327.594177	-5.819960	0.2489	FORS2
327.594299	-5.835439	0.4410	FORS2	XR21h21,OP21h139	XR21h21,OP21h139	XR21h21,OP21h139
327.594604	-5.839632	0.4394	CNOC2	XR21h21,OP21h139	XR21h21,OP21h139	XR21h21,OP21h139
327.594666	-5.748655	0.0276	FORS2
327.595245	-5.883424	0.5265	FORS2_HENDERSON

RA	Dec	z	source	l Mpc	$r_{200,\sigma}$	$r_{200,X}$
327.595842	-5.850478	0.3602	IMACS
327.596313	-5.688534	0.6387	FORS2
327.597015	-5.979140	0.2160	CNOC2
327.597137	-5.471347	0.2020	FORS2_HENDERSON
327.597260	-5.778262	0.3923	CNOC2+FORS2
327.597321	-5.520990	0.2515	IMACS
327.597473	-5.859488	0.8058	FORS2
327.597534	-5.772323	0.3920	FORS2
327.597656	-5.878143	0.4375	IMACS
327.598511	-5.727682	0.2201	FORS2
327.599518	-5.801964	0.6716	FORS2_HENDERSON
327.599549	-5.667504	0.2031	FORS2
327.599640	-5.926625	0.2598	CNOC2
327.600098	-5.630715	0.3169	IMACS
327.600281	-5.908971	0.2324	IMACS
327.600586	-5.681175	0.4361	CNOC2
327.600647	-5.732430	0.3384	FORS2
327.600769	-5.655251	0.4417	FORS2_HENDERSON
327.600769	-5.699460	0.3917	CNOC2	XR21h16,OP21h134
327.600922	-5.872853	0.7207	FORS2_HENDERSON
327.600952	-5.711427	0.3898	CNOC2	XR21h16,OP21h134
327.601166	-5.959118	0.0571	CNOC2
327.601257	-6.022199	0.6019	LDSS2
327.601318	-5.467420	0.5429	IMACS
327.601715	-5.762517	0.4070	FORS2
327.601837	-5.693641	0.6029	FORS2
327.602112	-5.701130	0.4678	CNOC2
327.602722	-5.601617	0.6407	IMACS
327.602753	-5.872346	0.4404	IMACS	XR21h21,OP21h139
327.603027	-5.807766	0.7780	FORS2
327.603333	-5.469871	0.5428	IMACS
327.603577	-5.713299	-0.0004	CNOC2
327.603607	-5.740171	0.7337	FORS2
327.603851	-5.486108	0.4265	CNOC2
327.604248	-5.582614	0.6975	IMACS
327.604401	-5.574816	0.9135	CNOC2
327.605347	-5.512002	0.4395	CNOC2
327.605713	-5.614372	0.3937	IMACS
327.605713	-5.643564	0.3931	CNOC2
327.605927	-5.590304	0.4764	CNOC2
327.606354	-5.562427	0.1643	IMACS
327.606506	-5.503323	0.3556	CNOC2
327.606567	-5.836092	0.7996	FORS2_HENDERSON
327.606598	-5.697680	0.4349	FORS2
327.607147	-5.845989	0.6701	FORS2
327.607209	-5.701567	0.4244	CNOC2
327.607300	-5.724768	0.7331	FORS2
327.607971	-5.710632	0.2409	CNOC2
327.608002	-5.618301	0.4412	IMACS
327.608032	-5.473279	0.3156	CNOC2
327.608093	-5.749840	0.2510	IMACS
327.608124	-5.763379	0.3911	CNOC2
327.608154	-5.716263	0.7339	FORS2
327.608398	-5.487474	0.6029	IMACS
327.608459	-5.615381	0.4278	IMACS
327.608521	-5.571199	0.4363	CNOC2
327.608795	-5.567392	0.3680	CNOC2
327.609497	-5.774129	0.3903	FORS2
327.609711	-5.636102	0.6404	CNOC2
327.610168	-5.486530	0.6036	FORS2_HENDERSON
327.610596	-5.603542	0.6887	IMACS
327.611084	-5.791088	0.1728	FORS2
327.611206	-5.499635	0.5439	CNOC2
327.611786	-5.845542	0.4398	CNOC2	XR21h21,OP21h139
327.611938	-5.601809	0.2994	CNOC2
327.612000	-5.711046	0.9987	FORS2
327.612274	-5.714367	0.6045	CNOC2
327.612366	-5.761476	0.2727	FORS2
327.612366	-5.785148	0.3904	CNOC2
327.612488	-5.712606	0.4762	CNOC2
327.612518	-5.868186	0.3925	FORS2_HENDERSON
327.612915	-5.498657	0.6526	FORS2_HENDERSON
327.612946	-5.524590	0.3020	IMACS
327.613831	-5.782690	0.1301	FORS2
327.613922	-5.644753	0.6555	IMACS
327.614044	-5.856704	0.1734	IMACS
327.614075	-5.742855	0.2937	FORS2
327.614410	-5.473735	0.3572	CNOC2
327.614471	-5.673078	0.4381	FORS2	...	XR21h14,OP21h138	...
327.614716	-5.692182	0.4382	CNOC2	...	XR21h14,OP21h138	...
327.615662	-5.711438	0.6701	FORS2
327.615662	-5.811569	0.8893	FORS2_HENDERSON
327.615845	-5.613026	0.3374	IMACS
327.616058	-5.738404	0.7409	IMACS
327.616119	-5.687305	0.4755	CNOC2
327.616119	-5.769732	0.6531	FORS2
327.616547	-5.814942	0.8894	FORS2

RA	Dec	z	source	l Mpc	$r_{200,\sigma}$	$r_{200,X}$
327.616730	-5.752960	0.6076	FORS2
327.616730	-5.795663	0.3659	CNOC2
327.616760	-5.697861	0.6041	CNOC2
327.616974	-5.863323	0.4416	IMACS	XR21h21,OP21h139
327.617035	-5.793266	0.1438	FORS2
327.617065	-5.859695	0.4399	CNOC2	XR21h21,OP21h139
327.617371	-5.768540	0.6260	FORS2
327.617584	-5.691247	0.4401	CNOC2	...	XR21h14,OP21h138	...
327.617737	-5.680682	0.4322	CNOC2	...	XR21h14,OP21h138	...
327.617798	-5.663293	0.4400	CNOC2	...	XR21h14,OP21h138	...
327.617859	-5.592026	0.4378	IMACS
327.617950	-5.689975	0.3909	CNOC2	XR21h16,OP21h134
327.618134	-5.876439	0.0984	CNOC2
327.618500	-5.701464	0.6060	CNOC2
327.618683	-5.693275	0.4388	CNOC2	...	XR21h14,OP21h138	...
327.618774	-5.504732	0.4241	CNOC2
327.618866	-5.789085	0.5364	FORS2_HENDERSON
327.619049	-5.669253	0.6575	IMACS
327.619110	-5.829306	0.5069	FORS2_HENDERSON
327.619171	-5.739235	0.2142	FORS2
327.619293	-5.486188	0.6524	CNOC2
327.619415	-5.482457	0.7157	FORS2_HENDERSON
327.619690	-5.722380	0.0871	CNOC2
327.619751	-5.748130	0.7335	FORS2
327.620087	-5.778279	0.3923	CNOC2
327.620392	-5.776168	0.3925	FORS2
327.620728	-5.864520	0.4798	CNOC2
327.620819	-5.647539	0.4409	CNOC2	...	XR21h14,OP21h138	...
327.621063	-5.691704	0.3924	CNOC2	XR21h16,OP21h134
327.621185	-5.764202	0.6556	FORS2
327.621582	-5.593930	0.3088	CNOC2
327.621948	-5.494715	0.3064	CNOC2
327.622223	-5.704244	0.6403	CNOC2
327.622400	-5.513282	0.4910	CNOC2
327.622620	-5.670123	0.4359	FORS2_HENDERSON	XR21h14,OP21h138	XR21h14,OP21h138	...
327.623108	-5.495191	0.6514	FORS2_HENDERSON
327.623383	-5.565892	0.2508	CNOC2
327.623413	-5.641254	0.4388	CNOC2	...	XR21h14,OP21h138	...
327.624451	-5.718572	0.3894	FORS2	XR21h16,XR21h18,OP21h134
327.624481	-5.466794	0.2215	FORS2_HENDERSON
327.624542	-5.804987	0.2673	CNOC2
327.624664	-5.780038	0.8050	FORS2
327.624725	-5.684986	0.3929	CNOC2	XR21h16,OP21h134
327.625427	-5.717971	0.3921	FORS2	XR21h16,XR21h18,OP21h134
327.625641	-5.496852	0.6566	IMACS
327.625854	-5.751557	0.7214	FORS2
327.625977	-5.692441	0.4418	FORS2	XR21h14,OP21h138	XR21h14,OP21h138	...
327.626068	-5.874164	0.5245	CNOC2
327.626129	-5.853255	0.3924	IMACS
327.626190	-5.540044	0.4396	CNOC2
327.626587	-5.492208	0.6565	FORS2_HENDERSON
327.627014	-5.490927	0.6545	CNOC2
327.627075	-5.784767	0.6564	FORS2
327.627258	-5.700591	0.4681	FORS2_HENDERSON
327.627838	-5.627718	0.1461	CNOC2
327.628021	-5.805248	0.8927	FORS2
327.628052	-5.722288	0.4368	FORS2_HENDERSON	...	XR21h14,OP21h138	...
327.628143	-5.660124	0.5798	CNOC2
327.628235	-5.783858	0.2484	CNOC2
327.628754	-5.701054	0.7312	CNOC2
327.628845	-5.700569	0.7333	FORS2+FORS2
327.628937	-5.645484	0.4396	IMACS	...	XR21h14,OP21h138	...
327.628998	-5.521539	0.4395	FORS2_HENDERSON
327.629120	-5.481169	0.3582	CNOC2
327.629425	-5.625337	0.4381	CNOC2
327.630096	-5.492232	0.4738	FORS2_HENDERSON
327.630310	-5.857190	0.2842	FORS2_HENDERSON
327.630493	-5.740848	0.4759	CNOC2
327.630524	-5.524900	0.5567	IMACS
327.630524	-5.666596	0.4763	CNOC2
327.630737	-5.704698	0.3927	CNOC2	XR21h16,OP21h134
327.631012	-5.725956	0.6572	FORS2
327.631165	-5.725329	0.6576	FORS2_HENDERSON
327.631226	-5.689448	0.4395	CNOC2	XR21h14,OP21h138	XR21h14,OP21h138	...
327.631226	-5.843164	0.3305	CNOC2
327.631805	-5.715664	0.8773	FORS2
327.631836	-5.495929	0.6661	CNOC2
327.631927	-5.668792	0.4387	CNOC2	XR21h14,OP21h138	XR21h14,OP21h138	...
327.632050	-5.523735	0.5768	FORS2_HENDERSON
327.632294	-5.752596	0.6712	CNOC2
327.632416	-5.629396	0.3014	CNOC2
327.632507	-5.726273	0.5055	FORS2
327.632599	-5.584482	0.3735	CNOC2
327.632721	-5.723308	0.3904	CNOC2	XR21h18,OP21h134
327.632751	-5.490543	0.4406	CNOC2
327.633148	-5.811586	0.2475	FORS2
327.633484	-5.629825	0.2496	CNOC2

RA	Dec	z	source	l Mpc	$r_{200,\sigma}$	$r_{200,X}$
327.633728	-5.492620	0.4731	CNOC2
327.634277	-5.625099	0.7998	FORS2_HENDERSON
327.634338	-5.486932	0.5427	IMACS
327.634369	-5.822947	0.3613	CNOC2
327.634796	-5.788300	0.1878	IMACS
327.635040	-5.774141	0.1439	CNOC2
327.635864	-5.653788	0.4365	FORS2_HENDERSON	XR21h14,OP21h138	XR21h14,OP21h138	...
327.636047	-5.510255	0.4281	FORS2_HENDERSON
327.636078	-5.529232	0.2566	CNOC2
327.636078	-5.696114	0.1537	CNOC2+FORS2
327.637390	-5.536906	0.5679	CNOC2
327.637390	-5.715114	0.6409	CNOC2+FORS2
327.637421	-5.820228	0.4927	CNOC2
327.637695	-5.724384	0.4385	CNOC2	...	XR21h14,OP21h138	...
327.638397	-5.488466	0.5657	CNOC2
327.638611	-5.487130	0.7655	IMACS
327.638794	-5.663049	0.4373	FORS2_HENDERSON	XR21h14,OP21h138	XR21h14,OP21h138	XR21h14,OP21h138
327.638824	-5.742120	0.4077	FORS2
327.639221	-5.731524	0.5400	FORS2_HENDERSON
327.639313	-5.487636	0.5465	FORS2_HENDERSON
327.639587	-5.475868	0.2166	CNOC2
327.639707	-5.718021	0.4403	FORS2	XR21h14,OP21h138	XR21h14,OP21h138	...
327.639923	-5.844426	0.2491	CNOC2
327.639984	-5.788426	0.2363	CNOC2
327.640198	-5.478940	0.3581	CNOC2
327.640320	-5.792563	0.6023	CNOC2
327.640656	-5.749266	0.3168	CNOC2
327.641113	-5.503989	0.4763	FORS2_HENDERSON
327.641357	-5.501633	0.4244	CNOC2
327.641357	-5.735613	0.2197	CNOC2
327.641388	-5.657999	0.7390	IMACS
327.641783	-5.496663	0.6952	IMACS
327.642059	-5.693288	0.3613	CNOC2+FORS2
327.642120	-5.495945	0.2193	CNOC2
327.642120	-5.508436	0.4756	CNOC2
327.642273	-5.691773	0.4334	FORS2	XR21h14,OP21h138	XR21h14,OP21h138	XR21h14,OP21h138
327.642609	-5.690351	0.3612	CNOC2
327.642914	-5.780361	0.2646	CNOC2
327.643005	-5.493923	0.4260	FORS2_HENDERSON
327.643097	-5.691802	0.9112	FORS2
327.643433	-5.687759	0.9111	FORS2
327.643646	-5.710430	0.3939	CNOC2
327.643707	-5.637327	0.4352	FORS2_HENDERSON	...	XR21h14,OP21h138	...
327.644440	-5.710821	0.4342	CNOC2	XR21h14,OP21h138	XR21h14,OP21h138	...
327.644562	-5.758377	0.4418	CNOC2
327.644684	-5.584144	0.4902	CNOC2
327.644867	-5.657543	0.7975	IMACS
327.645050	-5.721925	0.3583	CNOC2
327.645111	-5.650470	0.4346	CNOC2	XR21h14,OP21h138	XR21h14,OP21h138	...
327.645203	-5.688195	0.4425	FORS2	XR21h14,OP21h138	XR21h14,OP21h138	XR21h14,OP21h138
327.645233	-5.554178	0.4402	CNOC2
327.645505	-5.723215	0.1163	CNOC2
327.645721	-5.632921	0.6214	FORS2_HENDERSON
327.645844	-5.750236	0.4349	FORS2
327.646454	-5.488534	0.5357	CNOC2
327.646454	-5.676047	0.4670	CNOC2
327.646455	-5.668009	0.4664	FORS2_HENDERSON
327.647034	-5.858493	0.5652	CNOC2
327.647125	-5.684741	0.5151	FORS2_HENDERSON
327.647217	-5.589208	0.4406	CNOC2
327.647247	-5.786561	0.0552	CNOC2
327.647583	-5.682232	0.2599	FORS2
327.647583	-5.712825	0.4780	FORS2_HENDERSON
327.648071	-5.594063	0.5368	CNOC2
327.648285	-5.480966	0.1632	CNOC2
327.648407	-5.668332	0.4672	IMACS
327.648468	-5.827615	0.0987	CNOC2
327.648590	-5.865431	0.5882	CNOC2
327.648865	-5.505821	0.4408	IMACS
327.648895	-5.695096	0.1790	IMACS
327.649017	-5.651871	0.4396	CNOC2	XR21h14,OP21h138	XR21h14,OP21h138	XR21h14,OP21h138
327.649231	-5.506310	0.6540	CNOC2
327.649261	-5.676365	0.5022	CNOC2
327.649902	-5.667253	0.3376	CNOC2
327.650085	-5.569717	0.6546	CNOC2
327.650482	-5.689588	0.4417	FORS2	XR21h14,OP21h138	XR21h14,OP21h138	XR21h14,OP21h138
327.650574	-5.693706	0.4377	FORS2	XR21h14,OP21h138	XR21h14,OP21h138	XR21h14,OP21h138
327.650848	-5.679562	0.2597	IMACS
327.651215	-5.786292	0.3606	IMACS
327.651245	-5.706579	0.8201	FORS2_HENDERSON
327.651550	-5.479511	0.5657	CNOC2
327.651581	-5.704531	0.3933	CNOC2
327.651611	-5.668819	0.4377	CNOC2	XR21h14,OP21h138	XR21h14,OP21h138	XR21h14,OP21h138
327.651764	-5.503081	0.6514	FORS2
327.652008	-5.877636	0.5057	CNOC2
327.652039	-5.698525	0.9645	FORS2
327.652527	-5.828851	0.0559	CNOC2

RA	Dec	z	source	l Mpc	$r_{200,\sigma}$	$r_{200,X}$
327.652832	-5.484113	0.5212	FORS2
327.652954	-5.662974	0.8758	IMACS
327.653076	-5.509269	0.6166	FORS2
327.653198	-5.696500	0.5054	FORS2
327.653351	-5.491172	0.4259	CNOC2
327.653351	-5.491172	0.4259	CNOC2
327.653364	-5.697986	0.6545	FORS2
327.653364	-5.770828	0.1448	CNOC2
327.653395	-5.667067	0.3925	IMACS
327.653625	-5.892406	0.5880	CNOC2
327.653748	-5.499942	0.4050	FORS2_HENDERSON
327.654602	-5.880514	0.3926	IMACS
327.655487	-5.479821	0.4457	CNOC2
327.655548	-5.668376	0.3390	CNOC2
327.655853	-5.500511	0.4411	FORS2_HENDERSON
327.655914	-5.532699	0.4420	FORS2
327.656097	-5.600624	0.7977	IMACS
327.656647	-5.684175	0.3921	CNOC2
327.656647	-5.894525	0.2370	IMACS
327.656677	-5.677438	0.4384	CNOC2	XR21h14,OP21h138	XR21h14,OP21h138 XR21h14,OP21h138	XR21h14,OP21h138
327.656708	-5.681768	0.4406	FORS2	XR21h14,OP21h138	XR21h14,OP21h138 XR21h14,OP21h138	XR21h14,OP21h138
327.656769	-5.490607	0.4272	CNOC2
327.656830	-5.508890	0.6529	IMACS
327.656891	-5.621119	0.4348	CNOC2	...	XR21h14,OP21h138	...
327.657135	-5.488235	0.4252	CNOC2
327.657135	-5.502707	0.4407	FORS2_HENDERSON
327.657196	-5.799629	0.6034	CNOC2
327.657288	-5.688733	0.4377	FORS2	XR21h14,OP21h138	XR21h14,OP21h138 XR21h14,OP21h138	XR21h14,OP21h138
327.657379	-5.576871	0.4365	CNOC2
327.657471	-5.683995	0.4399	CNOC2	XR21h14,OP21h138	XR21h14,OP21h138 XR21h14,OP21h138	XR21h14,OP21h138
327.657654	-5.504922	0.6548	FORS2
327.657684	-5.741935	0.3658	CNOC2
327.657776	-5.549110	0.0584	CNOC2
327.657806	-5.681080	0.4358	FORS2_HENDERSON	XR21h14,OP21h138	XR21h14,OP21h138 XR21h14,OP21h138	XR21h14,OP21h138
327.657806	-5.885479	0.5668	CNOC2
327.658173	-5.840630	0.2478	CNOC2
327.658386	-5.485014	0.3002	CNOC2
327.658417	-5.740743	0.3669	IMACS
327.658630	-5.546409	0.2466	FORS2
327.658936	-5.694058	0.4307	IMACS
327.658997	-5.588363	0.4899	IMACS
327.659485	-5.492950	0.2197	CNOC2
327.659607	-5.590390	0.4873	CNOC2
327.659851	-5.526450	0.5319	FORS2_HENDERSON
327.659912	-5.691783	0.8025	FORS2
327.659973	-5.474441	0.3372	CNOC2
327.659973	-5.672145	0.4350	CNOC2	XR21h14,OP21h138	XR21h14,OP21h138 XR21h14,OP21h138	XR21h14,OP21h138
327.660004	-5.811733	0.3663	CNOC2
327.660156	-5.520762	0.3882	CNOC2
327.660187	-5.475720	0.3390	FORS2
327.660492	-5.884341	0.0988	IMACS
327.660522	-5.501524	0.6541	FORS2
327.660553	-5.690681	0.4660	IMACS+FORS2
327.660645	-5.646415	0.4423	FORS2_HENDERSON	XR21h14,OP21h138	XR21h14,OP21h138 XR21h14,OP21h138	XR21h14,OP21h138
327.660950	-5.521157	0.3880	FORS2_HENDERSON
327.660950	-5.697242	0.3578	CNOC2
327.660980	-5.636731	0.3602	CNOC2
327.660980	-5.853234	0.0983	CNOC2
327.661041	-5.685096	0.3368	CNOC2
327.661133	-5.573475	0.4368	FORS2
327.661194	-5.504038	0.4232	IMACS
327.661346	-5.471425	0.4728	CNOC2
327.661499	-5.506625	0.0548	CNOC2
327.661591	-5.670797	0.4388	CNOC2	XR21h14,OP21h138	XR21h14,OP21h138 XR21h14,OP21h138	XR21h14,OP21h138
327.662140	-5.647443	0.4095	CNOC2
327.662628	-5.535408	0.7226	FORS2
327.662689	-5.851482	0.5357	CNOC2
327.662994	-5.484213	0.3825	FORS2_HENDERSON
327.662994	-5.710315	0.1786	FORS2
327.663391	-5.628422	0.2159	CNOC2
327.663513	-5.497534	0.1565	CNOC2
327.663666	-5.478506	0.6087	CNOC2
327.663666	-5.685661	0.6295	FORS2
327.663727	-5.577849	0.2443	CNOC2
327.663757	-5.563319	0.5690	IMACS
327.664154	-5.633309	0.4332	CNOC2	XR21h14,OP21h138	XR21h14,OP21h138	...
327.664215	-5.711409	0.6930	CNOC2
327.664703	-5.770230	0.0180	CNOC2
327.664703	-5.893308	0.3928	IMACS
327.664886	-5.649447	0.4393	FORS2_HENDERSON	XR21h14,OP21h138	XR21h14,OP21h138 XR21h14,OP21h138	XR21h14,OP21h138
327.665179	-5.694958	0.7971	IMACS+FORS2
327.665741	-5.473434	0.4433	CNOC2
327.665833	-5.488245	0.5034	IMACS
327.666046	-5.728884	0.3734	FORS2_HENDERSON
327.666168	-5.736838	0.4450	CNOC2
327.666229	-5.668433	0.3577	CNOC2
327.666238	-5.689406	0.3669	IMACS+FORS2

RA	Dec	z	source	l Mpc	$r_{200,\sigma}$	$r_{200,X}$
327.666443	-5.483789	0.3382	FORS2_HENDERSON
327.666534	-5.789614	0.2651	CNOC2
327.666901	-5.677131	0.4375	FORS2_HENDERSON	XR21h14,OP21h138	XR21h14,OP21h138 XR21h14,OP21h138	
327.667236	-5.838163	0.4607	CNOC2
327.667236	-5.859952	0.2650	CNOC2
327.667480	-5.775402	0.1442	CNOC2
327.667542	-5.501342	0.1556	CNOC2
327.667572	-5.482793	1.0529	FORS2
327.667664	-5.497845	0.3390	CNOC2
327.667755	-5.597948	0.3741	CNOC2
327.667816	-5.576517	0.4434	FORS2
327.667816	-5.630121	0.6969	FORS2_HENDERSON
327.668121	-5.641755	0.4338	CNOC2	XR21h14,OP21h138	XR21h14,OP21h138	
327.668945	-5.484023	0.5566	FORS2_HENDERSON
327.669005	-5.667361	0.4458	CNOC2
327.669220	-5.732872	0.3171	FORS2_HENDERSON
327.669312	-5.594918	0.4372	CNOC2
327.669861	-5.525170	0.6544	IMACS
327.669952	-5.661741	0.3927	CNOC2
327.670013	-5.739481	0.3179	CNOC2
327.670105	-5.594732	0.5152	CNOC2
327.670296	-5.682178	0.4412	FORS2	XR21h14,OP21h138	XR21h14,OP21h138 XR21h14,OP21h138	
327.670410	-5.702808	0.5063	FORS2
327.670410	-5.870134	0.2648	CNOC2
327.670471	-5.778756	0.3713	IMACS
327.670563	-5.496984	0.4657	CNOC2
327.670746	-5.650736	0.2439	CNOC2
327.671021	-5.495399	0.4656	CNOC2
327.671051	-5.774687	0.1451	CNOC2
327.671104	-5.674189	0.4463	FORS2
327.671204	-5.742400	0.3174	CNOC2
327.671631	-5.837927	0.4620	CNOC2
327.671906	-5.524668	0.7476	IMACS
327.672272	-5.492025	0.4492	FORS2_HENDERSON
327.672485	-5.629941	0.6455	FORS2_HENDERSON
327.672607	-5.633357	0.2170	CNOC2
327.672663	-5.685689	0.4386	FORS2	XR21h14,OP21h138	XR21h14,OP21h138 XR21h14,OP21h138	
327.672943	-5.666086	0.7664	IMACS
327.672974	-5.761839	0.1444	CNOC2
327.673096	-5.712293	0.1466	CNOC2
327.673523	-5.732424	0.1451	CNOC2
327.673525	-5.696700	0.4369	FORS2	XR21h14,OP21h138	XR21h14,OP21h138 XR21h14,OP21h138	
327.673798	-5.661683	0.3610	CNOC2
327.673920	-5.712316	0.1455	CNOC2
327.674042	-5.477831	0.4662	CNOC2
327.674194	-5.605159	0.6551	CNOC2
327.674409	-5.801426	0.5652	CNOC2
327.674512	-5.684144	0.4359	IMACS+FORS2	XR21h14,OP21h138	XR21h14,OP21h138 XR21h14,OP21h138	
327.674652	-5.536475	0.6952	FORS2_HENDERSON
327.674927	-5.867228	0.5668	CNOC2
327.674988	-5.595005	0.4424	CNOC2
327.675262	-5.574527	0.0985	CNOC2
327.675568	-5.483389	0.5699	FORS2_HENDERSON
327.675812	-5.574289	0.1004	CNOC2
327.675873	-5.770778	0.5058	CNOC2
327.676025	-5.678772	0.4359	FORS2_HENDERSON	XR21h14,OP21h138	XR21h14,OP21h138 XR21h14,OP21h138	
327.676117	-5.876139	0.2648	CNOC2
327.676147	-5.467062	0.1150	CNOC2
327.676147	-5.838707	0.2612	CNOC2
327.676208	-5.604609	0.6557	CNOC2
327.677216	-5.570858	0.6546	FORS2
327.677216	-5.679613	0.2468	FORS2
327.677246	-5.468505	0.4651	CNOC2
327.677826	-5.486025	-0.0015	CNOC2
327.677826	-5.715082	0.4765	FORS2_HENDERSON
327.678101	-5.492379	0.6188	FORS2_HENDERSON
327.678162	-5.702566	0.5696	FORS2_HENDERSON
327.678619	-5.745242	0.6743	CNOC2
327.679108	-5.467869	0.2188	CNOC2
327.679108	-5.728332	0.4764	FORS2_HENDERSON
327.679688	-5.856947	0.3655	IMACS
327.679749	-5.471573	0.4666	CNOC2
327.679993	-5.591344	0.1634	CNOC2
327.680328	-5.500052	0.4427	CNOC2
327.680389	-5.761298	0.1647	CNOC2
327.680603	-5.671537	0.8202	FORS2_HENDERSON
327.680664	-5.684188	0.4395	FORS2	XR21h14,OP21h138	XR21h14,OP21h138 XR21h14,OP21h138	
327.680725	-5.708150	0.3727	FORS2
327.681580	-5.875398	0.5252	IMACS
327.681671	-5.480427	0.3373	FORS2
327.681854	-5.645900	0.3009	FORS2_HENDERSON
327.681976	-5.682778	0.4395	CNOC2	XR21h14,OP21h138	XR21h14,OP21h138 XR21h14,OP21h138	
327.683014	-5.687874	0.4337	IMACS+FORS2	XR21h14,OP21h138	XR21h14,OP21h138 XR21h14,OP21h138	
327.683136	-5.491304	0.4415	FORS2_HENDERSON
327.683441	-5.710363	0.4368	CNOC2	XR21h14,OP21h138	XR21h14,OP21h138 XR21h14,OP21h138	
327.683533	-5.578276	0.4374	IMACS
327.684082	-5.542359	0.5673	CNOC2

Appendix: Spectroscopic Redshifts

RA	Dec	z	source	l Mpc	$r_{200,\sigma}$	$r_{200,X}$
327.684113	-5.513149	0.4404	CNOC2
327.684967	-5.523105	0.8694	FORS2_HENDERSON
327.685364	-5.483251	0.4400	CNOC2
327.685822	-5.657099	0.4442	FORS2_HENDERSON	XR21h14,OP21h138	XR21h14,OP21h138 XR21h14,OP21h138	XR21h14,OP21h138 XR21h14,OP21h138
327.686127	-5.512786	0.2644	IMACS
327.686279	-5.473706	0.4469	FORS2_HENDERSON
327.686432	-5.649927	0.7528	IMACS
327.686737	-5.678755	0.4438	CNOC2	XR21h14,OP21h138	XR21h14,OP21h138 XR21h14,OP21h138	XR21h14,OP21h138 XR21h14,OP21h138
327.686798	-5.514737	0.5159	FORS2
327.686920	-5.484383	0.4512	CNOC2
327.686981	-5.480910	0.4504	CNOC2
327.687592	-5.669681	0.4352	FORS2_HENDERSON	XR21h14,OP21h138	XR21h14,OP21h138 XR21h14,OP21h138	XR21h14,OP21h138 XR21h14,OP21h138
327.687875	-5.546534	0.4666	CNOC2
327.687988	-5.775296	0.2642	CNOC2
327.688019	-5.682613	0.4378	FORS2_HENDERSON	XR21h14,OP21h138	XR21h14,OP21h138 XR21h14,OP21h138	XR21h14,OP21h138 XR21h14,OP21h138
327.688385	-5.477188	0.4438	CNOC2
327.688568	-5.604327	0.9087	IMACS
327.688629	-5.692801	0.5680	FORS2_HENDERSON
327.688667	-5.696670	0.6012	FORS2_HENDERSON
327.688721	-5.719557	0.4337	FORS2_HENDERSON	XR21h14,OP21h138	XR21h14,OP21h138	...
327.688965	-5.513303	0.3394	FORS2
327.689148	-5.674348	0.4380	CNOC2	XR21h14,OP21h138	XR21h14,OP21h138 XR21h14,OP21h138	XR21h14,OP21h138 XR21h14,OP21h138
327.689484	-5.665121	0.5692	FORS2_HENDERSON
327.689601	-5.461510	0.0864	FORS2
327.689758	-5.874241	0.7562	CNOC2
327.690216	-5.477694	0.4483	FORS2_HENDERSON
327.690216	-5.648036	0.6714	CNOC2
327.690521	-5.710735	0.4764	CNOC2
327.690765	-5.469174	0.4278	CNOC2
327.690948	-5.516223	0.3391	CNOC2
327.691010	-5.490814	0.6537	CNOC2
327.691132	-5.789901	0.6568	IMACS
327.691528	-5.520094	0.8666	FORS2
327.691864	-5.518754	0.3379	IMACS+FORS2
327.691925	-5.757803	0.3437	CNOC2
327.692139	-5.470611	0.4397	FORS2
327.692230	-5.647246	0.3929	IMACS
327.692413	-5.490765	0.4449	CNOC2
327.692932	-5.493342	0.3041	CNOC2
327.693054	-5.700292	0.4328	CNOC2	XR21h14,OP21h138	XR21h14,OP21h138 XR21h14,OP21h138	XR21h14,OP21h138 XR21h14,OP21h138
327.693237	-5.497927	0.2171	FORS2_HENDERSON
327.693298	-5.643625	0.3382	CNOC2
327.693634	-5.799811	0.2649	CNOC2
327.694000	-5.775781	0.1639	IMACS
327.694122	-5.481275	0.4467	CNOC2
327.694275	-5.757097	0.5674	CNOC2
327.694275	-5.803350	0.2651	CNOC2
327.694763	-5.721245	0.3444	FORS2_HENDERSON
327.694824	-5.695958	0.4429	CNOC2	XR21h14,OP21h138	XR21h14,OP21h138 XR21h14,OP21h138	XR21h14,OP21h138 XR21h14,OP21h138
327.694946	-5.467312	0.4506	FORS2_HENDERSON
327.695068	-5.468060	0.1555	FORS2
327.695251	-5.486912	0.4455	CNOC2
327.695404	-5.517021	0.3395	FORS2
327.695404	-5.566356	0.3970	FORS2
327.695404	-5.752626	0.3182	CNOC2
327.696228	-5.852136	0.2365	CNOC2
327.696503	-5.554237	0.4668	CNOC2
327.697113	-5.670072	0.1159	CNOC2
327.697114	-5.538674	0.6534	FORS2
327.697174	-5.717005	0.4759	FORS2_HENDERSON
327.697205	-5.539860	0.6547	FORS2
327.697215	-5.740337	0.4684	IMACS
327.697296	-5.469638	0.8644	FORS2
327.697723	-5.561015	0.8345	FORS2
327.697784	-5.758756	0.2197	CNOC2
327.697906	-5.541870	1.0338	FORS2
327.698242	-5.479211	0.7064	FORS2
327.698547	-5.467586	0.8973	CNOC2
327.698822	-5.858182	0.8175	IMACS
327.698853	-5.698500	0.1980	CNOC2
327.699310	-5.473655	0.3746	CNOC2
327.699432	-5.647099	0.3729	CNOC2
327.699432	-5.705993	0.4695	FORS2_HENDERSON
327.699615	-5.862729	0.3386	CNOC2
327.699982	-5.700705	0.1777	CNOC2
327.700134	-5.628277	0.3744	CNOC2
327.700195	-5.524344	0.4786	FORS2
327.700226	-5.563928	0.4044	FORS2
327.700409	-5.696859	0.2468	CNOC2
327.700867	-5.868113	0.6604	IMACS
327.700897	-5.482811	0.4918	IMACS
327.701080	-5.848275	0.3176	CNOC2
327.701202	-5.572984	0.3164	CNOC2
327.701447	-5.873759	0.2370	CNOC2
327.701752	-5.703978	0.8073	IMACS
327.701996	-5.636388	0.3727	CNOC2
327.702057	-5.494559	0.2650	CNOC2

RA	Dec	z	source	l Mpc	$r_{200,\sigma}$	$r_{200,X}$
327.702240	-5.781195	0.2644	CNOC2
327.702301	-5.711672	0.3931	FORS2_HENDERSON
327.702454	-5.479812	0.4430	CNOC2
327.702667	-5.621757	0.3340	CNOC2
327.702759	-5.601575	0.3935	CNOC2
327.702789	-5.516860	0.6537	FORS2_HENDERSON
327.702820	-5.865386	0.3381	IMACS
327.703003	-5.778695	0.2675	CNOC2
327.703156	-5.709276	0.3929	FORS2_HENDERSON
327.703461	-5.472288	0.8617	IMACS
327.703522	-5.706392	0.4276	CNOC2
327.703552	-5.626607	0.2211	FORS2_HENDERSON
327.703583	-5.699578	0.1687	CNOC2
327.703766	-5.750382	0.2007	CNOC2
327.703949	-5.825875	0.2631	CNOC2
327.703979	-5.653922	0.6236	FORS2_HENDERSON
327.704437	-5.667888	-0.0007	CNOC2
327.704620	-5.486641	0.8053	FORS2_HENDERSON
327.704956	-5.542400	0.1310	CNOC2
327.705139	-5.474428	0.4413	CNOC2
327.706329	-5.608818	0.3010	IMACS
327.706390	-5.757226	0.2152	CNOC2
327.706451	-5.838951	0.3882	CNOC2
327.706543	-5.869443	0.5925	IMACS
327.706665	-5.693083	0.8691	IMACS
327.706970	-5.868525	0.6023	LDSS2
327.707550	-5.562462	0.4383	CNOC2
327.707855	-5.713536	0.2657	CNOC2
327.708618	-5.463821	0.4454	FORS2
327.709106	-5.466526	0.8047	FORS2
327.709747	-5.863713	0.2645	CNOC2
327.710510	-5.697376	0.3876	CNOC2
327.710602	-5.517398	0.1016	IMACS
327.710964	-5.550235	0.3170	FORS2
327.710999	-5.575226	0.6552	CNOC2
327.711121	-5.732195	0.1777	CNOC2
327.711334	-5.504420	0.3885	CNOC2
327.711670	-5.505170	0.4056	CNOC2
327.711670	-5.567388	0.3943	FORS2
327.711700	-5.764162	0.2157	CNOC2
327.711731	-5.681522	0.4762	CNOC2
327.712006	-5.627038	0.2199	CNOC2
327.712189	-5.725092	0.6442	FORS2_HENDERSON
327.712220	-5.547717	0.3011	FORS2
327.712311	-5.887649	0.7216	IMACS
327.712555	-5.731404	0.1697	CNOC2
327.713074	-5.866814	0.2358	CNOC2
327.713348	-5.754682	0.3195	CNOC2
327.713409	-5.665219	0.4049	CNOC2
327.713562	-5.472644	0.3235	CNOC2
327.713593	-5.677128	0.4681	CNOC2
327.713989	-5.540770	0.4059	CNOC2
327.714050	-5.764075	0.4754	CNOC2
327.714081	-5.739629	0.0980	IMACS
327.714294	-5.537490	0.7817	FORS2
327.714294	-5.548305	0.5679	CNOC2
327.714417	-5.615119	0.1552	IMACS
327.715057	-5.837426	0.4638	IMACS
327.715515	-5.662100	0.2007	IMACS
327.715546	-5.479499	0.4058	CNOC2
327.716553	-5.518069	0.9544	IMACS
327.717010	-5.571883	0.6551	CNOC2
327.717102	-5.483265	0.2100	CNOC2
327.717407	-5.641141	0.3929	IMACS
327.718140	-5.551366	0.4379	FORS2
327.718658	-5.790824	0.3381	IMACS
327.719269	-5.496383	0.4451	CNOC2
327.719910	-5.685554	0.3177	CNOC2
327.720367	-5.747194	0.1213	CNOC2
327.720703	-5.537297	0.6537	IMACS
327.720795	-5.815422	0.3381	IMACS
327.721436	-5.839058	0.2654	CNOC2
327.721527	-5.738818	0.4339	CNOC2
327.721588	-5.609263	0.3185	IMACS
327.722046	-5.791148	0.2632	CNOC2
327.722198	-5.707805	0.4619	IMACS
327.722443	-5.633213	0.9098	IMACS
327.722504	-5.700575	0.0749	CNOC2
327.723114	-5.540643	0.0750	CNOC2
327.723236	-5.809231	0.6557	IMACS
327.723267	-5.513624	0.3368	CNOC2
327.723541	-5.699787	0.3601	CNOC2
327.723938	-5.714176	0.5694	CNOC2
327.724152	-5.565481	0.5698	CNOC2
327.724274	-5.670818	0.4366	CNOC2
327.724335	-5.662440	0.3004	CNOC2
327.724915	-5.679335	0.6930	IMACS
XR21h14,OP21h138						...

RA	Dec	z	source	l Mpc	$r_{200,\sigma}$	$r_{200,X}$
327.725342	-5.715364	0.3330	IMACS
327.725525	-5.495155	0.4057	IMACS
327.725922	-5.792182	0.2640	CNOC2
327.726227	-5.558226	0.3947	CNOC2
327.726257	-5.830368	0.1786	CNOC2
327.726471	-5.767619	0.4069	CNOC2
327.726746	-5.690910	0.3165	CNOC2
327.727112	-5.699669	0.8054	IMACS
327.727417	-5.630034	0.1452	CNOC2
327.727448	-5.489303	0.2184	FORS2
327.727539	-5.675238	0.3187	FORS2_HENDERSON
327.728363	-5.519593	0.3374	CNOC2
327.728455	-5.544731	0.4381	CNOC2
327.729431	-5.617971	0.5683	IMACS
327.729828	-5.492631	0.4480	CNOC2
327.729828	-5.773972	0.4361	IMACS
327.730133	-5.522030	0.4090	CNOC2
327.730255	-5.568655	0.6427	CNOC2
327.730530	-5.692339	0.3579	CNOC2
327.730682	-5.707541	0.4025	CNOC2
327.732361	-5.871586	0.5994	CNOC2
327.732727	-5.489746	0.2186	CNOC2
327.732910	-5.616797	0.5682	FORS2
327.733032	-5.835268	0.3649	CNOC2
327.733093	-5.685614	0.3168	IMACS
327.733124	-5.582164	0.3579	CNOC2
327.733185	-5.488098	0.4728	CNOC2
327.733246	-5.662617	0.4248	CNOC2+FORS2
327.733429	-5.511969	0.3173	CNOC2
327.733551	-5.877582	0.6805	IMACS
327.734161	-5.634609	0.3596	IMACS
327.734528	-5.765132	0.2639	CNOC2	XR21h48,OP21h123
327.734680	-5.744635	0.1221	CNOC2
327.734772	-5.676247	0.3165	CNOC2
327.734833	-5.713806	1.0654	IMACS
327.735931	-5.649043	0.1448	CNOC2
327.736145	-5.546957	0.3189	LDSS2
327.736359	-5.664586	0.9603	IMACS
327.736420	-5.568423	0.5916	CNOC2
327.736664	-5.736410	0.6411	CNOC2
327.736816	-5.773426	0.1443	CNOC2	XR21h20,OP21h102,OP21h103
327.737213	-5.665030	0.3169	FORS2
327.737379	-5.676520	0.2456	FORS2
327.737610	-5.482619	0.1216	CNOC2
327.737640	-5.674905	0.3163	CNOC2
327.737701	-5.851147	0.1070	CNOC2
327.738220	-5.641618	0.7715	FORS2
327.738251	-5.487902	0.1758	IMACS
327.738373	-5.736503	0.3325	CNOC2
327.738586	-5.647514	0.1444	CNOC2
327.738708	-5.584674	0.5917	FORS2
327.738922	-5.516815	0.4262	CNOC2
327.739685	-5.672854	0.3188	CNOC2
327.740234	-5.661438	0.7722	IMACS+FORS2
327.740692	-5.763071	0.4785	IMACS
327.740904	-5.678679	0.4622	IMACS
327.740997	-5.563581	0.6533	FORS2
327.741547	-5.860912	0.1065	CNOC2
327.741699	-5.631744	0.6692	FORS2
327.741791	-5.626260	0.2997	FORS2
327.742065	-5.556735	0.4408	IMACS
327.742310	-5.562013	0.3373	FORS2
327.742920	-5.777291	0.6112	IMACS
327.743317	-5.627819	0.3600	CNOC2
327.743894	-5.681051	0.3169	IMACS
327.743927	-5.632475	0.2482	CNOC2
327.744507	-5.675198	0.4031	CNOC2
327.744537	-5.787537	0.3975	CNOC2
327.744690	-5.760519	0.1214	CNOC2
327.745178	-5.762857	0.4017	IMACS
327.745239	-5.657508	0.3163	FORS2
327.745605	-5.516508	0.6288	CNOC2
327.745850	-5.713064	0.4415	CNOC2
327.746368	-5.625438	0.3600	FORS2
327.746613	-5.643732	0.2369	FORS2
327.746704	-5.658003	0.4760	CNOC2
327.746735	-5.789256	0.6741	CNOC2
327.747070	-5.632079	0.0748	CNOC2
327.747101	-5.569406	0.2649	FORS2
327.748077	-5.649953	0.3004	FORS2
327.748108	-5.642074	0.4686	FORS2
327.748138	-5.820453	0.4064	CNOC2
327.748474	-5.601383	0.5230	IMACS
327.749451	-5.601574	0.4452	FORS2
327.749512	-5.559452	0.4404	CNOC2
327.749603	-5.572450	0.8948	FORS2
327.750610	-5.880884	0.3600	CNOC2

RA	Dec	z	source	l Mpc	$r_{200,\sigma}$	$r_{200,X}$
327.750885	-5.508299	0.4098	CNOC2
327.751343	-5.605518	0.2194	FORS2
327.751526	-5.775498	0.3460	IMACS
327.751831	-5.871370	0.7004	IMACS
327.752136	-5.672964	0.3675	IMACS
327.752869	-5.672648	0.3673	CNOC2
327.752991	-5.624550	0.2648	IMACS
327.753052	-5.467132	0.1456	IMACS	XR21h6,XR21h7,OP21h104,OP21h105	XR21h6,OP21h104	...
327.753174	-5.318962	0.2627	CNOC2
327.753479	-5.636802	0.4629	FORS2
327.753632	-5.577265	0.5502	FORS2
327.753937	-5.738996	0.4015	CNOC2
327.754364	-5.634169	0.6052	FORS2
327.754517	-5.326874	0.2621	CNOC2
327.754669	-5.056952	0.3989	CNOC2
327.754822	-5.694115	0.0743	IMACS
327.754883	-5.745311	0.1455	IMACS	XR21h20,OP21h102,OP21h103
327.755157	-5.628959	0.2481	FORS2
327.755188	-5.716470	0.5544	CNOC2
327.755554	-5.435862	0.1449	IMACS	XR21h6,XR21h7,OP21h104,OP21h105	XR21h6,OP21h104	...
327.755641	-5.803550	0.3983	CNOC2
327.755798	-5.628511	0.2482	FORS2
327.756317	-5.636011	0.3664	CNOC2
327.756653	-5.627658	0.2483	FORS2
327.756958	-5.655195	0.4747	FORS2
327.757263	-5.126245	0.4292	CNOC2
327.757599	-5.582052	0.4771	FORS2
327.757660	-5.211260	0.5439	CNOC2
327.757935	-5.253478	0.4276	CNOC2
327.758148	-5.777864	0.2630	CNOC2	XR21h48,OP21h123
327.758331	-5.671905	0.8269	FORS2
327.758484	-5.679683	0.5672	IMACS
327.758759	-5.639676	0.9618	FORS2
327.759003	-5.538987	0.6513	IMACS
327.759003	-5.871737	0.4463	CNOC2
327.759033	-5.673406	0.3373	FORS2
327.759186	-5.385850	0.4848	IMACS
327.759186	-5.623802	0.2485	FORS2
327.759583	-5.518043	0.4443	CNOC2
327.759827	-5.084027	0.5236	CNOC2
327.759979	-5.578386	0.4751	FORS2
327.760498	-5.197253	0.1556	CNOC2
327.760498	-5.630794	0.2491	FORS2
327.760620	-5.561428	0.5811	FORS2
327.760986	-5.658856	0.5675	IMACS
327.761047	-5.110644	0.2626	CNOC2
327.761108	-5.367391	0.4436	CNOC2
327.761139	-5.704457	0.4050	CNOC2
327.761505	-5.341713	0.2600	CNOC2
327.761597	-5.620465	0.2198	FORS2
327.761688	-5.882747	0.1431	IMACS
327.761993	-5.809332	0.6046	CNOC2
327.762146	-5.570108	0.4773	FORS2
327.762390	-5.852280	0.0672	LDSS2
327.763123	-5.662003	0.6304	IMACS
327.763397	-5.535628	0.2365	CNOC2
327.763611	-5.235616	0.7277	CNOC2
327.763641	-5.342414	0.1473	CNOC2
327.763733	-5.500328	0.2368	CNOC2
327.763733	-5.642807	0.3009	CNOC2
327.764557	-5.607596	0.9557	FORS2
327.764709	-5.459607	0.4473	IMACS
327.765472	-5.599930	0.2623	IMACS+FORS2
327.765533	-5.845743	0.2409	CNOC2
327.765900	-5.061140	0.3162	CNOC2
327.767334	-5.412629	0.4267	IMACS
327.767487	-5.792846	0.1178	IMACS
327.767670	-5.599732	0.3731	FORS2
327.767761	-5.652980	0.4577	FORS2
327.767792	-5.359008	0.5341	CNOC2
327.768158	-5.580443	0.5067	FORS2
327.768372	-5.708286	0.4423	CNOC2
327.769318	-5.464160	0.4447	IMACS
327.769684	-5.694124	0.4476	IMACS
327.770660	-5.697388	0.3978	CNOC2
327.770752	-5.892855	0.9346	IMACS
327.770813	-5.614271	0.4695	FORS2
327.770905	-5.816657	0.4073	CNOC2
327.771027	-5.618755	0.4462	FORS2
327.771423	-5.519052	0.2373	CNOC2
327.771423	-5.590238	0.1227	CNOC2
327.771576	-5.683618	0.5807	IMACS
327.771606	-5.779746	0.1424	CNOC2
327.772400	-5.654050	0.4032	FORS2
327.772644	-5.514568	0.4462	CNOC2
327.772858	-5.074910	0.3167	CNOC2
327.773041	-5.646216	0.8916	FORS2

RA	Dec	z	source	l Mpc	$r_{200,\sigma}$	$r_{200,X}$
327.773529	-5.809434	0.4064	FORS2
327.773560	-5.822173	0.1219	FORS2
327.773804	-5.735332	0.3601	IMACS
327.773865	-5.655950	0.4033	CNOC2
327.774261	-5.866347	0.2207	CNOC2
327.774384	-5.354538	0.1468	CNOC2
327.774414	-5.884017	0.8769	IMACS
327.774597	-5.659895	0.4026	CNOC2
327.774811	-5.792079	0.4004	FORS2
327.774994	-5.780446	0.3335	CNOC2
327.775024	-5.608325	0.3597	IMACS+FORS2
327.775299	-5.658919	0.4039	IMACS+FORS2
327.775330	-5.418104	0.1456	IMACS	XR21h6,XR21h7,OP21h104,OP21h105	XR21h6,OP21h104	...
327.775482	-5.611342	0.4694	FORS2
327.775574	-5.729094	0.4475	CNOC2
327.775726	-5.120931	0.2979	CNOC2
327.775905	-5.552418	0.3956	CNOC2
327.775909	-5.844945	0.1986	FORS2
327.776154	-5.517909	0.4463	IMACS
327.776611	-5.570496	0.5991	FORS2
327.776978	-5.671465	0.2626	CNOC2
327.777130	-5.659247	0.9569	FORS2
327.777403	-5.676383	0.3404	IMACS
327.777618	-5.563365	0.1213	FORS2
327.777679	-5.638974	0.1309	FORS2
327.777710	-5.374422	0.6137	IMACS
327.778076	-5.657566	0.5246	FORS2
327.778137	-5.537655	0.2374	IMACS
327.778351	-5.876974	0.3989	CNOC2
327.778625	-5.590292	0.1223	CNOC2
327.778748	-5.703676	0.6974	IMACS
327.779846	-5.694587	0.4037	CNOC2
327.779938	-5.647806	0.6323	FORS2
327.780121	-5.833559	0.7546	FORS2
327.780365	-5.597706	0.4471	FORS2
327.780396	-5.878734	0.3989	CNOC2
327.780762	-5.581197	0.4751	FORS2
327.780762	-5.621356	0.8912	FORS2
327.780884	-5.695530	0.6434	IMACS
327.781128	-5.706102	0.6976	IMACS
327.781158	-5.161344	0.4371	CNOC2
327.781250	-5.671265	0.4760	FORS2
327.781616	-5.393557	0.2371	CNOC2
327.781647	-5.804149	0.4080	CNOC2
327.781738	-5.812678	0.1411	IMACS
327.781982	-5.606209	0.2008	CNOC2
327.782990	-5.245469	0.3162	CNOC2
327.783081	-5.678923	0.3956	CNOC2
327.783691	-5.587624	0.1475	FORS2+FORS2
327.783875	-5.065589	0.3930	CNOC2
327.783997	-5.560304	0.4496	FORS2
327.784241	-5.735287	0.3986	IMACS
327.784241	-5.862723	0.4669	FORS2
327.784760	-5.591355	0.4479	FORS2
327.784790	-5.433164	0.4428	IMACS
327.785431	-5.469427	0.2193	CNOC2
327.785553	-5.214029	0.4412	CNOC2
327.785583	-5.874379	0.3388	FORS2
327.785645	-5.716389	0.3018	LDSS2
327.785736	-5.848109	0.1433	FORS2
327.785950	-5.565353	0.6688	FORS2
327.786041	-5.176834	0.5883	CNOC2
327.786469	-5.590504	0.7130	FORS2
327.786469	-5.698612	0.4043	IMACS
327.786621	-5.594294	0.5498	IMACS
327.786682	-5.636477	0.7606	FORS2
327.786926	-5.816110	0.4066	CNOC2
327.786987	-5.287466	0.2003	CNOC2
327.787231	-5.216298	0.1527	CNOC2
327.787476	-5.844807	0.2721	FORS2
327.787659	-5.115315	0.1461	CNOC2
327.787750	-5.632145	0.2484	FORS2
327.788177	-5.353251	0.4849	IMACS
327.788239	-5.660316	0.1791	CNOC2
327.788361	-5.314783	0.2423	CNOC2
327.788361	-5.714941	0.5143	CNOC2
327.788483	-5.588937	0.4774	FORS2
327.788849	-5.845731	0.4470	IMACS
327.789001	-5.147516	0.4402	CNOC2
327.789032	-5.521545	0.1452	CNOC2	XR21h6,XR21h7,OP21h104,OP21h105	XR21h6,OP21h104	...
327.789062	-5.610218	0.4755	FORS2
327.789093	-5.867773	0.0975	CNOC2
327.789154	-5.832815	0.7581	FORS2
327.789246	-5.602879	0.5499	FORS2
327.789368	-5.606124	0.4698	FORS2
327.789429	-5.739946	0.2619	IMACS
327.790039	-5.595467	0.4728	IMACS+FORS2

RA	Dec	z	source	l Mpc	$r_{200,\sigma}$	$r_{200,X}$
327.790192	-5.841599	0.7026	FORS2
327.790253	-5.645196	0.3568	FORS2
327.790527	-5.864504	0.7218	FORS2
327.790588	-5.438700	0.3170	IMACS
327.790894	-5.801487	0.7032	FORS2
327.791046	-5.837764	0.7033	FORS2
327.791168	-5.597550	0.4748	FORS2
327.791260	-5.505651	0.1441	CNOC2	XR21h6,XR21h7,OP21h104,OP21h105	XR21h6,OP21h104	...
327.791351	-5.820731	0.6855	FORS2
327.791412	-5.653193	0.3670	CNOC2
327.791534	-5.826354	0.1229	CNOC2
327.791809	-5.141056	0.2162	CNOC2
327.791962	-5.374124	0.6133	CNOC2
327.792358	-5.063934	0.5459	CNOC2
327.792633	-5.885550	0.4358	CNOC2
327.792877	-5.734194	0.2602	CNOC2
327.792969	-5.345018	0.2363	CNOC2
327.793274	-5.574246	0.5498	FORS2
327.793518	-5.690641	0.6443	IMACS
327.793945	-5.583353	0.4472	FORS2
327.793945	-5.663399	0.1267	FORS2
327.793945	-5.674301	0.4454	CNOC2
327.793976	-5.623320	0.6134	CNOC2
327.794281	-5.812247	0.1432	CNOC2
327.794403	-5.603697	0.0338	CNOC2
327.794617	-5.176737	0.0978	CNOC2
327.794647	-5.805431	0.3990	FORS2
327.794983	-5.866624	0.1427	FORS2
327.795074	-5.169288	0.2820	CNOC2
327.795105	-5.902381	0.7230	FORS2
327.795258	-5.828714	0.1398	FORS2+FORS2
327.795441	-5.572925	0.4781	FORS2
327.795685	-5.531311	0.2305	CNOC2
327.795715	-5.110216	0.2619	CNOC2
327.795807	-5.583159	0.4471	CNOC2
327.795959	-5.057987	0.1108	CNOC2
327.796478	-5.650727	0.6525	FORS2
327.797119	-5.118257	0.3171	CNOC2
327.797333	-5.593697	0.4764	FORS2
327.797638	-5.810023	0.1436	CNOC2
327.798584	-5.405152	0.1449	CNOC2	XR21h6,XR21h7,OP21h104,OP21h105	XR21h6,OP21h104	XR21h7,OP21h106
327.798920	-5.594874	0.4739	FORS2
327.799408	-5.720119	0.2618	IMACS
327.799561	-5.587641	0.3935	CNOC2
327.800018	-5.634181	0.8666	FORS2
327.800537	-5.554405	0.1691	CNOC2
327.800720	-5.797368	0.6051	FORS2
327.800934	-5.812103	0.1222	FORS2
327.800964	-5.780802	0.1440	CNOC2
327.801147	-5.842296	0.7038	FORS2
327.801208	-5.801674	0.3335	CNOC2
327.801208	-5.889076	0.0973	FORS2
327.801300	-5.190836	0.1587	CNOC2
327.801514	-5.481303	0.2194	CNOC2
327.802155	-5.070835	1.3280	CNOC2
327.802185	-5.160258	0.5903	CNOC2
327.802643	-5.463334	0.2184	IMACS
327.802734	-5.612997	0.1977	FORS2
327.803101	-5.239329	0.5229	CNOC2
327.803833	-5.595820	0.4777	IMACS
327.803894	-5.861921	0.1214	FORS2
327.803955	-5.477935	0.2193	FORS2
327.804016	-5.706474	0.4379	CNOC2
327.804199	-5.155011	0.3153	CNOC2
327.804230	-5.663105	0.3670	CNOC2
327.804291	-5.702164	0.9278	IMACS
327.804321	-5.453983	0.2469	FORS2
327.804413	-5.213371	0.5218	CNOC2
327.804443	-5.523448	0.2153	CNOC2
327.804565	-5.567592	0.2441	FORS2
327.804871	-5.151372	0.3613	CNOC2
327.804901	-5.092911	0.3918	CNOC2
327.804901	-5.824967	0.2199	CNOC2+FORS2
327.805145	-5.567150	0.5157	FORS2
327.805145	-5.807358	0.5675	FORS2
327.805389	-5.870712	0.2235	FORS2
327.805908	-5.765164	0.1698	IMACS
327.806000	-5.586237	0.0901	FORS2
327.806122	-5.748963	0.4037	CNOC2
327.806549	-5.603097	0.4777	FORS2
327.806732	-5.881719	0.1437	FORS2
327.806915	-5.415337	0.2193	FORS2
327.806976	-5.895795	0.4467	FORS2
327.807190	-5.414582	0.1766	FORS2
327.807434	-5.810940	0.1785	CNOC2
327.808319	-5.877990	0.1395	FORS2
327.808807	-5.588772	0.4186	FORS2

RA	Dec	z	source	l Mpc	$r_{200,\sigma}$	$r_{200,X}$
327.808838	-5.784306	0.5896	IMACS
327.808990	-5.886892	0.4469	CNOC2
327.809082	-5.238930	0.4671	CNOC2
327.809387	-5.558119	0.8926	FORS2
327.809723	-5.799483	0.5680	FORS2+FORS2
327.809906	-5.396217	0.1773	CNOC2
327.809937	-5.414976	0.2191	IMACS
327.810181	-5.170310	0.3334	CNOC2
327.810394	-5.889151	0.4477	FORS2
327.810455	-5.729246	0.1772	CNOC2
327.810516	-5.498348	0.1432	CNOC2	XR21h6,XR21h7,OP21h104,OP21h105	XR21h6,OP21h104	XR21h7,OP21h106
327.810638	-5.895731	0.6027	FORS2
327.810822	-5.885478	0.6374	IMACS
327.810913	-5.789675	0.5675	FORS2
327.810974	-5.821345	0.3027	FORS2
327.811188	-5.613988	0.4400	CNOC2
327.811615	-5.881726	0.7590	FORS2
327.811646	-5.696182	0.4450	CNOC2
327.811676	-5.652082	0.2625	FORS2
327.811768	-5.396603	0.1782	FORS2
327.811859	-5.221153	0.2436	CNOC2
327.811981	-5.886234	0.5131	FORS2
327.812134	-5.144533	0.3583	CNOC2
327.812164	-5.710840	0.3979	CNOC2
327.812256	-5.566597	0.5155	IMACS
327.812408	-5.373849	0.1453	IMACS	XR21h6,XR21h7,OP21h104,OP21h105	XR21h6,OP21h104	...
327.812439	-5.591908	0.3741	CNOC2
327.812500	-5.221244	0.2450	CNOC2
327.812622	-5.330886	0.4066	CNOC2
327.812775	-5.796221	0.5695	FORS2+FORS2
327.812958	-5.892928	0.2118	FORS2
327.812988	-5.575786	0.8535	FORS2
327.813507	-5.819483	0.4915	FORS2
327.813721	-5.385614	0.4400	FORS2
327.814026	-5.834575	0.5516	FORS2
327.814301	-5.434874	0.7318	IMACS
327.814453	-5.883093	0.4475	FORS2
327.814484	-5.402078	0.1772	FORS2
327.814484	-5.873264	0.4510	CNOC2
327.814514	-5.391212	0.4251	FORS2
327.814728	-5.875370	0.8653	FORS2
327.815033	-5.821433	0.5645	CNOC2
327.815582	-5.835541	0.8704	FORS2
327.815613	-5.840949	0.5258	FORS2
327.816132	-5.567617	0.5153	CNOC2
327.816254	-5.382149	0.6667	FORS2
327.816345	-5.797450	0.9972	FORS2
327.816406	-5.263700	0.3210	CNOC2
327.816681	-5.905400	0.3641	FORS2
327.816742	-5.616439	0.5224	FORS2
327.816803	-5.217827	0.2635	CNOC2
327.817261	-5.565196	0.4776	FORS2
327.817352	-5.712375	0.4409	IMACS
327.817688	-5.596768	0.1968	IMACS
327.817719	-5.393328	0.4616	FORS2
327.818237	-5.618811	0.3672	CNOC2
327.818451	-5.117699	0.3990	CNOC2
327.818787	-5.394883	0.3205	FORS2
327.818787	-5.865641	0.8718	FORS2
327.818848	-5.823549	0.7019	FORS2
327.819366	-5.375989	0.2425	CNOC2
327.819824	-5.890405	0.6703	FORS2
327.820129	-5.883709	0.3872	CNOC2+FORS2
327.820557	-5.627467	0.4372	CNOC2
327.820618	-5.775004	0.4654	CNOC2
327.820648	-5.683915	0.4465	CNOC2
327.820801	-5.369803	0.7052	IMACS
327.821167	-5.663051	0.6536	IMACS
327.821350	-5.472821	0.2178	FORS2
327.821411	-5.803065	0.5674	FORS2+FORS2
327.821594	-5.660337	0.0967	CNOC2
327.821625	-5.644745	0.2613	IMACS
327.821869	-5.528843	0.3940	CNOC2
327.821991	-5.807517	1.4643	FORS2
327.822021	-5.864937	0.0986	CNOC2
327.822357	-5.461983	0.5368	CNOC2
327.822540	-5.869497	0.6271	FORS2
327.822937	-5.826095	0.2122	CNOC2
327.822968	-5.277506	0.3775	CNOC2
327.822998	-5.566489	0.1444	CNOC2
327.823059	-5.405084	0.7671	FORS2
327.823151	-5.809185	0.8604	FORS2
327.823395	-5.682296	0.4433	IMACS
327.823700	-5.496537	0.1474	FORS2	XR21h6,XR21h7,OP21h104,OP21h105	XR21h6,OP21h104	XR21h7,OP21h106
327.823944	-5.119788	0.3615	CNOC2
327.824432	-5.176294	0.0900	CNOC2
327.824615	-5.723526	0.4406	IMACS

RA	Dec	z	source	l Mpc	$r_{200,\sigma}$	$r_{200,X}$
327.824799	-5.679436	0.3583	CNOC2
327.825043	-5.398075	0.1729	FORS2
327.825073	-5.784358	0.3345	CNOC2
327.825104	-5.252502	0.3602	CNOC2
327.825165	-5.863661	0.8715	IMACS
327.825226	-5.420783	0.7668	FORS2
327.825531	-5.239113	0.2431	CNOC2
327.825623	-5.286810	0.0236	CNOC2
327.825684	-5.498743	1.0630	CNOC2
327.826080	-5.398028	0.1732	IMACS
327.826111	-5.124975	0.1468	CNOC2
327.826660	-5.341138	0.2372	CNOC2
327.826752	-5.845855	0.3324	CNOC2
327.827028	-5.369637	0.2627	CNOC2
327.827209	-5.860373	0.7017	FORS2
327.827209	-5.880594	0.7024	IMACS
327.827667	-5.612415	0.4873	IMACS
327.827789	-5.846455	0.3347	CNOC2
327.827911	-5.750004	0.2207	IMACS
327.828369	-5.696347	0.1791	IMACS
327.828552	-5.571367	0.4401	IMACS
327.828644	-5.668970	0.2997	CNOC2
327.828644	-5.679528	0.3562	CNOC2
327.828979	-5.864325	0.6435	FORS2
327.829407	-5.626863	0.2622	CNOC2
327.829620	-5.790204	0.4475	CNOC2
327.829803	-5.409433	0.3924	FORS2
327.829895	-5.812778	0.6702	FORS2
327.829987	-5.368709	0.4446	CNOC2
327.829987	-5.419658	0.4063	FORS2
327.830017	-5.869394	0.9275	FORS2
327.830139	-5.449560	0.5807	IMACS
327.830261	-5.858111	0.5136	FORS2
327.830414	-5.747341	0.2204	CNOC2
327.830597	-5.620546	0.2179	CNOC2
327.830963	-5.493565	0.6300	CNOC2
327.831268	-5.113206	0.5459	CNOC2
327.831329	-5.739563	0.1785	CNOC2
327.831451	-5.611646	0.6054	CNOC2
327.831757	-5.861447	0.6435	FORS2
327.832031	-5.824379	0.3638	FORS2
327.832306	-5.814902	0.5256	FORS2
327.832520	-5.894657	0.7471	FORS2
327.832703	-5.812646	0.2113	FORS2
327.833008	-5.383303	0.7666	FORS2
327.833130	-5.698634	0.2623	IMACS
327.833160	-5.770847	0.1794	CNOC2
327.833191	-5.609152	0.2608	IMACS
327.833252	-5.104795	0.2432	CNOC2
327.833344	-5.451867	0.2205	FORS2
327.833374	-5.441715	0.1434	FORS2	XR21h6,XR21h7,OP21h104,OP21h105	XR21h6,OP21h104	XR21h6,XR21h7,OP21h106
327.833862	-5.578438	0.3873	CNOC2
327.833893	-5.263628	0.1435	CNOC2
327.834442	-5.751031	0.5661	CNOC2
327.834564	-5.686485	0.6527	IMACS
327.834564	-5.794283	0.4759	FORS2+FORS2
327.834747	-5.624397	0.1407	CNOC2
327.834961	-5.281998	0.3594	CNOC2
327.834991	-5.388975	0.1456	FORS2	XR21h6,XR21h7,OP21h104,OP21h105	XR21h6,OP21h104	XR21h7,OP21h106
327.835693	-5.426745	0.4807	CNOC2
327.835846	-5.077090	0.2163	CNOC2
327.835846	-5.901336	0.8746	FORS2
327.836304	-5.757480	0.5718	CNOC2
327.836731	-5.528213	0.6302	CNOC2
327.837250	-5.849049	0.4536	FORS2
327.837585	-5.881439	0.7467	IMACS
327.837616	-5.851234	1.0612	FORS2
327.837677	-5.831747	0.6560	FORS2
327.837799	-5.892885	0.8752	FORS2
327.838318	-5.643760	0.4043	CNOC2
327.838837	-5.850518	0.7499	FORS2
327.839020	-5.559164	0.2213	CNOC2	XR21h9,XR21h12,OP21h115,OP21h116
327.839813	-5.436570	0.1450	CNOC2	XR21h6,XR21h7,OP21h104,OP21h105	XR21h6,OP21h104	XR21h6,XR21h7,OP21h106
327.840210	-5.810755	0.4265	CNOC2
327.840302	-5.685142	0.3344	CNOC2
327.840363	-5.066713	0.4261	CNOC2
327.840424	-5.792982	0.9946	FORS2
327.840851	-5.669488	0.1778	CNOC2
327.841064	-5.382652	0.1215	CNOC2
327.841370	-5.681932	0.3013	IMACS
327.841522	-5.436527	0.1471	CNOC2	XR21h6,XR21h7,OP21h104,OP21h105	XR21h6,OP21h104	XR21h6,XR21h7,OP21h106
327.841797	-5.751751	0.1414	CNOC2
327.841949	-5.714983	0.1447	CNOC2
327.842407	-5.457711	0.1412	FORS2
327.842529	-5.876921	0.3334	CNOC2
327.842560	-5.774821	0.1792	CNOC2

Appendix: Spectroscopic Redshifts

RA	Dec	z	source	l Mpc	$r_{200,\sigma}$	$r_{200,X}$
327.842682	-5.873067	0.3365	FORS2
327.843231	-5.463574	0.1485	FORS2	XR21h6,XR21h7,OP21h104,OP21h105	XR21h6,OP21h104	XR21h7,OP21h106
327.843292	-5.835442	0.6561	CNOC2
327.843414	-5.462366	0.1475	FORS2	XR21h6,XR21h7,OP21h104,OP21h105	XR21h6,OP21h104	XR21h7,OP21h106
327.843597	-5.330143	0.2628	CNOC2
327.843903	5.623421	0.6336	CNOC2
327.843933	-5.498921	0.1453	CNOC2	XR21h6,XR21h7,OP21h104,OP21h105	XR21h6,OP21h104	XR21h7,OP21h106
327.843964	-5.877251	0.9687	FORS2
327.844116	-5.283693	0.2017	CNOC2
327.844208	-5.759825	0.1416	IMACS
327.844238	-5.573861	0.7121	IMACS
327.844299	-5.700035	0.1783	CNOC2
327.844543	-5.675590	0.3988	IMACS
327.844635	-5.388347	0.1789	CNOC2
327.844757	-5.232380	0.1972	CNOC2
327.844940	-5.487618	0.2203	FORS2	XR21h9,OP21h115,OP21h116
327.845062	-5.062483	0.4254	CNOC2
327.845459	-5.854407	0.3594	FORS2
327.845703	-5.447756	0.1448	CNOC2	XR21h6,XR21h7,OP21h104,OP21h105	XR21h6,OP21h104	XR21h6,XR21h7,OP21h106
327.847137	-5.859958	0.4468	CNOC2
327.847870	-5.582301	0.6664	IMACS
327.847931	-5.456609	0.1424	FORS2	XR21h6,XR21h7,OP21h104,OP21h105	XR21h6,OP21h104	XR21h6,XR21h7,OP21h106
327.848511	-5.083627	0.1612	CNOC2
327.848938	-5.860082	0.4461	CNOC2
327.849030	-5.876263	0.7558	FORS2
327.849152	-5.152507	0.2446	CNOC2
327.849182	-5.440068	0.1434	CNOC2	XR21h6,XR21h7,OP21h104,OP21h105	XR21h6,OP21h104	XR21h6,XR21h7,OP21h106
327.849548	-5.445503	0.7815	FORS2
327.849823	-5.614256	0.4384	IMACS
327.849976	-5.091946	0.5903	CNOC2
327.850128	-5.801557	0.3753	FORS2
327.850342	-5.849233	0.2244	FORS2
327.850464	-5.894519	1.3293	FORS2
327.850616	-5.628512	0.4433	CNOC2
327.850739	-5.516449	0.4511	CNOC2
327.850800	-5.525310	0.2178	IMACS
327.850830	-5.686964	0.4411	IMACS
327.850922	-5.416853	0.6700	FORS2
327.851227	-5.701070	0.3339	CNOC2
327.851318	-5.235457	0.2616	CNOC2
327.851379	-5.053270	0.5913	CNOC2
327.851440	-5.592434	0.1475	FORS2
327.851654	-5.410826	0.3693	CNOC2
327.852051	-5.095617	0.4397	CNOC2
327.852051	-5.423004	0.1478	CNOC2	XR21h6,XR21h7,OP21h104,OP21h105	XR21h6,OP21h104	XR21h6,XR21h7,OP21h106
327.852051	-5.829781	0.6556	CNOC2
327.852081	-5.442564	0.6295	FORS2
327.852173	-5.682756	0.4395	CNOC2
327.852234	-5.712240	0.2624	IMACS
327.852295	-5.897951	0.7983	FORS2
327.852448	-5.568299	0.4245	FORS2
327.852509	-5.880039	0.1434	FORS2
327.852692	-5.887237	0.1801	FORS2
327.852875	-5.119442	0.1472	CNOC2
327.852875	-5.459350	0.1424	FORS2	XR21h6,XR21h7,OP21h104,OP21h105	XR21h6,OP21h104	XR21h7,OP21h106
327.853180	-5.120043	0.4477	CNOC2
327.853455	-5.281055	0.4673	CNOC2
327.853577	-5.670393	0.8860	CNOC2
327.854187	-5.424311	0.6881	FORS2
327.854370	-5.426745	0.1499	FORS2
327.854462	-5.439870	0.1479	FORS2	XR21h6,XR21h7,OP21h104,OP21h105	XR21h6,OP21h104	XR21h6,XR21h7,OP21h106
327.854523	-5.732215	0.7634	IMACS
327.854584	-5.128368	0.1478	CNOC2
327.854584	-5.360494	0.2003	CNOC2
327.854645	-5.817298	0.1442	CNOC2
327.854767	-5.602126	0.2482	CNOC2
327.855011	-5.848898	0.3032	IMACS
327.855225	-5.166441	0.2430	CNOC2
327.855682	-5.222024	0.3205	CNOC2
327.856201	-5.431742	0.1451	FORS2	XR21h6,XR21h7,OP21h104,OP21h105	XR21h6,OP21h104	XR21h6,XR21h7,OP21h106
327.856293	-5.575342	0.4769	IMACS
327.856354	-5.317524	0.1454	CNOC2
327.856537	-5.622141	0.6593	CNOC2
327.856567	-5.446409	0.1448	IMACS	XR21h6,XR21h7,OP21h104,OP21h105	XR21h6,OP21h104	XR21h6,XR21h7,OP21h106
327.856598	-5.675098	0.1695	CNOC2
327.856934	-5.080852	0.2434	CNOC2
327.857204	-5.475481	0.2206	FORS2	XR21h9,OP21h115,OP21h116
327.857391	-5.630717	0.4764	CNOC2
327.857483	-5.470472	0.3931	CNOC2
327.857819	-5.157606	0.5547	CNOC2
327.857941	-5.680415	0.5480	CNOC2
327.857971	-5.424363	0.1460	CNOC2	XR21h6,XR21h7,OP21h104,OP21h105	XR21h6,OP21h104	XR21h6,XR21h7,OP21h106
327.858307	-5.621238	0.3672	IMACS
327.858521	-5.594731	0.1452	FORS2
327.858551	-5.882751	0.1815	CNOC2
327.858856	-5.218832	0.2170	CNOC2
327.859253	-5.478473	0.1443	CNOC2	XR21h6,XR21h7,OP21h104,OP21h105	XR21h6,OP21h104	XR21h7,OP21h106

RA	Dec	z	source	l Mpc	$r_{200,\sigma}$	$r_{200,X}$
327.859467	-5.318690	0.1450	CNOC2
327.859741	-5.441994	0.5355	CNOC2
327.859772	-5.572489	0.2198	CNOC2	XR21h9,XR21h12,OP21h115,OP21h116
327.860077	-5.481687	0.2201	FORS2	XR21h9,OP21h115,OP21h116
327.860321	-5.678030	0.5255	IMACS
327.860687	-5.100716	0.3257	CNOC2
327.860840	-5.651285	0.5265	CNOC2
327.861023	-5.716152	0.5148	CNOC2
327.861237	-5.085033	0.6000	CNOC2
327.861664	-5.609462	0.6590	FORS2
327.862213	-5.128897	0.2427	CNOC2
327.862915	-5.431123	0.1457	IMACS	XR21h6,XR21h7,OP21h104,OP21h105	XR21h6,OP21h104	XR21h6,XR21h7,OP21h106
327.863373	-5.412855	0.8095	FORS2
327.863556	-5.570277	0.2609	IMACS
327.863708	-5.075558	0.0717	CNOC2
327.864807	-5.558450	0.6488	CNOC2
327.865021	-5.369782	0.1633	CNOC2
327.865051	-5.539381	0.2205	CNOC2	XR21h9,XR21h12,OP21h115,OP21h116
327.865784	-5.694564	0.1453	CNOC2
327.865814	-5.085041	0.2432	CNOC2
327.866119	-5.186729	0.5464	CNOC2
327.866364	-5.486245	0.1475	FORS2	XR21h6,XR21h7,OP21h104,OP21h105	XR21h6,OP21h104	XR21h7,OP21h106
327.866699	-5.706135	0.3260	IMACS
327.867279	-5.491455	0.7329	FORS2
327.867798	-5.838786	0.9280	IMACS
327.867889	-5.130655	0.2449	CNOC2
327.868073	-5.882178	0.3878	CNOC2
327.868195	-5.238509	0.1450	CNOC2
327.868561	-5.858703	0.3026	CNOC2
327.868713	-5.445012	0.1464	CNOC2	XR21h6,XR21h7,OP21h104,OP21h105	XR21h6,OP21h104	XR21h6,XR21h7,OP21h106
327.868988	-5.691636	0.2378	CNOC2
327.869049	-5.691636	0.7213	IMACS
327.869720	-5.494615	0.4479	CNOC2
327.869843	-5.452977	0.1452	CNOC2	XR21h6,XR21h7,OP21h104,OP21h105	XR21h6,OP21h104	XR21h6,XR21h7,OP21h106
327.869873	-5.577354	0.1451	IMACS
327.870148	-5.125282	0.2620	CNOC2
327.870392	-5.886213	0.3876	CNOC2
327.870453	-5.376488	0.1459	IMACS	XR21h6,XR21h7,OP21h104,OP21h105	XR21h6,OP21h104	XR21h6,XR21h7,OP21h106
327.870605	-5.718988	0.7193	IMACS
327.870667	-5.083397	0.3978	CNOC2
327.870728	-5.686852	0.5615	CNOC2
327.870850	-5.594005	0.6504	CNOC2
327.870880	-5.732798	0.4780	CNOC2
327.871460	-5.775533	0.4064	CNOC2
327.871979	-5.080342	0.5995	CNOC2
327.872040	-5.630348	0.3932	CNOC2
327.872345	-5.191533	0.2871	CNOC2
327.872559	-5.500471	0.6894	FORS2
327.872742	-5.594121	0.6056	IMACS
327.872833	-5.840164	0.8041	IMACS
327.872925	-5.351011	0.1686	IMACS
327.873352	-5.359232	0.4242	CNOC2
327.873627	-5.482146	0.4804	IMACS
327.873993	-5.585016	0.4379	CNOC2
327.874695	-5.420781	0.1637	CNOC2
327.874817	-5.840928	0.9979	IMACS
327.874878	-5.362537	0.4259	CNOC2
327.874939	-5.838892	0.1784	CNOC2
327.874969	-5.137924	0.2430	CNOC2
327.875549	-5.549481	0.6322	FORS2
327.875580	-5.688533	0.4785	CNOC2
327.875732	-5.588753	0.1478	IMACS
327.875916	-5.372041	0.4528	IMACS
327.876190	-5.551396	0.2622	FORS2
327.876312	-5.333725	0.2619	CNOC2
327.876343	-5.763394	0.5666	CNOC2
327.876373	-5.683930	0.8211	IMACS
327.876465	-5.407608	0.4366	FORS2
327.877045	-5.515627	0.3566	CNOC2
327.877319	-5.387173	0.8023	FORS2
327.877594	-5.880920	0.8880	CNOC2
327.877777	-5.557242	0.2609	IMACS
327.877869	-5.449823	0.3944	IMACS
327.877869	-5.577478	0.4514	FORS2+FORS2
327.878021	-5.695780	0.2416	CNOC2
327.878052	-5.436950	0.1439	CNOC2	XR21h6,XR21h7,OP21h104,OP21h105	XR21h6,OP21h104	XR21h6,XR21h7,OP21h106
327.878082	-5.468359	0.1445	FORS2	XR21h6,XR21h7,OP21h104,OP21h105	XR21h6,OP21h104	XR21h7,OP21h106
327.878571	-5.615121	0.4389	FORS2
327.879181	-5.691488	0.1785	IMACS
327.879395	-5.489850	0.1438	FORS2	XR21h6,XR21h7,OP21h104,OP21h105	XR21h6,OP21h104	XR21h7,OP21h106
327.879486	-5.410349	0.1474	FORS2
327.879547	-5.483917	0.9462	FORS2	XR21h6,XR21h7,OP21h104,OP21h105	XR21h6,OP21h104	XR21h7,OP21h106
327.879822	-5.389870	0.3235	IMACS
327.880615	-5.097751	0.4421	CNOC2
327.880737	-5.699252	0.1802	CNOC2
327.880798	-5.095096	0.3397	CNOC2

RA	Dec	z	source	l Mpc	$r_{200,\sigma}$	$r_{200,X}$
327.880890	-5.470804	0.1433	FORS2	XR21h6,XR21h7,OP21h104,OP21h105	XR21h6,OP21h104	XR21h7,OP21h106
327.881104	-5.591624	0.2376	CNOC2
327.881134	-5.698786	0.1789	CNOC2
327.881195	-5.827458	0.1771	CNOC2
327.881348	-5.125668	0.3413	CNOC2
327.881622	-5.465329	0.1453	CNOC2	XR21h6,XR21h7,OP21h104,OP21h105	XR21h6,OP21h104	XR21h7,OP21h106
327.881805	-5.431863	0.1447	IMACS	XR21h6,XR21h7,OP21h104,OP21h105	XR21h6,OP21h104	XR21h6,XR21h7,OP21h106
327.882019	-5.414292	0.4805	CNOC2
327.882507	-5.127916	0.1577	CNOC2
327.883514	-5.846440	0.1786	CNOC2
327.883759	-5.663872	0.2449	FORS2
327.883789	-5.542831	0.6632	FORS2
327.883972	-5.463241	0.7018	IMACS
327.884125	-5.673386	0.2213	CNOC2
327.884277	-5.507507	0.2201	FORS2	XR21h9,OP21h115,OP21h116	XR21h9,OP21h115	XR21h9,OP21h118
327.884460	-5.559109	0.2908	CNOC2
327.884644	-5.720598	0.7342	IMACS
327.884918	-5.093075	0.6444	CNOC2
327.884979	-5.437309	0.1450	FORS2	XR21h6,XR21h7,OP21h104,OP21h105	XR21h6,OP21h104	XR21h7,OP21h106
327.885315	-5.623418	0.2203	CNOC2
327.885468	-5.824509	0.4058	IMACS
327.885651	-5.674601	0.4432	CNOC2
327.885773	-5.493357	0.3568	FORS2
327.886047	-5.825444	0.4053	CNOC2
327.886292	-5.559272	0.2611	CNOC2
327.886353	-5.521496	0.6488	IMACS
327.886810	-5.748977	0.2157	CNOC2
327.886963	-5.464169	0.3196	CNOC2
327.886993	-5.878732	0.5476	CNOC2
327.887024	-5.460491	0.2621	CNOC2
327.887085	-5.384969	0.7046	IMACS
327.887634	-5.583001	0.2606	CNOC2
327.887756	-5.527403	0.5868	FORS2
327.887817	-5.688920	0.6448	IMACS
327.888367	-5.712270	0.5479	CNOC2
327.888397	-5.433436	0.2192	FORS2
327.888947	-5.857590	0.3606	CNOC2
327.889069	-5.391446	0.3591	IMACS
327.889099	-5.325667	0.1985	CNOC2
327.889130	-5.601382	0.5253	IMACS
327.889771	-5.405435	0.1403	CNOC2
327.890045	-5.605521	0.4491	FORS2+FORS2
327.890259	-5.125448	0.2432	CNOC2
327.890778	-5.782366	0.3595	CNOC2
327.890930	-5.503195	0.2197	CNOC2	XR21h9,OP21h115,OP21h116	XR21h9,OP21h115	XR21h9,OP21h118
327.891144	-5.353911	0.3728	CNOC2
327.891205	-5.619205	0.2768	FORS2
327.891327	-5.586896	0.1454	FORS2+FORS2
327.891998	-5.143773	0.3589	CNOC2
327.892059	-5.198428	0.2164	CNOC2
327.892670	-5.538575	0.2196	CNOC2	XR21h9,XR21h12,OP21h115,OP21h116	XR21h9,OP21h115	XR21h9,OP21h118
327.892700	-5.081642	0.3941	CNOC2
327.892731	-5.601054	0.5246	IMACS
327.892883	-5.314461	0.1459	CNOC2
327.892883	-5.505336	0.2167	FORS2
327.893219	-5.184092	0.1782	CNOC2
327.893311	-5.762722	0.1535	CNOC2
327.894012	-5.449273	0.4805	IMACS
327.894135	-5.502873	0.2201	CNOC2	XR21h9,OP21h115,OP21h116	XR21h9,OP21h115	XR21h9,OP21h118
327.894287	-5.864425	0.3341	CNOC2
327.894836	-5.316956	0.2010	CNOC2
327.895447	-5.358634	0.4445	CNOC2
327.895599	-5.524386	0.2609	CNOC2+FORS2
327.895660	-5.403881	0.7095	FORS2
327.895721	-5.093601	0.2740	CNOC2
327.895966	-5.779705	0.1449	CNOC2
327.896057	-5.083418	0.1455	CNOC2
327.896912	-5.515295	0.2186	CNOC2	XR21h9,XR21h12,OP21h115,OP21h116	XR21h9,OP21h115	XR21h9,OP21h118
327.897064	-5.609134	0.2617	CNOC2
327.897156	-5.427777	0.1461	FORS2	XR21h6,XR21h7,OP21h104,OP21h105	XR21h6,OP21h104	XR21h7,OP21h106
327.897552	-5.601989	0.4384	FORS2+FORS2
327.897614	-5.362955	0.2543	CNOC2
327.897766	-5.389600	0.1999	IMACS
327.897766	-5.458874	0.1558	CNOC2
327.897858	-5.511493	0.2185	CNOC2	XR21h9,OP21h115,OP21h116	XR21h9,OP21h115	XR21h9,OP21h118
327.898041	-5.606179	0.2202	CNOC2
327.898376	-5.170024	0.2419	CNOC2
327.898406	-5.579022	0.4799	FORS2
327.898560	-5.685661	0.5985	FORS2
327.898712	-5.446229	0.7104	FORS2
327.898956	-5.170730	0.2418	CNOC2
327.899109	-5.071916	0.2438	CNOC2
327.899261	-5.331378	0.3580	CNOC2
327.899384	-5.645989	0.4538	FORS2
327.899506	-5.599327	0.2211	FORS2+FORS2	XR21h12,OP21h115,OP21h116
327.899597	-5.627485	0.6296	CNOC2
327.899811	-5.312826	0.6650	CNOC2

RA	Dec	z	source	l Mpc	$r_{200,\sigma}$	$r_{200,X}$
327.899963	-5.659931	0.7605	FORS2
327.900421	-5.600707	0.2204	CNOC2	XR21h12,OP21h115,OP21h116
327.900604	-5.558108	0.2199	FORS2+FORS2	XR21h12,OP21h115,OP21h116
327.900787	-5.665480	0.5655	FORS2
327.901062	-5.607048	0.5658	FORS2+FORS2
327.901306	-5.413530	0.1682	FORS2
327.901520	-5.456773	0.1148	IMACS
327.901550	-5.114528	0.2417	CNOC2
327.901672	-5.611475	0.4388	FORS2+FORS2
327.901917	-5.508961	0.2188	CNOC2	XR21h9,OP21h115,OP21h116	XR21h9,OP21h115	XR21h9,OP21h118
327.902008	-5.596661	0.2189	CNOC2	XR21h12,OP21h115,OP21h116
327.902130	-5.872372	0.6455	CNOC2
327.902191	-5.501713	0.0982	FORS2
327.902283	-5.764733	3.1570	CNOC2
327.902466	-5.671941	0.3922	CNOC2
327.902710	-5.518916	0.2200	FORS2	XR21h9,XR21h12,OP21h115,OP21h116	XR21h9,OP21h115	XR21h9,OP21h118
327.902802	-5.509685	0.2602	FORS2
327.903137	-5.558624	0.2636	FORS2
327.903168	-5.603281	0.2192	CNOC2
327.903961	-5.451893	0.2588	FORS2
327.904053	-5.498188	0.4101	FORS2
327.904266	-5.442533	0.2608	CNOC2
327.904480	-5.394576	0.6137	CNOC2
327.905151	-5.526322	0.7337	FORS2
327.905609	-5.817458	0.1390	CNOC2
327.905670	-5.525256	0.2202	CNOC2	XR21h9,XR21h12,OP21h115,OP21h116	XR21h9,OP21h115	XR21h9,OP21h118
327.905670	-5.606022	0.2194	CNOC2
327.905945	-5.638102	0.6303	CNOC2
327.905975	-5.431331	0.2615	FORS2
327.906006	-5.380871	0.4257	CNOC2
327.906464	-5.558915	0.5253	CNOC2
327.906525	-5.579487	0.2644	FORS2
327.906921	-5.571063	0.4786	FORS2
327.907379	-5.400954	0.5233	FORS2
327.907501	-5.681432	0.1453	CNOC2
327.907928	-5.629019	0.4477	FORS2
327.908691	-5.855298	0.1774	CNOC2
327.908997	-5.448434	0.7532	FORS2
327.909332	-5.645409	0.5271	CNOC2
327.909637	-5.493799	0.2630	IMACS
327.909637	-5.698440	0.5253	CNOC2
327.909973	-5.594739	0.2426	CNOC2
327.910095	-5.597674	0.2166	IMACS
327.910248	-5.702143	0.5661	IMACS
327.910706	-5.557264	0.1445	FORS2
327.911499	-5.433447	0.3167	FORS2
327.912140	-5.544155	0.7047	FORS2
327.912170	-5.490276	0.1660	CNOC2
327.912384	-5.6611353	0.2617	FORS2
327.912994	-5.564939	0.3570	FORS2
327.913330	-5.525956	0.1674	CNOC2
327.913361	-5.689708	0.5649	FORS2
327.913391	-5.554412	0.1451	FORS2
327.913574	-5.747200	0.6607	CNOC2
327.913635	-5.793683	0.2414	CNOC2
327.914612	-5.455362	0.1455	FORS2	XR21h6,XR21h7,OP21h104,OP21h105	XR21h6,OP21h104	XR21h7,OP21h106
327.914673	-5.523779	0.4798	CNOC2
327.914703	-5.574385	0.4238	CNOC2
327.915131	-5.674902	0.2202	CNOC2
327.915558	-5.573852	0.4238	FORS2
327.915588	-5.521636	0.3007	FORS2
327.915802	-5.687142	0.5685	FORS2
327.915894	-5.656289	0.5658	FORS2
327.916016	-5.623406	0.2186	FORS2
327.916107	-5.670130	0.5668	FORS2
327.916595	-5.773144	0.6291	CNOC2
327.916656	-5.442108	0.1443	FORS2	XR21h6,XR21h7,OP21h104,OP21h105	XR21h6,OP21h104	XR21h7,OP21h106
327.916840	-5.820760	0.5482	CNOC2
327.916962	-5.619888	0.2176	CNOC2
327.917023	-5.728712	0.4909	CNOC2
327.918396	-5.631558	0.4114	FORS2
327.918457	-5.582419	0.3574	CNOC2
327.918518	-5.498940	0.5252	CNOC2
327.918640	-5.489885	0.1466	CNOC2	XR21h6,XR21h7,OP21h104,OP21h105	XR21h6,OP21h104	XR21h7,OP21h106
327.918762	-5.692759	0.2200	CNOC2
327.919281	-5.691026	0.1764	FORS2
327.919708	-5.581073	0.2626	FORS2+FORS2
327.919922	-5.601549	0.3574	CNOC2
327.920471	-5.527440	0.2425	CNOC2
327.920685	-5.472067	0.2634	FORS2
327.920929	-5.874536	0.1427	CNOC2
327.920959	-5.535993	0.3365	FORS2
327.921173	-5.840016	0.6743	CNOC2
327.921631	-5.591305	0.4505	FORS2
327.922607	-5.709019	0.3595	CNOC2
327.922760	-5.450842	0.2604	FORS2
327.923126	-5.783360	0.0894	CNOC2

RA	Dec	z	source	l Mpc	$r_{200,\sigma}$	$r_{200,X}$
327.923157	-5.586415	0.4802	IMACS
327.923157	-5.650350	0.3931	FORS2
327.923401	-5.562409	0.4564	CNOC2
327.924316	-5.595640	0.4796	CNOC2
327.924438	-5.443179	0.4736	FORS2
327.926514	-5.490021	0.4809	IMACS
327.926971	-5.429057	0.1654	FORS2
327.927063	-5.514792	0.2191	FORS2	XR21h9,OP21h115,OP21h116	XR21h9,OP21h115	XR21h9,OP21h118
327.927124	-5.505397	0.5238	CNOC2
327.928009	-5.407675	0.1473	FORS2	XR21h6,XR21h7,OP21h104,OP21h105	XR21h6,OP21h104	...
327.929016	-5.670729	0.5671	CNOC2
327.929504	-5.554149	0.2187	CNOC2	XR21h9,XR21h12,OP21h115,OP21h116
327.929565	-5.784691	0.0903	CNOC2
327.929596	-5.545938	0.2183	FORS2	XR21h9,XR21h12,OP21h115,OP21h116
327.929810	-5.434169	0.2616	FORS2
327.929901	-5.580293	0.2202	CNOC2	XR21h9,XR21h12,OP21h115,OP21h116
327.930664	-5.540838	0.6564	FORS2
327.930786	-5.542091	0.2208	CNOC2	XR21h9,XR21h12,OP21h115,OP21h116
327.930847	-5.851476	0.3335	CNOC2
327.931427	-5.415891	0.3946	FORS2
327.932587	-5.672215	0.3344	CNOC2
327.932800	-5.618672	0.4111	CNOC2
327.933380	-5.430980	0.2629	FORS2
327.933441	-5.683638	0.1528	FORS2
327.933838	-5.865019	0.6284	CNOC2
327.933990	-5.550395	0.2185	CNOC2	XR21h9,XR21h12,OP21h115,OP21h116
327.934204	-5.672873	0.7327	FORS2
327.934631	-5.675543	0.7338	FORS2
327.935303	-5.674445	0.7341	FORS2
327.935516	-5.530793	0.1216	IMACS
327.935944	-5.763629	0.2401	CNOC2
327.935974	-5.668264	0.8357	FORS2
327.936218	-5.594042	0.3578	CNOC2
327.936554	-5.648033	0.3407	FORS2
327.936646	-5.557135	0.2203	CNOC2	XR21h9,XR21h12,OP21h115,OP21h116
327.936676	-5.432182	0.2604	FORS2
327.936859	-5.673039	0.7299	IMACS
327.937439	-5.553978	0.7324	IMACS
327.937744	-5.865204	0.2188	CNOC2
327.937927	-5.801857	0.6580	CNOC2
327.938019	-5.430932	0.2609	FORS2
327.938660	-5.761243	0.2705	CNOC2
327.939301	-5.595479	0.1471	FORS2
327.939362	-5.525404	0.3942	IMACS
327.939819	-5.506314	0.5474	CNOC2
327.939972	-5.752508	0.3924	CNOC2
327.940002	-5.540254	0.2191	CNOC2	XR21h9,XR21h12,OP21h115,OP21h116
327.940277	-5.423165	0.2629	FORS2
327.940887	-5.786656	0.3681	CNOC2
327.941345	-5.870783	0.6525	CNOC2
327.941437	-5.524771	0.3945	CNOC2
327.941864	-5.837954	0.3356	CNOC2
327.942261	-5.495084	0.4815	IMACS
327.942719	-5.490846	0.4806	CNOC2
327.942780	-5.653921	0.8881	IMACS
327.943146	-5.443562	0.8666	FORS2
327.943787	-5.839831	0.1405	CNOC2
327.944061	-5.817684	0.3930	CNOC2
327.944183	-5.711241	0.1519	CNOC2
327.944397	-5.511195	0.4814	CNOC2
327.944885	-5.754159	0.4395	CNOC2
327.944916	-5.552519	0.4082	IMACS
327.945251	-5.528678	0.4389	CNOC2
327.945282	-5.417487	0.3926	FORS2
327.945862	-5.643091	0.4800	CNOC2
327.946106	-5.620427	0.2191	CNOC2
327.947174	-5.402036	0.2194	FORS2
327.947296	-5.837001	0.3594	CNOC2
327.947357	-5.757189	0.3599	CNOC2
327.947449	-5.653734	0.8885	FORS2
327.947571	-5.680886	0.8307	FORS2
327.947815	-5.637309	0.2192	FORS2
327.948517	-5.719003	0.5663	CNOC2
327.949280	-5.496430	0.6491	CNOC2
327.949371	-5.439014	0.6727	FORS2
327.949585	-5.676020	0.2261	IMACS
327.950256	-5.554820	0.2176	CNOC2	XR21h9,XR21h12,OP21h115,OP21h116
327.950531	-5.830557	0.0556	CNOC2
327.950562	-5.617025	0.5751	FORS2
327.950592	-5.840941	0.3339	CNOC2
327.951508	-5.445396	0.2623	FORS2
327.952087	-5.712646	0.2204	CNOC2
327.952240	-5.773900	0.3947	CNOC2
327.953278	-5.617996	0.2002	CNOC2
327.953369	-5.439678	0.1473	FORS2	XR21h6,XR21h7,OP21h104,OP21h105	XR21h6,OP21h104	...
327.953552	-5.669748	0.4548	CNOC2
327.955078	-5.681877	0.3892	IMACS

RA	Dec	z	source	l Mpc	$r_{200,\sigma}$	$r_{200,X}$
327.955292	-5.425520	0.1456	FORS2	XR21h6,XR21h7,OP21h104,OP21h105	XR21h6,OP21h104	...
327.955292	-5.478988	0.6479	IMACS
327.956543	-5.817746	0.3927	CNOC2
327.957092	-5.862337	0.1447	CNOC2
327.957367	-5.545897	0.4081	CNOC2
327.957611	-5.808332	0.3922	CNOC2
327.958167	-5.402014	0.0551	FORS2
327.958435	-5.521792	0.9085	IMACS
327.958771	-5.718554	0.1561	CNOC2
327.958801	-5.865265	0.1796	CNOC2
327.959595	-5.736546	0.4396	CNOC2
327.961029	-5.527007	0.4726	CNOC2
327.961182	-5.680108	0.7717	IMACS
327.961304	-5.643408	0.4382	CNOC2
327.961426	-5.611162	0.2201	CNOC2
327.961639	-5.442674	0.3745	FORS2
327.961639	-5.718208	0.1438	CNOC2
327.962097	-5.766638	0.1520	CNOC2
327.962402	-5.486284	0.8261	IMACS
327.963928	-5.855785	0.2436	CNOC2
327.964294	-5.404715	0.1454	FORS2
327.964386	-5.696590	0.6202	CNOC2
327.965210	-5.622362	0.2191	CNOC2
327.965607	-5.402897	0.2612	FORS2
327.965881	-5.545273	0.1966	CNOC2
327.966217	-5.642137	0.2190	IMACS
327.966797	-5.510782	0.6947	IMACS
327.967041	-5.772431	0.3349	CNOC2
327.967072	-5.557773	0.3345	CNOC2
327.967346	-5.858110	0.2534	CNOC2
327.967682	-5.608297	0.7326	IMACS
327.968933	-5.610317	0.3015	CNOC2
327.968994	-5.872806	0.6711	CNOC2
327.969177	-5.619832	0.2195	CNOC2
327.969238	-5.833406	0.3919	CNOC2
327.969269	-5.403457	0.1999	FORS2
327.969543	-5.774897	0.4396	CNOC2
327.969666	-5.824470	0.6698	CNOC2
327.969788	-5.676613	0.4566	CNOC2
327.969818	-5.748822	0.4388	CNOC2
327.970795	-5.605165	0.2185	IMACS
327.970856	-5.449847	0.2624	FORS2
327.971171	-5.839269	0.0950	CNOC2
327.972595	-5.674096	0.4575	CNOC2
327.972687	-5.627436	0.2199	CNOC2
327.972809	-5.463267	0.4491	FORS2
327.972839	-5.569849	0.5238	CNOC2
327.973389	-5.774630	0.0974	CNOC2
327.974121	-5.616734	0.1789	IMACS
327.974762	-5.582999	0.2623	CNOC2
327.974854	-5.401550	0.1680	FORS2
327.975189	-5.709311	0.3662	CNOC2
327.975372	-5.873521	0.1147	CNOC2
327.975677	-5.479227	0.3734	CNOC2
327.975708	-5.831365	0.1406	CNOC2
327.975769	-5.823626	0.4399	CNOC2
327.975800	-5.735908	0.0980	CNOC2
327.975830	-5.559887	0.3756	CNOC2
327.976532	-5.470612	0.3753	FORS2
327.976685	-5.512074	0.4483	CNOC2
327.977173	-5.603437	0.5172	CNOC2
327.977570	-5.809820	0.2217	CNOC2
327.977936	-5.564983	0.3754	CNOC2
327.978149	-5.836850	0.1405	CNOC2
327.978546	-5.692784	0.2441	CNOC2
327.979462	-5.879881	0.3584	CNOC2
327.980072	-5.472495	0.3763	FORS2
327.980560	-5.698082	0.3666	CNOC2
327.981659	-5.588474	0.2202	IMACS
327.981812	-5.596302	0.4383	CNOC2
327.982117	-5.439954	0.3162	FORS2
327.982971	-5.815300	0.2212	CNOC2
327.983185	-5.533549	0.5655	CNOC2
327.983276	-5.558276	0.4795	IMACS
327.983337	-5.760151	0.4379	CNOC2
327.983521	-5.430845	0.6461	FORS2
327.983734	-5.712704	0.2204	CNOC2
327.986725	-5.853581	0.1826	CNOC2
327.986816	-5.807428	0.5257	CNOC2
327.987793	-5.879085	0.3588	CNOC2
327.988007	-5.632268	0.2399	CNOC2
327.989044	-5.656086	0.2421	CNOC2
327.989136	-5.437206	0.3026	FORS2
327.989594	-5.705601	0.1918	CNOC2
327.989655	-5.888871	0.3655	CNOC2
327.990936	-5.655042	0.1417	CNOC2
327.991302	-5.813205	0.2524	CNOC2

RA	Dec	z	source	l Mpc	$r_{200,\sigma}$	$r_{200,X}$
327.992126	-5.834217	0.3666	CNOC2
327.992767	-5.786644	0.4716	CNOC2
327.993164	-5.612602	0.5071	CNOC2
327.993347	-5.733741	0.2844	CNOC2
327.993622	-5.802343	0.0905	CNOC2
327.994110	-5.512895	0.3747	CNOC2
327.995880	-5.720678	0.4778	CNOC2
327.995972	-5.439602	0.2013	FORS2
327.996552	-5.584366	0.2405	CNOC2
327.997345	-5.868152	0.2619	CNOC2
327.997406	-5.808715	0.1977	CNOC2
327.998016	-5.653798	0.1211	IMACS
327.998169	-5.422213	0.3597	FORS2
327.998413	-5.763225	0.3930	CNOC2
327.998566	-5.857102	0.6623	CNOC2
327.998657	-5.554066	0.2701	IMACS
327.998688	-5.654625	0.1228	CNOC2
327.999847	-5.647302	0.4392	CNOC2
328.000793	-5.500532	0.4645	CNOC2
328.001465	-5.727312	0.3327	CNOC2
328.001526	-5.756526	0.6524	CNOC2
328.002380	-5.448536	0.5058	FORS2
328.002411	-5.671349	0.1428	CNOC2
328.003937	-5.564415	0.5243	CNOC2
328.003998	-5.656388	0.2159	CNOC2
328.004547	-5.768601	0.4384	CNOC2
328.004883	-5.565817	0.4587	IMACS
328.005585	-5.653455	0.1212	CNOC2
328.006073	-5.707378	0.1434	CNOC2
328.006378	-5.663622	0.1219	CNOC2
328.006500	-5.560313	0.4675	CNOC2
328.006500	-5.764217	0.4387	CNOC2
328.006531	-5.737243	0.3694	CNOC2
328.006775	-5.885703	0.3604	CNOC2
328.007019	-5.485425	0.5609	CNOC2
328.007965	-5.607574	0.4573	CNOC2
328.009247	-5.562595	0.4582	CNOC2
328.009613	-5.453811	0.2044	FORS2
328.009613	-5.818404	0.5675	CNOC2
328.010651	-5.802024	0.3028	CNOC2
328.010681	-5.881969	0.3027	CNOC2
328.010925	-5.599359	0.4574	CNOC2
328.011047	-5.560609	0.5546	IMACS
328.011169	-5.678622	0.4250	CNOC2
328.014496	-5.517659	0.2303	CNOC2
328.014587	-5.567264	0.4576	CNOC2
328.015045	-5.778802	0.0780	CNOC2
328.015350	-5.677466	0.3140	CNOC2
328.015381	-5.620141	0.5184	CNOC2
328.016479	-5.752558	0.4717	CNOC2
328.017548	-5.645673	0.0716	CNOC2
328.017639	-5.649170	0.0707	CNOC2
328.018463	-5.879587	0.4621	CNOC2
328.019775	-5.856432	0.2222	CNOC2
328.020508	-5.571562	0.4589	CNOC2
328.020538	-5.811216	0.5533	CNOC2
328.021179	-5.723945	0.3859	CNOC2
328.021423	-5.781580	0.4773	CNOC2
328.021637	-5.513518	0.4497	CNOC2
328.023590	-5.519319	0.2523	CNOC2
328.023895	-5.576906	0.4585	CNOC2
328.024841	-5.569736	0.1098	IMACS
328.025177	-5.826642	0.1415	CNOC2
328.025330	-5.684679	0.1821	CNOC2
328.026672	-5.687104	0.3925	CNOC2
328.026764	-5.620733	0.0707	CNOC2
328.027161	-5.818361	0.1402	CNOC2
328.028198	-5.884835	0.3602	CNOC2
328.028381	-5.631364	0.5251	CNOC2
328.029358	-5.550179	0.1216	CNOC2
328.029694	-5.775622	0.4792	CNOC2
328.031128	-5.632762	0.2197	CNOC2
328.031342	-5.480843	0.5458	CNOC2
328.032227	-5.727334	0.2425	CNOC2
328.032593	-5.883197	0.1070	CNOC2
328.034454	-5.500769	0.2414	CNOC2
328.034790	-5.656108	0.0983	CNOC2
328.035248	-5.673904	0.3672	CNOC2
328.036133	-5.750843	0.1158	CNOC2
328.037994	-5.803963	0.3323	CNOC2
328.038025	-5.591545	0.2411	CNOC2
328.038269	-5.585209	0.2407	CNOC2
328.038391	-5.486037	0.2707	CNOC2
328.039032	-5.762007	0.4387	CNOC2
328.039429	-5.743783	0.2207	CNOC2
328.040039	-5.599546	0.3251	CNOC2
328.040100	-5.867044	0.3013	CNOC2

RA	Dec	z	source	1 Mpc	$r_{200,\sigma}$	$r_{200,X}$
328.040558	-5.549266	0.3573	CNOC2
328.042236	-5.712427	0.4719	CNOC2
328.042664	-5.772941	0.4387	CNOC2
328.043121	-5.871876	0.3014	CNOC2
328.043304	-5.559723	0.4683	CNOC2
328.044037	-5.775322	0.4377	CNOC2
328.044220	-5.825719	0.4778	CNOC2
328.045319	-5.531168	0.2013	CNOC2
328.046692	-5.737091	0.4373	CNOC2
328.046814	-5.656377	0.2197	CNOC2
328.046906	-5.593381	0.2421	CNOC2
328.047089	-5.792534	0.5215	CNOC2
328.049103	-5.869847	0.3018	CNOC2
328.049316	-5.589442	0.2420	CNOC2
328.049835	-5.579228	0.2409	CNOC2
328.049988	-5.784844	0.3023	CNOC2
328.050049	-5.518582	0.3610	CNOC2
328.051819	-5.696826	0.6699	CNOC2
328.053192	-5.668780	0.2428	CNOC2
328.053436	-5.775186	0.1071	CNOC2
328.053558	-5.802777	0.4390	CNOC2
328.055359	-5.880666	0.3010	CNOC2
328.056488	-5.782123	0.3659	CNOC2
328.057526	-5.685847	0.2405	CNOC2
328.057770	-5.789083	0.1069	CNOC2

*Column description: object R.A. and Decl. for Equinox J2000.0 (columns 1 & 2); object redshift (3); source of object redshift (4); X-ray and/or optical group(s) for which object is a member for 1 Mpc, $r_{200,\sigma}$, & $r_{200,X}$ radial cuts (5,6,7).

Bibliography

- Anderson, T. W., & Darling, D. A. 1952, *The Annals of Mathematical Statistics*, 23, 193
- Andreon, S. 2010, *MNRAS*, 407, 263
- Andreon, S., & Moretti, A. 2011, *A&A*, 536, A37
- Andreon, S., Valtchanov, I., Jones, L. R., Altieri, B., Bremer, M., Willis, J., Pierre, M., & Quintana, H. 2005, *MNRAS*, 359, 1250
- Appenzeller, I., et al. 1998, *The Messenger*, 94, 1
- Balogh, M. L., Babul, A., Voit, G. M., McCarthy, I. G., Jones, L. R., Lewis, G. F., & Ebeling, H. 2006, *MNRAS*, 366, 624
- Balogh, M. L., Mazzotta, P., Bower, R. G., Eke, V., Bourdin, H., Lu, T., & Theuns, T. 2011a, *MNRAS*, 412, 947
- Balogh, M. L., et al. 2002, *ApJ*, 566, 123
- . 2007, *MNRAS*, 374, 1169
- . 2009, *MNRAS*, 398, 754
- . 2011b, *MNRAS*, 71
- Beers, T. C., Flynn, K., & Gebhardt, K. 1990, *AJ*, 100, 32
- Berlind, A. A., et al. 2006, *ApJS*, 167, 1
- Bertin, E., & Arnouts, S. 1996, *A&AS*, 117, 393
- Böhringer, H., et al. 2000, *ApJS*, 129, 435
- . 2004, *A&A*, 425, 367
- Broadhurst, T., Takada, M., Umetsu, K., Kong, X., Arimoto, N., Chiba, M., & Futamase, T. 2005, *ApJL*, 619, L143
- Bruzual, G., & Charlot, S. 2003, *MNRAS*, 344, 1000
- Cappellari, M., et al. 2006, *MNRAS*, 366, 1126

- Carlberg, R. G., Yee, H. K. C., & Ellingson, E. 1997, ApJ, 478, 462
- Carlberg, R. G., Yee, H. K. C., Morris, S. L., Lin, H., Hall, P. B., Patton, D. R., Sawicki, M., & Shepherd, C. W. 2001, ApJ, 552, 427
- Carlberg, R. G., et al. 1999, Royal Society of London Philosophical Transactions Series A, 357, 167
- Chabrier, G. 2003, ApJL, 586, L133
- Chandra Project Science, MSFC. 2011, The Chandra Proposers Observatory Guide, CXC
- Charlot, S., & Fall, S. M. 2000, ApJ, 539, 718
- Christensen, N., & Meyer, R. 2000, preprint (ArXiv:astro-ph/0006401)
- Cooper, M. C., et al. 2007, MNRAS, 376, 1445
- D'Agostino, R., & Stephens, M. 1986, Goodness-of-fit Techniques (Marcel Dekker Inc.)
- Dahle, H. 2007, ArXiv Astrophysics e-prints
- Dariush, A. A., Raychaudhury, S., Ponman, T. J., Khosroshahi, H. G., Benson, A. J., Bower, R. G., & Pearce, F. 2010, MNRAS, 405, 1873
- Davis, M., et al. 2003, in SPIE Conference Series, Vol. 4834, Society of Photo-Optical Instrumentation Engineers (SPIE) Conference Series, ed. P. Guhathakurta, 161–172
- Davis, M., et al. 2007, ApJL, 660, L1
- Dressler, A., & Shectman, S. A. 1988, AJ, 95, 985
- Dunkley, J., et al. 2009, ApJS, 180, 306
- Efron, B. 1987, The Jackknife, the Bootstrap, and Other Resampling Plans (CBMS-NSF Regional Conference Series in Applied Mathematics) (Society for Industrial Mathematics)
- Eke, V. R., Baugh, C. M., Cole, S., Frenk, C. S., King, H. M., & Peacock, J. A. 2005, MNRAS, 362, 1233
- Eke, V. R., et al. 2004, MNRAS, 348, 866
- Fernández-Soto, A., Lanzetta, K. M., & Yahil, A. 1999, ApJ, 513, 34
- Ferrando, P., et al. 2003, in SPIE Conference Series, Vol. 4851, Society of Photo-Optical Instrumentation Engineers (SPIE) Conference Series, ed. J. E. Truemper & H. D. Tananbaum, 232–242
- Finoguenov, A., et al. 2007, ApJS, 172, 182

- . 2009, ApJ, 704, 564
- Font, A. S., et al. 2008, MNRAS, 389, 1619
- Geller, M. J., & Huchra, J. P. 1983, ApJS, 52, 61
- Gerke, B. F., et al. 2005, ApJ, 625, 6
- . 2007, MNRAS, 376, 1425
- Ghizzardi, S., & Molendi, S. 2002, in ESA SP, Vol. 488, Proceedings of the Estec Conference: New Visions of the X-ray Universe in the XMM Newton and Chandra Era, ed. Jansen, F.
- Gilbank, D. G., Bower, R. G., Castander, F. J., & Ziegler, B. L. 2004, MNRAS, 348, 551
- Gilks, W. R., Richardson, S., & J., S. D. 1996, Markov Chain Monte Carlo Methods in Practice (London, UK: Chapman and Hall)
- Giordini, S., et al. 2009, ApJ, 703, 982
- Girardi, M., Giuricin, G., Mardirossian, F., Mezzetti, M., & Boschin, W. 1998, ApJ, 505, 74
- Girardi, M., & Mezzetti, M. 2001, ApJ, 548, 79
- Gladders, M. D., Hoekstra, H., Yee, H. K. C., Hall, P. B., & Barrientos, L. F. 2003, ApJ, 593, 48
- Gladders, M. D., & Yee, H. K. C. 2005, ApJS, 157, 1
- Glazebrook, K., Blake, C., Economou, F., Lilly, S., & Colless, M. 1999, MNRAS, 306, 843
- Glazebrook, K., & Bland-Hawthorn, J. 2001, PASP, 113, 197
- Gonzalez, A. H., Zaritsky, D., & Zabludoff, A. I. 2007, ApJ, 666, 147
- Hasinger, G., et al. 2001, A&A, 365, L45
- Helsdon, S. F., & Ponman, T. J. 2000a, MNRAS, 319, 933
- . 2000b, MNRAS, 315, 356
- Henderson, R. D. E. 2010, Master's thesis, McMaster University, Open Access Dissertations and Theses Paper 4208
- Hoekstra, H., Franx, M., & Kuijken, K. 2000, ApJ, 532, 88
- Hoekstra, H., & Jain, B. 2008, Annual Review of Nuclear and Particle Science, 58, 99
- Holder, G. P., McCarthy, I. G., & Babul, A. 2007, MNRAS, 382, 1697
- Horner, D. J. 2001, PhD thesis, University of Maryland College Park

- Hou, A., Parker, L. C., Harris, W. E., & Wilman, D. J. 2009, ApJ, 702, 1199
- Hou, A., et al. 2012, MNRAS, 421, 3594
- Huchra, J. P., & Geller, M. J. 1982, ApJ, 257, 423
- Iovino, A., et al. 2010, A&A, 509, A40+
- Jeltema, T. E., Mulchaey, J. S., & Lubin, L. M. 2008, ApJ, 685, 138
- Jeltema, T. E., Mulchaey, J. S., Lubin, L. M., & Fassnacht, C. D. 2007, ApJ, 658, 865
- Jeltema, T. E., Mulchaey, J. S., Lubin, L. M., Rosati, P., & Böhringer, H. 2006, ApJ, 649, 649
- Kelly, B. C. 2007, ApJ, 665, 1489
- Kelson, D. D. 2003, PASP, 115, 688
- Kenter, A., et al. 2005, ApJS, 161, 9
- Kirsch, M. G. F., et al. 2004, in SPIE Conference Series, Vol. 5488, Society of Photo-Optical Instrumentation Engineers (SPIE) Conference Series, ed. G. Hasinger & M. J. L. Turner, 103–114
- Knobel, C., et al. 2009, ApJ, 697, 1842
- Koester, B. P., et al. 2007, ApJ, 660, 221
- Komatsu, E., et al. 2009, ApJS, 180, 330
- Kovač, K., et al. 2010, ApJ, 718, 86
- LaRoque, S. J., et al. 2003, ApJ, 583, 559
- Leauthaud, A., et al. 2010, ApJ, 709, 97
- . 2012, ApJ, 746, 95
- Lilly, S. J., Tresse, L., Hammer, F., Crampton, D., & Le Fevre, O. 1995, ApJ, 455, 108
- Lilly, S. J., et al. 2009, ApJS, 184, 218
- Łokas, E. L., & Mamon, G. A. 2001, MNRAS, 321, 155
- Longhetti, M., & Saracco, P. 2009, MNRAS, 394, 774
- Lumb, D. H., Finoguenov, A., Saxton, R., Aschenbach, B., Gondoin, P., Kirsch, M., & Stewart, I. M. 2003, Experimental Astronomy, 15, 89
- Lumb, D. H., Warwick, R. S., Page, M., & De Luca, A. 2002, A&A, 389, 93

- Madau, P., Pozzetti, L., & Dickinson, M. 1998, ApJ, 498, 106
- Mahdavi, A., Boehringer, H., Geller, M. J., & Ramella, M. 1997, ApJ, 483, 68
- Mahdavi, A., & Geller, M. J. 2001, ApJL, 554, L129
- Mainieri, V., et al. 2007, ApJS, 172, 368
- Marian, L., & Bernstein, G. M. 2006, Physical Review D, 73, 123525
- Marinoni, C., Davis, M., Newman, J. A., & Coil, A. L. 2002, ApJ, 580, 122
- Massey, R., et al. 2007, Nature, 445, 286
- McGee, S. L., Balogh, M. L., Henderson, R. D. E., Wilman, D. J., Bower, R. G., Mulchaey, J. S., & Oemler, Jr., A. 2008, MNRAS, 387, 1605
- McGee, S. L., Balogh, M. L., Wilman, D. J., Bower, R. G., Mulchaey, J. S., Parker, L. C., & Oemler, A. 2011, MNRAS, 413, 996
- Miller, C. J., et al. 2005, AJ, 130, 968
- Miyazaki, S., Hamana, T., Ellis, R. S., Kashikawa, N., Massey, R. J., Taylor, J., & Refregier, A. 2007, ApJ, 669, 714
- Mulchaey, J. S., Davis, D. S., Mushotzky, R. F., & Burstein, D. 2003, ApJS, 145, 39
- Mulchaey, J. S., Lubin, L. M., Fassnacht, C., Rosati, P., & Jeltema, T. E. 2006, ApJ, 646, 133
- Mulchaey, J. S., & Zabludoff, A. I. 1998, ApJ, 496, 73
- Navarro, J. F., Frenk, C. S., & White, S. D. M. 1995, MNRAS, 275, 56
- Nelson, L. 1998, Journal of Quality Technology, 30, 298
- Oguri, M., et al. 2009, ApJ, 699, 1038
- Okabe, N., Takada, M., Umetsu, K., Futamase, T., & Smith, G. P. 2010, Publications of the Astronomical Society of Japan, 62, 811
- Osmond, J. P. F., & Ponman, T. J. 2004, MNRAS, 350, 1511
- Parker, L. C., Hudson, M. J., Carlberg, R. G., & Hoekstra, H. 2005, ApJ, 634, 806
- Peeples, M. S., & Shankar, F. 2011, MNRAS, 417, 2962
- Planck Collaboration et al. 2011, A&A, 536, A12
- Ponman, T. J., Bourner, P. D. J., Ebeling, H., & Böhringer, H. 1996, MNRAS, 283, 690

- Popesso, P., & Biviano, A. 2006, *A&A*, 460, L23
- Popesso, P., Biviano, A., Böhringer, H., & Romaniello, M. 2007a, *A&A*, 461, 397
- Popesso, P., Biviano, A., Böhringer, H., Romaniello, M., & Voges, W. 2005, *A&A*, 433, 431
- Popesso, P., Biviano, A., Romaniello, M., & Böhringer, H. 2007b, *A&A*, 461, 411
- Popesso, P., Böhringer, H., Brinkmann, J., Voges, W., & York, D. G. 2004, *A&A*, 423, 449
- Pratt, G. W., Croston, J. H., Arnaud, M., & Böhringer, H. 2009, *A&A*, 498, 361
- Ramella, M., Boschin, W., Geller, M. J., Mahdavi, A., & Rines, K. 2004, *AJ*, 128, 2022
- Refregier, A. 2003, *ARA&A*, 41, 645
- Rykoff, E. S., et al. 2008a, *ApJ*, 675, 1106
- . 2008b, *MNRAS*, 387, L28
- Salim, S., et al. 2007, *ApJS*, 173, 267
- Sanderson, A. J. R., Edge, A. C., & Smith, G. P. 2009, *MNRAS*, 398, 1698
- Saxton, R. D., et al. 2005, in *5 years of Science with XMM-Newton*, ed. U. G. Briel, S. Sembay, & A. Read, 149–152
- Serra, A. L., Diaferio, A., Murante, G., & Borgani, S. 2011, *MNRAS*, 412, 800
- Sheldon, E. S., et al. 2009, *ApJ*, 703, 2232
- Smith, G. P., & Taylor, J. E. 2008, *ApJL*, 682, L73
- Snowden, S. L., Mushotzky, R. F., Kuntz, K. D., & Davis, D. S. 2008, *A&A*, 478, 615
- Sun, M., Voit, G. M., Donahue, M., Jones, C., Forman, W., & Vikhlinin, A. 2009, *ApJ*, 693, 1142
- Sunyaev, R. A., & Zeldovich, Y. B. 1972, *Comments on Astrophysics and Space Physics*, 4, 173
- Tran, K.-V. H., Moustakas, J., Gonzalez, A. H., Bai, L., Zaritsky, D., & Kautsch, S. J. 2008, *ApJL*, 683, L17
- Tyler, K. D., et al. 2011, *ApJ*, 738, 56
- Valtchanov, I., et al. 2004, *A&A*, 423, 75
- Vikhlinin, A., McNamara, B. R., Forman, W., Jones, C., Quintana, H., & Hornstrup, A. 1998, *ApJ*, 502, 558
- Vikhlinin, A., et al. 2009, *ApJ*, 692, 1033

- Voit, G. M. 2005, *Reviews of Modern Physics*, 77, 207
- Watson, M. G., et al. 2001, *A&A*, 365, L51
- White, S. D. M., et al. 2005, *A&A*, 444, 365
- Wilman, D. J., Balogh, M. L., Bower, R. G., Mulchaey, J. S., Oemler, A., Carlberg, R. G., Morris, S. L., & Whitaker, R. J. 2005a, *MNRAS*, 358, 71
- Wilman, D. J., Oemler, Jr., A., Mulchaey, J. S., McGee, S. L., Balogh, M. L., & Bower, R. G. 2009, *ApJ*, 692, 298
- Wilman, D. J., et al. 2005b, *MNRAS*, 358, 88
- . 2008, *ApJ*, 680, 1009
- Wilson, G., Cowie, L. L., Barger, A. J., & Burke, D. J. 2002, *AJ*, 124, 1258
- XMM-Newton SOC. 2011, XMM-Newton Users Handbook, ESA
- Xue, Y.-J., & Wu, X.-P. 2000, *ApJ*, 538, 65
- Yang, X., Mo, H. J., & van den Bosch, F. C. 2009, *ApJ*, 695, 900
- Yang, X., Mo, H. J., van den Bosch, F. C., & Jing, Y. P. 2005, *MNRAS*, 357, 608
- Yang, X., Mo, H. J., van den Bosch, F. C., Pasquali, A., Li, C., & Barden, M. 2007, *ApJ*, 671, 153
- Yee, H. K. C., et al. 2000, *ApJS*, 129, 475
- Zabludoff, A. I., & Mulchaey, J. S. 1998, *ApJ*, 496, 39
- . 2000, *ApJ*, 539, 136
- Zhang, Y.-Y., Andernach, H., Caretta, C. A., Reiprich, T. H., Böhringer, H., Puchwein, E., Sijacki, D., & Girardi, M. 2011, *A&A*, 526, A105
- Zhang, Y.-Y., Finoguenov, A., Böhringer, H., Ikebe, Y., Matsushita, K., & Schuecker, P. 2004, *A&A*, 413, 49
- Zimer, M. E., Mulchaey, J. S., & Zabludoff, A. I. 2002, in *Astronomical Society of the Pacific Conference Series*, Vol. 268, Tracing Cosmic Evolution with Galaxy Clusters, ed. S. Borgani, M. Mezzetti, & R. Valdarnini, 459

Acknowledgements

Gratitude must first go to my graduate advisor, Dave Wilman, whose intellectual creativity and unwavering passion for his (and my) work were invaluable. Second, to Alexis Finoguenov, whose support both figuratively and literally made completing this thesis work possible. Thanks also to the OPINAS group at MPE and especially my advisor Roberto Saglia. To the GEEC, many thanks for being such an excellent group (pun intended) of collaborators. Specific thanks go to John Mulchaey, for being not just an eminent scientist but one of the best observing partners around, and to Annie Hou, a student who is an absolute joy to work with. I thank also Stefania Giolini for extremely helpful research discussions. To the best officemate and friend a graduate student could ask for, Francesco Montesano, I am forever indebted. I am also indebted to Frau Ingram for going above and beyond the call duty of a secretary on more than one occasion and Achim Bohnet for superb technical support.

I acknowledge support from and participation in the International Max-Planck Research School on Astrophysics at the Ludwig-Maximilians University. I would like to thank the CNOC2 team for the use of their unpublished data and ESO and The Carnegie Institution of Washington for their amazing facilities. I acknowledge the use of the FORS and COSMOS pipelines and thank Dr. Carlo Izzo at ESO for pipeline assistance and insight which I could not have managed without and Renbin Yan for providing the ZSPEC software. I thank Russell Blackport for the reduction of and measurements of redshifts from GMOS data. Marisa Girardi also provided valuable input. To the High Energy Group at MPE, a ‘late adopter’ of this graduate student, I thoroughly appreciate both the support and the dynamic environment provided at the end of my PhD.

Thanks to my mother and father for always encouraging their children to explore the sciences and work hard at their chosen endeavor, however unconventional it may be. To my younger siblings, Sean and Kate, and to my older sister, Sandi, thanks for all the empathy and perspective. Thanks to the whole family, wonderful grandmothers included, who made me feel less far from ‘home.’ I am very privileged and grateful to have had an undergraduate advisor, Robert Boyle, who has been a constant source of encouragement and guidance since my very first intro astro course. I am also thankful to the Department of Astrophysics at the American Museum of Natural History for giving me the opportunity to do excellent research after my master’s degree and specifically to Dave Zurek, Michael Shara, and Mordecai-Mark Mac Low for encouraging me to pursue and aiming me at Germany for my doctoral studies. Thanks to the ESME singers here in Munich, both for being such a lovely group to make music with and for their patience with this novice conductor. To Jill Gerke, Camilla Juul Hansen, Libby Jackson, Emily Tuffley, James Aslaksen, Barbara Gaerte, Genevieve Holmes, Daniel Plappert, and all who have given love, advice, and support and listened to lengthy monologues about research and graduate student struggles these past few years, thank you so much. Final thanks go to Kate Reader for

proofreading so much of this tome and providing moral support and proper tea during defense preparation.

Curriculum Vitae

Jennifer Lynn Connelly

Departmental Address

Max Planck Institute for Extraterrestrial Physics
Giessenbachstrasse 1
85748 Garching, Germany
+49-89-30000-3775
jcon@mpe.mpg.de

Address Until 9/2012

Zittelstrasse 4
80796 Munich
Germany

Permanent Address

1306 Mountain Rd
Montoursville, PA
17754
USA

EDUCATION

International Max-Planck Research School on Astrophysics

Ludwig Maximilian University, Munich, Germany

Qualifying Exam - passed 2007
Dissertation Defense - expected July 2012

Wesleyan University, Middletown, CT

Masters of Arts in Astronomy
Graduation Date: 05/2006
Overall GPA: 3.39/4.0

Dickinson College, Carlisle, PA

Bachelor of Science, *Magna Cum Laude*
Graduation Date: 05/2004
Majors: Political Science & Physics
Minor: Astronomy
Overall GPA 3.69/4.0

RELEVANT WORK EXPERIENCE

8/01/2006 - 8/01/2007

American Museum of Natural History Department of Astrophysics

Research Data Analyst – New York City, NY

Retrieved and analyzed near- and far-UV HST data of the central region of globular cluster NGC 6681. Combined observations to obtain the deepest image of a globular cluster in these wavebands to date. Identified the hot stellar populations.

9/01/2004 - 6/01/2006

Wesleyan University Department of Astronomy, Middletown, CT

Teaching Assistant Introductory & Advanced Undergraduate Astronomy Courses

Assisted professors in lecturing. Led laboratory sessions and held office hours. Graded.

24 Inch Perkin Telescope Observing Program

Obtained data and calibration fields once a week using the 24" Perkin telescope. Data used primarily for studying T Tauri stars in a program directed by Dr. Bill Herbst.

Public Observing Program

Operated 16" telescope for public outreach nights. Produced and gave presentations to visiting groups.

6/01/2004 - 8/10/2004

National Academy of Sciences

Space Studies Board Intern – Washington, DC

Worked with the Space Studies Board, its committees, and staff on several advisory projects. Conducted background research, attended and assisted in meetings, and compiled presentations and written reports for committees including the Committee on the Origin and Evolution of Life and the Committee on Planetary and Lunar Exploration. Attended and reported on House congressional science committee hearings.

11/01/2001 - 5/26/2004

Dickinson College Department of Physics and Astronomy, Carlisle, PA

Charles M. Kanev Planetarium

Operated all planetarium equipment. Wrote, recorded, programmed, set up, organized, and presented planetarium shows to the college and surrounding community. Oversaw general outreach programs.

Observatory Teaching Assistant

Operated all telescopes including 24 Michael Britton telescope. Taught constellations and other celestial objects. Administered quizzes.

Laboratory Teaching Assistant Workshop Physics, Intro Astronomy, Optics

Assisted professors in basic teaching. Answered questions. Set-up and maintained equipment and lab safety where appropriate. Graded.

Student Director Michael Britton Observatory

Supervised public outreach involving 24 telescope.

5/26/2003 - 8/16/2003

National Optical Astronomy Observatory/Kitt Peak National Observatory Research Experience for Undergraduates

Research Assistant – Tucson, AZ

Conducted research with Dr. Katy Garmany and Dr. John Glaspey on M18. Analyzed UBVRI photometry using IRAF and IDL, obtained spectra of target stars using Kitt Peak 2.1 meter and performed preliminary reduction, presented talk to NOAO scientists.

7/16/2001 - 7/27/2001

Lycoming College, Williamsport, PA

Teacher Lycoming College For Kids Program

Developed lesson plans, gathered necessary materials and equipment, and taught elementary chemistry and physics concepts to students in second through fourth grades.

7/01/2000 - 1/31/2000

**Penn State University Department of Agronomy, State College, PA
Laboratory Assistant**

Performed field and laboratory work including gathering and measuring of plant and soil samples, running laboratory experiments with root samples, operating rain shelters and other technical equipment, measuring light and determining the chemical composition of samples, and organizing data. Work contributed to graduate thesis of Dr. Maria Labreveux.

Refereed Publications

Connelly, J. L., Wilman, D., Finoguenov, A., Hou, A., et al., Exploring the Diversity of Groups at $0.1 < z < 0.8$ with X-ray and Optically Selected Samples, ApJ, accepted

Hou, A., Parker, L., Wilman, D. McGee, S., Harris, W., Connelly, J.L., et al., Substructure in the GEEC Groups: Field-like Populations in Dynamically Active Groups, MNRAS, accepted

Balogh, M. L., McGee, S. L., Wilman, D. J., Finoguenov, A., Parker, L. C., Connelly, J. L., et al. 2010, Direct observational evidence for a large transient galaxy population in groups at $0.85 < z < 1$, MNRAS, 412, 4

Finoguenov, A., Connelly, J. L., Parker, L. C., et al. 2009, The roadmap for unification in galaxy group selection: I. A search for extended X-ray emission in the CNOC2 survey, ApJ, 704, 564

Non-Refereed Publications

Comparing the Multiwavelength Properties of Nearby and Distant Obscured Active Galaxies
Masters Thesis, Wesleyan University, 2006

CCD Photometry and Analysis of the Eclipsing Binary System HH Ursae Majoris
Honors Thesis, Dickinson College, 2004

External Talks and Posters

The Fingerprint of the IGM: Galaxy Populations in X-ray Bright and X-ray Faint Groups at Intermediate Redshift, 2010, Talk, American Astronomical Society Meeting #215

The Fingerprint of the IGM: Galaxy Populations in X-ray Bright and X-ray Faint Galaxy Groups at $0.2 < z < 0.6$, 2009, Poster, Galaxy Evolution and Environment Conference

The Deepest UV Observations of a Globular Cluster: Preliminary Results for NGC 6681, 2007,
Poster, American Astronomical Society Meeting #209

Integrated Spectral Energy Distributions of Nearby Seyfert 2 Galaxies: Implications for the Nature of Distant GOODS Sources 2006, Poster, American Astronomical Society Meeting #207

Photometry of the Open Cluster M18 (NGC 6613), 2004, Poster, American Astronomical Society

Meeting #203

Scientific Observing Experience

- Very Large Telescope (VLT) 8.2m, ESO (PI & CoI, 3 nights)
Focal Reducer and low dispersion Spectrograph 2 (FORS2)
- Magellan 6.5m Telescope, Carnegie Observatories (CoI, 3 nights)
Inamori Magellan Areal Camera and Spectrograph (IMACS)
- 24" Perkin Telescope, Wesleyan University (~26 nights)
- National Undergraduate Research Observatory 31" telescope, Lowell Observatory (~14 nights)
- 24" Michael Britton telescope, Dickinson College (~14 nights)

Public Outreach

- Open Houses at the Max Planck Institute for Extraterrestrial Physics (2010-2011)
- Wesleyan University Public Observing Program (2004-2006)
Operated telescope for public outreach. Produced and gave presentations to visitors.
- Nightly Observing Program at Kitt Peak National Observatory (Summer 2003)
Assisted with talks and observations.
- Student Director Charles M. Kanev Planetarium (2003-2004)
Wrote, recorded, programmed, organized, and presented planetarium shows.
- Student Director Michael Britton Observatory (2003-2004)
Supervised and presented public outreach involving 24" telescope.

Professional Societies

American Astronomical Society (AAS)

Computing Experience

Operating Systems: PC, Mac, Linux, Unix, and Sun

Software/languages:

- Image Reduction and Analysis Facility (IRAF) – 7 years
- IDL – 5 years

- Python – 2 years
- Bash – 3 years
- Java – 6 months
- Latex – 5 years
- Excel – 6 years
- Mathematica – 1 year
- Maple – 6 months

Languages

- English (native)
- German (intermediate)
- Spanish (basic)